Vol. 291, No. 1–2, June 10, 1994

ISSN 0003-2670

ANALYTICA CHIMICA ACTA

An international journal devoted to all branches of analytical chemistry

ELSEVIER

ANALYTICA CHIMICA ACTA

Scope. *Analytica Chimica Acta* publishes original papers, rapid publication letters and reviews dealing with every aspect of modern analytical chemistry. Reviews are normally written by invitation of the editors, who welcome suggestions for subjects. Letters can be published within **four months** of submission. For information on the Letters section, see inside back cover.

Submission of Papers

Americas

Prof. Harry L. Pardue
Department of Chemistry
1393 BRWN Bldg, Purdue University
West Lafayette, IN 47907–1393
USA

Tel:(+1-317) 494 5320
Fax:(+1-317) 496 1200

Computer Techniques

Prof. J.T. Clerc
Universität Bern
Pharmazeutisches Institut
Baltzerstrasse 5, CH-3012 Bern
Switzerland

Tel:(+41-31) 6314191
Fax:(+41-31) 6314198

Prof. Sarah C. Rutan
Department of Chemistry
Virginia Commonwealth University
P.O. Box 2006
Richmond, VA 23284-2006
USA
Tel:(+1-804) 367 7517
Fax:(+1-804) 367 8599

Other Papers

Prof. Alan Townshend
Department of Chemistry
The University
Hull HU6 7RX
Great Britain

Tel:(+44-482) 465027
Fax:(+44-482) 466410

Prof. Willem E. van der Linden
Laboratory for Chemical Analysis
Department of Chemical Technology
Twente University of Technology
P.O. Box 217, 7500 AE Enschede
The Netherlands
Tel:(+31-53) 892629
Fax:(+31-53) 356024

Prof. Paul Worsfold
Dept. of Environmental Sciences
University of Plymouth
Plymouth PL4 8AA
Great Britain

Tel:(+44-752) 233006
Fax:(+44-752) 233009

Submission of an article is understood to imply that the article is original and unpublished and is not being considered for publication elsewhere. *Anal. Chim. Acta* accepts papers in English only. There are no page charges. Manuscripts should conform in layout and style to the papers published in this issue. See inside back cover for "Information for Authors".

Publication. *Analytica Chimica Acta* appears in 16 volumes in 1994 (Vols. 281–296). *Vibrational Spectroscopy* appears in 2 volumes in 1994 (Vols. 6 and 7). Subscriptions are accepted on a prepaid basis only, unless different terms have been previously agreed upon. It is possible to order a combined subscription (*Anal. Chim. Acta* **and** *Vib. Spectrosc.*).
Our p.p.h. (postage, packing and handling) charge includes surface delivery of all issues, except to subscribers in the U.S.A., Canada, Australia, New Zealand, China, India, Israel, South Africa, Malaysia, Thailand, Singapore, South Korea, Taiwan, Pakistan, Hong Kong, Brazil, Argentina and Mexico, who receive all issues by air delivery (S.A.L.–Surface Air Lifted) at no extra cost. For Japan, air delivery requires 25% additional charge of the normal postage and handling charge; for all other countries airmail and S.A.L. charges are available upon request.

Subscription orders. Subscription prices are available upon request from the publisher. Subscription orders can be entered only by calendar year and should be sent to: Elsevier Science B.V., Journals Department, P.O. Box 211, 1000 AE Amsterdam, The Netherlands. Tel: (+31-20) 5803 642, Telex: 18582, Telefax: (+31-20) 5803598, to which requests for sample copies can also be sent. Claims for issues not received should be made within six months of publication of the issues. If not they cannot be honoured free of charge. Readers in the U.S.A. and Canada can contact the following address: Elsevier Science Inc., Journal Information Center, 655 Avenue of the Americas, New York, NY 10010, U.S.A. Tel: (+1-212) 6333750, Telefax: (+1-212) 6333990, for further information, or a free sample copy of this or any other Elsevier Science journal.
Advertisements. Advertisement rates are available from the publisher on request.

US mailing notice – Analytica Chimica Acta (ISSN 0003-2670) is published 3 times a month (total 48 issues) by Elsevier Science B.V. (Molenwerf 1, Postbus 211, 1000 AE Amsterdam). Annual subscription price in the USA US$ 3035.75 (valid in North, Central and South America), including air speed delivery. Second class postage paid at Jamaica, NY 11431. *USA Postmasters*: Send address changes to Anal. Chim. Acta, Publications Expediting, Inc., 200 Meacham Av., Elmont, NY 11003. Airfreight and mailing in the USA by Publication Expediting.

ANALYTICA CHIMICA ACTA

An international journal devoted to all branches of analytical chemistry

(Full texts are incorporated in CJELSEVIER, a file in the Chemical Journals Online database available on STN International; Abstracted, indexed in: Aluminum Abstracts; Anal. Abstr.; Biol. Abstr.; BIOSIS; Chem. Abstr.; Curr. Contents Phys. Chem. Earth Sci.; Engineered Materials Abstracts; Excerpta Medica; Index Med.; Life Sci.; Mass Spectrom. Bull.; Material Business Alerts; Metals Abstracts; Sci. Citation Index)

VOL. 291 NO. 1–2 JUNE 10, 1994

CONTENTS

Chemometrics

Projection of Prim's minimal spanning tree into a Kohonen neural network for identification of airborne particle sources by their multielement trace patterns
D. Wienke (Nijmegen, Netherlands) and P.K. Hopke (Potsdam, NY, USA) 1

Feature extraction of polysaccharides by low-dimensional internal representation neural networks and infrared spectroscopy
S.P. Jacobsson (Uppsala, Sweden) 19

Knowledge-based fault detection and diagnosis in flow-injection analysis
J. Brandt and B. Hitzmann (Hannover, Germany) 29

Electroanalytical Chemistry and Sensors

Impulse–response functions of flow-through detectors based on the membrane-stabilised liquid–liquid interface. Part I. Mathematical treatment
S. Wilke and R. Picht (Merseburg, Germany) 41

Polarographic behaviour and determination of norfloxacin in tablets
A.M.Y. Jaber and A. Lounici (Dhahran, Saudi Arabia) 53

Surface studies of quinhydrone pH sensors
C. Aquino-Binag, P.J. Pigram, R.N. Lamb and P.W. Alexander (Kensington, Australia) 65

Study of cathodic stripping of copper in hydrochloric acid medium. Simultaneous determination of cadmium, lead and copper by combined anodic and cathodic stripping voltammetry
T. Nedeltcheva, L. Costadinnova and M. Athanassova (Sofia, Bulgaria) 75

Mercury(II) acetate–Nafion modified electrode for anodic stripping voltammetry of lead and copper with flow-injection analysis
R.R. Dalangin and H. Gunasingham (Singapore) 81

Atomic Spectrometry

Vapour generation atomic absorption spectrometry. Review
X.-P. Yan and Z.-M. Ni (Beijing, China) 89

Metal ion interferences in determination of sulphur by flame molecular emission spectrometry
S. Hauge, K. Marøy (Bergen, Norway) and A. Thorlacius (Reykjavík, Iceland) 107

Determination of aluminium in biological materials by electrothermal atomic absorption spectrometry with a tungsten tube atomizer
K. Ohta, M. Yokoyama, S.-i. Itoh, S. Kaneco and T. Mizuno (Mie, Japan) 115

Indirect determination of polychlorinated organic compounds in environmental samples by molecular emission cavity analysis
V.I. Rigin (Krasnoyarsk, Russian Federation) 121

(Continued overleaf)

Contents (continued)

Mass Spectrometry

Graphite furnace hydride preconcentration and subsequent detection by inductively coupled plasma mass spectrometry
I. Marawi, J. Wang and J.A. Caruso (Cincinnati, OH, USA) 127

Molecular Spectrometry

Cold decomposition procedure for the spectrophotometric determination of manganese in rocks, ores and minerals
C.R.M. Rao (Madras, India) 137

Spectrofluorimetric determination of reserpine in pharmaceutical preparations and biological fluids
F.A. Aly, A. El-Brashy and F. Belal (Mansoura, Egypt) 141

Surface-enhanced Raman spectrometry on a silver substrate prepared by the nitric acid etching method
A. Rupérez and J.J. Laserna (Málaga, Spain) 147

Chromatography

Gas chromatographic–mass spectrometric confirmation of a clostebol metabolite in urine
G. Debruyckere, R. De Sagher, C. Van Peteghem, G. Van Vyncht, G. Maghuin-Rogister (Gent, Belgium) and E. De Pauw (Liège, Belgium) 155

Platinum species analysis in plant material by gel permeation chromatography
J. Messerschmidt, F. Alt and G. Tölg (Dortmund, Germany) 161

Chromatographic behaviour of novel zinc(II) carboxylates with nitrogen-donor ligands. Part I. Formates and acetates
A. Oriňák (Košice, Slovak Republic), E. Matisová (Bratislava, Slovak Republic), K. Györyová (Košice, Slovak Republic) and L. Šlesárová (Košice, Slovak Republic) 169

Capillary micellar electrokinetic chromatography based on indirect semiconductor laser fluorescence detection
T. Fuchigami and T. Imasaka (Fukuoka, Japan) 183

2,2′-Dithiobis(1-amino-4,5-dimethoxybenzene) as a highly sensitive, selective and stable fluorescence derivatization reagent for aromatic aldehydes in liquid chromatography
S. Hara, M. Nakamura, F. Sakai, H. Nohta, Y. Ohkura and M. Yamaguchi (Fukuoka, Japan) 189

A fluorogenic reagent for amino acids in liquid chromatography, 4-(2-cyanoisoindolyl)phenylisothiocyanate
O. Imakyure, M. Kai and Y. Ohkura (Fukuoka, Japan) 197

Determination of 2,4,6-trinitrotoluene and its biodegradation products by normal-phase liquid chromatography
H. Zou (Dalian, China), S. Zhou, X. Hu (Nanjing, China), M. Hong, Y. Zhang and P. Lu (Dalian, China) 205

ANALYTICA CHIMICA ACTA
VOL. 291 (1994)

ANALYTICA CHIMICA ACTA

An international journal devoted to all branches of analytical chemistry
Revue internationale consacrée à tous les domaines de la chimie analytique
Internationale Zeitschrift für alle Gebiete der analytischen Chemie

Anal. Chim. Acta, Vol. 291 (1994)

ELSEVIER, Amsterdam–Lausanne–New York–Oxford–Shannon–Tokyo

0003-2670/94/$07.00

ELSEVIER

Analytica Chimica Acta 291 (1994) 1–18

ANALYTICA CHIMICA ACTA

Projection of Prim's minimal spanning tree into a Kohonen neural network for identification of airborne particle sources by their multielement trace patterns

Dietrich Wienke [a], Philip K. Hopke [b,*]

[a] *Catholic University of Nijmegen, Laboratory for Analytical Chemistry, Toernooiveld 1, 6525 ED Nijmegen, Netherlands*
[b] *Clarkson University, Department of Chemistry, Potsdam, NY 13699-5810, USA*

(Received 28th October 1993)

Abstract

A hybrid pattern recognition method has been developed as an alternative receptor modelling technique for the identification of sources of coarse airborne particles. The Kohonen self-organizing neural network is first applied to yield a topological map of an m-dimensional variables space. Unfortunately, during the projection into a low-dimensional subspace, most of the information about the correct distance between the sample vectors is lost. However, the Kohonen network is a useful a priori step of data compression before application of the minimal spanning tree. Prim's minimal spanning tree partly compensates for this loss yielding the distance interrelationships between groups of the samples. This combination of both projection techniques can overcome some of their individual deficiencies. Several illustrative examples are presented to demonstrate the nature of the analysis results. Then a set of airborne particle compositions for samples obtained at a single sampling site were analysed. After transferring the combined map to a geographical unit circle (GUC), a correct pattern of the main industrial emission sources around a sampling site in Granite City (Illinois, USA) has been obtained by decoding a 35-dimensional space of chemical-analytical variables into a visually and geographically interpretable 2-D space.

Key words: Artificial neural networks; Airborne particles; Minimal spanning tree; Multielement trace analysis; Neural Networks; Pattern recognition

1. Introduction

In the last few years, receptor modeling based on chemical analytical measurements of airborne particle compositions has become an instrument for scientific and political decisions regarding the control of air pollution in a given geographical area [1]. The main aim of receptor modelling is the processing of univariate and multivariate data for the detection of local and regional sources of air pollution, for the combination of meteorological information with chemical-analytical data and for the comparison of the modelling results with the knowledge about the emission inventory in the given geographical area. However, neither receptor modelling techniques such as classical

* Corresponding author.

SSDI 0003-2670(94)00083-X

pattern recognition by hierarchical cluster analysis or non-linear mapping [1–3] nor receptor modelling on basis of two or three dimensional factor analysis methods [1–4] provide geographically direct interpretable maps of the location of the distinct air pollution sources. One receptor modelling method that simultaneously processes chemical, geographical and meteorological information is potential source contribution function (PSCF) analysis [5]. A PSCF analysis combines the ambient concentrations of a single chemical species with meteorological data in the form of backward air parcel trajectories and is able to yield a gridded map identifying the possible geographic locations of emission sources for this particular species. However, the results are only as good as the back trajectory results are.

The present work explores the possibilities for the application of artificial neural networks as an alternative for environmental analytical receptor modelling. Artificial neural networks are mathematical models of the brain and since the early forties, have been studied as part of the development of neural sciences, mathematics and computer sciences. Among the several types of artificial neural networks, Kohonen's neural network describes a special model of the brain. This model is based on the discovery, that the brain seems to be able to map images, noise, language, knowledge, etc. into extremely highly organized by physically low-dimensional packets of 1-D, 2-D and 3-D arrangements of neurons. On this basis, Kohonen presented in 1981 [6] a self-organizing feature map [7] with algorithmic simplicity and high quality of the topological correctness of the projected data vectors.

Currently Kohonen's feature maps have been found also of interest in chemistry. Gross and Seibert [8] evaluated satellite images of remote spectrochemical measurements of environmental data. They mapped the images by Kohonen's method and used the detected qualitative clusters to form representative training classes for back-propagation neural networks and for supervised pattern recognition with the vector quantizer method. Arrigo et al. [9] used the method to evaluate nucleic acid sequences. An application to a quantitative activity structure relationship study (QSAR) has been reported recently by Ross et al. [10]. Melssen et al. [11] clustered a data base of IR spectra by a parallel implementation of the network. Zupan et al. [12,13] projected multivariate chemical data, characterizing several kinds of Italian wines into a low-dimensional subspace.

However, the pure Kohonen map has a deficiency as do any other classical projections down to a lower dimensionality. During the projection of the data, the information about correct distance is lost. A close neighbour in the low-dimensional Kohonen map is not necessarily a close neighbour object in the m-space.

A completely different projection technique called minimal spanning tree (MST) became well known to the chemometricians by the distribution of the early PDP-version of the ARTHUR software package of Kowalski [14]. Literature about the MST can be traced back to the work of Florek (see [15–17]) in the early fifties. The method continues to be of interest for chemical pattern recognition as shown by recent publications of Dussert et al. in cluster chemistry [18] and in monitoring of the growth of thin films [19]. Kohonen used a small artificial data set for a comparison of the MST with his feature map ([7], pp. 141–142).

In contrast to a Kohonen feature map, a minimal spanning tree yields information about distance relationships between sample vectors and groups of them. However, the MST is not a data projection technique. This missing topological information about the relative spatial location of linked clusters in the m-space reduces the usefulness of the MST for chemical data interpretation. To overcome this problem the MST can be drawn between the objects in a 2-D or 3-D scores plot obtained from a principal component analysis (PCA), for example. However, a second limitation with the MST exists. On quickly looses the overview because of the large number of MST connection lines if there are more than 100 objects to project simultaneously. Furthermore, to find a suitable pairwise PCA plot becomes difficult if a large number of principal components is significant. In such a situation a high number of PCA plots has to be evaluated to avoid a lost of

information by projection error. Another trick is using the longest connection line in the Tree as the central axis of the plot. Even this approach can produce a confusing plot for more than 100 objects.

To overcome the discussed problems the present work proposes to superimpose a Kohonen self-organizing feature map with Prim's minimal spanning tree. There is a second aim behind this new algorithm. The aim is to force the projection into a directly geographical interpretable 2-D map. The new technique is developed to examine the structure of airborne particle compositions so as to assist in the identification of possible source–receptor relationships.

To explore the new algorithm, it is first applied to several simulated data sets with known structure. As an application of the combined techniques to real data, a projection of trace element patterns of airborne particles is reported. By decoding of the m-dimensional space of chemical variables a geographically interpretable 2-D map of sources for the air pollution in Granite City (Illinois, USA) has been obtained.

2. Theory

2.1. Analytical receptor site model

According to Fig. 1, a receptor site, X, is located in a given geographical area. An unknown number of p air pollution sources S with unknown geographic locations emit patterns of trace elements in m particles or gaseous species.

However, neighbouring pollution sources and meterological factors (wind speed, wind direction, wind duration, rain etc.) change the $l = 1..n$ source profiles $\mathbf{a}_m$ to $l = 1..n$ multivariate vectors of sample concentrations $\mathbf{c}_m$. This variation of a source profile, $a_{k,j}$ with $k = 1..p$ and $j = 1..m$, during its transport in atmosphere can be considered as a weighting according to $c_{l,j} = \Sigma_{k=1}^{p} b_{l,k} * a_{k,j} + e_{l,j}$, whereby $e_{l,j}$ represents noise. If written in a matrix notation that is transposed to the classical receptor model ([1], p. 2), the

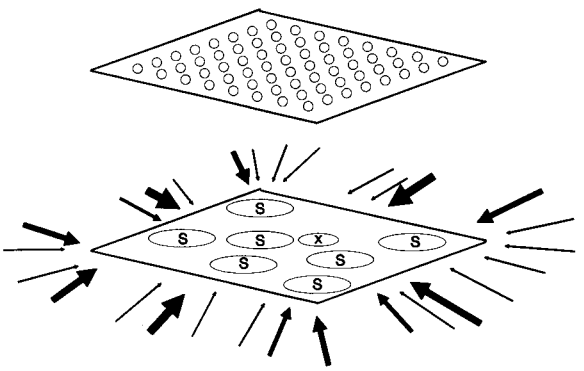

Fig. 1. A model arrangement of a sampling site (x) affected by seven emission sources (S) for airborne particles. Distinct orientation, thickness and length of arrows symbolize distinct sample vectors $\mathbf{c}_m$ that have been emitted by a source as source profile, weighted by distinct meterological conditions and finally transported through the atmosphere to the sampling site. The considered geographical area is thought to be superimposed with a computer internal two-dimensional Kohonen neural network (above).

matrix $\mathbf{A}_{p,m}$ of p source profiles is weighted by a source contribution matrix $\mathbf{B}_{n,p}$ according to

$$\mathbf{C}_{n,m} = \mathbf{B}_{n,p} * \mathbf{A}_{p,m} + \mathbf{E}_{n,m} \quad (1)$$

The present model uses a further assumption: The larger the number m is of the same analytes that are measured at the sampling site, the higher the chance is for a given source profile to become specifically weighted because of its neighbouring source profiles and because of its geographical position. With this increasing probability of a specific weighting, the probability also increases that this geographical information becomes coded as a specific chemical mixture in the sample vectors. Every source becomes coupled with its neighbour sources in the m-dimensional space of analytical concentration variables. This individual coupling of neighbours is expected to create a global network of couplings of all the emission sources in the m-space.

For illustration, assume a single sampling site that is affected by two refineries and a power plant arranged in a triangle, where the power plant is located closer to one of the refineries. If Ni and V that are emitted by the combustion of oil are the only species determined, and both refineries emit an identical ratio of them (for

example, both use the same input crude oil), they would be indistinguishable without using any additional geographical or meteorological information. However, an additional analysis of the power plant's combustion product SO_2 could solve this problem, because the geographic information is coded by distinct mixing of both source profiles of the refineries with the profile of the power plant.

Different lengths, thicknesses and orientations of the arrows for the n sample vectors, $\mathbf{c}_m$, in Fig. 1 symbolize the distinct weighting of the source profiles. The more distinctive meteorological situations are available, the more diverse geographic information is coded in these chemical sample vectors $\mathbf{c}_m$ by distinctively created coupled mixtures of source profiles $\mathbf{a}_m$.

For the computer internal presentation of the present neural network model, the studied geographical area in Fig. 1 (bottom) is thought to be superimposed with a two-dimensional Kohonen neural network containing u neurons (Fig. 1, top). This superposition creates a two-dimensional data projection that can be compared with a real geographical map. In Fig. 1, a square of 8×8 neurons has been chosen ($u = 64$). Alternative two-dimensional neural arrangements can be, for example, a circle, a rectangular or an ellipse.

2.2. Kohonen self-organizing feature map

Compared with an ordinary hierarchical cluster analysis or with classical nonlinear multivariate data mapping techniques [2,3], Kohonen's self-organizing neural network provides another kind of unsupervised pattern recognition.

Kohonen's neural network is designed to visually evaluate linear, two- or three-dimensional graphical arrangements of u neurons (Figs. 1–2). In reality, the u neurons are an index expression for u weight vectors $\mathbf{w}_m$ of the same length m as the $l = 1..n$ sample vectors $\mathbf{c}_m$. The essence of Kohonen's algorithm is a repeated comparison of the n sample vectors $\mathbf{c}_m$ with these u weight vectors using a distance metric such as the Euclidian distance or the correlation coefficient, for example. During each comparison, a winner i among all u weight vectors can be found that has the highest degree of similarity (smallest distance) to l. After that, the j elements, $w_{ij,old}$, of the winning weight vector i become adapted a small step closer to the elements x_{lj} of the actual presented lth input sample vector using the Kohonen learning rule

$$w_{ij,\mathrm{new}} = w_{ij,\mathrm{old}} + \eta * (x_{lj} - w_{ij,\mathrm{old}}) \qquad (2)$$

The learning rate, η, is chosen as a positive, real number < 0.1.

Simultaneously with the winner, i, other weight vectors are modified around the winner within a topological neighbourhood, R. Squares or hexagons have been used as topological neighbourhoods R [7,11,20,21]. In the beginning R is large but decreases slowly with the training time (Fig. 2).

After this adaption, the subset of weight vectors within R becomes slightly more similar to the actual input vectors in terms of the chosen distance metric.

The comparison of all n sample vectors with all u neural weight vectors and their modification is called one epoch. After repeating this process over a large number of epochs, n_e, a self-organi-

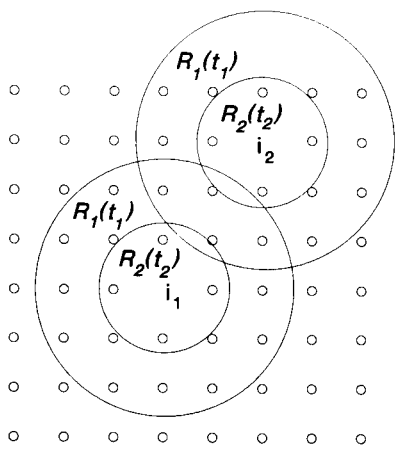

Fig. 2. A circle with the topological radius R around the winning neuron i for a certain input vector corresponding to a certain time point t (training epoch) with $t_1 < t_2$. R includes all neurons that are modified by the Kohonen learning rule together with the winner i. R slowly decreases with the training time including simultaneously less and less neurons and giving in this way less and less overlap between the R values of winners for distinct input samples.

zation behaviour of the n samples in the low-dimensional neural array is found. The samples form a visual topological structure due to their arrangement in the original m-dimensional space of analytical concentration variables.

The final result of this training process is an unsupervised clustering of subsets of sample vectors dedicated to certain weight vectors in the neural array. The trained weight vector for such an aggregated cluster of input vectors comes numerically very close to their mean vector. The present work calls its corresponding neuron a "loaded neuron". Another result might be, that other weight vectors do not collect any input vectors. Their corresponding neurons will be defined as "unloaded neurons".

2.3. A hybrid algorithm combining Prim's minimal spanning tree with a special Kohonen's self-organizing feature mapping neural network

The concept of "loaded" and "unloaded" neurons developed in this present work, allows to consider a Kohonen map as an a priori data compression procedure before applying the minimal spanning tree. After this compression of the n input samples to a few v "loaded" neurons, with $v \leqslant u$, they are presented in a low dimensional map that preserves the topology.

It is straightforward and logical to add as a third step, a procedure that allows the visualization of the global relation between all v "loaded" neurons simultaneously. The technique chosen in this present work is a calculation of the minimal spanning tree between the "loaded" neurons of a trained Kohonen self-organizing feature map.

The minimal spanning tree method is one of the oldest unsupervised pattern recognition methods based on a graph theoretical consideration. Its aim is the grouping of v data vectors, each characterized by m variables, into clusters of higher similarity based on a given distance metric. As alternative kinds of metrics, for example, the Euclidian distance or the correlation coefficient can be used. Based on the $(v^2 - v)/2$ possible pairwise distances in the m-space, distinct hierarchical organized trees (graphs) of $v - 1$ connection lines (edges) can be drawn between the v objects. Among them at least one graph can be found, that minimizes the sum over all $v - 1$ edge lengths. A second restriction is that closed arrangements such like rings, for example, are forbidden. However, multiple links of one object with many other ones are tolerated.

There are basically three algorithms that perform this task, and these are Florek's method [15], Kruskal's method [16] and Prim's method [17]. In this present work Prim's algorithm is used, but there is no limitation to the use of the other ones for their projection into the Kohonen map.

The complete algorithm is given as a flowchart in the Appendix. This algorithm will be discussed here in detail in such points in which it deviates from the classical Kohonen algorithm and from the classical minimal spanning tree. The new Kohonen algorithm [20] used in this present work differs slightly to those previously cited chemical applications in several ways. It contains automatic control of the former free parameters of the learning rate, η, and topological radius, R, over the distinct phases of the training epochs. This algorithm has been further modified in this present work by substituting Kohonen's hexagonal shaped topological neighbourhood, R, by a circle [21].

The second modification made in this present work is that the final topological radius, R, at the end of the training, is not fixed to $R = 1$ but can have larger values. This change allows the generation of the minimal spanning trees with the desired distinct resolution in the map as a tool for data exploration.

2.4. Scaling of data and similarity measures

There are two basically different ways to preprocess the $n \times m$ input data matrix to be a suitable input for the combined algorithm. After scaling within every single of the n rows over all variables, the absolute differences between the n sample vectors disappear. On the other hand, the ratios between the variable amplitudes within a sample vector will be retained. The sample vectors will then be classified according to their relative shape. To illustrate this, suppose an unit

length scaling of the four artificial sample vectors $x1 = [0.5\ 5]$, $x2 = [1\ 10]$, $x3 = [100\ 1000]$, and $x4 = [1\ 5]$. After such a row scaling, $x1$, $x2$ and $x3$ will become identical and only $x4$ will be recognized as deviating sample vector.

Scaling the m variables separately over all n samples to a standard length gives every variable a comparable meaning – including those variables that have no meaning, incorrect meaning, or represent only noise. However, the ratios between the four sample vectors will be preserved. Note that after this type of variable scaling over the four example vectors the network will now recognize sample $x3$ as the strongly deviating vector and $x1$, $x2$ and $x4$ would form a close cluster.

The data set can also be scaled both in the directions of the rows and the columns. Note that effects obtained after scaling can also be reached in a similar way by a suitable choice of the similarity measures. An Euclidian norm-based measure conserves the absolute ratios between the samples, while a correlation coefficient-based similarity measure destroys these absolute differences but conserves the amplitude ratios between the variables within a single samples vector. These observations hold true for the Kohonen network training phases as well as in the MST calculation.

2.5. Initialization of scaled input data and of the neuron's weight vectors

An alternative technique called convex combination method [22] has been used instead of the classical initialization of all elements of the u weights vectors by small random numbers. This approach ensures that the initialization result does not propagate through the training process to the final result. It works as follows.

All of the $u \times m$ elements of the u weight vectors are assigned the same initial value,

$$w = 1/\sqrt{m} \tag{3}$$

Simultaneously, the $n \times m$ elements of the sample data matrix $\mathbf{X}$ are scaled to

$$x_{lj,\text{scaled}} = \alpha * x_{lj,\text{original}} + \left[1/\sqrt{m}\right] * [1 - \alpha] \tag{4}$$

The α is incremented linearly over the first part ne_1 of all training epochs starting with a small value and continuing until α reaches 1.

2.6. Automatic control of the learning rate η

Kohonen suggests [20] decrementing the learning rate η over time t of training epochs by using the formulae

$$\eta_1 = k_1 * (1 - t_1/ne_1) \tag{5}$$

$$\eta_2 = k_2 * (1 - t_2/ne_2) \tag{6}$$

over two phases 1 and 2 of the training with ne_1 and ne_2 epochs. The recommended choice of the constants of $k_1 = 0.1$ and $k_2 = 0.008$ works well for very different numbers of training epochs, different sizes u of the neural map and different dimensions of the input data matrices described in this article.

2.7. Decrementing the topological radius R

Fig. 2 shows the essential part of the Kohonen algorithm: Decreasing the topological radius over the time with $t_1 < t_2$. As modification the present algorithm uses a circle around the winning neuron in place of a hexagon or a square.

Kohonen [20] suggests decrementing R linearly by small steps within the first training epochs ne_1 from $R_o = 12$ to $R_e = 1$ as final value for R. In a 2-D map, $R = 1$ means that around a winning neuron, four neurons (left, above, right, down) are trained by the learning rule together with the winner.

Sometimes it is recommended to change the weights as function of the closeness of a neuron to the winner neuron. This so-called inhibitor function can be chosen as a Gaussian-like function around the winner, as pyramidal or, as a step function [21].

For the formation of MST with different resolutions, in the outer loop R was decremented in the present work to final integer values that were allowed to be greater than 1. Here, the present hybrid algorithm differs again from the pure Kohonen algorithm. This explorative handling of R allows the generation of different levels of ten-

sion in the Kohonen map by different amounts of overlap between the topological neighbourhoods. The neurons are not allowed to relax completely. Consequently, a large R yields only a few loaded neurons. The MST then produced, has only a low resolution. The rough data structure can be explored. Alternatively, a small R yields many singly loaded neurons giving a fine resolution of the MST. A similar result can be reached by variation of the size u of the map alone or in combination with a variable R.

3. Experimental

The basic behaviour of the hybrid algorithm was studied using four simulated data sets with known topological structure and known neighbourhood interrelationships. After that, data from an environmental measuring program were analysed.

3.1. Simulated data sets

Table 1 contains the data that were simulated in a three variable space to have very distinct spatial sample patterns. One group of the data set is formed by simulated tetrahedral and simulated crosslike arrangements of 16 data vectors. The second group is formed by a curved and a straight line digitized into 15 sample vectors in a three variables space. Fig. 3a–c shows plots calculated from the data in Table 1. The simulated straight line (not shown, column 4 in Table 1) is the diagonal line of a cube of edge length 2.

3.2. Identification of sources of airborne particles

Airborne particle samples were taken by the Illinois State Water Survey at a single sampling site, located in Granite City (Illinois, USA) between March 1986 and July 1987. A dichotomous sampler was used with sampling intervals of 12 and 24 h. 48 coarse fraction filters and 49 fine fraction filters were analysed using neutron activation analysis and x-ray fluorescence spectroscopy, so that for each sample, a sample vector of 48 trace element concentrations (variables) was determined. Of these 48 variables, 33 analytes Na, Al, Si, P, S, Cl, K, Ca, Sc, Ti, V, Cr, Mn, Fe, Co, Ni, Cu, Zn, As, Se, Br, Rb, Sr, Sb, La, Ce, Eu, Dy, Yb, Hf, Pb, Th and U were selected

Table 1
Four distinct artificial data sets arranged as tetrahedral clusters, crosslike clusters, as a curved line and as a straigth line of data vectors in a three-dimensional vector space

Sample No.	Four tetrahedral arranged clusters			Four crosslike arranged clusters			Digitized curved line			Digitized space diagonal line		
	$x1$	$x2$	$x3$	$x1$	$x2$	$x3$	$x1$	$x2$	$x3$	$x1$	$x2$	$x3$
1	−0.90	−1.20	−0.90	−0.90	−1.10	0.10	1.00	1.00	1.00	−1.00	−1.00	−1.00
2	−1.10	−0.90	−0.90	−1.10	−1.00	0.00	0.80	0.90	0.94	−0.85	−0.85	−0.85
3	−0.80	−0.80	−1.10	−0.80	−0.90	−0.10	0.63	0.80	0.89	−0.70	−0.70	−0.70
4	−1.20	−1.10	−0.90	−1.00	−0.80	−0.20	0.50	0.70	0.85	−0.55	−0.55	−0.55
5	0.80	0.90	−0.80	0.10	0.00	−1.40	0.40	0.60	0.81	−0.40	−0.40	−0.40
6	0.80	1.00	−0.90	−0.20	0.00	−1.50	0.32	0.50	0.80	−0.25	−0.25	−0.25
7	1.20	0.80	−1.20	0.00	−0.10	−1.30	0.25	0.40	0.79	−0.10	−0.10	−0.10
8	0.90	0.90	−1.00	0.10	−0.10	−1.40	0.22	0.30	0.74	0.00	0.00	0.00
9	1.10	−0.90	1.00	0.00	0.10	1.30	0.22	0.20	0.58	0.10	0.10	0.10
10	0.90	−1.20	1.10	0.10	−0.10	1.40	0.28	0.15	0.41	0.25	0.25	0.25
11	1.10	−1.20	0.90	0.10	−0.10	1.50	0.35	0.12	0.27	0.40	0.40	0.40
12	1.20	−0.80	1.10	−0.20	0.00	1.30	0.45	0.10	0.20	0.55	0.55	0.55
13	−1.10	1.00	1.00	1.10	1.00	0.00	0.58	0.09	0.17	0.70	0.70	0.70
14	−0.90	1.00	0.90	1.00	0.80	−0.10	0.76	0.05	0.15	0.85	0.85	0.85
15	−0.90	0.80	1.20	0.90	1.10	0.10	1.00	0.00	0.14	1.00	1.00	1.00
16	−1.10	1.10	0.90	0.90	0.90	−0.10	–	–	–	–	–	–

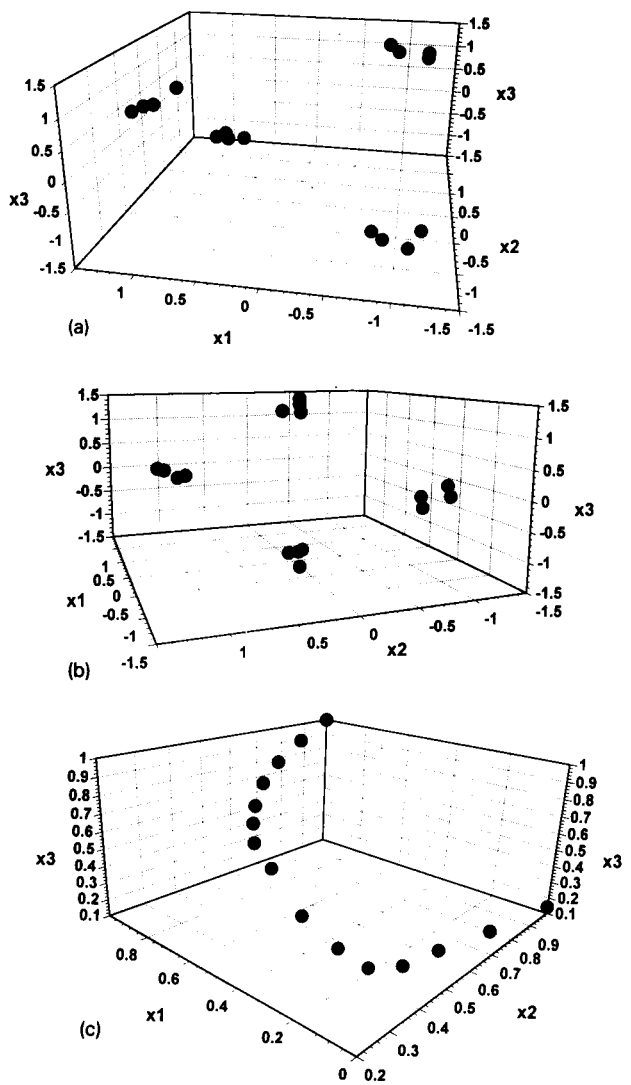

Fig. 3. (a) 3-D scatterplot of the tetrahedral arranged points calculated from the 16 data vectors in Table 1 (columns 2–4). (b) 3-D scatterplot of the crosslike arranged points calculated from the 16 data vectors in Table 1 (columns 5–7). (c) 3-D scatterplot of the at a curved line arranged points calculated from the 15 data vectors in Table 1 (columns 8–10).

having concentrations above the detection limits. For further analytical details refer to [23]. Recently these data were studied by Glover et al. [23] using PCA with varimax rotation and by chemical mass balance (CMB) calculations. Trace element pattern have been detected in the fine and in the coarse particle fraction that were identified as being correlated to emission sources in Granite City. Sources included non-ferrous metals smelters, steel industry, car traffic, soil, etc. For this study, the 48×33 coarse fraction data matrix was augmented with the main wind direction during the sampling period coded as sine-cosine. In this way the two wind variables were used together with 33 chemical variables to create the map. All 35 variables were scaled to unit length to give them a comparable influence. This final 48×35 data matrix formed the input to the hybrid algorithm of Prim's minimal spanning tree, superimposed to a Kohonen neural network.

4. Computation

First experiments were done using 386-MATLAB on an 80486-MS-DOS personal computer and with UNIX-MATLAB on an IBM 6000/RISC workstation. Subsequently, a program package 3MAP (minimal spanning tree self-organizing feature map) was written in TurboPascal 5.5 for the MS-DOS computer. 3MAP/DOS presents an on-line view at the self-organization process within the map on the screen for up to 19×19 neurons sized two-dimensional feature maps. Because of the rapidly decreasing speed of the Kohonen algorithm with increasing number of samples an 80486 processor is recommended. ASCII files are used for the input of the data matrix and for the output of the minimal spanning tree, projected into a Kohonen Map. 3MAP/DOS can process some hundred input samples with up to a hundred variables depending on the available computer memory and calculation time. In a subsequent development phase, 3MAP has been implemented in Standard Pascal on an IBM 6000/RISC workstation under the UNIX operating system. 3MAP/UNIX is able to project data sets of a thousand samples and a hundred variables in much larger arrangements of neurons in up to twenty times shorter time compared to the 80486-PC (50 MHz). For this comparison it has been assumed that the available workstation can be used exclusively for that task.

5. Results and discussion

5.1. Simulated data sets

Fig. 4a and b shows that a 4 × 4 arrangement of neurons for the tetrahedron and the cross yield four clusters that are located in four distinct corners of the map. However, the mapping alone only gives the topological information about the existence of 4 clusters in the three dimensional variables space. From these results, it can be concluded that the classical Kohonen map is not able to distinguish between the tetrahedron and the planar cross.

The addition of the minimal spanning tree allows the visualization of the distance interrelationships. Based on these minimal spanning trees and the distance matrix structures (Tables 2–3), the tetrahedron can be clearly distinguished from the crosslike arrangement as follows. In case of an ideal tetrahedron (without noise), its four nodes would be equidistant from another. The same would be true for the four corresponding loaded weight vectors. In this way, any kind of link would be allowed between the four neurons in the map for a calculation of a tree with a minimal length. In case of the mapped cross, the diagonal lines in the map also represent the longer connections inside the original cross. Thus, in contrast to an ideal tetrahedron, an ideal cross contains forbidden links, that, if they were used, would rapidly increase the length of the spanning tree. The distance matrices used for the calculation of the minimal spanning tree between the trained loaded neurons show this more clearly (Tables 2–3). As expected, the distance matrix corresponding to the cross shows two groups of distances in contrast to that of the tetrahedron. To explore the limitations of the proposed approach, a centrally located sample vector [0,0,0] was added to both data sets as a seventeenth sample. For both data arrangements, this new sample formed a fifth separate group as well as a further element for symmetry operations. The minimal spanning tree was obtained for both data arrangements as the straight connections of the four former weight vectors to this single, central located fifth weight vector. In both cases, a cross became visible in the map. The conclusion is, that highly similar and highly symmetrical data arrangements cannot be distinguished by using only

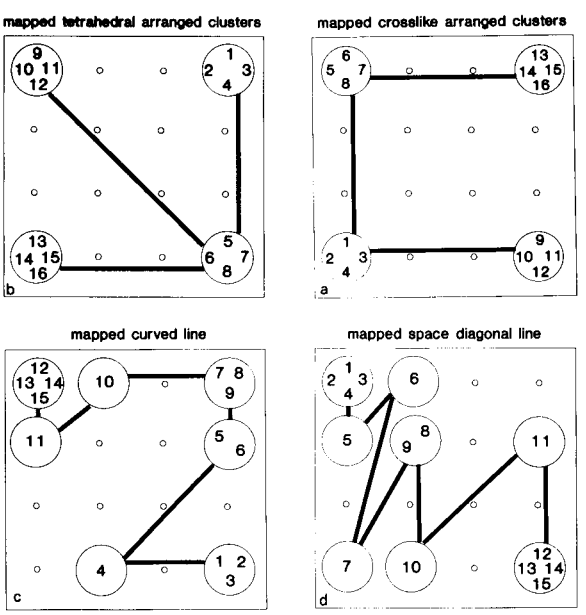

Fig. 4. (a–d) Minimal spanning trees projected into trained 4×4 Kohonen self-organizing feature maps ($R_o = 4$, $R_e = 1$, $ne_1 = 2000$, $ne_2 = 500$) obtained for the data from Table 1 and Fig. 3a–c. For discussion see text.

Table 2
The lower half distance matrix between the four weight vectors corresponding to four loaded neurons obtained after mapping a tetrahedral arranged set of clusters from Table 1 (see Figs. 3a and 4b)

2.87		
2.86	2.73	
2.76	2.72	2.72

Table 3
The lower half distance matrix of the four weight vectors corresponding to four loaded neurons obtained after mapping the crosslike arranged sets of clusters from Table 1 (see Figs. 3b and 4a)

1.95		
1.89	2.70	
2.76	1.96	1.93

the graphical approach. The elements of the distance matrices have to be evaluated separately.

Considering the next two 4×4 mappings (Fig. 4c and d.), much less symmetry is observed because of the arrangement of the loaded neurons compared to Fig. 4a and b. Groups of loaded neurons are observed (Fig. 4c, upper corners, Fig. 4d, left corners). Without a minimal spanning tree, the two new Kohonen maps yield the incorrect impression, that the data contain an unsymmetrical cluster constellation. Note further the seeming similarity of both maps. Drawing the minimal spanning tree helps to avoid these wrong impressions and in both cases gives the impression of more continuous but differing data arrangements.

An increase of the size of the maps (Fig. 5a–d) allows the exploration of more details of the data sets. The tetrahedron and the planar cross yield crosslike minimal spanning trees (Fig. 5a and b). In contrast to that, the mapped curved line yields a kind of open circle and in this way provides the correct impression of a continuous but curved sample arrangement.

Considering the diagonal line (Fig. 5d) more in detail, two groups of loaded neurons (upper left, lower right), two single loaded neurons (upper right and lower left) and a larger region with unloaded neurons (center of the map) are obtained. However, the superimposed minimal spanning tree corrects this wrong impression about two larger clusters in the data set. A clear linear trend from one corner on the upper left to the lower right side can be seen. The tension can be observed in the rapid oscillations that are seen in this small map. The 15 neurons have no opportunity to relax to a linear topology in the 8×8 network. So they move to the left and right hand side of the map's diagonal line.

Making the network larger from 4×4 to 8×8, relaxed the neurons because there is less overlap between the topological radii. The topology improved and the minimal spanning tree yielded a clearer pattern of the real data structure.

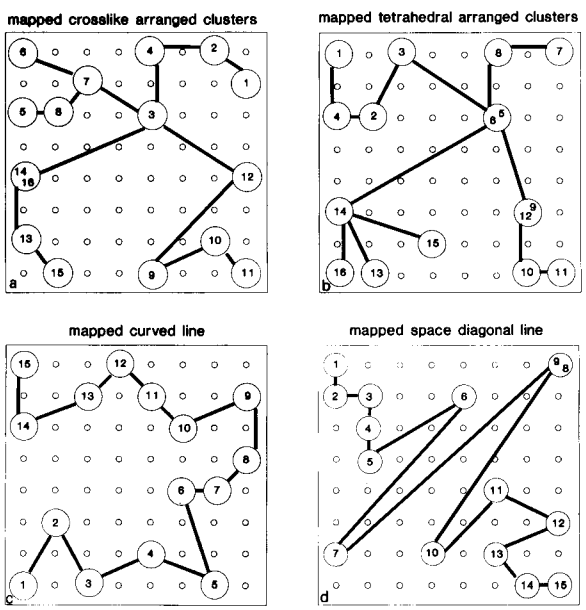

Fig. 5. (a–d) Minimal spanning trees projected into trained 8×8 Kohonen self-organizing feature maps ($R_o = 8$, $R_e = 1$, $ne_1 = 3000$, $ne_2 = 1000$) obtained for the data from Table 1 and Fig. 2a–c. For interpretation see text.

5.2. *Identification of sources for airborne particles in Granite City*

The sampling in Granite City (IL, USA) is affected by contributions from the steel and iron plants in the western and eastern directions (Figs. 1 and 2 in [23]). Smelters as sources of emission of non-ferrous metals are located to the north and to the south. Refineries are concentrated to the north and power plants and other combustion sources to the south. An evaluation of the different wind directions for the 48 samples (Fig. 6) shows that only the non-industrialized north-west and north-east directions are not represented by any data. A representative overall set of wind directions is essential for the present model, because it implicitly assumes, that a given wind direction causes a higher probability for a specific source's air pollution pattern, that affects the particle composition at the receptor site. On the other hand, it is not necessary that the model has pure source profiles to be able to function correctly.

The initial exploration of the rough structure of the 48×35 input concentration was performed

by using a small 7×7 network. This small network generates high tensions between the neurons (Fig. 7). It can be seen that the data cluster is a minimum of two large groups (Fig. 7, left lower and left upper corner). For addition, two to three smaller clusters are also contained in the map. The projected minimal spanning tree connects the clusters one after each other forming a chain that is folded as an open circle into the narrow network. In a 19×19 network, the two larger clusters also can be recognized (Fig. 8). They are again located in the two left hand corners of the map. A 19×19 map allows the data to relax better, so that they tend to scatter into the available empty regions of the map. The final topological radius was chosen with a value $R_e = 4$. This choice avoids forcing the resolution of the minimal spanning tree into too many subclusters and keeps its global structure more visible. The chain structure of the linked clusters can be identified now more clearly. Focusing on cluster 8 (right upper corner), for example, it is obvious that the spanning tree is not able to unfold completely. The distance of cluster 8 to the remaining data set is still to large for this small 19×19 network.

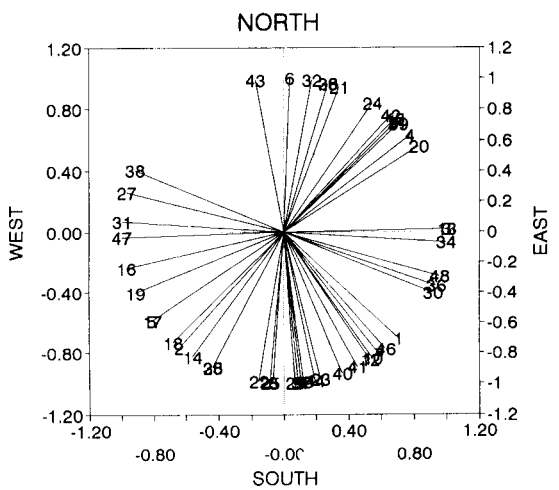

Fig. 6. A projection of the measured wind directions belonging to the 48 single sampling intervals taken at a single sampling site in Granite City (IL, USA) between 1986 and 1987 (see text).

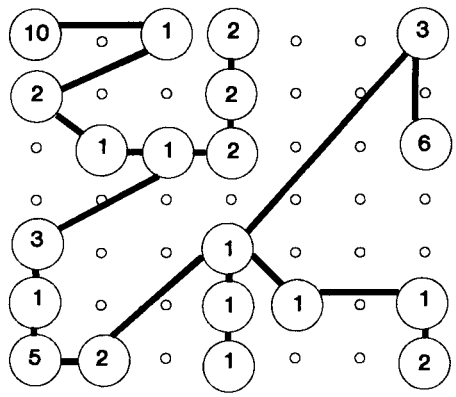

Fig. 7. Mapping of the 48×35 data matrix of 33 element concentrations and 2 wind directions of 48 samples of airborne particles into a small and narrow 7×7 neurons 2-D Kohonen map, followed by a link of the loaded neurons using Prim's minimal spanning tree. Training parameters: variables unit length scaled, Euclidian distance measure, $R_o = 7$, $R_e = 2$, $ne_1 = 3000$, $ne_2 = 1000$, $k_1 = 0.1, k_2 = 0.008$. Numbers within the loaded neurons equal to the number of aggregated input samples (histogram).

For a quantitative evaluation of the combined map (Fig. 8), the concept of a geographical unit circle (GUC) is introduced (Fig. 9). Plotting the ten extracted clusters on a GUC around the sampling site in Granite City helps to explain the cluster chain structure (Fig. 9). Considering the chain in a clockwise direction corresponds to the wind directions. The lower half of the Kohonen map corresponds to the lower half of a windrose. The upper half of the Kohonen map represents the upper half of a windrose going in this case from east (left upper corner) to west (right upper corner). Note the correct position of cluster 8 in the tense unfolded state.

Comparing Fig. 9 with the original geographical situation in Granite City (Figs. 1–2 in [23]), it becomes clear that the minimal spanning tree projected into the trained Kohonen map is able to visualize a continuous cyclic arrangement of distinct emission sources affecting the centrally located sampling site. However, using data from only a single sampling site yields no information about the distance between source and sampling site but the geographic directions are correct.

The similarity between the map in Fig. 9 and the geographical reality of Granite City is recog-

nizable. The southern part of Fig. 9 reflects the higher industrialization of this region of the town. In the north, a gradient with a pollution maximum between the non-industrialized northeast and northwest regions can be seen. The regional refineries and a brass plant are potential sources for cluster 1, 2 and 10, but their averaged pollution level is lower than that of the southern part of Granite City because they are much further away. The highest average pollution levels come from the directions of the steel plants and the iron works (west and east directions) and from the non-ferrous smelters (south and southeast).

The identified and reasonable qualitative differences between the refineries and steel and iron production can be further quantified as follows. By calculating the median sample values

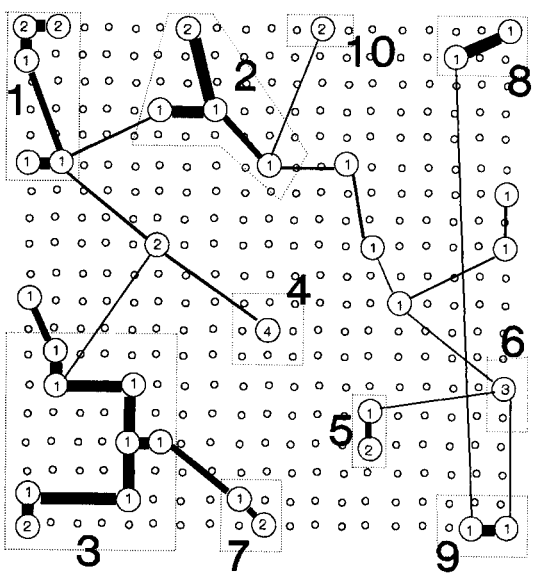

Fig. 8. Mapping of the data set from Fig. 6 into a large scale 19×19 Kohonen map, followed by a link of the loaded neurons using Prim's minimal spanning tree. Training parameters: variables unit length scaled, Euclidian distance measure, $R_o = 19$, $R_e = 4$, $ne_1 = 10000$, $ne_2 = 3000$, $k_1 = 0.1$, $k_2 = 0.008$. Numbers within the loaded neurons equal to the number of aggregated input samples (histogram). Four decreasing line thicknesses represent four categories of increasing Euclidian distance D between the several elements of the minimal spanning tree (huge, $D < 0.1$; large, $D > 0.1$; normal, $D > 0.2$; thin, $D > 0.3$). Dotted lines and huge bold numbers characterize ten identified clusters (see text and Fig. 9 for interpretation of clusters).

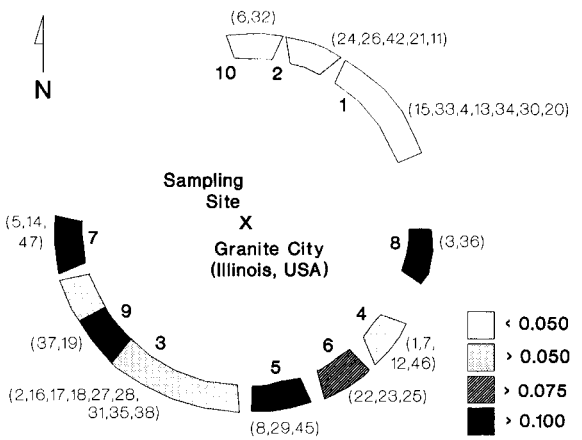

Fig. 9. Arrangement of the ten clusters (as detected in the 19×19 neurons map in Fig. 8) around a geographic unit circle. The position of a cluster on the circle corresponds to the averaged wind direction of all samples contributing to this cluster. Three chosen segment sizes represent the variance of wind directions contributing to this cluster. Four pattern levels represent the median value of total pollution taken over 33 unit length scaled elemental concentrations within the mean sample vector for a considered cluster as given in Fig. 10 (the medians for cluster 1–10 are: 0.03, 0.07, 0.06, 0.08, 0.14, 0.10, 0.11, 0.12, 0.11, 0.05).

within a given cluster, specific emission source profiles can be obtained (Fig. 10a–j). The nature of the source as well as its direction to the sampling site can be identified. The profiles for clusters e and f (Fig. 10), for example, can be identified as belonging to a source of non-ferrous metal emission from the south-east direction. This direction is exactly where the smelters are located relative to Granite City. The profiles of clusters g and i (western direction) and h (eastern direction) correspond to an emission pattern of steel and iron plants. There are the correct locations of those sources in Granite City. Close to cluster a and b with a rather low emission level but higher phosphorus and bromine concentrations, cluster j is located. Its elemental background pattern looks not much different from those of clusters a and b, but the high Cu and Yb peaks are obvious. Moreover, some elements such as La, Sb and Zn are higher. Thus, cluster j is a clear indicator for the brass plant located between sampling site and refineries. The increased La peak indicates the

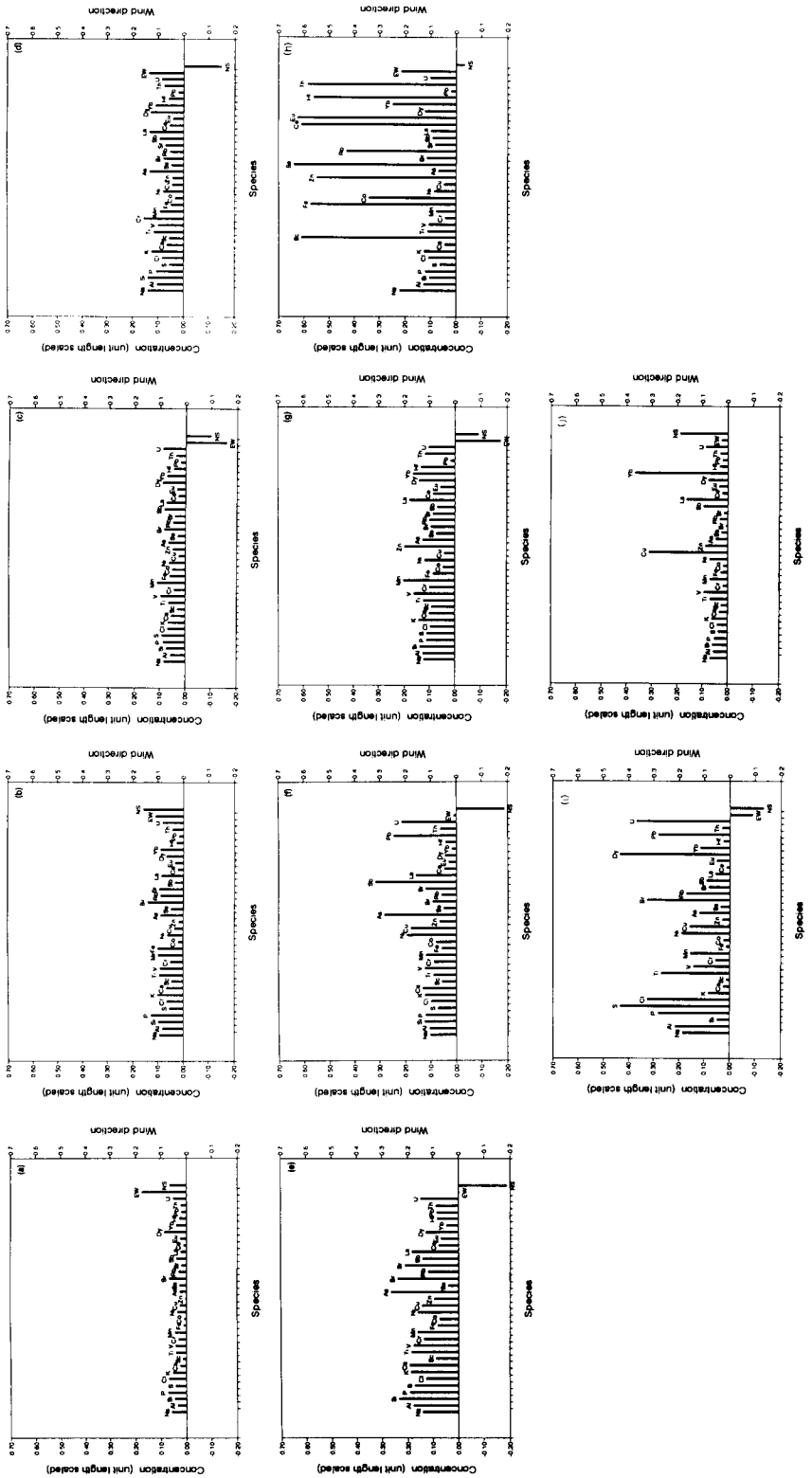

Fig. 10. (a–j) Source concentration profiles for the ten clusters as detected by the minimal spanning tree in the 19×19 neural map (Fig. 8) for the distinction and characterization of ten different emission sources in Granite City (see text). (The labels a–j correspond to labels 1–10 in Figs. 8 and 9.)

coupling of the refinery emission pattern with that pattern from the brass plant. The 3MAP method seems to be able to locate sources of the same direction but located behind each other relative to the site. Only slight variations of wind directions and intensities, causing variations of the elemental patterns, are needed to load different neurons in the map.

5.3. Comparison of 3MAP with a principal component plot

In agreement with the results of Glover et al. [23] a PCA of the twice unit length scaled 48×35 data matrix provided at least ten significant principal components. This requires a visual evaluation of $(10^2 - 10)/2 = 45$ pairwise plots. Two of them (Fig. 11a and b) are shown for direct comparison with the high resolved 3MAP (Fig. 8). The plot of PC1 versus PC2 (Fig. 11a) shows a circular structure of the ten labelled emission sources that is similar to the 3MAP. However, without the 3MAP labels 1–10 rather a scattering than a clustering would have found. The reason is the projection error of more than 70%. In this way the information is lost that the profile of emission source '8' is distant to the other sources. A first indication for this is found in the plot PC1 versus PC3 (Fig. 11b). However, the projection error of the first three PCs is still larger than 60%. In contrast to that the 3MAP reflects in one single picture all the geographical information about the mutual arrangement of the ten emission sources around the sampling site. The data compression and clustering within the 3MAP provides a quick topological overview about the data structure. The superimposed MST adds distance information and linkage of the clusters. There is a further problem with PCA scores plots of environmental analytical data. PCA tends to combine any correlated variables to each other, even if this correlation is random and without geographical and environmental meaning. Such meaningless correlations can occur in the environment, for example, by co-emission, by co-location and by meteorological mixing effects. An example for co-emission are the steel plants with similar emission patterns, but located in two opposite directions for the Granite City site.

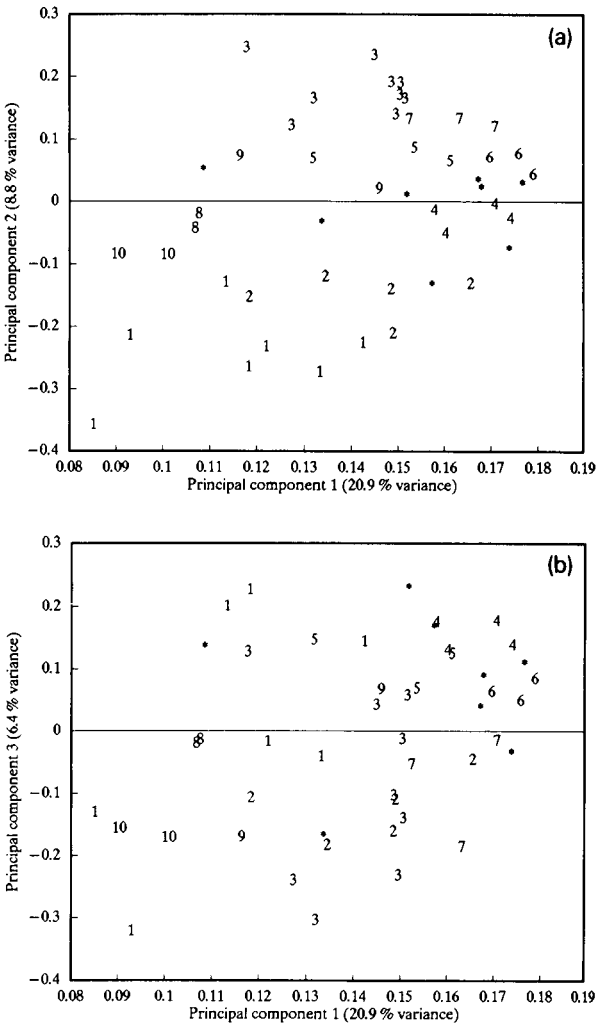

Fig. 11. (a–b) Plots of 48 samples in their subspace of the principal components 1 and 2 (a) and 1 and 3 (b) out of 35 original variables. The labels 1–10 correspond to ten emission sources detected by 3MAP (Fig. 8). * represents unlabelled samples forming no specific clusters.

Distinct directions of distinct sources are reflected by a chain of clusters linked via the minimal spanning tree in the Kohonen map in Fig. 8. With this result of the single site model, the clusters can be arranged around the GUC according to their geographic origin and their chemical

profile (for example, Figs. 9–10). As already stated, a deficiency of the single site mapping is, that it only yields the correct geographic direction of an emission source and its correct chemical profile, but not its geographic distance to the site. This information is available from a projection of the data from a multi-site sampling network. In a related study Wienke et al. [25] mapped a large scale data matrix (> 400 samples) from such a network of sampling sites. Processing of this kind of data by the 3MAP algorithm provided geographic direction as well as geographic distances of the air pollution sources.

The main disadvantage of Kohonen's mapping neural network is its slowness in training. For data sets with $n > 150$ objects it is recommended to use a computer workstation in place of a PC with 80486 processor. For much larger data sets (> 1500 samples) parallel implementations as cited or supercomputing are required.

6. Conclusions

The disadvantage of a classical topology preserving a Kohonen feature map is the loss of most information about correct distances between the mapped samples. The 3MAP combination method studied here, has tried to overcome this by a sequential superimposing of Prim's minimal spanning tree and a trained self-organizing 2-D features map. In this way the high quality of the topological maps has been upgraded with the missing distance information and the missing linkage of the clusters. Kohonen's method forms a preprocessing step for data compression within the proposed 3MAP algorithm. After that step the minimal spanning tree connects the loaded neurons giving a simpler and clearer picture of the data structure compared to the higher number of $n-1$ links between n original sample vectors. The minimal spanning tree method develops an increased value. Its ability to yield correct distance interrelations is upgraded with the missing correct topology information that is provided by a Kohonen neural network. The combination of correct topology with a correct distance and correct linkage is essential for any kind of projection method. A mapping algorithm becomes interesting for practical use, if it yields the complete information in a way that is easily processable by human beings.

It was shown that a data set of medium size (48 samples) can be evaluated successfully by this combination of the two established but different pattern recognition methods, despite the fact that the few data vectors seem to be scattered over the whole map. The projected spanning tree was able to impose a clear and evaluable structure on the seeming chaotic data arrangements.

The simulated data and the experimental data represent two distinct arrangements of the vectors in the m-dimensional variables space: clustered data and trend data. Both of them yielded quantitative interpretable mappings. In the experimental data set, the minimal spanning tree yielded the information about a chain link of the clusters. They arrange themselves cyclically in the 35-dimensional variables space according to their chemical origin (emission profile of the source) and according to their wind direction, e.g., according to the absolute direction between sampling site and emission source. 3MAP decoded the high-dimensional space of 35 chemical-analytical variables into a two-dimensional visually interpretable geographically subspace. The projected spanning tree was able to extract both abrupt changes and higher aggregations in the data (clusters) as well as continuous changes (trends) between the cluster areas.

Focusing on more specific results in the environmental study, the 3MAP algorithm promises to become a further mathematical independent tool for receptor site modelling together with such well-established techniques like principal component analysis and chemical mass balance calculations.

In this present work, different types of data scaling, different sized networks, and different final topological radii were applied to the same data set. These analysis allowed a control of the number of loaded neurons and in this way actively controlling the resolution of the projected minimal spanning tree. This explorative strategy allowed the extraction of global as well as fine structures of the data.

From the results obtained to date, no 'optimal' scaling, 'optimal' sized Kohonen network, and no 'optimal' setting for R_o and R_e for one given data set exist. In analogy to the choice of different distance measures in classical cluster analysis, the desired information out of the data matrix should determine the choices for the settings in 3MAP.

The projection of Prim's minimal spanning tree into Kohonen's feature mapping neural network will be studied further according to its numerical and algorithmic limitations and its utility for environmental chemical pattern recognition. A more difficult case, for example, is the analysis of fine fractions of airborne particles that tend to meteorological mixing and chemical change. Recent results obtained by Wienke and Hopke [24] in a study for the fine particle fraction of the Granite City sampling are reasonable. Additionally to that Wienke et al. [25] generalized the present 3MAP algorithm for its use in the case of a multi-sites sampling network. The projected large scale data set (more than 400 samples) of the Southern California Air Quality Study (SCAQS) provided a reasonable geographical pattern of air pollution sources [25]. For data sets from digital chemical image analysis the 3MAP algorithm provided encouraging results too as recently demonstrated by Wienke et al. [26].

In the future, there is likely to be a need for statistical or other test strategies for the quantification of trends or clusters in such a combined mapping. Such strategies are needed to be able to distinguish trends, clusters and noises in the combined map.

Acknowledgements

The authors are grateful to Professor Larry Eno, Clarkson University, Potsdam (NY, USA) for discussions and to Ms. Marcia Barnett for carefully checking the manuscript. This research project was funded by the U.S. National Science Foundation under grant No. ATM 9114750.

3MAP/DOS and 3MAP/UNIX are available from D. Wienke.

Appendix

3MAP – A hybrid algorithm superimposing Prim's minimal spanning tree with a modified Kohonen self-organizing feature mapping neural network

For a suitable numerical choice of the initial settings, the Theory section and the examples provide guidance on making their decisions.

Initial settings

Scale the $n \times m$ input data matrix using a method that preserves the desired information (see theory).

Define the size u of the graphical feature map (number u of units or Kohonen neurons) according to the desired resolution of the minimal spanning tree.

Assign to every neuron a weight vector of length m.

Initialize all u weight vectors by convex combination as described by Eq. 3.

After scaling, initialize all n input sample vectors by convex combination using Eq. 4.

Set the large starting value, R_o, and smaller final value, R_e, of the topological radius and step size $\mathrm{d}R$.

Set the desired number of epochs ne_1 and ne_2 in training phases 1 and 2.

Set the learning rate controllers, k_1 and k_2.

Set the initial learning rate η using k_1 and k_2 in Eqs. 5 and 6.

Set the step size $\mathrm{d}\alpha$ for the convex combination factor α, so that α will be linear incremented over the first ne_1 training epochs.

Presentation

The next steps are done for each of the n sample vectors separately by random selection from the input data:

Compare the single incoming sample vector l with all u neuron's weight vectors by using a similarity measure in the m-dimensional variables space.

Find for l a winner i among all u weight vectors having the highest degree of similarity (smallest distance) to l.

Adapt the j elements $w_{ij,old}$ of this winning weight vector i a small step closer to the elements x_{lj} of the actual presented lth input sample vector using the learning rule given by Eq. 2.

Also adapt the weights of all further neurons that are inside the border of the actual topological radius R around the winning neuron i in accordance Fig. 2 using Eq. 2.

After presenting n randomly selected input vectors to the u weight vectors of the map, one epoch of training has been finished. New parameter settings are then calculated:

Increment control parameters

Decrement linearly the actual topological radius R by one step dR.

Calculate the new smaller learning rate η using k_1 and k_2 in Eqs. 5 and 6.

Increment the convex scaling factor α by one step $d\alpha$.

Scale the whole data set of n samples with the new α convex scaling factor using Eq. 4.

Inner loop

Go back to "Presentation" and repeat over all $(ne_1 + ne_2)$ epochs. If finished, go to "Loaded neurons".

Loaded neurons

The network training is finished after $(ne_1 + ne_2)$ epochs. The n input sample vectors aggregated to v clusters at v weight vectors of the u-dimensional neurons array with $v \leqslant u$. These v weight vectors are assigned as the v loaded neurons. The remaining $u-v$ weight vectors are assigned as the unloaded neurons.

Calculate the lower half similarity matrix between the v weight vectors of the v loaded neurons in the m-dimensional feature space using the same similarity metric as in the network training.

Minimal spanning tree

Calculate from the similarity matrix the minimal spanning tree between the v weight vectors corresponding to the v loaded neurons using Prim's algorithm [17].

Recommended outputs

Plot the u dimensional feature map by labelling loaded neurons with the names or with the number of input samples clustered at this neuron. Label unloaded neurons with 0.

Connect the loaded neurons specified as nodes by the minimal spanning tree by their tree edges using straight lines.

Output distance matrix, distances to closest neighbours, and edge lengths between nodes of the minimal spanning tree

Outer loop

Define a new value for the final topological radius R and/or a new array size u and go to "Initial settings". Stop, if minimal spanning trees with distinct resolutions have been generated in various sized Kohonen maps.

References

[1] P.K. Hopke (Ed.), Receptor Modeling for Air Quality Management, Data Handling in Science and Technology, Vol. 7, Elsevier, Amsterdam, 1991.
[2] M.A. Sharaf, D.L. Illman and B.R. Kowalski, Chemometrics, Wiley, New York, 1986.
[3] D.L. Massart, B.G.M. Vandeginste, S.N. Deming, Y. Michotte and L. Kaufman, Chemometrics - A Textbook, Elsevier, Amsterdam, 1988.
[4] Y. Zeng and P.K. Hopke, J. Chemom., 6 (1992) 65.
[5] P.K. Hopke, N. Gao and M.D. Cheng, Chemom. Intell. Lab. Syst., 19 (1993) 187.
[6] T. Kohonen, Proc. 2nd Scandinavian Conf. on Image Analysis, Suomen Hahmontunnistustutkimuksen Seura r.y., Helsinki, 1981, pp. 214–220.
[7] T. Kohonen, Self-Organization and Associated Memory, Springer Verlag, Heidelberg, 1989.
[8] M. Gross and F. Seibert, Neural Network for Image Analysis of Environmental Protection, in R. Denzer (Ed.), Visualisierung von Umweltdaten, Springer Verlag, Berlin, 1991.

[9] P. Arrigo, F. Giuliano, F. Scalia, A. Rapallo and G. Damiani, Computer Applications in the Biosciences, 7 (1991) 353.
[10] V.S. Ross, I.F. Croall and H.J.H. Maefic, Quantitative Structure Activity Relationships, 10 (1991) 6.
[11] W.J. Melssen, J.R.M. Smits, G.H. Rolf and G. Kateman, Chemom. Intell. Lab. Syst., 18 (1993) 195.
[12] J. Zupan and J. Gasteiger, Anal. Chim. Acta, 248 (1991) 1.
[13] J. Zupan and J. Gasteiger, Neural Networks for Chemists, VCH, Weinheim, 1993, p. 79.
[14] B.R. Kowalski, ARTHUR, Fortran Program Package for Statistical Data Analysis, University of Washington, Seattle.
[15] K. Florek, Colloq. Math., 2 (1951) 282.
[16] J.B. Kruskal, Proc. Am. Math. Soc., 7 (1956) 48.
[17] R.C. Prim, Bell. System Techn. J., 36 (1957) 1389.
[18] C. Dussert, M. Rasigni and G. Rasigni, Z. Phys. D, Atoms, Molecules and Clusters, 12 (1989) 41.
[19] C. Dussert, G. Rasigni and A. Llebaria, Thin Solid Films, 177 (1989) 245.
[20] T. Kohonen, Speech Recognition Based on Topology – Preserving Neural Maps, in I. Aleksander (Ed.), Neural Computing Architectures, MIT press, Cambridge MA, 1989, pp. 26–40.
[21] Y.H. Pao, Adaptive Pattern Recognition and Neural Networks, Addison-Wesley, Reading MA, 1989.
[22] P.D. Wasserman, Neural Computing – Theory and Practice, Van Nostrand Reinhold, New York, 1989, pp. 65–70.
[23] D.M. Glover, P.K. Hopke, S.J. Vernette, S. Landsberger and D.R. D'Auben, J. Air and Waste Management Assoc., 41 (1991) 294.
[24] D. Wienke and P.K. Hopke, Environ. Sci. Technol., 28 (1994) in press.
[25] D. Wienke, N. Gao and P.K. Hopke, Environ. Sci. Technol., 28 (1994) in press.
[26] D., Wienke, Y. Xie and P.K. Hopke, Anal. Chem., (1994) submitted for publication.

ELSEVIER

Analytica Chimica Acta 291 (1994) 19–27

ANALYTICA CHIMICA ACTA

Feature extraction of polysaccharides by low-dimensional internal representation neural networks and infrared spectroscopy

Sven P. Jacobsson

Kabi Pharmacia Therapeutics, S-75182 Uppsala, Sweden

(Received 29th November 1993; revised manuscript received 4th January 1994)

Abstract

A new method for exploratory data analysis of spectroscopic data by neural networks is described. The method is based on the weight distribution associated with objects in narrow layered neural networks in which the input spectra are identical to the output spectra. The objects are displayed in 2- or 3-dimensional plots in analogy to principal component plots. The information content of the plots generated by low-dimensional internal representation neural networks, in their non-linear mode, appears to be at least as good as that of principal component analysis.

Key words: Infrared spectrometry; Feature extraction; Multivariate analysis; Neural networks; Polysaccharides; Principal component analysis

1. Introduction

In exploratory analysis based on multivariate data, principal component analysis (PCA) has proven to be a viable tool, giving projection techniques by linear transformation and compression of high-dimensional data sets [1]. PCA generates principal components which explain the variance in a decreasing order. High-dimensional data sets can thus often be compressed to data sets with significantly lower dimensions, onto which in turn samples can be projected. In complex data sets it is thus possible to generate information from the data, as similarity of structure and properties which are not otherwise directly accessible. The transformations may, however, occasionally lead to projections where the properties or structure of interest are obscured by or hidden in the principal components with the largest variance. Furthermore, since PCA imposes a linear structure of the data set, non-linearity within the data set will consequently be less efficiently analysed and modelled for.

Feed-forward neural networks (NN) with back-propagation of the error have been shown to have substantial modelling powers. By use of neural networks, any arbitrary continuous function could be modelled to any degree of precision [2]. Feed-forward back-propagation neural networks are used in supervised modes, although there exist implementations of neural networks which are used in unsupervised modes, most notably the Kohonen's self-organizing feature maps [3].

In this study feed-forward neural networks, with back-propagation of the error, were exam-

SSDI 0003-2670(94)00084-Y

ined as a complement to PCA for exploratory data analysis. The key element of such an approach is to map the data set on itself, i.e. the input values are the same as the output values. It is further assumed that the internal representation of the back-propagation neural networks in some way reflects salient features of the sample under study. Baldi and Hornik [4] have shown that the quadratic error function of the connection weights of a back-propagation network with linear transfer functions has a unique minimum, which corresponds to the projections onto a low-dimensional space generated by the first principal components associated by the training objects.

In the present study symmetric one- or three-hidden-layer network architectures with at least one hidden layer with only two or three nodes have been used. The one-hidden-layer architecture consists of a projection layer in-between the input and output layers. The three-hidden-layer neural network consists of an architecture with an encoding and a decoding layer, and a projection layer in-between these two layers, see Fig. 1. The manner in which neural networks are approached, in this study, resembles to some degree the auto-association (-encoding) technique by Ackley et al. [5] and identity mapping technique by Elman and Zipser [6]. The transfer function in this study is based on a non-linear function, to provide a means of feature extraction complementary to a linear reduction, which is a principal component analysis.

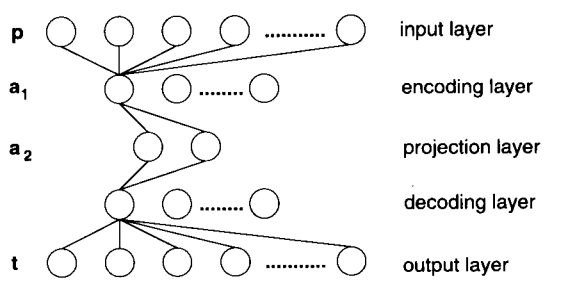

Fig. 1. Schematic of a neural networks architecture with three hidden layers. The bias, not shown, adjusts each node assuming an output of unity. The central layer, that is the projection layer, is used throughout this study for the generation of the 2- and 3-dimensional plots.

Since the projection, which is the low-dimensional internal representation (L-DIR) of even a relatively modest number of input variables, can be computational demanding, due to the fact that four different weight matrices, at most, have to be adjusted for, improvements of the neural networks performances were sought for. To meet this need the use of an adaptive learning rate rule was examined, and further, the initialization method of Nguyen and Widrow [7] was implemented. It should also be possible to obtain a considerable decrease in analysis time if the number of variables could be reduced, without loss of information content, in a pre-processing step. Thus, the scores of each object from a limited number of principal components (i.e. 10 components) were examined in the L-DIR neural network studies as a means to increase the learning speed.

In the present work a study of the low-dimensional internal representation neural networks of carrageenans, an anionic polysaccharide commonly used in pharmaceutical and food industry, by use of the infrared spectrum has been carried out. A designed ternary data set of carrageenans has been used in the L-DIR neural network studies. Furthermore, the results generated by neural networks are compared with those of PCA.

2. Theory

The development of artificial neural networks was originally inspired by the analogy to the human brain. Various forms of artificial neural networks have, by mimicking the function of the brain, been successfully applied to tasks stated as memorization, association, generalization and pattern recognition. Especially the use of feed-forward fully connected neural networks with back-propagation of the error have been used extensively. Such networks are based on the presentation of a number of exemplar/objects with known response, which is in a supervised mode. A more comprehensive description of various neural nets is given in the review by Lippmann [3]. An essential part of the feed-forward neural network with back-propagation of the error is to derive an output from the network, which could

be compared with the desired/target output. And, if a difference is established, this difference is used to adjust the net in a cyclic process towards lesser and lesser differences between the actual output and the desired/target output.

Schematically and with reference to the human brain a multi-layer neural network can be represented as in Fig. 1. The architecture of the network can take various forms, but always consists of an input layer and an output layer. In between these two layers there can be any number of hidden layers with any number of connection points, nodes, within each layer. The complexity and architecture of a such a net is largely governed by the complexity of the model characteristics between the input and the output layer. Each connection between nodes in the net consists of the output(s) from the connected node(s) and a weight associated with the connection(s). The input for node j is given by

$$\text{net}_j = \sum_i w_{ij} o_i \tag{1}$$

in which o_i is the output form the node(s) in the previous layer and w_{ij} the connection weight(s) between the node(s) in layer i and node j. The output of node j is governed by the transfer function or activation function, which commonly is a sigmoid function which squashes the output between 0 and 1. However, in this work the tanh transfer function

$$o_j = f(\text{net}_j) = \frac{e^{[2*(\text{net}_j+\theta_j)]} - 1}{e^{[2*(\text{net}_j+\theta_j)]} + 1} \tag{2}$$

has been used. The transfer function squashes the output from node j between -1 and 1, and is thus a suitable transfer function when the target values contain negative numbers. The term θ_j is a bias which shifts the transfer function along the net_j axis. A key element for the proper functioning of the neural network is the adjustment of weights and the biases. The back-propagation algorithm, the learning rule, as proposed by Rumelhart and McClelland [8] is based on the iterative presentation of exemplars/objects to the network. The difference between the actual output of the net and the target output is used to adjust the weights according to the learning rule

$$\Delta w_{ji}(n+1) = \alpha \Delta w_{ji}(n) + (1-\alpha)\eta \delta_j o_i \tag{3}$$

in which η is the learning rate and α is the momentum constant. The learning rule used in this study deviates from the rule proposed by Rumelhart and McClelland [8] by use of the additional term $(1-\alpha)$ in Eq. 3.

The momentum provides a means for the network to respond to recent trends in the error surface and not only to the local gradient. Thereby the risk is lessened for the network to get stuck in a shallow local minimum.

For the projection by using the internal representation neural networks, a symmetric network architecture consisting of an input and output layer with one or three hidden layers in between, has been used, although there exists no prerequisite for the use of symmetrically architectured networks. The input and output layer are the same and consist of the spectra variables of each object. The first hidden layer constitutes the encoding layer, the second hidden layer the projection layer, and the third hidden layer the decoding layer. For example, the encoding layer could consist of 10 nodes, the projection layer of 2 nodes, and the decoding layer of 10 nodes. For the network with only one hidden layer that layer also constitutes the projection layer. The coordinates of the object in the projection layer (a_1 or a_2) are generated by the following matrix operations

$$a_1 = \frac{e^{[2*(\sum w_1 p + b_1)]} - 1}{e^{[2*(\sum w_1 p + b_1)]} + 1} \tag{4}$$

$$a_2 = \frac{e^{[2*(\sum w_2 a_1 + b_2)]} - 1}{e^{[2*(\sum w_2 a_1 + b_2)]} + 1} \tag{5}$$

where p is the input spectrum variable, w_1 and b_1 the weight matrix and the bias, respectively, for the input to the encoding layer or projection layer. w_2 and b_2 are the weight matrix and bias, respectively, for the encoding layer to the projection layer.

The learning of the network is commonly initiated by giving all of the weights in the network small random values at the first presentation of

the network to the training set. However, since neural networks are computationally intensive, improvements of the starting conditions may substantially improve the learning process, i.e. a satisfactory network in fewer training cycles. By implementing the initialization method of Nguyen and Widrow [7], the starting weights w_{ij} between the input and the next layer is chosen according the following scheme, using Matlab notation

$$magw = 0.7s^{(1/r)} \quad (6)$$

$$w_{ij} = magw \times randnr(s,r) \quad (7)$$

$$w_{ij} = 2w_{ij}/rng \quad (8)$$

in which s is the size of the node layer (i.e. number of nodes), and r is the number of inputs. *Randnr* is an algorithm that generates a matrix whose row vectors point in random directions and have unity magnitudes. *Rng* is a vector containing the range of each input variable.

To further improve the learning characteristics and speed of the network the addition of an adaptive learning rate algorithm was implemented in the back-propagation learning rule. In order to adjust the learning rate, the back-propagation algorithm has to be changed so as to allow a comparison of the present error of the network with the previous epoch network error. If the error exceeds the previous with a predefined ratio, the new weights and biases are rejected, together with letting the momentum take zero value. If the present error is less than the previous, the weights, biases, output and error are kept and the learning rate is increased by a predefined learning rate increment.

Table 1
Relative chemical composition of the carrageenans in the ternary data set

Sample no.	κ (%)	ι (%)	λ (%)
1(κ)	100	0	0
2(ι)	0	100	0
3(λ)	0	0	100
4	49.9	32.9	17.2
5	16.8	49.6	33.6
6	33.1	17.3	49.6
7(κ)	89.8	10.2	0
8(κ)	90	0	10
9(λ)	0	10.3	89.7
10(λ)	9.6	0	90.4
11(κ)	100	0	0
12(ι)	0	100	0
13(λ)	0	0	100
14(ι)	11.3	77.4	11.3
15	67	20.4	12.6
16(λ)	10.3	11.4	78.3
17	32	31.5	36.5
18	31	18.6	50.4
19	53.4	30.6	16
20(ι)	0	90	10
21(κ)	90.7	9.3	0
22	49	51	0
23	52.4	0	47.6
24	0	51	49
25 [a]	19.8	55.6	24.6
26 [a]	21.8	60.3	17.9
27 [a]	11	48.2	40.8
28 [a](λ)	18.1	4.9	77
29(ι)	0	100	0
30(κ)	100	0	0
31(λ)	0	0	100

[a] As determined in Ref. 9, indices within the parentheses indicate that the sample contains one carrageenan form for more than 75%. Samples 1–24 were composed of carrageenans supplied by Sigma. Samples 1–10 had a different batch origin than samples 11–24. Samples 25–31 were supplied by various suppliers. Samples 29–31 were stated as pure carrageenan forms.

3. Experimental

The three forms of carrageenans, namely κ, ι and λ, were supplied by Sigma (St. Louis, MO) in two different batches of each carrageenan form. A designed ternary data set, consisting of 24 objects (including an additional run of each pure carrageenan form, but of a different batch), was established by dry mixing of the carrageenans, to span the composition domain of the three carrageenan forms, see Table 1. For the analysis of the ternary data set seven additional carrageenan samples from various suppliers were added.

Approximately 5 mg of each carrageenan, in KBr tablets, were analysed by infrared spectroscopy. A Perkin-Elmer dispersive IR instrument, Model 580 B, was used in this study. To reduce the computational load, the analogue IR spectrum was digitized to a data table consisting of 34 spectra variables/features, described elsewhere [9]. Since some of the digitized variables

were generated by measuring the distance to a reference line set between 1350 and 660 cm^{-1}, negative values were also obtained. Thus, the variables were scaled to fall between −1 and 1, either by mean-centering followed by a simple multiplication with a constant for all of the variables or by scaling each variable to span the same interval within the interval −1 to 1.

The neural network used in this study was written in Matlab language (The MathWorks, Natick, MA) and by use of the extended functionality of the Neural Network toolbox. Principal component analysis was run on the SIRIUS data package (Pattern Recognition Systems, Bergen, Norway) or by use of the Chemometric toolbox provided by Matlab.

4. Results and discussion

A network that consists of 34 input variables and consequently 34 output values and with 10 nodes in each of the encoding and decoding layers, and two nodes in the projection layer, has to account for the adjustment of 720 weights and 56 biases. If the standard type of network is used, i.e. random generation of starting weights, a constant learning rate of 0.05 and with a momentum of 0.70, a sum-squared error of 787 after 500 iterations is obtained. The corresponding network but with adaptive learning rate generates a sum-squared error of 3.2 after 500 iterations. In this case the adaptive rules were set as follow; if the sum-squared error of the present iteration was lower than 1.04 of the previous iteration than the learning rate was increased by a factor of 1.05 and the momentum kept at its set value of 0.70. However, if the sum-squared error of the present iteration was equal or above 1.04 than the learning rate was decreased by a factor of 0.7 and the momentum set to zero. If the standard type of network is used but with the Nguyen–Widrow starting conditions a sum-squared error of 793 after 500 iteration is obtained. By use of the

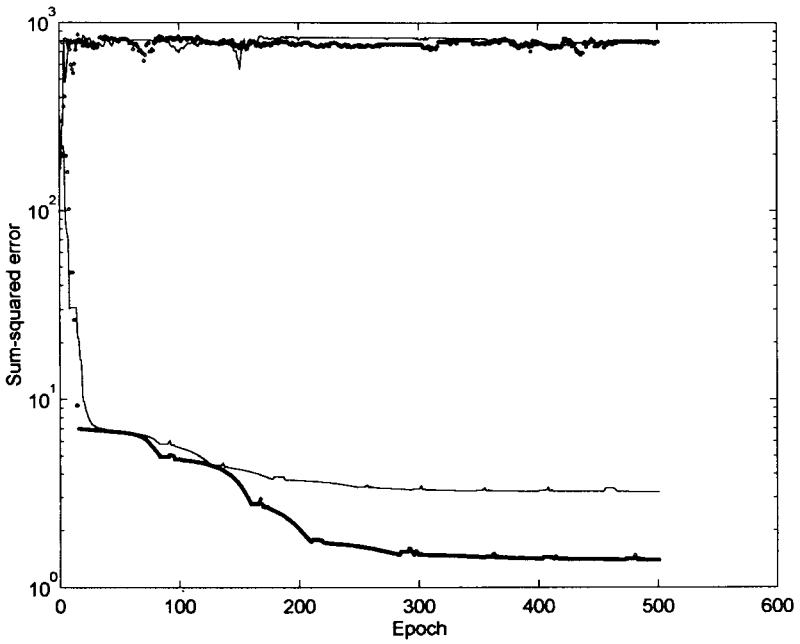

Fig. 2. The sum-squared error as a function of number of epochs and starting conditions of a network containing three hidden layers. The upper solid line represents a network of standard type, i.e. fixed momentum and learning rate. The upper dotted line corresponds to a network of the standard type and the use of the Nguyen–Widrow initialization conditions [7]. The lower solid line corresponds to a network with an adaptive learning rate and randomly generated starting conditions. The lower dotted line corresponds to a network with an adaptive learning rate rule and initialization according to Nguyen–Widrow [7].

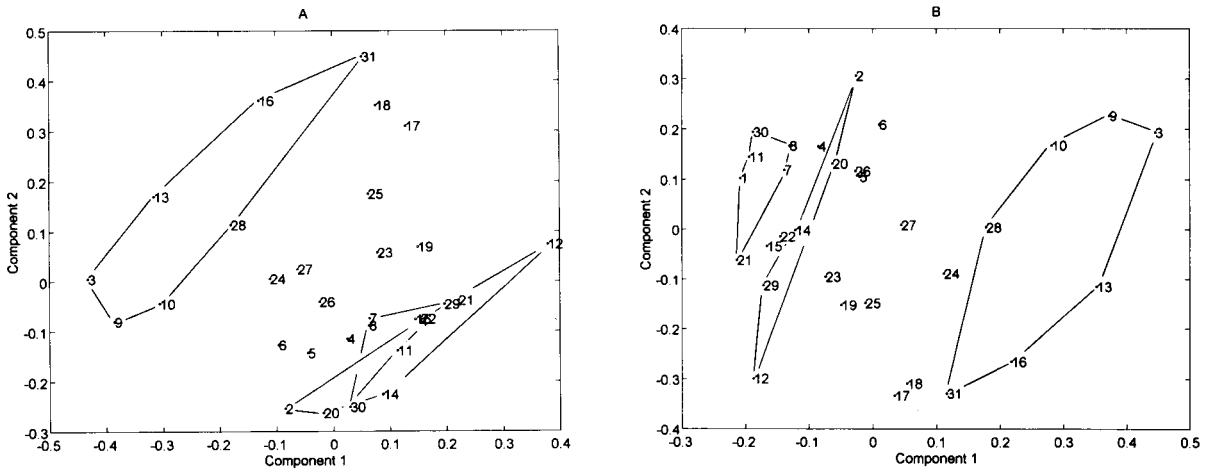

Fig. 3. Principal component plot of the mean-centered carrageenan data set. The three different rich/pure carrageenan forms are interconnected, respectively. The indices of the objects correspond to those given in Table 1. (A) Variables mean-centered; (B) variables mean-centered and scaled by the inverse of the variables standard deviation (auto-scaled).

Nguyen–Widrow initialization method and adaptive learning rate a sum-squared error of 1.4 was obtained after 500 iterations, see Fig. 2. The results summarized in Fig. 2 clearly indicate that improvements of the standard back-propagation neural networks algorithm could be achieved, and

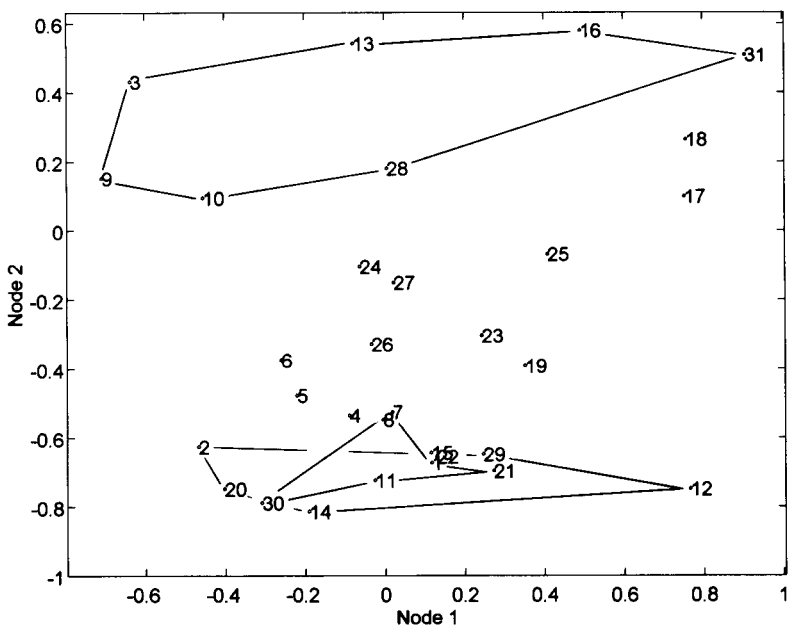

Fig. 4. Two-DIR neural networks plot of the mean-centered carrageenan data set. Network architecture: one hidden layer with two nodes. The three different rich/pure carrageenan forms are interconnected. The indices of the objects correspond to those given in Table 1.

that further improvements of the learning/training speed and modelling capability are justified and asked for.

Since the low-dimensional internal representations neural networks are generated by the use of a non-linear transfer function, a comparison with principal component analysis (PCA), a linear classification technique, has been conducted. The plot of the scores of the objects for the two first components by PCA is given in Fig. 3. The first two components account for 64.7% (for only mean-centered variables 82%) of the variance in the carrageenan data set. In the present study samples that contain more than 75% of one of the three primary forms have been defined as a carrageenan-rich/pure form of either κ, ι, or λ. Using this definition, one distinctive cluster, namely λ-carrageenan appears to be fairly well separated from the other forms in the two-dimensional PCA plot. The κ- and ι-carrageenans, at least for the mean-centered data set, are less well separated from each other than from mixed forms of the carrageenans. The corresponding L-DIR generated by the one- and three-hidden-layer networks are given in Figs. 4 and 5, respectively. Whereas the one-hidden-layer network performs a similar classification characteristics as that of PCA, a substantial increase in resolution is generated by the three-hidden-layer network. The plots were generated on variables obtained by mean-centering and a simple scalar multiplication, so that the maximum absolute value of the variable matrix was set to 0.9215. Thus, the L-DIR plots in Figs. 4 and 5 are to be compared by the one given in Fig. 3A. The three-dimensional internal representation by the neural networks of the polysaccharide data is shown in Fig. 6.

The L-DIR neural networks of the second derivative of spectral variables is given Fig. 7A for the one-hidden-layer network. This plot, which corresponds to a high degree to the ternary mixture design employed in this study, is also similar to the plot generated by the two first principal components of the second derivative spectra. The plot generated by the three-hidden-layer network, however, deviates and shows a more elabo-

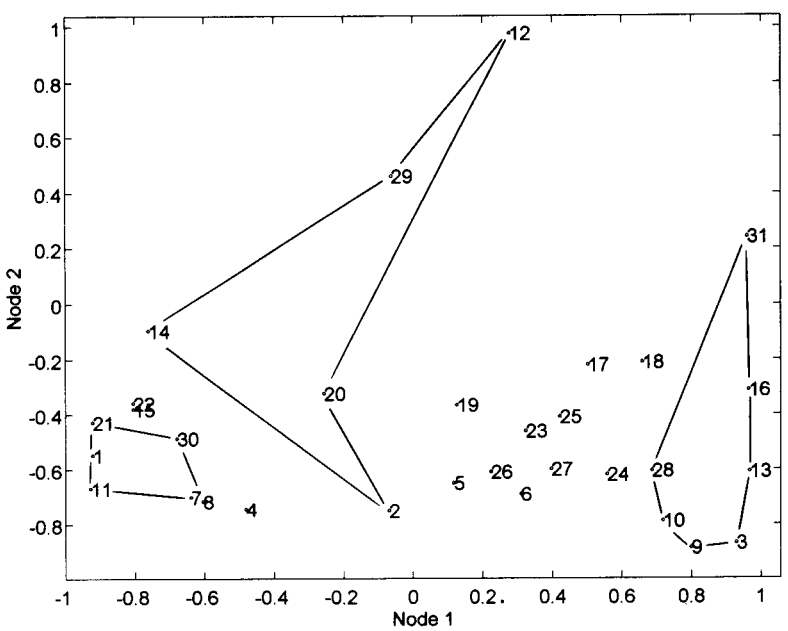

Fig. 5. Two-DIR neural networks plot of the mean-centered carrageenan data set. Network architecture: three hidden layers with 10 nodes in each en- and decoding layer, and two nodes in the projection layer. The three different rich/pure carrageenan forms are interconnected, respectively. The indices of the objects correspond to those given in Table 1.

rate utilization of the weight representation then the one-hidden-layer representation, for the same kind of pre-processed data set, see Fig. 7B.

Thus, additional information can be extracted beyond what can be provided by a linear transformation and compression of the data set. This may provide additional insight into structure and properties of the studied data. However, the price to be paid is a considerable increase in computer demands and time (e.g. processing times > 24 h). The observation that the generated L-DIR neural network plots deviate from the PC plots is most probably due to the non-linear transfer function. However, the network architecture also appears to be of importance, since the L-DIR plots from the networks with three hidden layers differ more pronounced from the PC plots than the one-hidden-layer networks. For all multivariate analysis methods the modelling properties and predictive capabilities have to be balanced, that is, overfitting has to be circumvented. For the network with one hidden layer containing two or three nodes the risk of overfitting is negligible since this corresponds to two or three principal components. For the network consisting of three hidden layers the risk of overfitting, that is extraction of redundant or spurious information, is less clear. Provided that the number of nodes in each of the en- and decoding layers is significantly lower than the number of input nodes (in this study 30% or lower), the network converges to one with a stable error minimum and with interpretable plots.

The programme used in this study has been written in Matlab language; if the code had been written in for example C an increase in computational speed up to a factor of 100 could have been obtained. But nevertheless, in comparison to PCA, this would still be considered as slow. PCA generates components in a decreasing order of explained variance, hence a limited number of the first components can explain the larger part of the variance in the data set, especially if the variables are redundant and/or covarying. In the present data set two components (auto-scaled data) account for ca. 65% of the explained variance, 4, 8 and 10 components for 89, 95 and 96%, respectively. If the objects in the data set are instead represented by the scores of the principal components, the complexity of the L-DIR neural networks weight matrix could be substantially reduced. By use of the scores from 10 principal

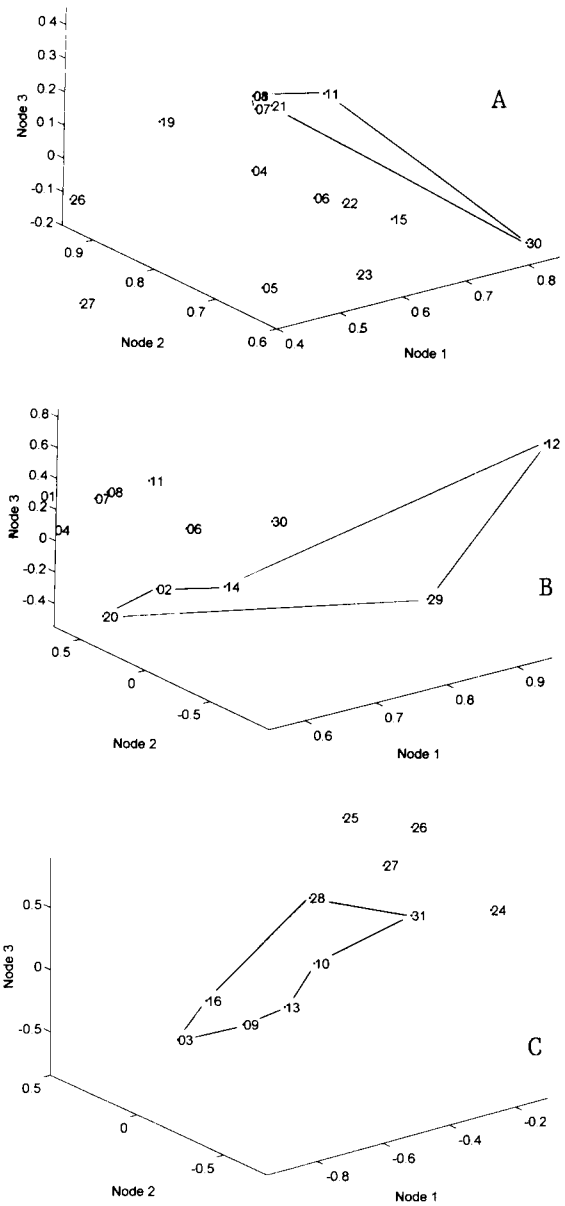

Fig. 6. Three-DIR neural network plots of the mean-centered carrageenan data set showing the 3D-subspaces occupied by the three different rich/pure carrageenan forms. Network architecture: three hidden layers with 10 nodes in each en- and decoding layer, and three nodes in the projection layer. (A) κ-carrageenan; (B) ι-carrageenan; (C) λ-carrageenan.

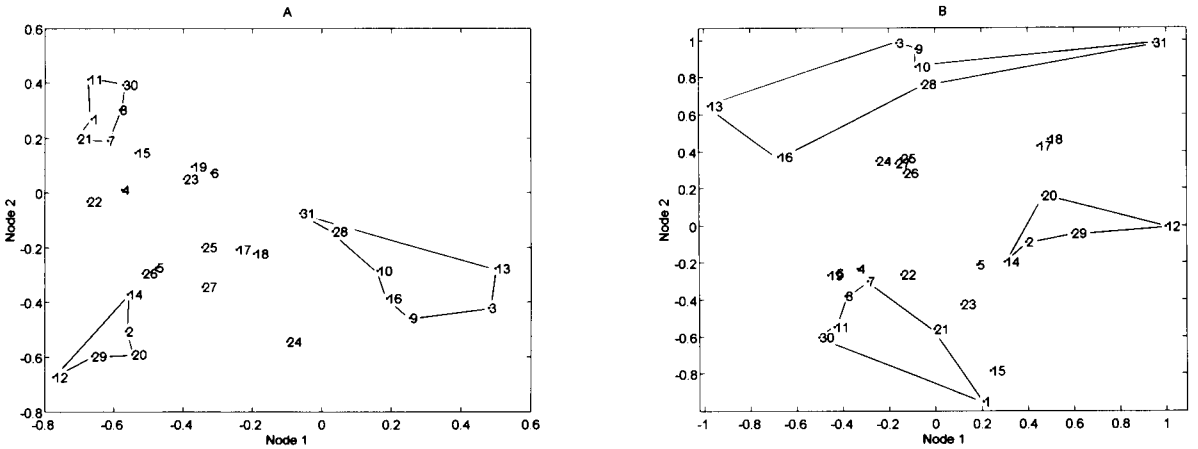

Fig. 7. Two-DIR neural network plots of the second derivative of the spectral variables of carrageenan data set. (A) one hidden layer; (B) three hidden layers.

components the weight matrix could be reduced by a factor of 3 for the L-DIR network consisting of three hidden layers with 10 nodes in the en- and decoding layers and 2 nodes in the projection layer. The result generated by the L-DIR neural networks resembles that which can be provided by the one-hidden-layer network or PCA on mean-centered variables. The analysis capacity, expressed as the number of epoch per seconds, of the network has, however, increased by 56%.

The information content in the two- and three-dimensional plots generated by the L-DIR neural networks appears to be on the same order or higher as that of PCA. In the neural network plots, however, the carrageenans are clustered to some degree differently than a purely linear transformation/compression and in some cases also a more efficient utilization of the low-dimensional plot area is obtained. Thus, it appears that the internal representation neural networks perform, on a basically linear composed data set, similar to PCA but also give some additional feature extraction of the studied carrageenans. It can thus be used as a valid and useful complement to linear techniques for exploratory analysis on multivariate data.

References

[1] R.G. Brereton (Ed.), Multivariate Pattern Recognition in Chemometrics, Illustrated by Case Studies. Data Handling in Science and Technology, Vol. 9, Elsevier, Amsterdam, 1992.

[2] K. Hornik, M. Stinchcombe and H. White, Neural Networks, 2 (1989) 359

[3] R.P. Lippmann, IEEE ASSP Mag., April (1987) 4

[4] P. Baldi and K. Hornik, Neural Networks, 2 (1989) 53

[5] D.H. Ackley, G.E. Hinton and T.J. Sejnowski, Cogn. Sci., 9 (1985) 147

[6] J.L. Elman and D. Zipser, Institute for Cognitive Science, University of California, Technical Report-8701.

[7] D. Nguyen and B. Widrow, Int. Joint Conf. on Neural Networks, 3 (1990) 21

[8] D.E. Rumelhart, J.L. McClelland and PDP Research Group, Parallel Distributed Processing: Explorations in the Microstructure of Cognition, Vol. 1, MIT Press, Cambridge, MA, 1986.

[9] S.P. Jacobsson and A. Hagman, Anal. Chim. Acta, 284 (1994) 137.

ELSEVIER

Analytica Chimica Acta 291 (1994) 29–40

ANALYTICA CHIMICA ACTA

Knowledge-based fault detection and diagnosis in flow-injection analysis

Jens Brandt, Bernd Hitzmann *

Institut für Technische Chemie, Universität Hannover, Callinstr. 3, 30167 Hannover, Germany

(Received 29th November 1993; revised manuscript received 28th January 1994)

Abstract

The reliable operation of flow-injection analysis systems (FI systems) demands a high degree of knowledge and experience. This a priori knowledge is of great importance, especially for a fast detection and diagnosis of faults. Transferring it into the form of a knowledge-based system and combining it with information received on-line from the recorded detector signal enables automatic operational supervision of FI systems. This contribution presents a real-time knowledge-based system for the supervision of FI systems applied in on-line bioprocess monitoring. The special conditions of real-time systems are explained and the basic structure of the knowledge base is illustrated. Examples of typical faults of the FI system are given to explain how symbolic knowledge processing can be combined with numerical analysis of data to perform a fast and reliable fault detection and fault diagnosis.

Key words: Flow injection; Knowledge-based systems; Fault diagnosis; Real-time system; On-line analysis; Bioprocess monitoring

1. Introduction

Flow-injection (FI) analysis techniques are used for the automation of a wide range of analytical chemical procedures [1]. In general, FI systems represent a combination of wet chemistry, mechanics (e.g., pump, valves) and electronics and the complexity of these systems implies an increased potential of faults. Thus, an extensive automation of FI systems, as it is required especially for applications in industrial process control, has to include the automation of supervising functions. However, the fast and reliable detection and diagnosis of faults in FI systems requires a high degree of knowledge and experience (know-how). This a priori knowledge has to be transformed into a computer processable form, to take advantage of it for the automation of FI systems.

Conventional computer programs that are developed with programming languages like C or FORTRAN are not yet well-suited for the representation and processing of knowledge and experience. Consequently, special techniques (tools, shells and programming languages) have been developed in the field of artificial intelligence (AI) to imitate human problem-solving behaviour. Up to now, the most successful applications of AI

* Corresponding author.

SSDI 0003-2670(94)00082-W

techniques are knowledge-based systems (expert systems), that are qualified to represent and process verbally formulated knowledge in a very efficient manner.

Various knowledge-based systems (expert systems) have been developed for applications in analytical chemistry. They are generally used as interactive systems, meaning that the user has to interact with the knowledge-based system to solve a certain problem. Examples are assistance and advisory systems for optimising analytical procedures [2] or for the interpretation of spectra [3]. Other examples are expert systems for the quantitative validation of chromatographic [4] or FI methods [5]. These expert systems evaluate calibration procedures, effects of the sample matrix and the reliability of the analytical methods. Additional examples for expert system applications in analytical chemistry are given by Hohne and Pierce [6].

Interactive knowledge-based systems are commonly used in domains where the data are static and no time-critical responses are required. However, a knowledge-based system for fault detection and diagnosis has to be capable of recognising changes in the state of a FI system without loss of time and to guarantee a response after a fixed time has elapsed. Hence a real-time knowledge-based system has to be connected directly (via a data acquisition system) to the FI system and it has to be supplied continuously with measurement data.

The special requirements of real-time knowledge-based systems are discussed in detail by Laffey et al. [7]. The basic points are

the capability of continuous operation, e.g., the possibility to operate until stopped by an operator;

the ability to focus the attention on important goals, when a significant event occurs;

a temporal reasoning, e.g., the ability to reason about past, present and future events;

the integration with procedural components to perform sensor readings, signal processing and feature extraction.

To perform a fault detection and diagnosis, some specific features of FI systems have to be considered. The basic principle of flow-injection analysis is the exact reproducibility during a calibration and the following measurements. The

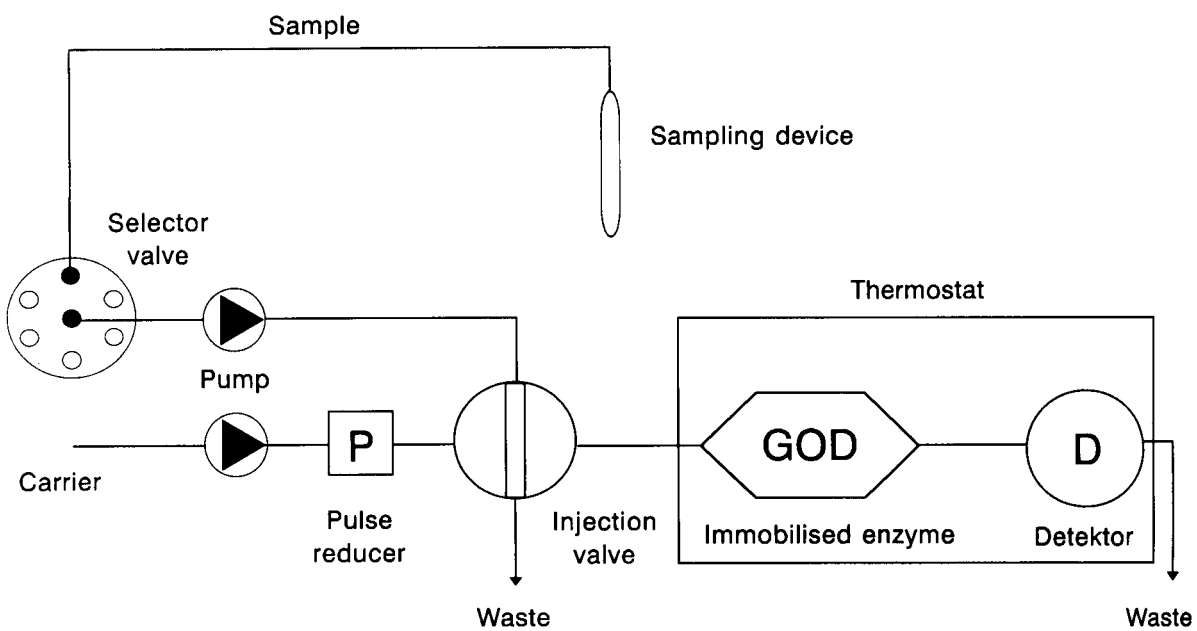

Fig. 1. FI system for glucose determination using glucose oxidase (GOD).

shape of the FI signal is characteristic of a given FI system. It is controlled by the system parameters such as flow-rate, geometry of the flow system, reaction kinetics and response characteristics of the detector. This means that the recorded FI signal contains, apart from the required analytical information, additional information about the measuring process and the state of the FI system. Changes in the system parameters, either intentionally caused by the operator or unintentionally caused by a fault, influences the recorded signal and often lead to a characteristic changing of the peak shape.

As known to the authors, systematic investigations of possible faults of FI systems and their influence on the FI signal have rarely been performed. The influence of the main parameters of FI systems on the output signal can partly be described by mathematical models [8]. However, a lot of the relevant faults of FI systems are hardly accessible by exact deterministic approaches, especially for a fault diagnosis under real-time conditions. Chen and Zeng [9] reported a peak recognition technique to identify and remove interferences from air bubbles in the flow system [9]. Szostek and Trojanowicz [10] used

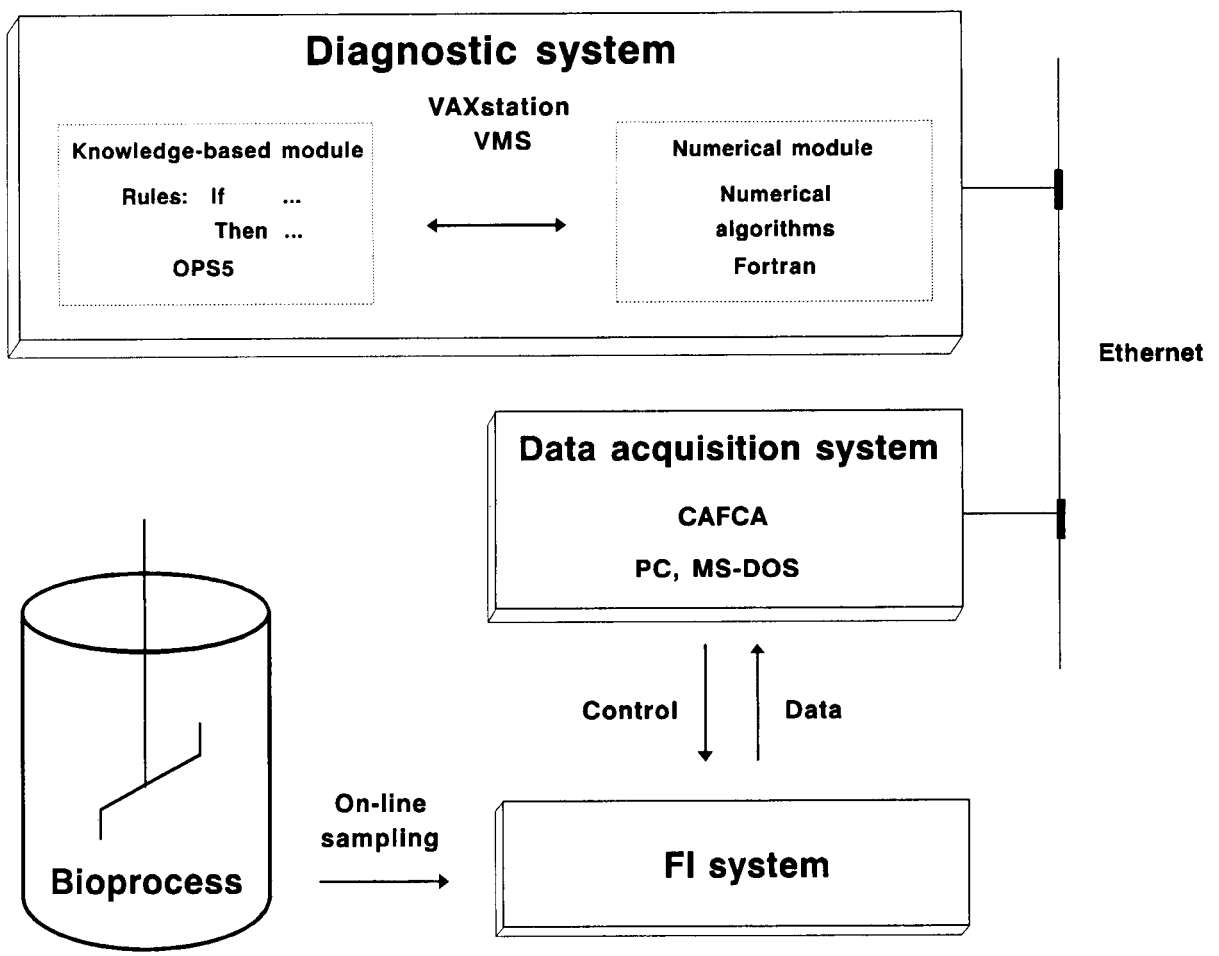

Fig. 2. Connections of bioprocess, FI system, data acquisition system and diagnostic system.

digital filters to remove high frequency noise from FI signals and Giné et al. [11] determined the dependence of signal fluctuations along the FI signal profile on the parameters of a single line FI system. Hence, a major part of this work was the analysis of a certain FI system, the investigation of possible faults of this FI system, their influence on the FI signal and hints for their remedy.

2. Experimental

2.1. FI system

The FI system used for this investigation contained all standard components usually employed in FI systems (pump, injection valve, manifold and detector). As can be seen in Fig. 1, additional components such as an on-line sampling device and a selector valve were required for the application in process monitoring. The manifold consisted of a column containing immobilised enzyme (Glucose oxidase, GOD). An oxygen sensor was employed as a detector. It determined the oxygen utilisation caused by the enzymatic conversion of glucose via GOD, that is, in a certain range, proportional to the glucose concentration of the sample. Each measuring cycle lasted 3 min. A more detailed description of the FI method is given by Dullau and Schügerl [12]. The FI system under consideration was used for the on-line determination and control of glucose concentration during the cultivation of fungi (*Penicillium chrysogenum*). Up to 3000 FI measuring cycles were run during a typical cultivation lasting about 150 h.

2.2. Data acquisition

The automation and basic evaluation of the FI measurements were realised using the FI automation and data acquisition system CAFCA (Computer Aided Flow Control and Analysis, Anasyscon, Hannover). It operates on MS-DOS computers and enables the automation and evaluation of all requested FI procedures, including stopped-flow techniques and the running of calibration cycles. The signal was recorded at a sampling rate of 2 Hz.

2.3. Knowledge-based system

The knowledge-based system was developed on a VAXstation 3100 (Digital Equipment, Maynard, MA) and combines numerical data analysis with symbolic knowledge processing. The knowledge-based module was developed in VAX-OPS5 (Digital Equipment), a development tool for production systems [13]. This means that the knowledge in this module is represented in rules of the form IF ⟨*condition*⟩ THEN ⟨*action*⟩. The numeric module was developed in FORTRAN using well-tried algorithms for statistics and signal processing. The knowledge-based system was connected to the FI system by a very fast link (Ethernet, DECnet) via CAFCA. The connection of the knowledge-based system, the data acquisition system and the FI system is shown in Fig. 2.

3. Results and discussion

Experience enables the operator of an FI system to relate a characteristic pattern in the measurement signal in a temporary as well as causal fashion. To identify certain faults he combines general a priori knowledge about the FI system, temporal knowledge about the state of the FI system and the connected process as well as knowledge about characteristic changes of the FI signal caused by a fault. On account of his experience, he is able to take steps to the remedy of faults without loss of time. To solve these problems with a knowledge-based system, the relevant knowledge has to be collected and structured first. In a second step the knowledge has to be implemented in the computer system and than, in a third step, the constructed knowledge base has to be tested and extended.

3.1. Knowledge acquisition

The knowledge acquisition is the most important as well as difficult part in the development of knowledge-based systems. However, for the auto-

mated supervision of FI systems, it is not necessary to implement the complete knowledge of an experienced FI operator. Small knowledge fragments in the form of simple rules can provide very effective results.

In order for a fault detection and diagnosis to be performed by the knowledge-based system, all known faults were collected and structured according to various criteria. Empirical methods, e.g., watching and interviewing experienced FI operators, were combined with systematical methods such as failure mode and effect analysis (FMEA) to reach an extensive consideration of all possible faults.

3.2. Analysis of the FI system

For a systematical approach, the FI system was divided into five subsystems, each of which was subdivided into several functional groups. As an example it is shown in Fig. 3 by example of the injection valve, a furthergoing division into single functional units was carried out. The possible faults of each functional unit were examined to

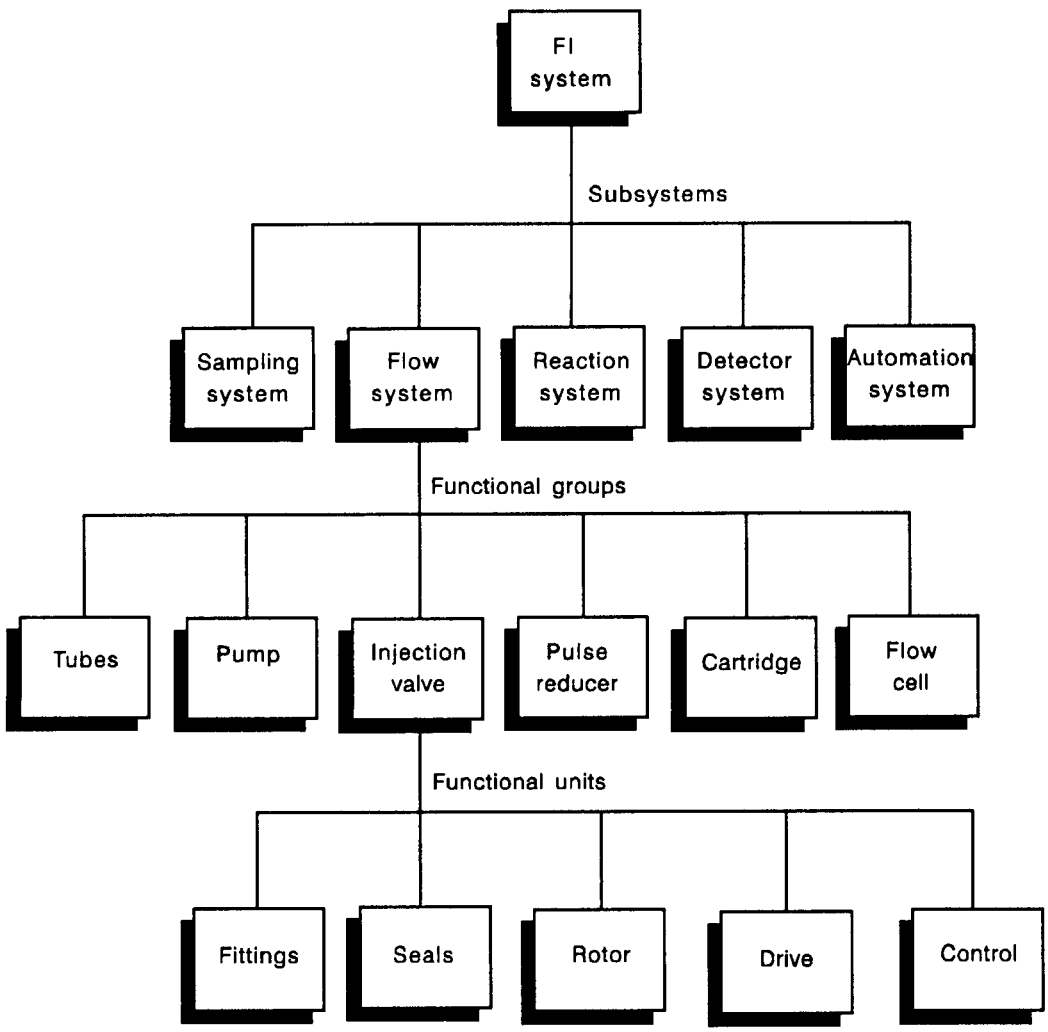

Fig. 3. For the analysis of the FI system, it was divided into subsystems, functional groups and functional units.

Table 1
Examples of typical faults observed in the FI system

Faults of the sampling system	Faults of the flow system	Faults of the reaction system	Faults of the detector system	Faults of the automation system
Plugging of filtration device, microbial contamination of sampling device, tube disconnected, malfunction of calibration valve, plugging of calibration valve plugging of drain, wrong stand ard solutions, fluctuating dilution rate	Air bubbles, change of flow rate, disconnection of a tube, plugging of a tube, malfunction of the injection valve, leaking fittings, loss of the pump, ageing of the pumping tube, burst of a tube fitting	Changing of the temperature, sample containing enzyme inhibitors, wrong composition of the carrier, wrong linear range, wrong sensitivity, cartridge containing the wrong enzyme, sample containing proteases	Ageing of the membrane, damaging of the membrane, coating of the electrode, electrical noise, wrong polarization voltage, signal exceeds amplification range, baseline falls below the detection limit	Hardware breakdown, control or data wire disconnected, wrong I/O ports selected, wrong A/D range selected, wrong input of concentration of standards for calibration, wrong input of cycle times

determine their influence on the entire FI system and the FI signal. Some examples of typical faults observed in the FI system are given in Table 1.

3.3. Analysis of the FI signal

The recorded FI signal is the most important source of information for the knowledge-based diagnostic system. A typical FI signal recorded during an undisturbed FI cycle is shown in Fig. 4. Four different signal phases can be distinguished that were called initial phase, rising phase, falling phase and asymptotic phase. This division is very useful for a fast detection of changes of the FI signal even before the actual FI cycle is completed. If, for example, the slope of the signal suddenly turns to large positive values during phases 3 or 4, a fault is very likely. A collection of examples of FI peaks recorded during disturbed measurements can be seen in Fig. 5.

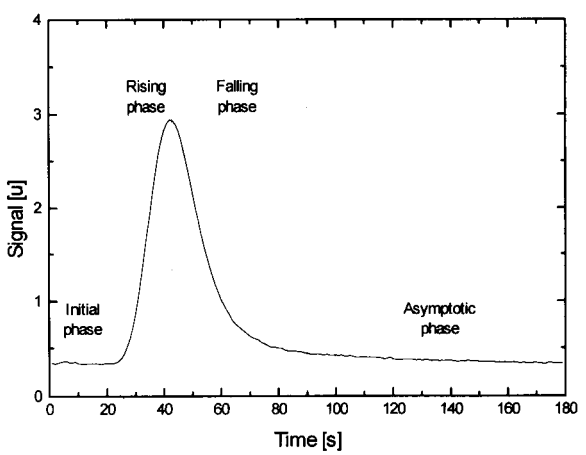

Fig. 4. Four phases can be distinguished in an undisturbed FI signal.

In order to recognise a disturbance, numerical algorithms were applied to calculate numerical values that characterise the shape of the FI signal (feature extraction). Examples of useful characteristics are: peak height and integral, peak width at 5, 50 and 95% of the peaks height, retention time, baseline drift, tailing factor, noise factor, rise and fall time of the peak, length of signal phases, statistical moments of the peak, and distance to the limits of the measurement range.

An example of a very important characteristic is the retention time, i.e., the time that elapses between the injection of a sample and its arrival in the detector. The retention time is strongly influenced by changes of the flow system parameters, e.g., the flow rate.

As an illustration, Fig. 5a shows two FI signals that were recorded one after the other during a cultivation of *Penicillium chrysogenum*. A fault in the flow system occurred caused by a squeezed tube. This led to a decreased flow rate and consequently the residence time of the sampling zone in the manifold increased and led to a higher conversion during the following FI cycle. As a result, the glucose concentration was determined to be much higher than it really was. As can bee seen in Fig. 6, the values of the retention time

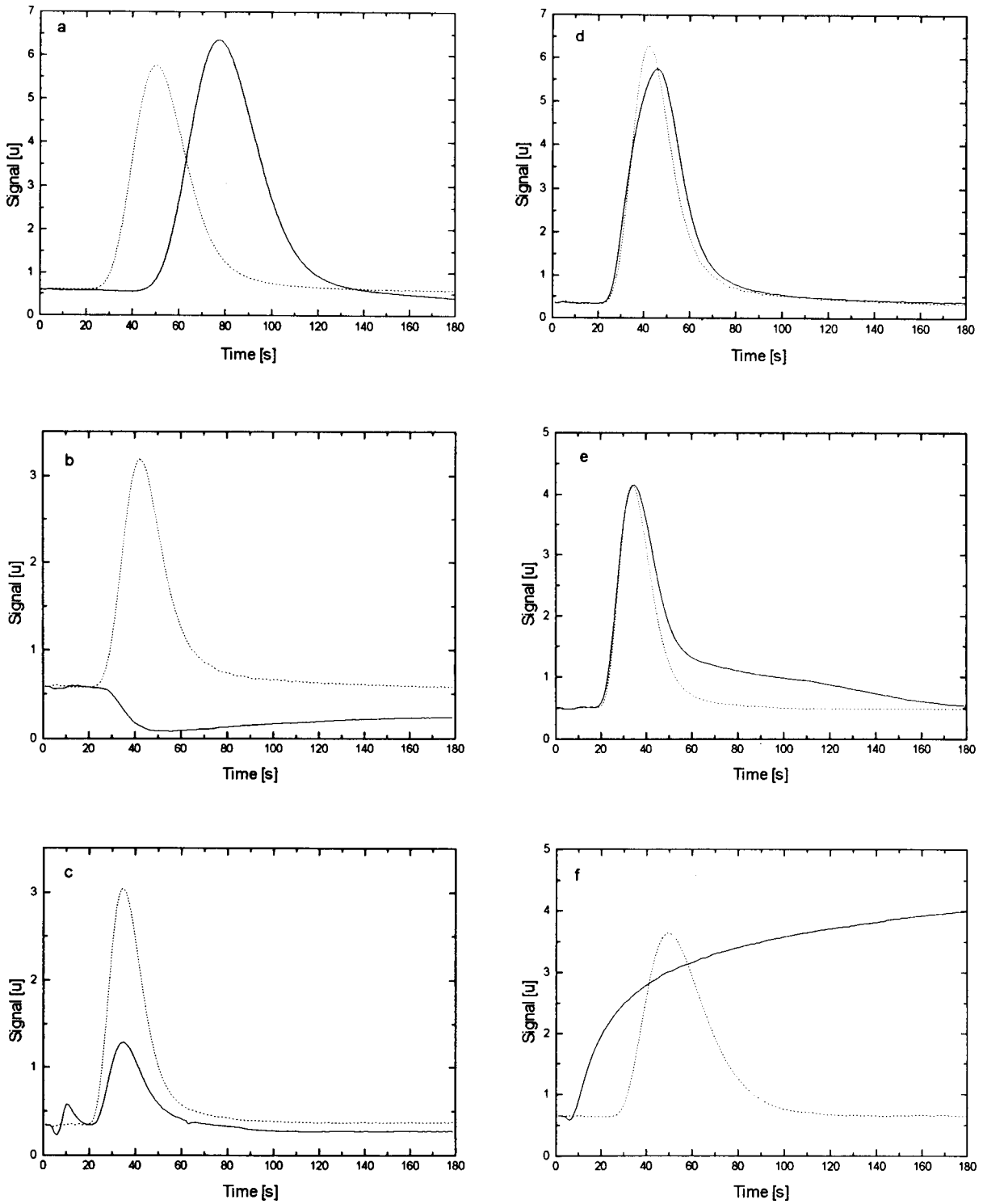

Fig. 5. Examples of disturbed FI signals (recorded signal, solid lines; expected signals, dotted lines). (a) Flow system: squeezed tube. (b) Sampling system: plugged sampling device. (c) Flow system: plugged injection valve. (d) Reaction system: linear range exceeded. (e) Flow system: microbial contamination. (f) Flow system: burst of a tube.

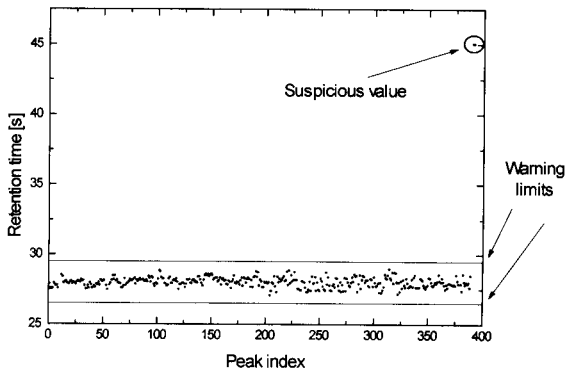

Fig. 6. The retention time versus peak index as a source of information. If the retention time is not between characteristic limits, a fault is very likely.

had stayed in a small interval during the previous 380 FI cycles. The sudden increase indicates very clearly the changing of the flow rate.

3.4. Additional a priori knowledge

Additional knowledge and experience about operating an FI system and about the connected process was collected to increase the selectivity and reliability of the fault diagnosis. This knowledge often is given in simple rules of thumb, such as:

"If the system is running for more than 10 h, then the danger of faults caused by microbial contamination increases."

or

"If the connected process is a cultivation of *Bacillus licheniformis*, then the production of proteases starts after 15 h and can lead to a degradation of the enzyme."

or

"If the FI system is running a calibration cycle then the probability of the appearance of air

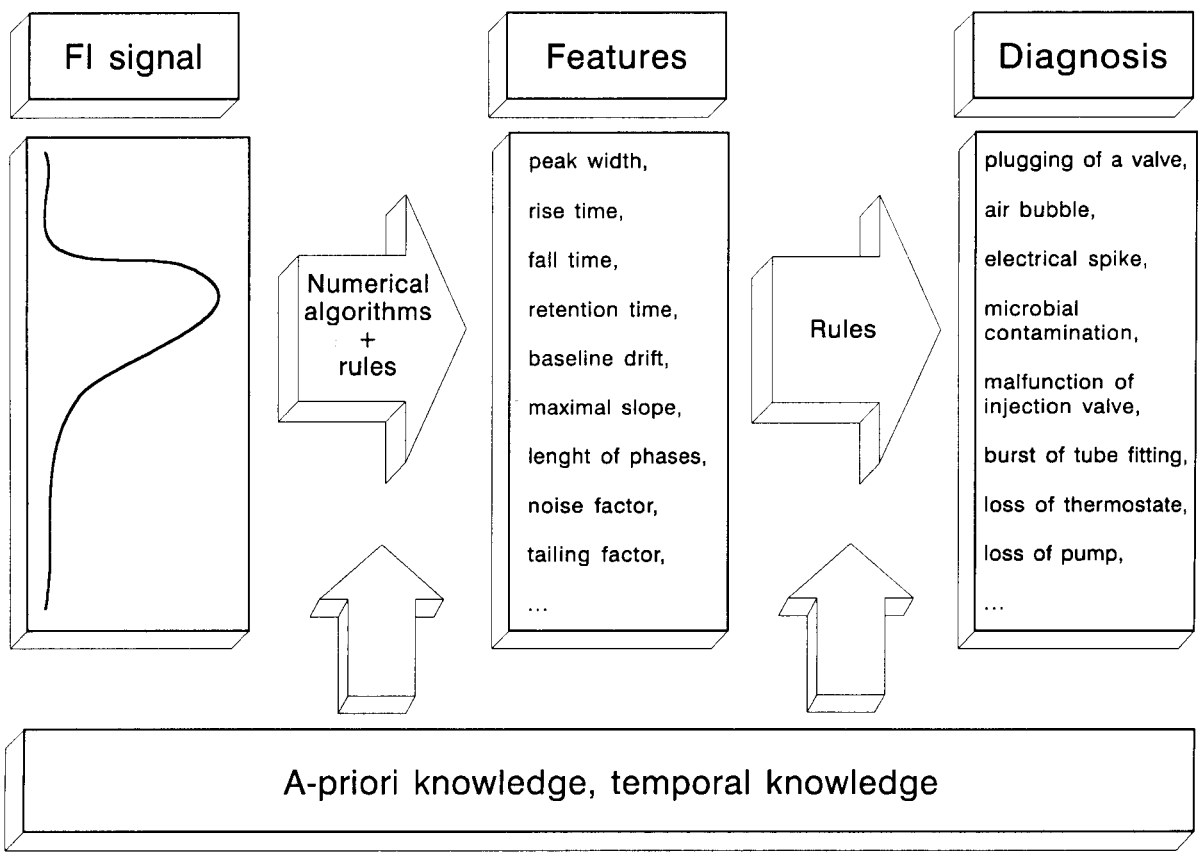

Fig. 7. Feature extraction for fault detection and diagnosis.

bubbles is increased, because bubbles may have gathered in the selector valve."

This kind of knowledge is very important as it provides the system ability to offset missing sources of information, e.g., direct observation of the FI system.

3.5. Knowledge representation and processing

The basic structure of the knowledge-based module of the diagnostic system is analogous to the general structure of production systems developed with OPS5. It consists of three parts, the working memory, the production memory and the inference engine. The working memory is a collection of elements called attribute-value pairs (structured symbols) that represent data and facts such as life time, probabilities of faults or rated values of characteristics. For example, the characteristic "Retention time" is represented as an element called "Retention_time" and has the attributes "Peak_Nr.", "Rated_value" and "Actual_value":

(Retention_time
Peak_Nr. 383
Rated_value 27.3 s
Actual_value 26.8 s)

The production memory is a set of rules of the form IF ⟨*condition 1*⟩ AND ⟨*condition 2*⟩ AND ⟨*condition 3*⟩ THEN ⟨*action*⟩. The conditional part of these rules consists of structured symbols or patterns that have to be compared with symbols contained in the working memory. These rules are used to control the evaluation of the FI signal as well as to draw conclusions of the extracted features. Hypotheses of possible faults are postulated and either verified or rejected.

The set of rules is partitioned into distinct subsets according to their specific knowledge domain:

rules that analyse individual values and parts of the FI signal to identify short-term changes,

rules that analyse a complete FI signal to identify changes of the peak shape,

rules that analyse several FI signals to identify long-term changes,

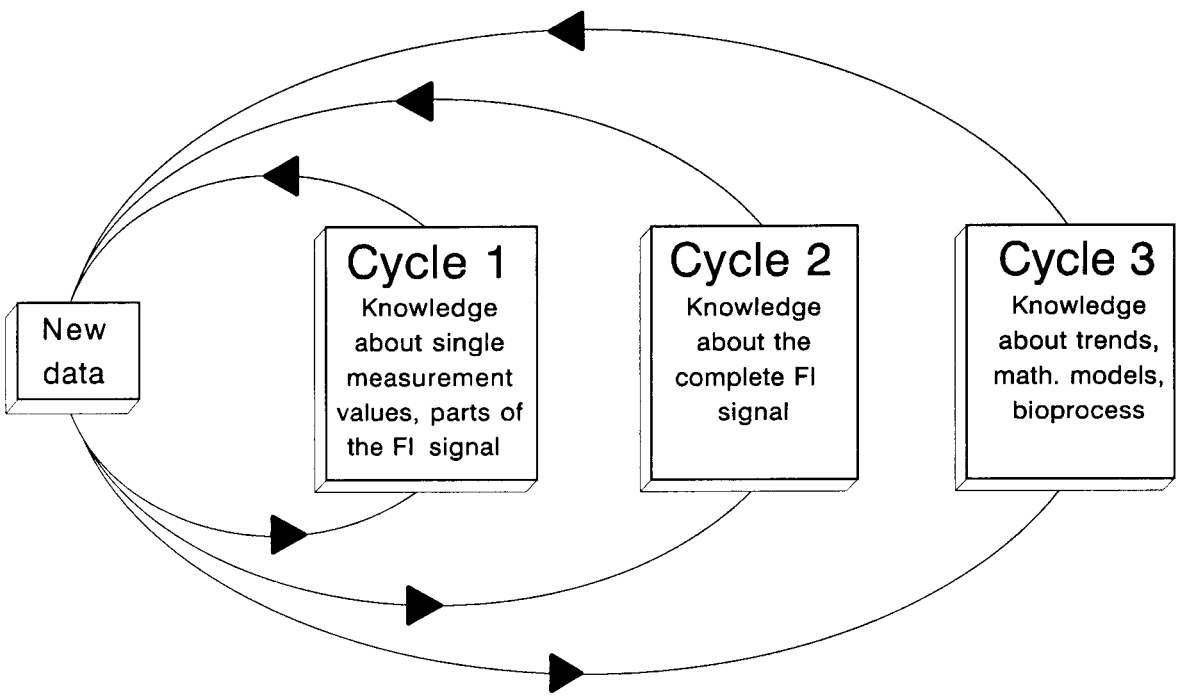

Fig. 8. Interconnected cycles of knowledge processing in the diagnostic system.

rules that control the actions of the system,

rules that control the knowledge processing itself (meta rules).

The search for rules that have a fulfilled conditional part (pattern matching), the conflict resolution and the execution of the action part of the rules is done by the inference machine.

3.6. Realisation of the fault detection and diagnosis

An experienced operator of FI systems is able to recognise characteristic changing in the measurement signal and to relate it to certain faults. As can be seen in Fig. 7, the automated fault detection is performed in a similar way. Rules control the extraction of features from the FI signal by using numerical procedures. Other rules draw conclusions to relate these symptoms to particular faults. All rules are based on the a priori knowledge and are subdivided into three particular subsets according to their information content.

As illustrated in Fig. 8, these rule subsets are activated in three interconnected cycles with the help of meta rules. In the first cycle, every actually recorded measurement is examined. If there is an unusual large deviation between calculated and expected values, a hypothesis that a potential fault exists is formulated. With this hypothesis as a starting point, additional rules that attempt either to validate or reject the hypothesis are activated. During the second cycle the actual FI signal is examined after its completion. In this cycle changing of the shape of the entire FI signal are recognised.

A more general analysis is performed during the third cycle. Features of different FI signals are compared, trends are recognised and mathematical models are fitted. A priori knowledge about the connected process is also activated during the third cycle. If, for example, the substrate concentration in a batch bioprocess has to be determined and the measured concentration is expected to decrease, then a fault is very probable if the FI system reports constant or increasing concentrations. Cycles two and three are interrupted each time when new data are recorded. If any disturbance is detected while performing cycles one, two or three, another set of rules is activated that controls the actions performed by the knowledge-based system. The operator is immediately informed with a message and an explanation of all decisions and actions carried out by the knowledge-based system.

3.7. Application example

The main conclusions pertaining to a fault in the flow system will be described here. Fig. 5f shows the signal recorded during this particular FI cycle. A slight abnormality of the signal can be observed immediately after the injection. This abnormality is the result of a decrease of the flow rate during injection caused by plugging of the sample loop. As a consequence, the pressure in the flow system between pump and injection valve increased, that resulted in the burst of the tube fitting and the stopping of the carrier flow. The continuously rising signal without return to the baseline is characteristic for this event. Simplified rules that contributed to the diagnosis of this fault are as follows:

IF the measurement data in the initial phase of the FI cycle differ from a straight line THEN make the hypothesis "Injection disturbed";

IF the actual cycle is not in the rising phase AND the gradient of the signal has a large positive value THEN make the hypothesis "Fault of the flow system";

IF the hypothesis "Fault of the flow system" exists AND the gradient of the baseline is positive for more then 20 s THEN verify the hypothesis, make another hypothesis "Burst of the carrier tube", and alert the operator: "Attention! Fault of the flow system: burst of the carrier tube";

IF the hypothesis "Injection disturbed" exists AND the hypothesis "Burst of the carrier tube" exists AND the burst of the carrier tube occurred during the initial phase THEN make the hypothesis "Burst of the carrier tube caused by fault of the injection valve";

IF the hypothesis "Burst of the carrier tube caused by fault of the injection valve" exists AND no disturbance of the injection had been registered in the cycles before THEN make the diagnosis "Burst of the carrier tube caused by a particle plugging the injection valve";

The coincidence of the disturbed injection and the burst of the carrier tube is an important clue to the cause of this fault. However, a more precise diagnosis can be done considering the temporal development of the disturbance. If a sudden large disturbance occurs, it is generally caused by a single particle plugging the injection valve. Plugging as a cause of microbial contamination would have resulted in a slowly rising disturbance of the injection.

4. Conclusion

Complex process analysers, such as on-line FI systems, require continuous operational supervision especially if they are used in process control. This contribution shows how a real-time knowledge-based system can be applied for the fast detection and diagnosis of faults in FI systems. Empirical and systematical methods of knowledge acquisition were combined to reach an extensive consideration of all possible disturbances. The result is a hybrid diagnostic system in which symbolic knowledge processing is combined with the numerical analysis of data. Small knowledge fragments in the form of simple rules provide very effective results in order to enhance speed, reliability and selectivity of the fault diagnosis.

This investigation was using a FI system for glucose determination that applies a column containing immobilised glucose oxidase. With an oxygen detector a peak shaped signal is detected from which characteristics are extracted by numerical algorithms. The characteristics are than analysed by language-based heuristics for a fast detection and diagnosis of faults. This concept can be extended to other FI modes as well as more complex FI systems or other complex process analysers such as process liquid chromatography. In the stopped-flow mode, for instance, the signal will be different and more complex than in the continuous-flow mode. Other characteristics might need to be calculated and most probably an additional signal phase must be introduced to consider the kinetics of the reaction taking place. But if the specific knowledge of such a FI system is transferred to the knowledge-based system, then a fault can be detected and diagnosed in the same manner as described. The extension of the knowledge-based system to more complex FI systems, e.g., one with several channels, will lead to a faster and more reliable detection and diagnosis of some faults. For instance, a fault in the sampling system will cause specific symptoms in the measurement signals of all channels. The simultaneous occurrence of these symptoms might be an important hint for the knowledge-based system. Therefore, the higher evidence of the information coming from several channels will improve the detection and diagnoses of faults.

Although it is not necessary to implement the complete knowledge of an experienced FI system operator, the building of a knowledge-based real-time diagnostic system means a high effort. Nevertheless, the benefits of automated supervision of FI systems, e.g., enhanced reliability of the analytical results and reduced down times of the FI system, are worth this effort.

Acknowledgement

We thank the Deutsche Forschungsgemeinschaft (DFG) for financial support of this work.

References

[1] J. Ruzicka, E.H. Hansen, Flow Injection Analysis, Wiley, New York, 1988.
[2] P.J. Schoenmakers, N. Dunand, A. Cleland, G. Musch and Th. Blaffert, Chromatographia, 26 (1988) 37.
[3] R. Wehrens, L. Buydens and G. Kateman, Chemom. Intell. Lab. Syst., 12 (1991) 57.
[4] J.A. van Leeuwen, L.M.C. Buydens, B.G.M. Vandeginste and G. Kateman, Anal. Chim. Acta, 235 (1990) 27.
[5] R. Wolters, M.A.J. van Opstal and G. Kateman, Anal. Chim. Acta, 233 (1990) 65.
[6] B.A. Hohne and T.H. Pierce, Expert System Applications in Chemistry, American Chemical Sociaty, Washington, DC, 1989.
[7] T.J. Laffey, P.A. Cox, J.L. Schmidt, S.M. Kao and J.Y. Read, AI Magazine, 9 (1988), 27.
[8] S.D. Kolev and E. Pungor, Anal. Chim Acta, 208 (1988) 117.
[9] D. Chen and Y. Zeng, Anal. Chim. Acta, 235 (1990) 337.

[10] B. Szostek and M. Trojanowicz, Anal. Chim. Acta, 261 (1992), 509.
[11] M.F. Giné, R.L. Tuon, F.J. Krug and M.A.Z. Arruda, Anal. Chim. Acta, 261 (1992) 533.
[12] T. Dullau and K. Schügerl, in R.D. Schmid (Ed.), Flow Injection Analysis (FI) based on Enzymes or Antibodies, VCH Verlag, Weinheim, 1990.
[13] L. Brownston, R. Farell, E. Kant, N. Martin, Programming Expert Systems in OPS5: An Introduction to Rule-based Programming, Addison-Wesley, Boston, MA, 1985.

ELSEVIER

Analytica Chimica Acta 291 (1994) 41–52

ANALYTICA CHIMICA ACTA

Impulse–response functions of flow-through detectors based on the membrane-stabilised liquid–liquid interface Part I. Mathematical treatment

Stefan Wilke [a,*], Roswitha Picht [b]

Martin-Luther-Universität Halle-Wittenberg, [a] Fachbereich Chemie and [b] Fachbereich Mathematik und Informatik, D-06217 Merseburg, Germany

(Received 11th October 1993)

Abstract

Based on mass transfer across a single diffusion layer at a planar electrode surface, analytical expressions of concentration profiles at the electrode surface and for the dynamic response of amperometric and potentiometric electrochemical detectors after application of an infinitely short concentration pulse (δ-function) were derived using Laplace transformation. The data describing the maximum of these impulse–response functions are presented. It was found, that the response achieved with dc amperometry is almost twice as fast as with potentiometry and ac amperometry. Furthermore, the common dc amperometric technique has the advantage that the maximum of the impulse-response function is closer to the steady state than in potentiometry and ac amperometry.

Key words: Amperometry; Potentiometry; Cellulose membrane; Dynamic response; Impulse–response function; Liquid–liquid interface;

1. Introduction

The detection of electroactive species in flowing streams is an expanding field of the application of electrochemical sensors (for a review see e.g. [1]). The dynamic response of the detector can be a very important feature, particularly if it has to be applied in flow-injection analysis (FIA) or liquid chromatography (LC). It is often determined by diffusion of the electroactive species across a stagnant diffusion layer. This can be a stagnant boundary layer with a flow rate dependent thickness or a hydrophilic membrane or coating at the electrode surface. Such layers can be employed for protecting electrodes from poisoning and for improving their selectivity [2–6], or to stabilise the electrode surface when liquid electrode materials are used (membrane polarography, membrane-stabilised water/oil interface) [7–13]. So far, most of papers on the dynamic response of potentiometric and amperometric detectors have been concerned with the response to a concentration step (excitation signal) [1,6,7,14–16]. However, the response of a detector to a short concentration pulse or a Gaussian concen-

* Corresponding author.

SSDI 0003-2670(93)E0708-F

tration function [17] is, in our opinion, more adequate for modelling the dynamic behaviour of a FIA or LC system. It was pointed out by Sternberg [18] for a gas chromatographic system and later suggested by Poppe [19] for LC and FIA, that the flow system behaves as signal transmission line and the detector output signal $s(t)$ is the result of the convolution (denoted by the symbol $*$) of the concentration input function $c(t)$ with the impulse–response functions $f_1(t) \ldots f_n(t)$ of the n various components which contribute to the peak broadening in the flow system, and the impulse–response function of the detector $g(t)$:

$$s(t) = c(t) * f_1(t) * f_2(t) * \ldots * f_n(t) * g(t)$$

The peak broadening can be treated also in terms of the statistical moments of the signal [18–21]. An impulse–response function (IRF) has the advantage that it can be expressed as a graph and in this way giving a better visualisation of the transient processes. IRF of various components of a FIA system such as tubes, mixing coils and T-pieces have been measured employing a deconvolution method based on Fourier transformation [22–23]. Computer simulated IRF have been presented for film coated electrodes, where convective-diffusional transport in the solution and diffusional transport in the film was taken into account [21]. So far, only few examples for analytical expressions of IRF of electrochemical detectors can be found in the relevant literature [24,25], in contrast to the response to a concentration step. The aim of this paper is to present analytical expressions of IRF of electrochemical detectors based on ion transfer across the interface of two immiscible electrolyte solutions and to show, that under some conditions these calculations can be applied also to other electrochemical detectors. To get a better picture of the diffusion processes at the electrode surface, concentration profiles of the diffusing species were also calculated. Three different measurement techniques are considered.

(i) Direct current (dc) amperometry, where the species of interest are transferred across the electrode surface at a constant electrode potential and the resulting Faraday current is monitored as a function of time.

(ii) Alternating current (ac) amperometry, where the constant electrode potential is superimposed by an alternating voltage (of small amplitude and a frequency being much higher than the rate of the exciting concentration function) and the alternating current is monitored.

(iii) The case where approximately no mass or charge is transferred across the electrode surface and the concentration at the electrode surface is monitored, e.g., as for sampling techniques (pulsed amperometry, fast cyclic voltammetry) and potentiometry (under some conditions and after linearisation of the electrode function). This case will be called only "potentiometry" in this paper.

The calculations are based on the following assumptions.

(a) The rate of the mass transfer towards and away from the electrode surface is determined only by planar diffusion across a single diffusion layer of uniform thickness d adjacent to the electrode surface.

(b) The mass transport in the aqueous phase outside of this diffusion layer is determined only by convection, so that the exciting concentration function $c_W(t)$ entering the electrochemical detector applies for every point of the interface between the diffusion layer and the layer of convective mass transport.

(c) In the case of amperometry, the charge transfer reaction is electrochemically reversible. After the electrode reaction (transfer from the aqueous to the organic phase), the transfer of the analyte species is described by semi-infinite diffusion in the organic phase.

(d) In the case of potentiometry, mass or charge transfer across the electrode surface is negligible. When working with ion-selective electrodes, this condition is fulfilled when the ion-selective electrode operates in the Nernstian range, interfering ions are absent, and the concentration changes are small so that the charging of the double layer can be neglected. The impedance of the voltmeter and the electrode cable must be also sufficiently high. In the case of voltammetric sampling techniques, the sampling interval (during which the concentration profile at the interface is disturbed) must be much shorter than the interval between two successive samplings.

The potentiometric model to be derived should not be restricted to electrodes which elucidate the partition of ions at the liquid–liquid interface. It can be applied to any other potentiometric detector for which the above conditions hold. The amperometric models should also be applicable to stationary mercury electrodes, when mercury soluble metals are detected. When the limiting diffusion current is considered only, the dc amperometric model is applicable for all amperometric detectors whose dynamic response is determined by diffusion across a single diffusion layer since the diffusion problem is then reduced to the diffusion layer in the analyte containing phase. The diffusion of the reaction product into the bulk of the electrode material (organic phase or mercury) or back into the flowing aqueous solution needs not to be considered in this case. In principle, a film coated electrode has two diffusion layers. The film layer or "membrane" and the convective diffusion layer [21]. However, the convective diffusion layer in the flowing phase can be neglected in first approximation, when the mass transport in the hydrodynamic layer is fast compared with the diffusion in the film, i.e., when the thickness of the film is high, the diffusion coefficient in the film is small or the flow rate is high. When the single layer model is compared with the conditions holding for a real flow-through electrochemical detector without any film coating or supporting membrane, one must state that there is usually no strictly defined interface between the "diffusion layer" and the streaming solution. The change between these idealised layers is a gradual one and defined by the conditions of convective diffusion. The thickness of the Nernstian diffusion layer is defined for the steady state and thus not necessarily applicable for transient processes. Moreover, the assumption that the diffusion layer is of uniform thickness is allowed only for few kinds of flow-through electrodes. The thickness of the Nernstian diffusion layer often depends on the considered position at the electrode surface. In the case of the wall-jet arrangement, it depends on the distance from the center of the electrode where the axis of the jet hits the electrode surface. The IRF must be considered then as an integral of each particular IRF included holding for a particular point of the electrode surface. It seems rather certain, that this problem can not be solved analytically. However, it might be assumed that an

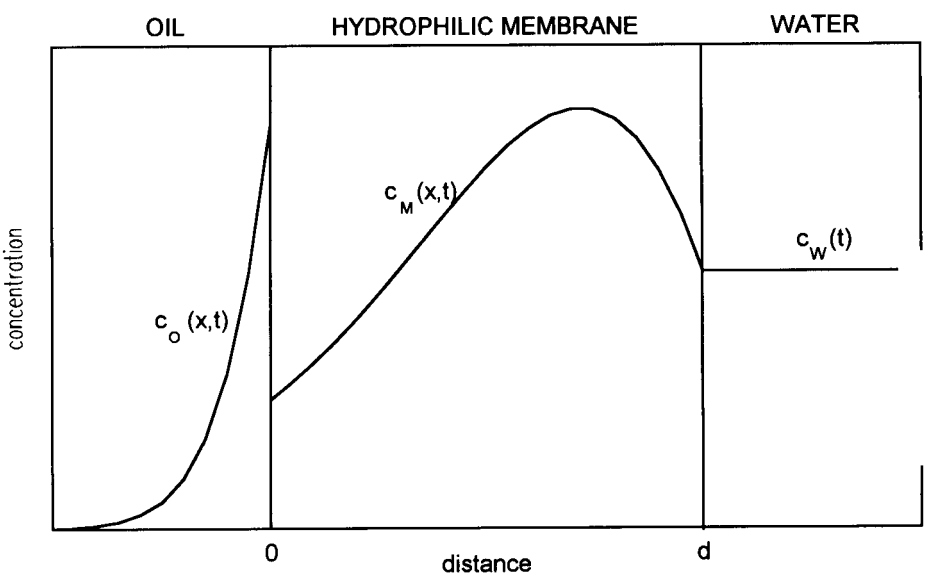

Fig. 1. Scheme of the concentration profile at the water/oil interface separated by a hydrophillic membrane after the application of a Gaussian concentration pulse.

apparent or mean diffusion layer thickness can be defined in such a case. Finally, it should be mentioned that a laminarly flowing liquid entering the detector has, besides the axial concentration profile usually considered, a radial concentration profile. This is negligible for gases, but not for liquids, assuming conditions typical for chromatography or FIA. The problem is, that this radial concentration profile is neglected in principle when the IRF model is applied to flow analysis.

2. dc Amperometry

A scheme of the diffusion problem in dc amperometry at the water/oil interface stabilised by a permeable hydrophillic membrane is shown in Fig. 1. Semi-infinite diffusion in the oil phase ($-\infty < x < 0$) and finite diffusion in the membrane ($0 < x < d$) must be considered. The concentrations of the diffusing species in the oil phase and the membrane, $c_O(x,t)$ and $c_M(x,t)$, respectively, are functions of both time t and distance from the origin x and governed by Fick's second law

$$\frac{\partial c_O(x,t)}{\partial t} = D_O \frac{\partial^2 c_O(x,t)}{\partial x^2}; \quad -\infty < x < 0;\ 0 < t < \infty \tag{1}$$

$$\frac{\partial c_M(x,t)}{\partial t} = D_M \frac{\partial^2 c_M(x,t)}{\partial x^2}; \quad 0 < x < d;\ 0 < t < \infty \tag{2}$$

The initial conditions are

$$c_O(x,t) = 0 \text{ and } c_M(x,t) = 0;\ t = 0$$

The boundary conditions are given by

$$c_O(x,t) = 0;\ x \to -\infty$$

$$c_M(x,t) = c_W(t);\ x = d$$

The function $c_W(t)$ describes the exciting concentration change in the aqueous phase ($x > d$) and in this way also at the boundary membrane/aqueous phase. D_O, D_M and d are the diffusion coefficient in the oil phase, in the membrane and the thickness of the membrane, respectively. At the boundary of membrane and oil phase ($x = 0$), the continuity of fluxes

$$D_O \left.\frac{\partial c_O(x,t)}{\partial x}\right|_{x \to -0} = D_M \left.\frac{\partial c_M(x,t)}{\partial x}\right|_{x \to +0} \tag{3}$$

and Nernst's equation (written in a modified form so that the standard potential is replaced by the polarographic half-wave potential $\Delta_O^W\Phi_{1/2}$) hold:

$$\frac{c_O(-0,t)}{c_M(+0,t)} = \sqrt{\frac{D_M}{D_O}}\, e^{-j};\ c_M(+0,t) \neq 0 \tag{4}$$

$$j = \frac{zF}{RT}\left(\Delta_O^W\Phi_{1/2} - \Delta_O^W\Phi\right)$$

$\Delta_O^W\Phi$ is the Galvani potential difference between water and oil phase and, by definition, equal to the Galvani potential difference across the membrane/oil interface. R, T, z and F, have their usual meaning.

The method of Laplace transformation (for the principles see e.g. [26]) was employed to reduce Eqs. 1 and 2 to the ordinary differential equations:

$$pC_O(x,p) - c_O(x,0) = D_O \frac{\partial^2 C_O(x,p)}{\partial x^2} \tag{5}$$

$$pC_M(x,p) - c_M(x,0) = D_M \frac{\partial^2 C_M(x,p)}{\partial x^2} \tag{6}$$

$C_O(x,p)$ and $C_M(x,p)$ are the Laplace transforms with respect to t of $c_O(x,t)$ and $c_M(x,t)$ respectively, and p is a complex parameter. The Eqs. 5 and 6 can be integrated to the general solutions

$$C_O(x,p) = A_O(p)\exp\left(-x\sqrt{p/D_O}\right) + B_O(p)\exp\left(+x\sqrt{p/D_O}\right) \tag{7}$$

$$C_M(x,p) = A_M(p)\exp\left(-x\sqrt{p/D_M}\right) + B_M(p)\exp\left(+x\sqrt{p/D_M}\right) \tag{8}$$

where the coefficients $A_O(p)$, $B_O(p)$, $A_M(p)$ and $B_M(p)$ are determined by the boundary conditions.

For $-\infty < x < 0$ and $0 < x < d$, respectively, the solution in the Laplace domain is

$$C_O(x,p) = C_W(p)\frac{2e^{-j}}{1+e^{-j}}\sqrt{\frac{D_M}{D_O}}\left[\exp\left(+x\sqrt{p/D_O}\right)\right] \times\left[\left(\frac{1-e^{-j}}{1+e^{-j}}\right)\times\exp\left(-d\sqrt{p/D_M}\right)+\exp\left(+d\sqrt{p/D_M}\right)\right]^{-1} \quad (9)$$

$$C_M(x,p) = C_W(p)\left\{1+\left(\frac{1-e^{-j}}{1+e^{-j}}\right)\exp\left(-2x\sqrt{p/D_M}\right)\right\} \times\left\{\left(\frac{1-e^{-j}}{1+e^{-j}}\right)\exp\left[-(x+d)\sqrt{p/D_M}\right]+\exp\left[-(x-d)\sqrt{p/D_M}\right]\right\}^{-1} \quad (10)$$

After expanding Eqs. 9 and 10 in the series

$$C_O(x,p) = C_W(p)\frac{2}{1+e^{-j}}\sqrt{\frac{D_M}{D_O}}\sum_{n=0}^{\infty}\left\{\left(\frac{1-e^{j}}{1+e^{j}}\right)^n \times\exp\left[-\left(2n+1-\frac{x}{d}\sqrt{\frac{D_M}{D_O}}\right)d\sqrt{p/D_M}\right]\right\} \quad (11)$$

$$C_M(x,p) = C_W(p) \times\left\{\sum_{n=0}^{\infty}\left\{\left(\frac{1-e^{j}}{1+e^{j}}\right)^n\exp\left[-(N-x)\sqrt{p/D_M}\right]\right\} - \sum_{n=0}^{\infty}\left\{\left(\frac{1-e^{j}}{1+e^{j}}\right)^{n+1}\exp\left[-(N+x)\sqrt{p/D_M}\right]\right\}\right\}$$

$$N = d(2n+1) \quad (12)$$

the inverse transformation with respect to the time can be made using a table [27]. The concentration profiles in the time domain are:

$$c_O(x,t) = c_W(t) * \frac{1}{(1+e^{j})D_O^{1/2}\pi^{1/2}t^{3/2}} \times\sum_{n=0}^{\infty}\left\{\left(\frac{1-e^{j}}{1+e^{j}}\right)^n\left(N-x\sqrt{D_M/D_O}\right) \times\exp\left[-\frac{\left(N-x\sqrt{D_M/D_O}\right)^2}{4D_Mt}\right]\right\}$$

$$-\infty < x < 0,\ t > 0 \quad (13)$$

$$c_M(x,t) = c_W(t) * \frac{1}{2\pi^{1/2}D_M^{1/2}t^{3/2}} \times\left\{\sum_{n=0}^{\infty}\left\{\left(\frac{1-e^{j}}{1+e^{j}}\right)^n(N-x) \times\exp\left[-\frac{(N-x)^2}{4D_Mt}\right]\right\} - \sum_{n=0}^{\infty}\left\{\left(\frac{1-e^{j}}{1+e^{j}}\right)^{n+1}(N+x) \times\exp\left[-\frac{(N+x)^2}{4D_Mt}\right]\right\}\right\}$$

$$0 < x < d,\ t > 0 \quad (14)$$

The expression $[(1-e^{j})/(1+e^{j})]^0$ is defined to be 1 also for $j = 0$ to have a simpler form of the formulas.

The electric current $i(t)$, which is the signal in amperometry, and the concentration are related by

$$i(t) = zFAD_M\left.\frac{\partial c_M(x,t)}{\partial x}\right|_{x\to+0} \quad (15)$$

where A denotes the area of the electrode surface. The Laplace transform of the current is then given by the product

$$I(p) = C_W(p) \times G(p)$$

$$G(p) = \frac{2zFAD_M^{1/2}}{1+e^{j}}\sum_{n=0}^{\infty}\left\{\left(\frac{1-e^{j}}{1+e^{j}}\right)^n p^{1/2} \times\exp\left[-(2n+1)d\sqrt{p/D_M}\right]\right\} \quad (16)$$

$G(p)$ is the so-called transfer function, which is in fact the Laplace transform of the IRF $g(t)$:

$$g(t) = \frac{zFAD_M^{1/2}}{(1+e^j)\pi^{1/2}t^{5/2}} \sum_{n=0}^{\infty} \left\{ \left(\frac{1-e^j}{1+e^j} \right)^n \times \left[(2n+1)^2 \frac{d^2}{2D_M} - t \right] \times \exp\left[-(2n+1)^2 d^2 / 4D^M t \right] \right\} \quad (17)$$

The function $i(t)$ is a result of the convolution of the concentration function $c_W(t)$ with the impulse–response function $g(t)$:

$$i(t) = c_W(t) * g(t) \quad (18)$$

The first three terms of Eq. 17 with $n = 0, 1, 2$ are shown in Fig. 2 for the case $e^j = 0$ (limiting diffusion current). They were reduced to the response in the steady state $h(\infty)$

$$h(\infty) = \lim_{t \to \infty} h(t)$$

and to the time constant d^2/D_M. The function $h(t)$ is the step response function, which corresponds with the impulse response function by the relationship

$$h(t) = \int_0^t g(\tau) d\tau$$

The dc amperometric response in the steady state is

$$h(\infty) = zFAD_M d^{-1}(1+e^j)^{-1} \quad (19)$$

Beside of the reduced response, a reduced time $t/(d^2/D_M)$ was defined.

From Fig. 2 is evident, that $g(t)$ is determined practically only by the first three terms of Eq. 17 when the time interval $0 \leqslant t < \approx d^2/D_M$ is considered. Longer times need not to be considered, since the function $g(t)$ has approached zero very closely after this time. For $0 \leqslant t < \approx 0.3d^2/D_M$, it is adequate to consider only the first term. Hence, the maximum of $g(t)$ can be determined analytically in good approximation by differentiation of the first term of Eq. 17. The maximum is then given by:

$$t_{max} \approx \left(1/2 - \sqrt{1/6}\right) d^2/D_M \approx 0.0918 d^2/D_M \quad (19)$$

$$g_{max} = g(t_{max}) \approx 5.92 zFAD_M^2 d^{-3}(1+e^j)^{-1} \quad (20)$$

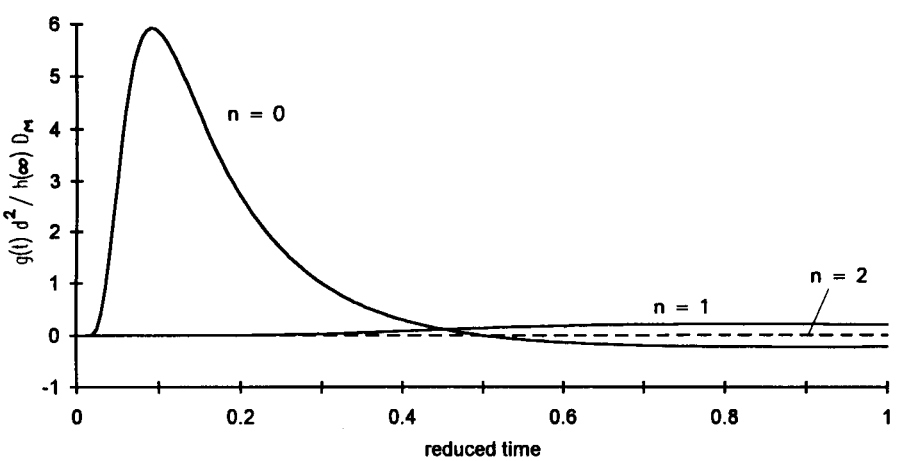

Fig. 2. The first three terms of the dc amperometric impulse–response function (reduced to the response in the steady state and the time constant d^2/D_M).

Practically the same value of t_{max}, namely 0.092 d^2/D_M, was derived by Olsson et al. [24] from an equation, which converges for long times and was derived from an equation describing the concentration step response. When the limiting diffusion current is considered ($j \ll 0$), Eq. 20 becomes

$$g_{lim}(t) = \frac{zFAD_M^{1/2}}{\pi^{1/2}t^{5/2}} \sum_{n=0}^{\infty} \left\{ \left[(2n+1)^2 \frac{d^2}{2D_M} - t \right] \times \exp\left[-(2n+1)^2 d^2/4D_M t \right] \right\} \quad (21)$$

Eq. 21 can be derived also from an expression describing the heat profile in a solid of finite dimension after application of a temperature step at one side [28]. After exchanging the equivalent quantities like concentration and temperature, the impulse–response function was obtained by successive differentiation with respect to x and then t (for $x \to 0$).

When the half-wave potential is applied to the detector, Eq. 20 is simplified to:

$$g_{1/2}(t) = \frac{zFAD_M^{1/2}}{2\pi^{1/2}t^{5/2}} \left[\frac{d^2}{2D_M} - t \right] \exp\left[-d^2/4D_M t \right] \quad (22)$$

which contains only the $n = 0$ term of Eq. 17. It seems to be noteworthy, that a minimum appears after the time

$$t_{min} = \left(1/2 + \sqrt{1/6}\right) d^2/D_M \approx 0.908 d^2/D_M \quad (23)$$

In general, this minimum of the $n = 0$ term is compensated more or less by the next term ($n = 1$)

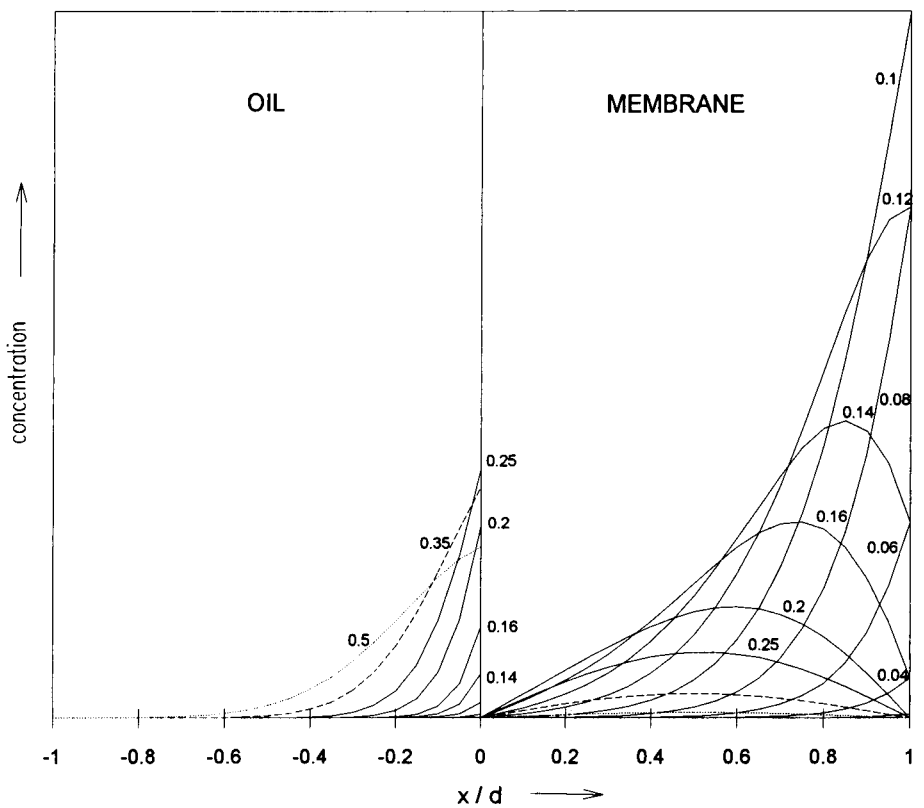

Fig. 3. Concentration profiles for various values of reduced time $t/(d^2/D_M)$ in amperometry after the application of a Gaussian concentration pulse.

in the case $e^j \approx 0$ (c.f. Fig. 2). This is not so for $e^j = 1$, i.e., when the half-wave potential is applied. When e^j is increased further, the minimum that is related to the height of the maximum becomes more pronounced although its absolute hight tends to zero. This minimum or "negative" part of the IRF occurs when the partition ratio of the electroactive ions between oil and water phase is in the order of unity or higher, and arises by the inverse transfer of ions from the organic phase back to the aqueous phase when the concentration "plug" has passed the membrane surface.

Concentration profiles for various values of reduced time are shown in Fig. 3 to make the diffusion process more understandable. The conditions $e^j \approx 0$ and $D_O = 0.1\ D_M$, and a Gaussian concentration function $c_W(t)$ were assumed. The maximum of the Gaussian peak appears at the time $0.1d^2/D_M$, the standard deviation is $0.025d^2/D_M$. This parameters were chosen to have similar contributions of the IRF and the excitation signal $c_W(t)$ to the response. The concentration profiles were calculated from the Eqs. 13 and 14 using the software ASYST 4.0 (Keithley Instruments). The increments of time and distance were $0.005d^2/D_M$ and $0.05d$, respectively.

3. Potentiometry

In potentiometry, diffusion takes place in the hydrophilic membrane only and can be described by Eq. 2. Taking into consideration that the carrier solution often contains the species to be measured in a low concentration c_W^* when a potentiometric detector is used in FIA, the initial condition is

$$c_M(x,t) = c_W^*;\ 0 \leqslant x;\ t = 0$$

The boundary conditions are given by the definition, that there is no flux across the oil/membrane interface

$$D_M \frac{\partial c_M(x,t)}{\partial x} = 0;\ x = 0$$

and by the concentration function at the interface between the membrane and the aqueous phase

$$c_M(x,t) = c_W(t);\ x = d$$

The application of the Laplace transformation, which considers the initial condition automatically, gives

$$pC_M(x,p) - c_W^* = D_M \frac{\partial^2 C_M(x,p)}{\partial x^2} \tag{24}$$

Eq. 24 can be integrated to

$$C_M(x,p) = A_M(p)\ \exp\left(-x\sqrt{p/D_M}\right) + B_M(p)\ \exp\left(+x\sqrt{p/D_M}\right) + C_W^* \tag{25}$$

where $C_W^* = c_W^*/p$ is the Laplace transform of c_W^*. The coefficients $A_M(p)$ and $B_M(p)$ are determined by the boundary conditions. The solution in the Laplace domain is

$$C_M(x,p) = [C_W(p) - C_W^*] \times \frac{\exp\left(-x\sqrt{p/D_M}\right) + \exp\left(+x\sqrt{p/D_M}\right)}{\exp\left(-d\sqrt{p/D_M}\right) + \exp\left(+d\sqrt{p/D_M}\right)} + C_W^* \tag{26}$$

or, after expanding Eq. 26 into a series,

$$C_M(x,p) = [C_W(p) - C_W^*] \times \sum_{n=0}^{\infty} \left\langle (-1)^n \left\{ \exp\left[-\sqrt{p/D_M}(N+x)\right] + \exp\left[-\sqrt{p/D_M}(N-x)\right] \right\} \right\rangle + C_W^* \tag{27}$$

The concentration function in the time domain is

$$c_M(x,t) = [c_W(t) - c_W^*] * \frac{1}{2\pi^{1/2} D_M^{1/2} t^{3/2}} \times \sum_{n=0}^{\infty} \left\langle (-1)^n \left\{ (N-x)\exp\left[-\frac{(N-x)^2}{4D_M t}\right] + (N+x)\exp\left[-\frac{(N+x)^2}{4D_M t}\right] \right\} \right\rangle + c_W^*$$

$$0 \leqslant x \leqslant d \tag{28}$$

Examples for concentration profiles induced by a peak-shaped concentration function (Gaussian peak) are shown in Fig. 4. The function of the concentration at the oil/membrane interface with respect to t is

$$c_M(0,t) = [c_W(t) - c_W^*] * g(t) + c_W^* \quad (29)$$

where $g(t)$ is the potentiometric IRF now:

$$g(t) = \frac{d}{\pi^{1/2} D_M^{1/2} t^{3/2}} \sum_{n=0}^{\infty} \left\{ (-1)^n (2n+1) \times \exp\left[-(2n+1)^2 \frac{d^2}{4 D_M t} \right] \right\} \quad (30)$$

The corresponding Laplace transformed expressions are

$$C_M(0,p) = [C_W(p) - C_W^*] \times G(p) + C_W^* \quad (31)$$

$$G(p) = 2 \sum_{n=0}^{\infty} \left\{ (-1)^n \exp\left[-(2n+1) d \sqrt{p/D_M} \right] \right\} \quad (32)$$

For presentation and comparison, it is advantageous to reduce equations to the steady state $h(\infty)$, which is 1 in potentiometry. The first three terms of the to the steady state reduced Eq. 30 are shown in Fig. 5. Like for dc amperometry, the first term is predominant for $0 \leqslant t < \infty \approx$

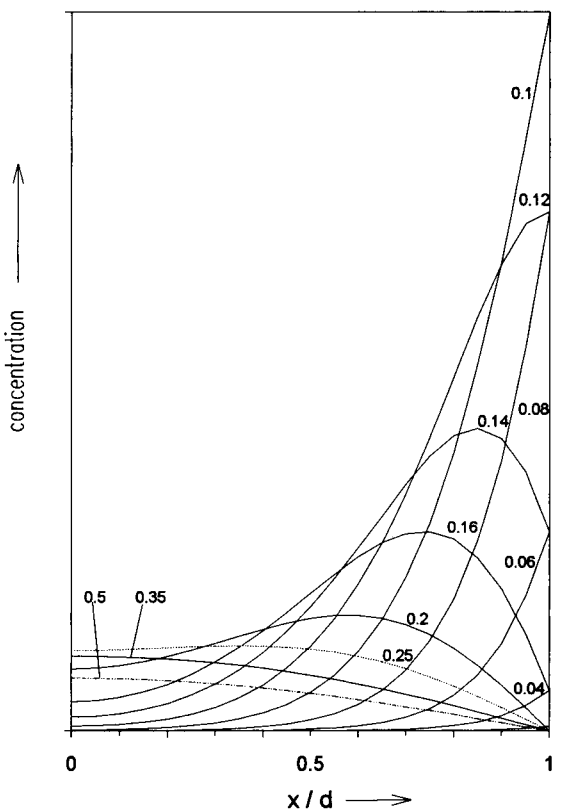

Fig. 4. Concentration profiles for various values of reduced time $t/(d^2/D_M)$ in potentiometry after the application of a Gaussian concentration pulse.

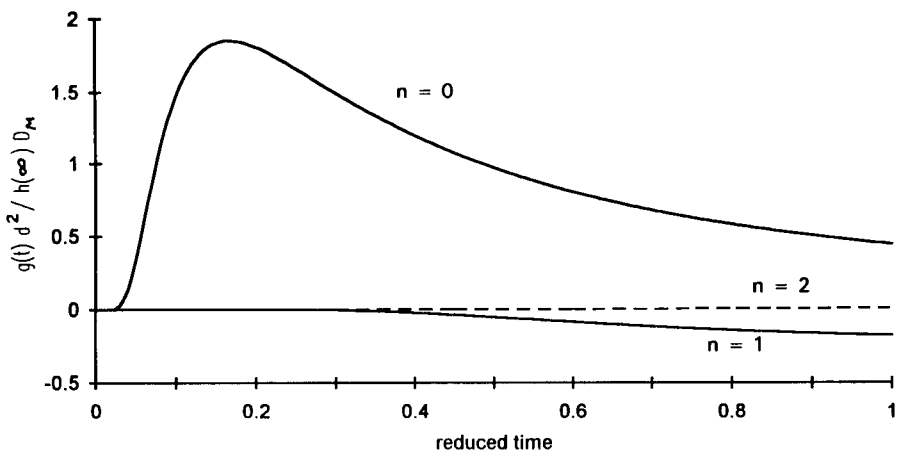

Fig. 5. The first three terms of the potentiometric impulse–response function (reduced to the response in the steady state and the time constant d^2/D_M).

$0.3d^2/D_M$. The maximum of g(t) was determined from this first term analytically:

$$t_{max} = d^2/6D_M \approx 0.16d^2/D_M \quad (33)$$

$$g_{max} = 6\sqrt{6/\pi}\, e^{-3/2} D_M/d^2 \approx 1.850 D_M/d^2 \quad (34)$$

Another and independent way to obtain an impulse response function is to differentiate the adequate step response function, if known, with respect to the time. Starting from the step response of ion-selective electrodes [15] and from equations describing the conduction of heat in solids [28], the same result was obtained like that given in Eq. 30.

4. ac Amperometry

Since the time scales of the excitations in ac amperometry, the ac voltage of a high frequency on the one hand and the slow concentration function $c_W(t)$ on the other hand, are much different, the diffusion problem to be considered is the same as in dc amperometry. The concentrations are then described by Eqs. 13 and 14. For a reversible Faradaic process, the real component of the alternating current $i^{ac}(t)$ is given by

$$i^{ac}(t) = \frac{z^2F^2A\omega^{1/2}}{RT[1/D_O^{1/2}c_O(-0,t) + 1/D_M^{1/2}c_M(+0,t)]} E^{ac} \quad (35)$$

where E^{ac} is the amplitude (peak-to-peak, $\leqslant 8/z$ mV) and ω is the angular frequency of the exciting sinusoidal ac voltage. The concentrations at the interface of oil and membrane phase oscillate about the mean concentrations $c_O(-0,t)$ and $c_M(+0,t)$, which can be obtained from the Eqs. 13 and 14. The ac response of the detector operating at a constant dc potential is then

$$i^{ac}(t) = c_W(t) * \frac{z^2F^2\omega^{1/2}E^{ac}Ad}{4RT\pi^{1/2}t^{3/2}\cosh^2(j/2)} \times \sum_{n=0}^{\infty} \left\{ \left(\frac{1-e^j}{1+e^j} \right)^n (2n+1) \times \exp\left[\frac{-(2n+1)^2 d^2}{4D_M t} \right] \right\} \quad (36)$$

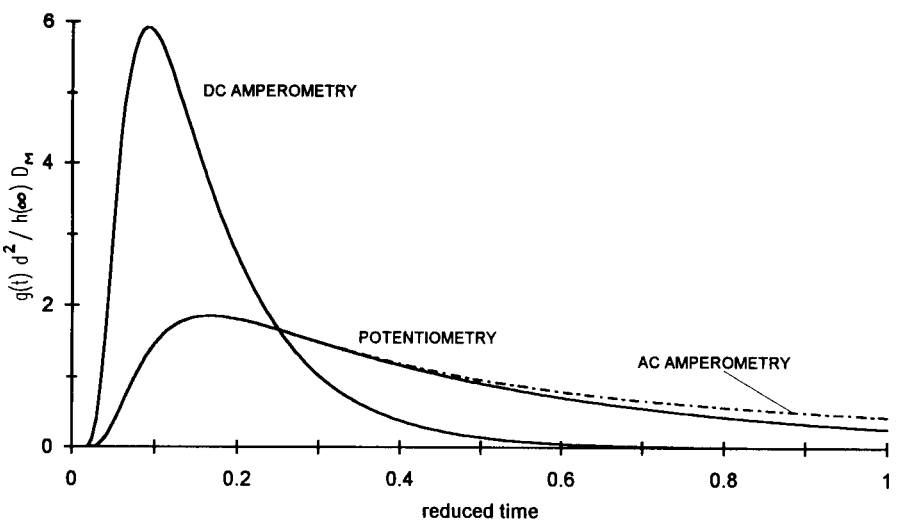

Fig. 6. Comparison of the reduced impulse–response functions for dc amperometry (limiting diffusion current), ac amperometry (peak or half-wave potential) and potentiometry.

The term $[(1 - e^j)/(1 + e^j)]^0$ is defined to be 1 also for $j = 0$ here. In the usual case that the peak or half-wave potential $E_{1/2}$ is applied to the detector, Eq. 36 takes the simpler form

$$i^{ac}_{peak}(t) = c_W(t) * \frac{z^2F^2\omega^2E^{ac}Ad}{4RT\pi^{1/2}t^{3/2}} \exp\left(\frac{-d^2}{4D_M t}\right) \quad (37)$$

which involves the same time dependence like the $n = 0$ term of Eq. 30 describing the potentiometric response. Therefore, the maximum response is defined by

$$t_{peak,max} = d^2/(6D_M) \quad (38)$$

$$g_{peak,max} = 0.4625z^2F^2\omega^{1/2}E^{ac}AD_M^{3/2}/(RTd^2) \quad (39)$$

The ac amperometric response in the steady state, which is needed to calculate the reduced response, is

$$h(\infty) = z^2F^2\omega^{1/2}E^{ac}AD_M^{1/2}/[4RT\cosh^2(j/2)] \quad (40)$$

5. Comparison

Plots of the derived IRF are shown in Fig. 6. While the IRF of ac amperometry and potentiometry are very similar, those of dc amperometry has a significantly higher maximum, which appears after a time which is only half the time for both other methods. Although this is not very much, it can be important in some cases. The (to the steady state reduced) maximum data are summarised in Table 1. The expression d^2/D_M appears for all methods and is the time constant of the detector, however, it is determined only by the properties of the hydrophilic membrane. The reason for the faster response of dc amperometry is, that the gradient of the concentration at the electrode surface rather than the concentration itself determines the response in dc amperometry. The electroactive species approaching to the electrode surface produce the maximum concentration gradient faster than they need to accumulate at the electrode surface and to increase the concentration at this place up to the maximum. The relaxation of the dc amperometric detector response is also faster and the tailing of the peak is much less pronounced. This is attributed to the fact that the electroactive species are removed from the membrane not only by diffusion back to the flowing aqueous phase, but also by the transfer across the electrode surface. Although the relaxation of the amperometric signal (in particular the limiting diffusion current) is better than for the two other methods (Fig. 6), the relaxation of the concentration profiles in the oil and the membrane phase is the same as for ac amperometry, as the Eqs. 13 and 14 apply in both cases.

Table 1
Maximum data of the IRF of three electrochemical detection principles

	dc amperometry	potentiometry	ac amperometry
t_{max}	$0.09d^2/D_M$	$0.17d^2/D_M$	$0.17d^2/D_M$
$g_{max}/h(\infty)$	$5.9D_M/d^2$	$1.9D_M/d^2$	$1.9D_M/d^2$

Finally, it should be noted that the data presented in Fig. 6 and Table 1 characterise the IRF only, i.e., the response to a infinitely short concentration pulse. The real conditions can be subdivided in three cases. When the concentration pulse is much faster than the dynamic response of the detector (expressed by the IRF), the shape of the signal is determined by the IRF alone. This can be employed to obtain the IRF from the experiment and will be the subject of a future paper. In analytical applications however, the detector would be too slow, when a high speed of the whole system or a good resolution (in chromatography) is required. In order to make the detector faster, the thickness of the hydrophilic membrane (or the stagnant boundary layer) must be decreased, or the permeability (described by D_M) of the membrane must be increased. When the dynamic of the detector and the exciting concentration function is similar, the response of the detector will be mixed. Finally, when the concentration function is even slower, the detector has enough time to reach the steady state and the dynamic properties of the detector are not significant. Only the "static" or steady state re-

sponse, which is described by $h(\infty)$, must be considered.

References

[1] K. Stulik and V. Pacakova, Electroanalytical Measurements in Flowing Liquids, Ellis Horwood, Chichester, 1987.

[2] L.C. Clark, R. Wolf, D. Granger and Z. Taylor, J. Appl. Physiol., 6 (1953) 189.

[3] G. Sittampalam and G.S. Wilson, Anal. Chem., 55 (1983) 1608.

[4] G.A. Gerhard, A.F. Oke, G. Nagy, B. Moghaddam and R.N. Adams, Brain Res., 290 (1984) 390.

[5] J. Wang and L.D. Hutchins, Anal. Chem., 57 (1985) 1536.

[6] E.W. Kristensen, W.G. Kuhr and R.M. Wightman, Anal. Chem., 59 (1987) 1752.

[7] R.C. Bowers and A.M. Wilson, J. Am. Chem. Soc., 80 (1958) 2968.

[8] O. Fischer, Collect. Czech. Chem. Commun., 27 (1962) 1119.

[9] J. Ross, Science, 156 (1967) 1378.

[10] B. Hundhammer, S.K. Dhawan, A. Bekele and H.-J. Seidlitz, J. Electroanal. Chem., 217 (1987) 253.

[11] Y. Yamamoto, T. Osakai and M. Senda, Bunseki Kagaku, 39 (1990) 655.

[12] S. Wilke, H. Franzke and H. Müller, Anal. Chim. Acta, 268 (1992) 285.

[13] R. Voigtländer, H. Matschiner and B. Matschiner, Patent G 01 N DD 265 4158, 19/071984; H. Matschiner and H.H. Rüttinger, Analytiktreffen, Neubrandenburg, 10–14 Nov. 1985.

[14] W.E. Morf, E. Lindner and W. Simon, Anal. Chem., 47 (1975) 1596.

[15] R.P. Buck, in H. Freiser (Ed.), Ion-Selective Electrodes in Analytical Chemistry, Plenum Press, New York, 1978, p. 117.

[16] C. McCallum and D. Pletcher, Electrochim. Acta, 20 (1975) 811.

[17] J. Cassidy, W. Breen and M.E.G. Lyons, Electroanalysis, 3 (1991) 293.

[18] J.C. Sternberg, in J.C. Giddings and R.A. Keller (Eds.), Advances in Chromatography, Vol. 2, Marcel Decker, New York, 1966, p. 205.

[19] H. Poppe, Anal. Chim. Acta, 114 (1980) 59.

[20] S.H. Brooks and J.G. Dorsey, Anal. Chim. Acta, 229 (1990) 35.

[21] W.Th. Kok, A.J. Tüdös and H. Poppe, Anal. Chim. Acta, 228 (1990) 39.

[22] I.C. van Nugteren-Osinga, M. Bos and W.E. van der Linden, Anal. Chim. Acta, 214 (1988) 77.

[23] I.C. van Nugteren-Osinga, E. Hoogendam, M. Bos and W.E. van der Linden, Anal. Chim. Acta, 239 (1990) 245.

[24] B. Olsson, H. Lundbäck, G. Johansson, F. Scheller and J. Nentwig, Anal. Chem., 58 (1986) 1046.

[25] R.C. Engstrom, R.M. Wightman and E.W. Kristensen, Anal. Chem., 60 (1988) 652.

[26] G. Doetsch, Anleitung zum praktischen Gebrauch der Laplace-Transformation und der Z-Transformation, R. Oldenbourg, München, 1989.

[27] A. Erdelyi, Tables of Integral Transforms, McGraw Hill, New York, 1964.

[28] H.S. Carslaw and J.C. Jaeger, Conduction of Heat in Solids, Oxford University Press, London, 1959, p. 309.

ELSEVIER

Analytica Chimica Acta 291 (1994) 53–64

ANALYTICA CHIMICA ACTA

Polarographic behaviour and determination of norfloxacin in tablets

A.M.Y. Jaber *, A. Lounici

King Fahd University of Petroleum and Minerals, Chemistry Department, Dhahran 31261, Saudi Arabia

(Received 28th April 1993; revised manuscript received 9th August 1993)

Abstract

The direct current (dc) and differential pulse (dp) polarographic reduction of the antibacterial drug norfloxacin has been studied in various base electrolytes at different pH values in the presence of dimethyl formamide. Only one reduction wave in the range -0.95 to -1.05 V was observed in strongly acidic medium (pH < 1). Using a base electrolyte of pH $\geqslant 7.5$, two well defined irreversible waves were observed in the ranges of -1.48 to -1.67 V (wave C) and -1.79 to -1.93 V (wave D) for norfloxacin concentrations of 1×10^{-4} M. These potential limits showed little shifts on both sides with norfloxacin concentration. At pH $\geqslant 10$, only wave D has been observed, but all waves disappeared completely in 0.1 M NaOH. In addition, two ill-defined waves appeared in the range -0.06 to -0.42 V within the pH range 6.5–8.5 for norfloxacin concentrations $> 5 \times 10^{-5}$ M. The single dp wave which appeared in 2 M HCl and the dp wave C which appeared in the other base electrolytes showed a useful rectilinear relationship between concentration and wave heights from 32 to > 560 μg ml^{-1} norfloxacin. These two dp waves have been utilized for determination of norfloxacin in Noroxin tablets with good recoveries. The polarographic behaviour of norfloxacin has been compared to that of nalidixic acid which has been also determined successfully in Negram tablets as the individual component and in the presence of norfloxacin as an interferent.

Key words: Polarography; Antibacterial drugs; Norfloxacin

1. Introduction

Norfloxacin (1-ethyl-6-fluoro-1,4-dihydro-4-oxo-7(1-piperazinyl)-3-quinoline carboxylic acid) is one of the 4-quinolone synthetic antibiotics [1,2]. These antibacterial drugs have the potential to work against the microorganisms that are resistant to the traditional antibiotics.

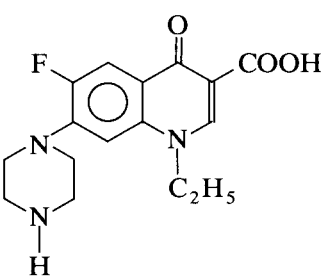

Norfloxacin

Norfloxacin and some other 4-quinolone drugs have been determined by liquid chromatography

* Corresponding author.

SSDI 0003-2670(94)00002-4

[3,4] and electrochemical methods of analysis [5–10]. Electrochemical assays have been utilized extensively [11,12] for pharmaceutical analysis and proved to be fast, precise and produce low cost results with minimal interference from the excipients of the drugs.

Some preliminary studies on the differential pulse polarographic reduction of norfloxacin dissolved in sodium hydroxide have been reported [5]. The polarographic behaviour of norfloxacin and nalidixic acid in the presence of dimethyl formamide has been further examined here in more detail and applied to the determination of these compounds in commercial tablets.

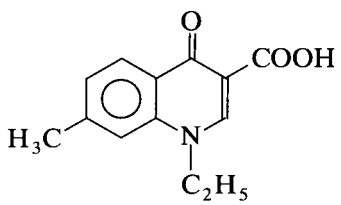

Nalidixic acid

2. Experimental

Norfloxacin was supplied by the Jordanian Pharmaceutical Manufacturing and Medical Equipment, Naor, Jordan, nalidixic acid from Fluka, Buchs, Switzerland, and all supporting electrolytic salts were of analytical reagent grade. Tablets of norfloxacin (Noroxin) and nalidixic acid (Negram) were obtained from Merck Sharp and Dohme, Haarlem, Netherlands and Winthrop Laboratories, Newcastle upon Tyne, UK, respectively. Purum grade dimethyl formamide (DMF) was from Fluka. Distilled deionized water was used.

A PAR174 (EG and G, Princeton, NJ) polarographic analyzer in conjunction with a Model 303 static mercury drop electrode with a small size drop and X–Y recorder (Model RE 0074) were utilized. Sample solutions were deaerated with oxygen-free nitrogen and the temperature was 25 ± 1°C. A differential pulse amplitude of 25 mV and a scan rate of 5 or 10 mV s^{-1} were used. An EG and G Model 264A polarographic analyzer/stripping voltammeter in conjunction with X–Y recorder (Model RE 0150) was used to record the cyclic voltammograms. A pH meter (Corning 215) was used for measuring and adjusting the pH of the base electrolytes.

2.1. Analytical procedure

10.0 ml of 0.1 M base electrolyte was transferred to the cell and deaerated for 8 min. A stock solution of 0.01 M norfloxacin or nalidixic acid prepared in dimethyl formamide was spiked

Table 1
Polarographic data for norfloxacin in various base electrolytes

Base electrolyte	Wave C			Wave D						
	$E_{1/2}$ (V)	$E_{3/4}-E_{1/4}$ (mV)	αn_a	E_p (V)	$W_{1/2}$ (mV)	$E_{1/2}$ (V)	$E_{3/4}-E_{1/4}$ (mV)	αn_a	E_p (V)	$W_{1/2}$ (mV)
LiCl	−1.55	92	0.49	−1.52	75	−1.85	54	0.73	−1.84	93
KCl	−1.53	85	0.54	−1.48	130	−1.78	35	0.98	−1.79	67
$LiClO_4$	−1.56	93	0.53	−1.55	153	−1.84	52	0.67	−1.85	93
NaOAc–HOAc (pH 7.4)	−1.56	50	0.64	−1.54	82	−1.88	58	0.36	−1.87	120
NaOAc	−1.60	105	0.43	−1.55	130	−1.88	52	0.54	−1.86	80
K_3Citrate	−1.53	55	0.84	−1.53	93	−1.81	45	0.70	−1.93	71
K_3Citrate–K_2Hcitrate (pH 8.0)	−1.58	65	0.59	−1.55	40	−1.89	60	0.40	−1.87	95
NH_3–NH_4Cl (pH 9.0)	−1.68	65	0.72	−1.67	100	−1.88	40	0.59	−1.85	67
K_2HPO_4	−1.55	75	0.56	−1.59	93	−1.79	110	0.64	−1.80	60
$K_2B_4O_7$	−1.57	75	0.61	−1.61	117	−1.86	120	0.52	−1.79	93

into the base electrolyte. The current–voltage curves were recorded after each addition. The limiting currents were measured and calibration curves in several base electrolytes were constructed.

2.2. Sample preparation

Eight tablets of Noroxin or Negram were ground to a fine powder. A quantity equivalent to one tablet was weighed, dissolved in DMF, transferred to a 100-ml volumetric flask and diluted to the mark with DMF. The solution was slightly turbid but no further treatment was made. Known volumes (0.05–0.5 ml) of the sample solution were added to 10 ml aliquots of the base electrolyte. The percent composition of DMF was kept constant as about 6% in the unknown and standard solutions. The total volume of the sample was kept as 10.60 ml. Calibration solutions were prepared in the same manner.

3. Results and discussion

Various buffered and unbuffered 0.1 M electrolyte solutions were utilized as base electrolytes. The direct current (dc) and differential pulse (dp) polarographic data for 1×10^{-4} M norfloxacin in 1% DMF are reported in Table 1. Two main well-defined waves in the ranges -1.48 to -1.67 V (wave C) and -1.79 to -1.93 V (wave D) were obtained in each of the base electrolytes used. Fig. 1 shows a typical dp polarogram for 1×10^{-4} M norfloxacin in 0.1 M sodium acetate. Table 1 shows also values of αn_a (α is the transfer coefficient, and n_a is the number of electrons involved in the rate determining step) calculated from the analysis of $\log(i_d - i)/i$ plots for the dc polarograms, $E_{3/4} - E_{1/4}$ for the dc polarograms and $W_{1/2}$ (the dp peak half width) for the dp polarograms for the two main waves C and D. In general, the values of αn_a, $E_{3/4} - E_{1/4}$ and $W_{1/2}$ lie far from those given for the reversible waves. It has been shown [13] that the values of α, $E_{3/4} - E_{1/4}$ and $W_{1/2}$ at 25°C for reversible waves should be 1, $56.4/n_a$ V and $90.4/n_a$ V respectively. Thus, the rate determining step is irreversible for the two waves. This has also been confirmed from the preliminary cyclic voltammograms for norfloxacin in various base electrolytes (Fig. 1, voltammogram 2). The waves corresponding to the dp peaks C and D on the cyclic voltammogram did not appear in the an-

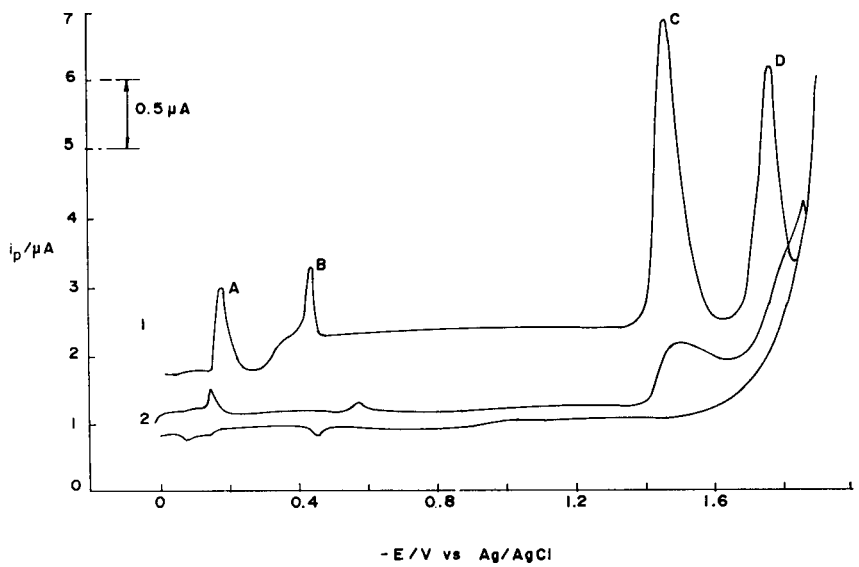

Fig. 1. dp polarogram (1) and cyclic voltammogram (2) for norfloxacin in 0.1 M sodium acetate in the presence of 1×10^{-4} M norfloxacin and 0.1% DMF. Scan rate was 10 mV s^{-1} for the dp polarogram and 100 mV s^{-1} for the cyclic voltammogram.

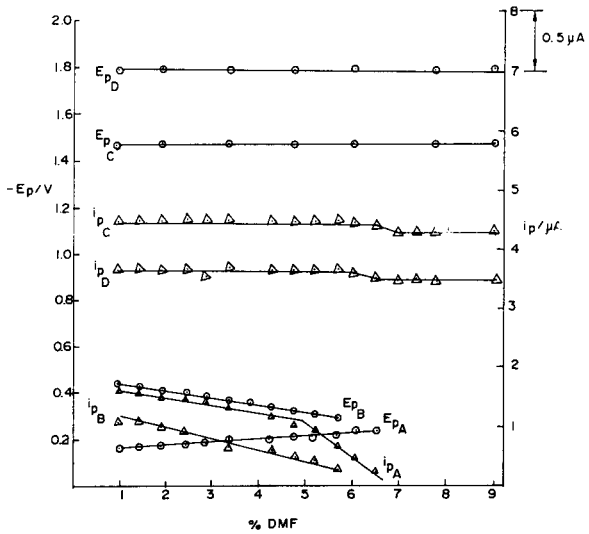

Fig. 2. The effect of DMF on the dp polarographic peak height and peak potential for 1×10^{-4} M norfloxacin in 0.1 M sodium acetate. E_p and i_p represent the peak potential and the peak height, respectively.

odic scan. This confirms the irreversibility of the two waves.

Two ill-defined waves (Fig. 1, polarogram 1, waves A and B) were observed at a more positive potential. The dp peaks corresponding to these two waves started to appear for base electrolytes of pH $\geqslant 6.5$. For example, they appeared at -0.06 V and -0.2 V in sodium acetate of pH 6.5 when norfloxacin concentration was 5×10^{-5} M. Waves A and B showed an increase in height and anodic shift in potential with increasing norfloxacin concentrations up to 2×10^{-4} M after which they became almost concentration independent. The two waves were significantly affected by DMF. Fig. 2 shows that an increase in DMF content in the sample solution was associated with a cathodic shift for wave A and anodic shift for wave B both decreasing in height until they disappeared completely when the DMF concentration exceeded 7%. These observations may indicate that the two waves are of adsorptive nature.

Fig. 2 also shows that the peak heights and peak potentials for waves C and D are almost independent of DMF concentration in the sample solution up to about 6%, above which some insignificant changes were observed. The decrease observed in the heights of peaks C and D (Fig. 2) may be due to an increase in the viscosity of the medium, ion-pair formation, and a decrease in

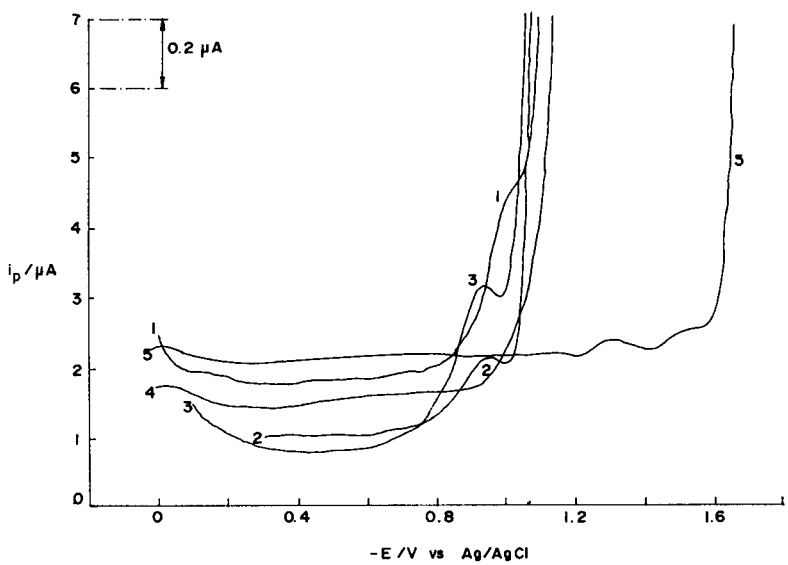

Fig. 3. dp polarograms for 1×10^{-4} M norfloxacin in hydrochloric acid solutions of various concentrations in the presence of 0.1% DMF. Polarograms 1, 2, 3 and 4 are for 0.1, 4, 2 and 0.01 M HCl base electrolytes. Polarogram 5 is for 0.1 M NaOH base electrolyte.

adsorbability on the electrode surface. These effects may result in retardation of the electrode process [14].

3.1. pH effect on the polarographic behaviour of norfloxacin

Figs. 3 and 4 show dp polarograms for 1×10^{-4} M norfloxacin in the presence of 0.1% DMF and 0.1 M of various base electrolytes, namely, hydrochloric acid solutions (Fig. 3), acetic acid–sodium acetate buffers, unbuffered sodium acetate and ammonia–ammonium chloride buffers (Fig. 4). It has been observed that norfloxacin shows only one reduction peak in the range −0.95 to −1.05 V in 4, 2 and 0.1 M HCl base electrolyte. The peak has diminished in height and became a shoulder in 0.1 M HCl and finally disappeared in 0.01 M HCl (Fig. 3). When the pH has been raised to higher values, the above mentioned reduction peak has been replaced by main and ill-defined peaks in the range −0.06 to −1.93 V. At pH 6.5, only one main peak appeared at −1.39 V and one ill-defined peak at −0.11 V (Fig. 4, polarogram 2). However, when the pH of the solution was in the range 7.5 to 10, two main reduction waves in the ranges −1.48 to −1.67 V (wave C) and −1.79 to −1.93 V (wave D) and two ill-defined peaks in the ranges −0.11 to −0.18 V and −0.20 to −0.42 V developed completely (Fig. 4, polarogram 3). The two ill-defined waves have been disappeared in ammonia–ammonium chloride buffers of pH > 9. They were obscured by a huge wave situated around 0 V. Finally only one reduction peak in the range −1.79 to −1.93 V remained when the pH of the base electrolyte was 10–11.5. When 0.1 M sodium hydroxide was used as the base electrolyte, all peaks vanished completely (Fig. 3, polarogram 5).

Fig. 5 shows the shift in the dp polarographic peak potentials for the four peaks with pH. The E_p − pH dependence for wave C is described by two segments of E_p/pH of 39.8 and 140 mV below and above pH 8.5, respectively (Fig. 5). The E_p/pH dependence for wave D was found to be −14 and 36 mV below and above pH 9.5, respectively (Fig. 5). Other antibacterial drugs of the same type, namely, nalidixic acid [6], ciprofloxacin [7] and flumequine [8] showed a similar behaviour. The shift of E_p with pH to-

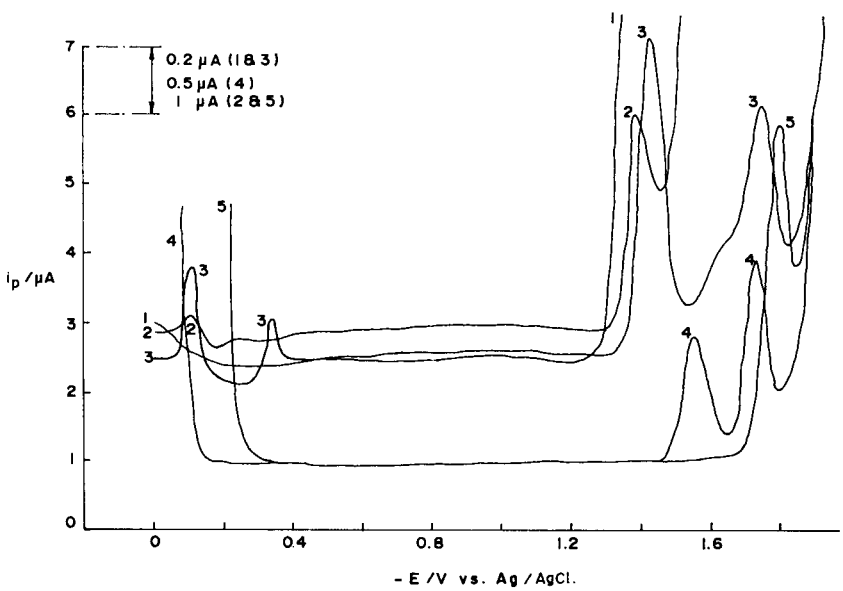

Fig. 4. dp polarograms for 1×10^{-4} M norfloxacin in acetic acid–sodium acetate buffer (pH in the case of polarograms 1, 2 and 3 was 4.5, 6.5 and 7.5, respectively) and in NH_3–NH_4Cl buffers (pH in the case of polarograms 4 and 5 was 9.0 and 11.5, respectively) in the presence of 0.1% DMF.

wards more negative values may indicate that the electron uptake is preceded by a proton transfer as proposed earlier for nalidixic acid [6].

Fig. 6 shows the change in the peak heights (i_p) corresponding to the two waves C and D with pH. The plot representing the dp peak height for wave C versus pH shows an increase in the wave height with a maximum at pH 8 followed by a decrease until the wave almost disappears at pH 10. This behaviour has been observed previously for ciprofloxacin [7] which showed a dp polarographic peak at −1.44 V in the pH range 6 to 10.5 whose height was markedly dependent on pH reaching a maximum at pH 8.5. However, nalidixic acid [6] showed i_p–pH plots for two dc waves in the shape of dissociation curves with inflection points at pH values of 6.7 and 8.5, where the second one was assumed to be the polarographic pK [15] of nalidixic acid.

3.2. Proposed mechanism for norfloxacin reduction at the DME

Norfloxacin is expected to exist in aqueous media in the intermediate pH range (≈ 7) as a zwitterion, HA_Z, a neutral molecule, HA_N and a small proportion of the conjugate acid H_2A^+. It is expected that zwitterion HA_Z will be the major species since one of the nitrogen atoms in the piperazine moiety is more basic than the carboxylate ion. However, in a basic medium (pH ⩾ 10) the conjugate base A^- predominates. Meanwhile, in a strongly acidic medium (2 M HCl, for example) the diprotonated species, H_3A^{2+} would be the major species existing in the solution. The enamine double bond in the azinone ring is protonated in a strongly acidic medium leading to the formation of the iminium ion moiety as in H_3A^{2+}. These equilibria are indicated in Scheme

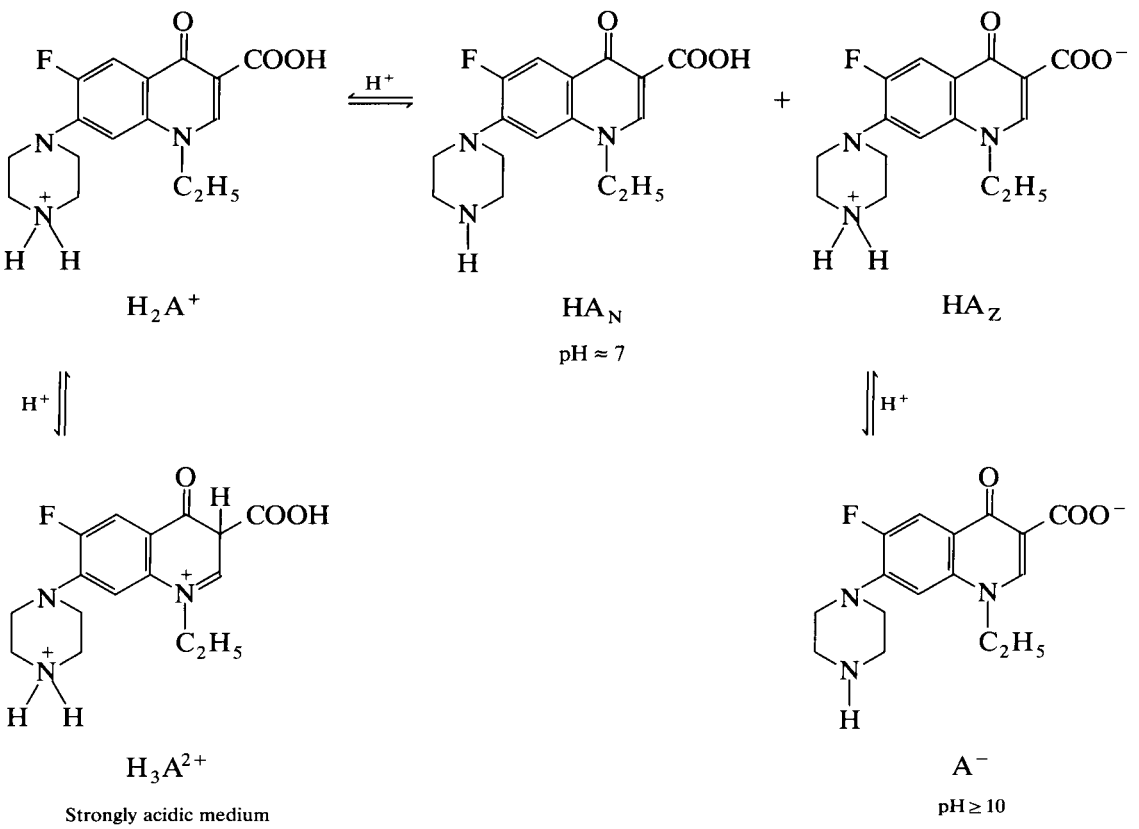

Scheme 1. Acid–base equilibria for norfloxacin in aqueous media.

1 below. As the pH of the base electrolyte increases the concentration of H_3A^{2+}, which is predominant in strongly acidic media, is expected to decrease. The disappearance of the dp polarographic peak at -1.02 V when the concentration of HCl base electrolyte became $\leqslant 0.01$ M HCl may indicate a drastic decrease in the concentration of H_3A^{2+} at higher pH values.

Based on the dp polarograms in base electrolytes of wide pH range, the appearance and disappearance of waves according to pH values of the solutions, the above-mentioned proposed equilibria and the one-electron steps mechanism proposed previously for nalidixic acid [6], the reduction of norfloxacin at the DME may take place according to the equations of Scheme 2.

Thus, the peak at -1.02 V in strongly acidic media (HCl) and peaks corresponding to waves C and D in the intermediate and basic media could be attributed to one-electron reduction steps of the species, H_3A^{2+}, HA_Z and A^- respectively. This reduction will produce the radical products, $H_3A^{+\cdot}$, $HA_Z^{-\cdot}$, and $A^{2-\cdot}$ as indicated in Scheme 2.

The radicals produced as a result of electrochemical reduction at the DME may deactivate by dimerization, disproportionation or reaction

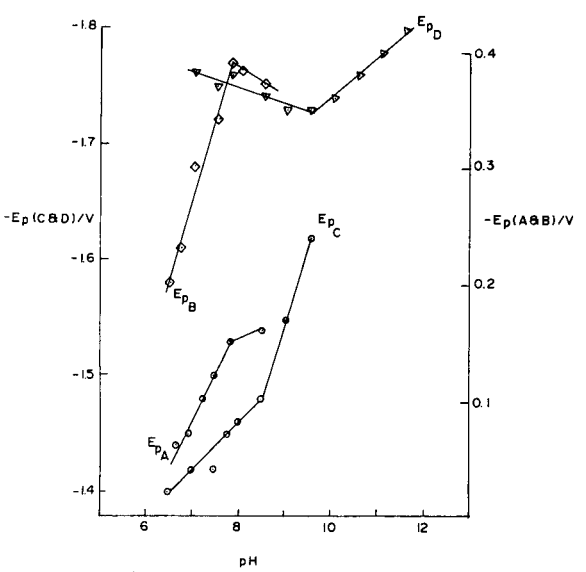

Fig. 5. dp peak potentials vs. pH for 1×10^{-4} M norfloxacin in various buffering systems made of acetic acid–sodium acetate and NH_3–NH_4Cl covering a pH range of 4.5 to 11.5.

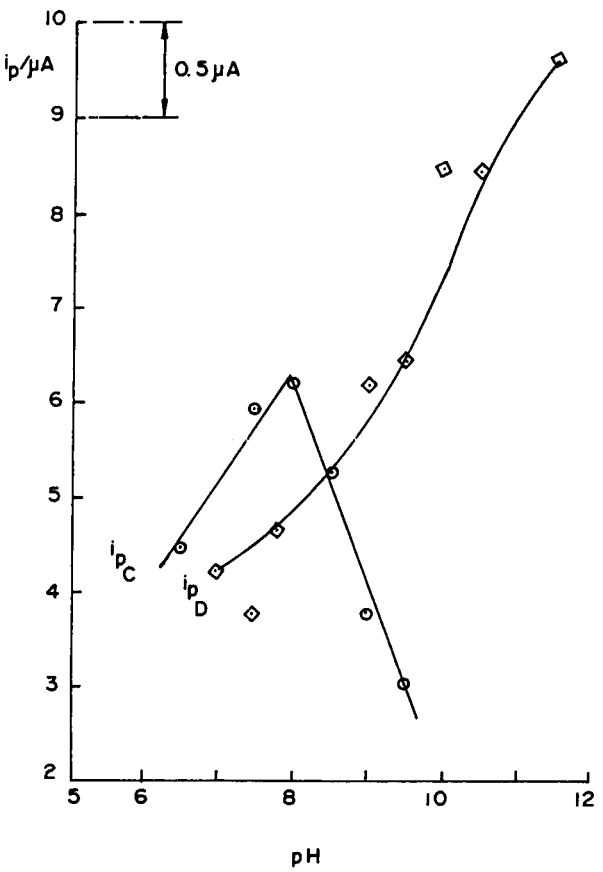

Fig. 6. dp peak heights vs. pH for 1×10^{-4} M norfloxacin in various buffering systems made of acetic acid–sodium acetate and NH_3/NH_4Cl covering a pH range of 4.5 to 11.5.

with the solvent as suggested for nalidixic acid [6]. It can also be suggested that the radicals may undergo a further one-electron reduction step producing waves shifted to potentials more negative than the discharge potential of the base electrolyte, thus they did not appear within the experimental potential range. The absence of peaks related to the species HA_N and H_2A^+ may be ascribed to their limited concentrations in solutions of intermediate pH. Although these two species are expected to predominate in slightly acidic medium, no dp polarographic peaks were detected over this range. This may be ascribed to either their reduction at potentials outside the experimental potential range or that the waves were not sensitive enough to be detected under the experimental conditions.

3.3. Linearity of calibration plots for norfloxacin in various base elecrolytes

The concentration dependence of the dp polarographic peak heights of norfloxacin in the presence of various base electrolytes was checked for the two well-defined peaks C and D at pH values from slightly acidic to slightly alkaline. The linearity was tested for norfloxacin concentrations in the range 2 to 560 μg ml^{-1} (5×10^{-6} to 1.7×10^{-3} M) according to the analytical procedure mentioned above. The results are shown in Table 2. Over some of the concentration ranges more than one linear segment was observed. A curvature has also been observed in the calibration curves in some cases. The breaks or curvature in the calibration curves are ascribed to a change in the mechanism of reduction at the electrode, which is dependent upon the concentration of protonated, uncharged, and anionic species of norfloxacin. It has also been observed that the dp peak potentials are concentration dependent. Peak C showed a significant shift to a more positive potential at norfloxacin concentrations less than about 5×10^{-5} M above which the shift has been reversed to the opposite direction i.e., to a more negative potential. The shift in the potential of peak D with concentration was in the negative direction.

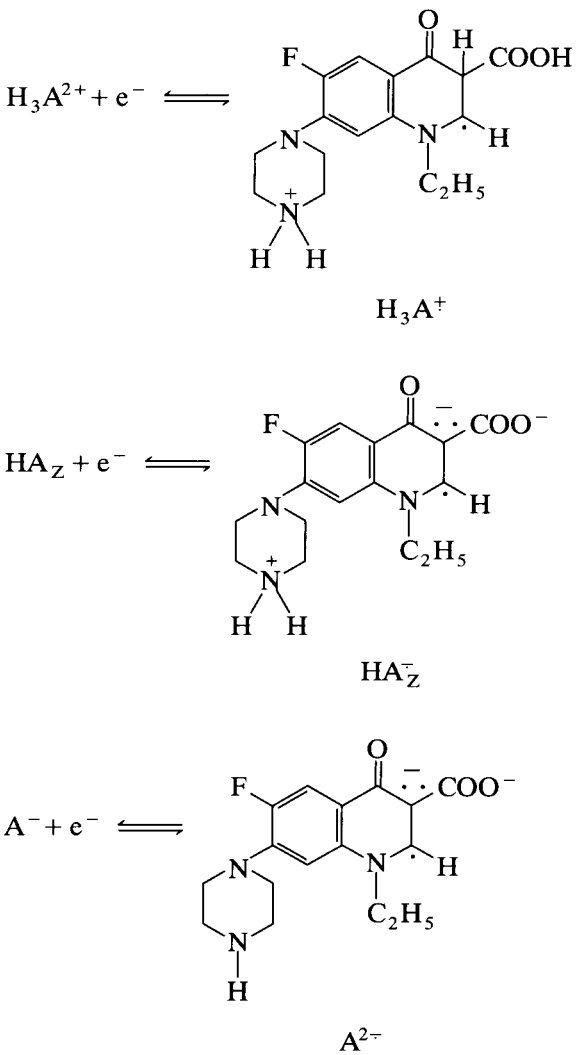

Scheme 2. Electrochemical reduction of norfloxacin at the DME.

The dp peak C was always well defined and far from the discharge of the base electrolyte, thus giving a reasonable calibration linearity within a rectilinear range reaching, for example, 32 to >560 μg ml^{-1} (9.9×10^{-5} to $>1.7 \times 10^{-3}$ M) norfloxacin in the cases of 0.1 M KCl and $LiClO_4$ base electrolyte. Thus, this peak was used to test the validity of the method for determination of the drug in commercial tablets.

The calibration behaviour of norfloxacin in 2 M hydrochloric acid based on the single wave observed therein has been checked also and was found to be linear within the studied range, namely, 32 to 300 μg ml^{-1} (1×10^{-4} to 9×10^{-4} M) norfloxacin (Table 2) with a nonsignificant shift in the peak potential.

3.4. Determination of norfloxacin in noroxin tablets

Noroxin tablets were assayed by this method after grinding and dissolving in DMF according to the procedure mentioned above. The results are shown in Table 3. The table shows good recoveries (an average of 99.5% recovery and a relative standard deviation, R.S.D., of 2.5%) for the base electrolytes tested including the 2 M hydrochloric acid. It is obvious that the drug excipients and the slight turbidity in the sample solutions did not affect the polarographic behaviour of norfloxacin.

3.5. Determination of nalidixic acid as individual component in tablets and in the presence of norfloxacin

The possibility of determining nalidixic acid as the individual component in tablets and in the presence of norfloxacin has been investigated. Figs. 7 and 8 show the dp polarograms for norfloxacin, nalidixic acid and their mixtures in 2 M hydrochloric acid and 0.1 M sodium acetate base electrolytes, respectively. Nalidixic acid showed two dp reduction peaks in the 2 M HCl base electrolyte at -0.78 and -1.01 V for 4.3×10^{-5} M nalidixic acid. These two peaks were close to the $E_{1/2}$ values reported for nalidixic acid [6]. Using sodium acetate or tripotassium citrate as the base electrolyte, three reduction peaks at -1.32, -1.52 and -1.78 V have been observed for 4.3×10^{-5} M nalidixic acid. These dp peak potentials correspond to $E_{1/2}$ values of the three dc waves reported for nalidixic acid at similar pH values [6]. Nalidixic acid as the individual component in the sample solution was determined in Negram commercial tablets and gave good recoveries (an average of 101% recovery and R.S.D. = 1.0%) as observed from Table 3.

Figs. 7 and 8 also show that the reduction peaks for either norfloxacin or nalidixic acid in mixtures appear almost at the same potentials as those for the individual components. Polarograms

Table 2
Linearity of calibration plots for norfloxacin in 0.1 M solutions of various base electrolytes

Base electrolyte	Peak C			Peak D		
	Range (μg ml^{-1})	Corr. coeff. [a]	Slope ($\times 10^{-2}$) (μA l mg^{-1})	Range (μg ml^{-1})	Corr. coeff.	Slope [b] ($\times 10^{-2}$) (μA l mg^{-1})
$K_2B_4O_7$	0– 94	0.9990(10)	2.836	16– 94	0.9983(9)	2.930
	94–320	0.9994(9)	2.189	94–320	0.9995(9)	2.108
K_3Citrate	0– 16	0.9995(6)	5.436	0– 10	0.9980(5)	6.000
	16– 35	0.9999(7)	3.781	10– 35	0.9970(9)	3.228
	60–540	0.9986(10)	1.259	Continuous curvature with new peak starting at -1.94 V		
LiCl	0– 20	Curved	–	0– 25	0.9983(9)	5.120
	16–400	0.9993(10)	1.141	124–345	0.9987(8)	1.361
KCl	0– 10	0.9976(5)	6.988	2– 13	0.9996(5)	5.455
	13– 30	0.9996(6)	3.571	2– 13	Curved	–
	32–560	0.9997(10)	1.195	Continuous curvature with a new peak starting at -1.90 V, above 80 μg ml^{-1}		
$LiClO_4$	0– 10	0.9985(5)	7.010	0– 20	0.9994(8)	5.371
	32–560	0.9997(10)	1.020	Continuous curvature		
K_2HPO_4	0– 45	0.9992(8)	3.972	2– 32	0.9976(7)	4.612
	50–106	0.9990(7)	2.739	57–106	0.9968(8)	2.992
	120–400	0.9996(10)	1.994	120–400	0.9997(10)	1.458
NaOAc	32–422	0.9990(10)	1.273	Continuous curvature		
HOAc–NaOAc (pH 7.4)	32–539	0.9995(10)	1.014	Continuous curvature		
NH_3–NH_4Cl	0– 32	0.9987(10)	4.228	0– 25	0.9998(9)	5.472
(pH 9.0)	32–130	0.9994(9)	2.785	32–106	0.9988(7)	3.005
	124–320	0.9996(8)	2.159	32–249	0.9986(10)	2.634
K_3Citrate–	0– 20	0.9975(8)	6.342	0– 20	0.9996(5)	7.553
K_2Hcitrate	57–130	0.9994(7)	1.593	–		
(pH 8.0)	160–494	0.9994(10)	0.961	63–267	0.9993(8)	1.228
HCl(2 M)	32–300	0.9994(10)	0.498	–		

[a] Number of data points in parentheses.
[b] The current range was 2 and 10 μA for low and high concentrations, respectively and the scan rate was 10 mV s^{-1}.

Table 3
Determination of norfloxacin and nalidixic acid in Noroxin and Negram tablets respectively using the external standards calibration method

Base electrolyte	Range (μg ml^{-1})	Corr. coeff. [a]	Quantity added [b] (μg ml^{-1})	Quantity found (μg ml^{-1})	Recovery (%)
I. Norfloxacin					
$K_2B_4O_7$	3– 12	0.9997(4)	10.0	9.7	97.0
	3– 32	0.9998(6)	8.0	8.1	101
	6–124	0.9993(7)	59.1	61.8	105
			97.6	99.1	102
	63–345	0.9995(6)	198	200	101
K_3Citrate	63–153	0.9990(6)	62.7	59.5	94.9
			93.1	91.2	98.0
			123	121	98.4
			138	133	96.4
	60–500	0.9990(9)	190	187	98.4
			296	300	101
			386	390	101
NaOAc [c]	32–125	0.9978(7)	31.7	31.3	98.7
			62.7	62.9	100
			93.1	91.0	97.7
			123	115	93.5
HCl(2 M)	32–300	0.9994(10)	31.7	31.7	100
			42.3	43.5	103
			62.7	61.7	98.4
			93.1	93.4	100
			152	153	101
			181	180	99.4
			237	237	100
			264	269	102
				Average	99.5
				R.S.D.	2.5%
II. Nalidixic acid					
NaOAc	20– 90	0.9993(8)	23.0	23.5	102
(peak at −1.32 V)			34.3	34.5	101
			45.6	45.5	99.8
			67.7	68.8	102
			89.4	90.8	102
K_3Citrate	34–100	0.9958(10)	34.3	35.4	103
(peak at −1.52)			45.6	45.9	101
			67.7	68.0	100
			89.4	91.1	102
			100	102	102
HCl (2 M)	10–110	0.9992(10)	11.6	11.8	102
(peak at −0.78 V)			34.3	35.1	102
			45.6	45.6	100
			67.7	68.4	101
			89.4	88.9	99.4
				Average	101
				R.S.D.	1.01%

[a] Number of data points in parentheses.
[b] According to the nominal value reported by the manufacturers.
[c] Peak D was used here. Peak C gave very high recovery.

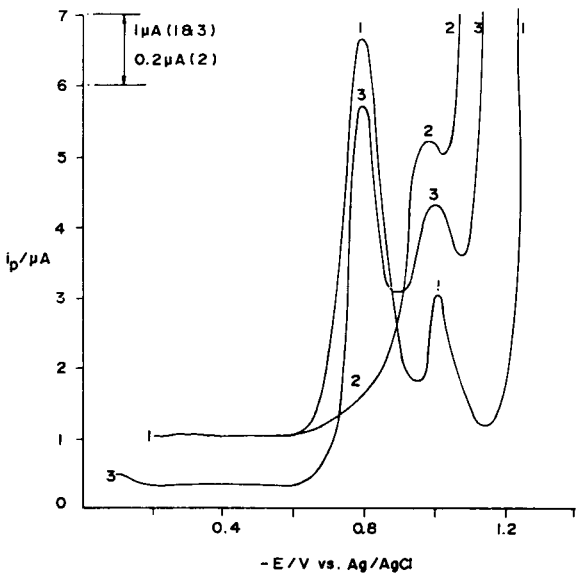

Fig. 7. dp polarograms for 4.8×10^{-4} M nalidixic acid (polarogram 1), 4.8×10^{-4} M norfloxacin (polarogram 2) and a mixture of 4.8×10^{-4} M of each (polarogram 3) in 2 M HCl.

recorded after incremental additions of nalidixic acid to a sample solution of norfloxacin in sodium acetate or tripotassium citrate base electrolytes show an increase in the dp peak at −1.32 V only. This peak belongs exclusively to nalidixic acid in such base electrolytes, thus it was chosen for determination of nalidixic acid in the presence of norfloxacin (Table 4).

When 2 M HCl was used as the base electrolyte, polarograms recorded for nalidixic acid showed two dp peaks at −0.78 V and −1.01 V. However, norfloxacin showed only one peak at −1.02 V. Polarograms recorded after incremental additions of nalidixic acid to a sample solution of norfloxacin showed a significant increase in the height of the peak at −0.78 V only. Therefore, this peak was used for nalidixic acid determination in the presence of norfloxacin in 2 M HCl base electrolyte (Table 4). Good recoveries for nalidixic acid (an average of 100% recovery and R.S.D. = 1.8%) have been obtained using the external standards calibration method (Table 4).

Table 4
Determination of nalidixic acid in Negram in the presence of 60 μg ml^{-1} (1.9×10^{-4} M) norfloxacin, using the external standards calibration method. Same quantity of norfloxacin was added to both standard and unknown sample solutions

Base electrolyte	Range (μg ml^{-1})	Corr. coeff. [a]	Nalidixic acid added [b] (μg ml^{-1})	Nalidixic acid found (μg ml^{-1})	Recovery (%)
NaOAc	22–90	0.9993(8) [b]	21.9	21.1	96.3
			43.8	44.9	103
			65.8	65.4	99.4
K_3Citrate	22–88	0.9965(8)	32.9	33.2	101
			43.8	43.8	100
			65.8	66.1	101
			87.7	87.3	99.5
HCl (2 M)	22–77	0.9991(7)	21.9	22.4	102
			32.9	33.6	102
			43.8	43.5	99.3
			54.8	54.3	99.1
			65.8	67.0	102
				Average	100
				R.S.D.	1.8%

[a] Number of data points in parentheses.
[b] According to the nominal value reported by the manufacturers.

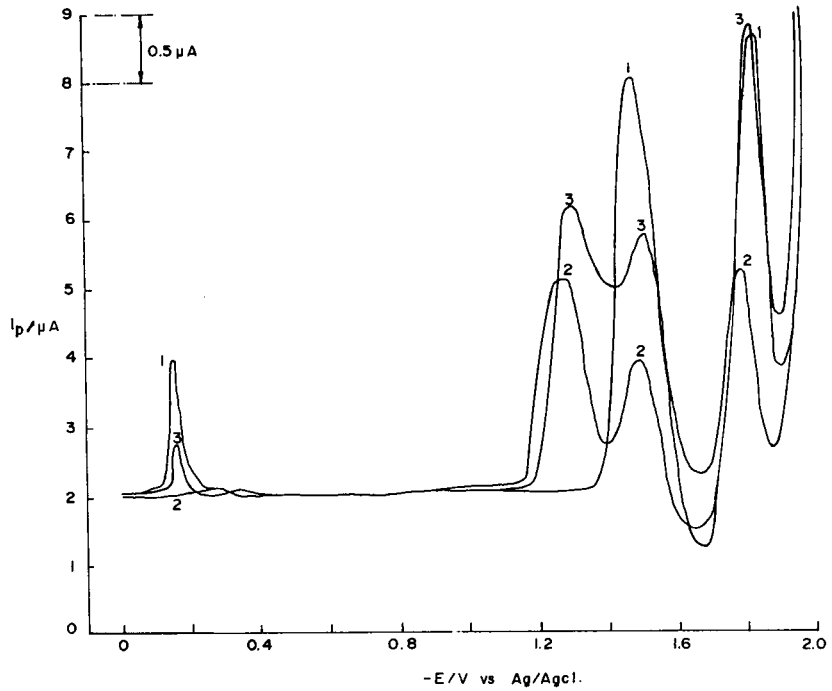

Fig. 8. dp polarograms for 2.9×10^{-4} M norfloxacin (polarogram 1), 2.9×10^{-4} M nalidixic acid (polarogram 2) and a mixture of 2.9×10^{-4} M of each (polarogram 3) in 0.1 M sodium acetate.

Acknowledgement

The King Fahd University of Petroleum and Minerals is thanked for supporting this research project. Dr. S.A. Ali of KFUPM is thanked for the helpful discussions.

References

[1] J.T. Smith, Pharm. J., 233 (1984) 299.
[2] K. Grohe, Chem. Br., 28 (1992) 34.
[3] L.T. Pauliukonis, D.G. Musson and W.F. Bayne, J. Pharm. Sci., 73 (1984) 99.
[4] A.J.N. Groeneveld and J.R.B.J. Brouwers, Pharmaceutisch Weekblad Scientific Edition, 8 (1986) 79.
[5] A. Veber, M. Veber, F. Kozjek and S. Gomiscek, Acta Pharm. Yougosl., 39 (1989) 321.
[6] W.J. Van Oort, R.H.A. Sorel, D. Brussee, S.G. Schulman, P. Zuman and J. Den Hartigh, Anal. Chim. Acta, 149 (1983) 175.
[7] P. Odea, A.C. Gracia, A.J.M. Ordieres, P.T. Blanco and M.R. Smyth, Electroanalysis, 2 (1990) 637.
[8] F. Belal and M. Sharaf El-Din, Microchem. J., 42 (1990) 300.
[9] H. Hoffmann and Dybowski, Fresenius' Z. Anal. Chem, 312 (1982) 625.
[10] M. Telting-Diaz, A.J.M. Ordieres, A. Gracia, P.T. Blanco, D. Diamond and M.R. Smith, Analyst, 115 (1990) 1215.
[11] M. Smyth and G.J. Vos (Eds.), Analytical Voltammetry, Comprehensive Analytical Chemistry, Vol. XXVII, Elsevier, Amsterdam, 1992, p. 159.
[12] P.T. Kissinger and W.R. Heineman, Laboratory Techniques in Electroanalytical Chemistry, Marcel Dekker, New York, 1984, p. 569.
[13] A.J. Bard and L.R. Faulkner, Electrochemical Methods, Wiley, New York, 1980, p. 136.
[14] A.K. Mishra and K.D. Gode, Analyst, 110 (1985) 31.
[15] J. Hyrovsky and J. Kuta, Principles of Polarography, Academic Press, New York, 1966, p. 339.

ELSEVIER

Analytica Chimica Acta 291 (1994) 65–73

ANALYTICA CHIMICA ACTA

Surface studies of quinhydrone pH sensors

C. Aquino-Binag, P.J. Pigram *, R.N. Lamb, P.W. Alexander

School of Chemistry, University of New South Wales, P.O. Box 1, Kensington, NSW 2033, Australia

(Received 6th September 1993; revised manuscript received 24th November 1993)

Abstract

A polymer-modified non-g'ass electrode was fabricated using quinhydrone (QH) in a poly(vinyl chloride) (PVC) matrix supported by a low porosity carbon rod. The electrode has a Nernstian response with a slope of 34.1 ± 7.3 mV/pH (25°C), a linear working range of pH 3 to 10 and an average response time of 5 to 7 min. Electrode stability was maintained over a period of 36 days without the need of pre-treatment prior to use or immersion in solution when not in use. X-ray photoelectron spectroscopy (XPS) was used to probe the composition and surface characteristics of the electrode in attempt to understand the chemical basis of electrode performance. Angle resolved XPS showed that electrodes with a poor performance had an oxygen enhanced surface attributed to increased surface concentration of oxygen containing QH. This electroactive species is readily oxidised when in contact with solution. Electrodes with a high performance had a chlorine enhanced surface, indicating a PVC-rich surface. The PVC serves both as a matrix and a protective layer for the embedded QH. The comparison of electrochemical and XPS data indicates that electrode composition and performance are closely related to fabrication techniques.

Key words: Sensors; Quinhydrone; Poly(vinyl chloride); X-Ray photoelectron spectroscopy; Surface studies

1. Introduction

Glassy carbon has been used extensively as the working electrode for a variety of electrochemical applications [1]. Coating electrode surfaces with polymers is an attractive means of increasing the selectivity of electrochemical analysis. In this study poly(vinyl chloride) (PVC) has been used as a matrix to which quinhydrone (QH) has been added.

Quinhydrone is a combination of benzoquinone and hydroquinone (1:4) and is used as the neutral carrier for hydrogen ions in pH sensor applications. It has been shown that platinum or gold foil coated with QH forms a pH-responsive electrode [2–4]. In practice, the solution to be measured may simply be contained in a small beaker and sufficient pure, solid QH added with stirring until the solution is saturated and a slight excess is present [3]. A piece of clean platinum or gold foil is then immersed into the solution saturated with solid QH [4]. The QH electrode is of little or no use at pH values greater than 8 or 9. However, the error does not appreciably affect

* Corresponding author.

SSDI 0003-2670(94)00014-D

the location of the equivalence point of an acid–base titration performed with a QH electrode, provided that this does not occur at a pH higher than about 9 [2]. A carbon supported electrode was used in this study, as its simple and robust construction allows easy renewal of the ion-sensitive surface [5–6]. Low cost, porosity and radiation resistance are properties which make carbon rods ideal for this application. Rod porosity, in particular, promotes adhesion as the polymer-filled pores anchor the pH responsive membrane onto the carbon surface [7].

PVC has been used as the matrix and the support for various ions including potassium [8,9], hydrogen [10–16], thallium(III) [5], sodium [9], zinc [6], hydrogencarbonate [17], and compounds such as sulfur containing substances [18], and vitamin B_{12} [19]. Derivatives of hydroquinone such as poly(mercaptohydroquinone) and poly(methylmercaptohydroquinone) [20] have been used to modify carbon fibre electrodes (CFE) by electrochemical polymerisation and used as pH sensors.

This paper describes the fabrication and characterisation of a novel non-glass pH electrode using a PVC/QH membrane supported with bulk carbon in form of rods and discs. Electrochemical electrode performance is correlated with investigations of the membrane structure and composition using x-ray photoelectron spectroscopy (XPS). An enhanced understanding of the sensor is obtained using this method.

2. Experimental

2.1. Electrode fabrication

Spectrographic carbon rods (Ringsdorff, Germany) of varying porosities were used to support the membrane. For electrochemical studies, 15 mm long carbon rods (4 or 6 mm diam.) were used; for XPS studies, 1.5 mm thick carbon discs of similar diameters were used. The end faces of the rods and discs were polished using abrasive paper (240 grit). Loose graphite particles were removed using an ultrasonic bath and air drying. Copper wire was attached to the upper end of the sensor rod to form an electrical connection. Low molecular weight poly(vinyl chloride), (LMW PVC) (Sigma) and QH (AnalaR) were dissolved in THF and ultrasonically mixed. Tetrahydrofuran (THF) was used as received without using any process to remove stabilizers. THF typically contains a low percentage of hydroquinone as a stabilizer. This compound is well known as half of the reversible couple in the classical QH electrode used for the measurement of pH [21], which is also the active species for this sensor. A solution of 1.5% PVC–QH (2:1, w/w) in THF was applied to the end surface of the carbon rod with a fine brush (15 applications with drying after each application) resulting in a coating thickness of ~ 130 μm. Film thicknesses were estimated using scanning electron microscopy. Analytical grade reagents were used as received. Deionised water with resistivity of 18 MΩ cm (Millipore, Milli-Q) was used in all experiments.

The carbon support acts as the conductive inert body of the electrode and does not play any other part in establishment of the measured potentials [5]. Graphite exhibits pH sensitivity because of the presence of chemisorbed oxygen on its surface [22]. This sensitivity can be minimised by coating the surface with materials such as poly(vinyl chloride) or paraffin wax or by modification of the surface chemistry, i.e., acidic groups at the graphite surface [5]. In this study, methacrylate aerosol (Borden, Australia) was applied to the sides of the electrode to provide insulation.

2.2. Electrode performance characterisation

Potentiometric and pH measurements were made with a pH/mV meter (Activon Model 209) and a calomel reference electrode (Metrohm Model B-NS 14/15) at 25°C. Potentiometric response curves were measured using the following cell:

Carbon rod//PVC–QH sensor/sample//SCE

Calibration plots were obtained for solutions containing hydrogen ion concentrations ranging from 10^{-3} to 10^{-10} M. Phosphate–citrate–borate buffers (pH 3–10) were used for electrode evaluation. The response time of the PVC/QH indica-

tor electrode was evaluated by immersion in increasing concentrations of H^+ solutions.

Electrode performance, sensitivity and selectivity were investigated in the presence of various interfering ions. Electrode stability was studied over a period of 36 days by storing the electrode dry in air. A fixed interference method was used; interfering anions were added as sodium salts and cations as iodides, chlorides, sulphates, or nitrates. Selectivity coefficients were then calculated using the extended Nernstian equation. Titration of 0.1 M HCl with 0.1 M NaOH was carried out using the PVC/QH pH electrode in comparison with a glass membrane electrode.

2.3. Electrode surface characterisation

Surface characterisation of the fabricated electrode was undertaken using XPS. Experiments were performed in ultrahigh vacuum using a Kratos AXIS 800 surface analysis instrument. The perpendicularly mounted Mg anode x-ray source was operated at 188 W. Electron energies were determined with a concentric hemispherical analyser (CHA) incorporating three channeltron electron detectors. The maximum energy resolution of the CHA was 0.87 eV operated for XPS analysis in the fixed analyser transmission (FAT) mode with a pass energy of 20 eV for the Ag $3d_{5/2}$ emission [23]. The electron binding energies (E_B) were calibrated against the Au $4f_{7/2}$ emission at $E_B = 84$ eV [24]. XPS analysis areas of 6 mm × 4 mm and 600 μm diameter were used [25]. Angle resolved XPS was undertaken by varying the angle between the sample surface and the analyser lens axis. Peak areas were quantified using appropriate sensitivity factors.

3. Results and discussion

3.1. Sensor performance

In this study, LMW PVC was mixed with QH, the electroactive species. The quinone and hydroquinone system is a reversible oxidation–reduction system in which hydrogen ions take part in the electrode reaction. The half-reaction is

$$H_2Q = Q + 2H^+ + 2e^- \quad (1)$$

where Q represents quinone, H_2Q, hydroquinone, and QH, quinhydrone [3]. The electrochemical mechanism of the PVC/QH pH electrode is shown in Fig. 1. There is an exchange of ions between the solution and cation vacancies at the electrode surface and an interfacial potential is generated by a space-charge mechanism [26]. While this PVC/QH pH electrode showed a working linear range from pH 3–10, with a Nernstian slope of 34.1 ± 7.3 mV/pH (25°C), Hauser et al. [10] used two different ionophores to obtain a wider pH range of pH 1–13. The potential–pH plots obtained with this electrode under fixed temperature cyclic change showed an ideal behaviour with slope of 29.2 ± 0.1 mV/pH (25°C), as shown in Fig. 2. A delay of 5–7 min was required to attain a steady-state potential reading. Electrode performance was monitored for up to 36 days without soaking or prior treatment before use. Theoretically for QH, potential

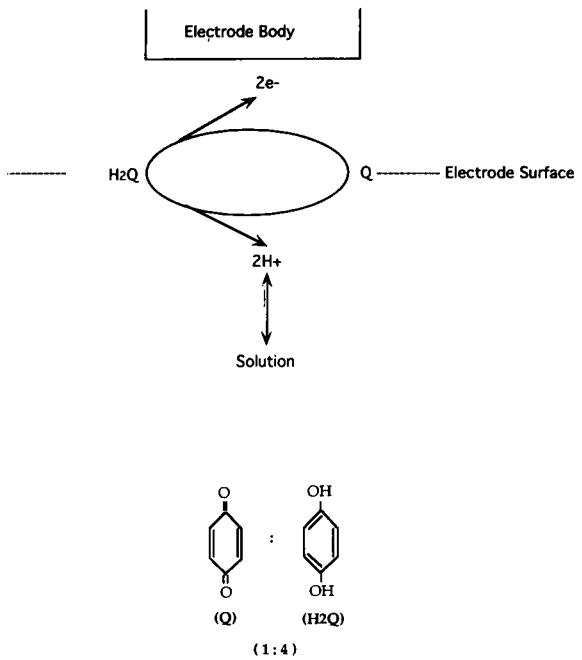

Fig. 1. Mechanism of the fabricated electrode.

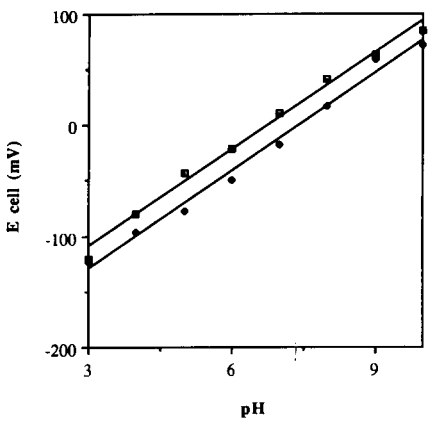

Fig. 2. PVC/QH pH electrode response characteristics at 25°C. Hysteresis, pH 10–3 (■) has a slope of 29.1 mV/pH; pH 3–10 (♦) has a slope of 29.3 mV/pH.

change per decade change in concentration of H^+ is expected to be close to 29.5 mV (25°C).

The PVC/QH pH electrode responded well in alkaline solution (pH 8–10) and gave an insignificant salt error throughout the study. The electrode gave a good and reproducible response in the presence of borates in the buffer solutions. Boric acid has the property of forming complexes with dihydrobenzenes like hydroquinone. The interference effects of a number of cations and anions were studied.

Potentials were measured in a series of solutions containing a constant concentration of interfering ion and increasing concentrations of hydrogen. The presence of reducing agents like SO_3^{2-} and $S_2O_3^{2-}$, seriously influences potentials of QH electrode. Selectivity coefficients, however, were small (see Table 1). The PVC/QH pH electrode and glass electrode gave identical endpoints for potentiometric titration of 0.1 M hydrochloric acid with 0.1 M sodium hydroxide.

3.2. Surface studies of sensor materials

The membrane surface of the electrodes was analysed using XPS; results are shown in Figs. 3–5. The surface of the membrane presents analytical difficulties as the components (PVC and QH) each contain carbon. The strategy used to overcome this problem is to analyse the components individually, then make a comparison with the membrane. The QH, PVC and PVC/QH membrane were not supported by carbon in these initial experiments to determine peak deconvolutions. QH and PVC powders were supported in a gold plated powder cup; the PVC/QH mem-

Table 1
Potentiometric selectivity coefficients (fixed interference method)

Interfering ions, (1×10^{-2} M)	Selectivity coefficient, K_i
SO_3^{2-}	1.48×10^{-6}
$S_2O_3^{2-}$	1.97×10^{-7}
$S_2O_5^{2-}$	7.17×10^{-7}
NO_3^-	2.09×10^{-8}
Fe^{2+}	4.42×10^{-4}
Fe^{3+}	2.21×10^{-6}
Cu^{2+}	8.39×10^{-6}

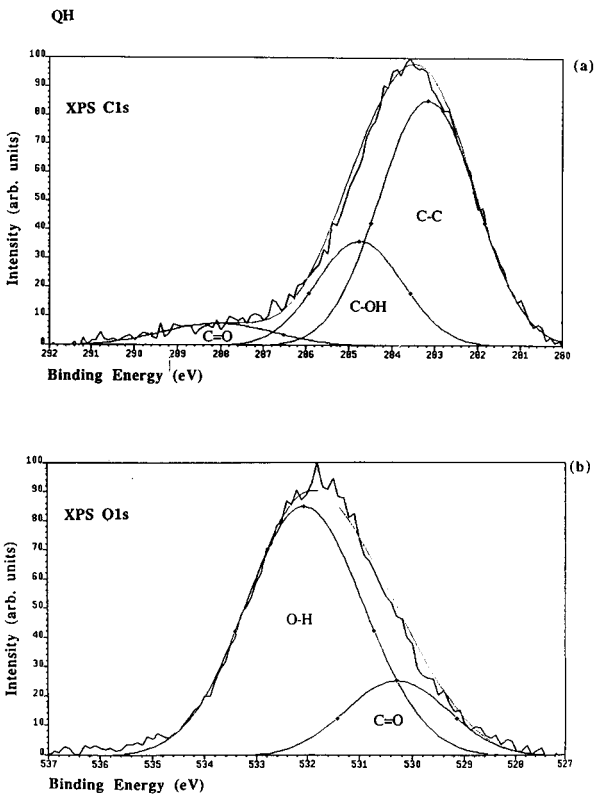

Fig. 3. Quinhydrone (QH) crystalline powder curve fit analysis of (a) C 1s and (b) O 1s photoelectron spectra.

brane was formed on polished copper using the method described above for carbon supported membranes.

The QH carbon 1s photoelectron spectrum was deconvoluted into three component peaks as shown in Fig. 3a; ($QH = O_2C_6H_4 : HOC_6H_4$–OH; ratio = 1:4). The largest peak at $E_B \sim 283$ eV is assigned to C–C, the peak at $E_B \sim 285$ eV is assigned to C–OH and the peak at $E_B \sim 288$ eV is assigned to C=O [27]. The ratio of the areas of the components peaks, C–C:C–OH:C=O, is equal to the stoichiometric ratio of 10:4:1. The oxygen 1s photoelectron spectrum (Fig. 3b) was deconvoluted into two component peaks: a peak at $E_B \sim 532$ eV assigned to hydroxyl species (O–H) [27] and a small peak at $E_B \sim 530$ eV assigned to C=O. The ratio of O–H:C=O was determined to be $\sim 3.4:1$ which is in reasonable agreement with the stoichiometric ratio of 4:1 for QH.

The PVC carbon 1s photoelectron spectrum was deconvoluted into two component peaks as shown in Fig. 4; ($PVC = -(CH_2CHCl)_n^-$). The two components are separated approximately by their respective line widths [28]. The peak centred at $E_B \sim 286$ eV is assigned to C–C species and the peak centred at $E_B \sim 284$ eV is assigned to C–Cl species. The ratio of the peak area of C:Cl was determined to be $\sim 1.8:1$, which was consistent with the stoichiometric ratio of 2:1 for PVC.

The carbon 1s photoelectron spectrum for the PVC/QH membrane was deconvoluted into four

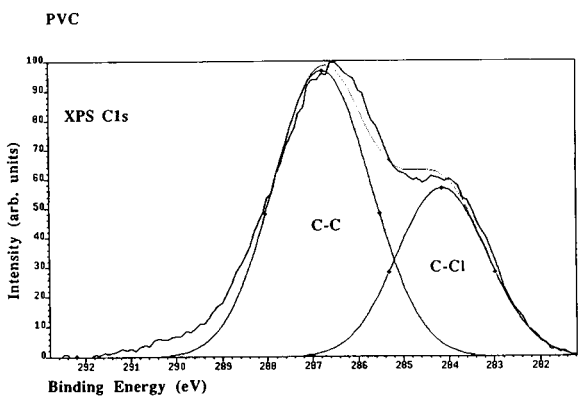

Fig. 4. PVC membrane curve fit analysis of a C 1s photoelectron spectrum.

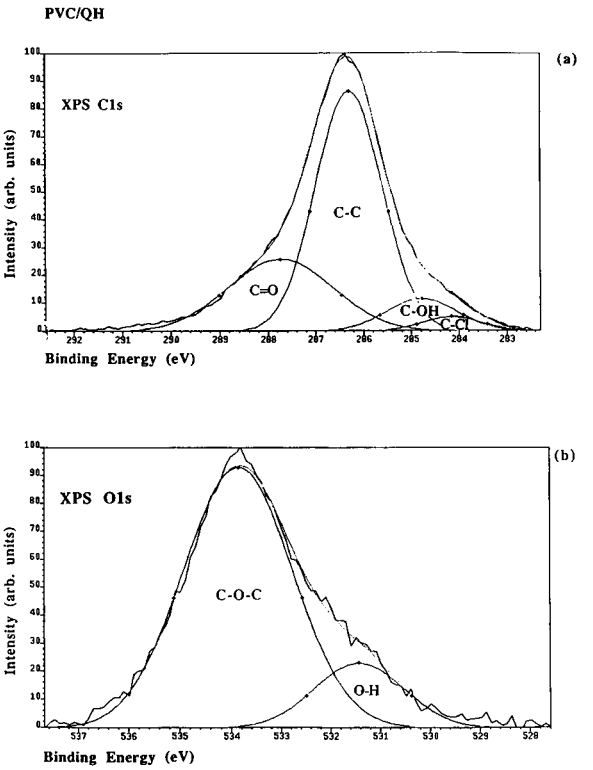

Fig. 5. PVC/QH membrane curve fit analysis of (a) C 1s and (b) O 1s photoelectron spectra.

component peaks as shown in Fig. 5a. The largest peak centred at $E_B \sim 286$ eV is assigned to the C–C, the peak at $E_B \sim 285$ eV is assigned to C–OH, the peak at $E_B \sim 288$ eV is assigned to C=O and the smallest peak at $E_B \sim 284$ eV is assigned to C–Cl. The peak area ratio of the four components, C–C:C–OH:C=O:C–Cl was determined to be 19:3:9:1 in comparison with the stoichiometric ration of 16:2:8:1. The excess carbon content may originate from occluded THF solvent or adventitious carbon contamination.

The oxygen 1s photoelectron spectrum for the PVC/QH membrane was deconvoluted into two component peaks as shown in Fig. 5b. The peak centred at $E_B \sim 533.8$ eV is assigned to C–O–C which is consistent with ether oxygen with $E_B \sim$ 533.2 eV [27] as an outcome of a possible cross-polymerisation of QH and PVC during fabrication of the membrane. The peak centred at $E_B \sim$ 531 eV is assigned to O–H. The peak area ratio

of C–O–C : O–H species was determined to be 5 : 1 in comparison with the stoichiometric ratio of 4 : 1. The excess oxygen probably originates from residual water present in the hygroscopic THF solvent.

Angle resolved XPS of the PVC/QH membrane was used to reveal changes in the structure

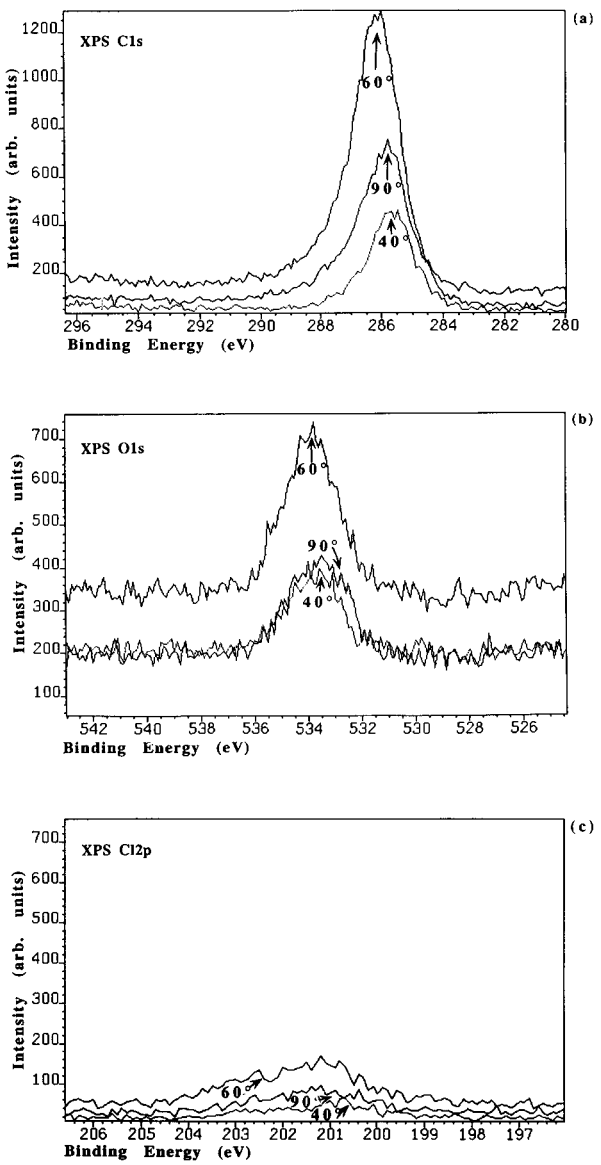

Fig. 6. Angle resolved XPS of the PVC/QH membrane of the (a) C 1s, (b) O 1s and (c) Cl 2p photoelectron spectra as a function of take-off angles of 90°, 60° and 40°.

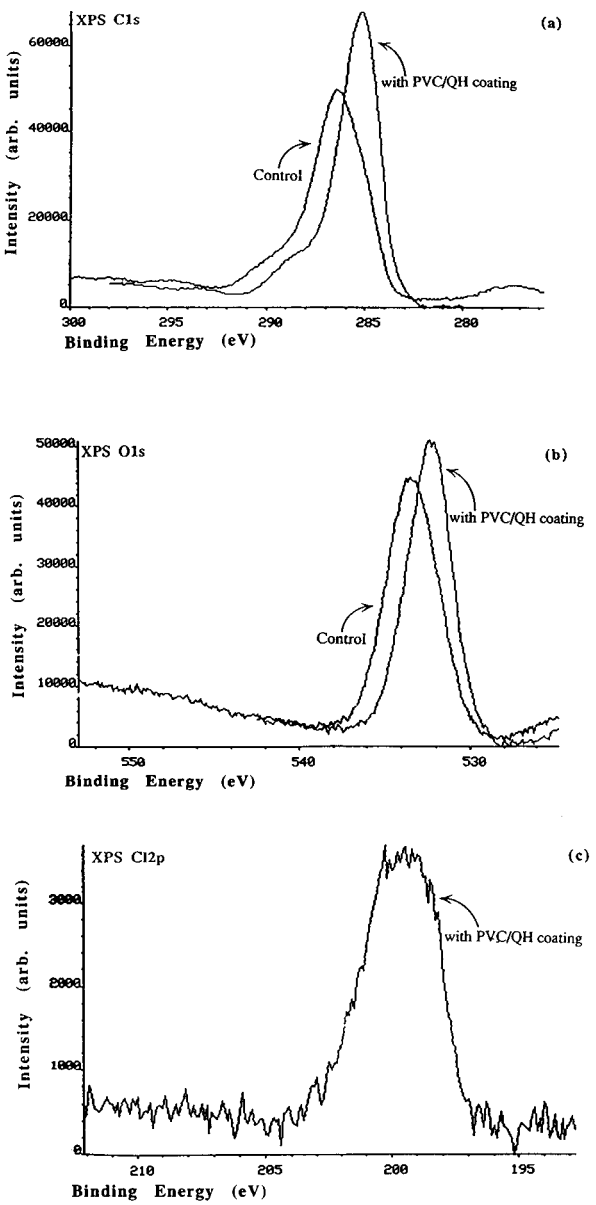

Fig. 7. Comparison of (a) C 1s, (b) O 1s, and (c) Cl 2p photoelectron spectra of the uncoated carbon disc (control) and the carbon disc with membrane coating.

of the outermost layer of the membrane surface as a function of depth (~ 10 nm). Changes in the line shape of the principal photoelectron peaks as a function of angle for (a) carbon, (b) oxygen and (c) chlorine are shown in Fig. 6 at 90, 60 and 40°.

The photoelectron take off angle (in fact, the cosine of the angle between the sample surface and the analyser lens axis) and the mean free path of electrons in the membrane determine the maximum depth from which photoelectrons are detected. The peak area ratio of C:O:Cl was determined to be 20:4:1 at 90°, 13:5:1 at 60° and 18:6:1 at 40°. From these ratios it can be seen that the oxygen 1s photoelectron peak, indicative of QH, is enhanced in the region closest to the surface, that is at 40°.

An uncoated (control) carbon disc and a carbon disc coated with the PVC/QH membrane were analysed by XPS. The principal carbon, oxygen and chlorine photoelectron peaks are shown in Fig. 7a–c, respectively. Carbon and oxygen are the main species on the surface of carbon disc with a C:O peak area ratio of 3:1. There is a weaker peak (Fig. 7c) at $E_B \sim 200$ eV for the coated carbon disc corresponding to chlorine from

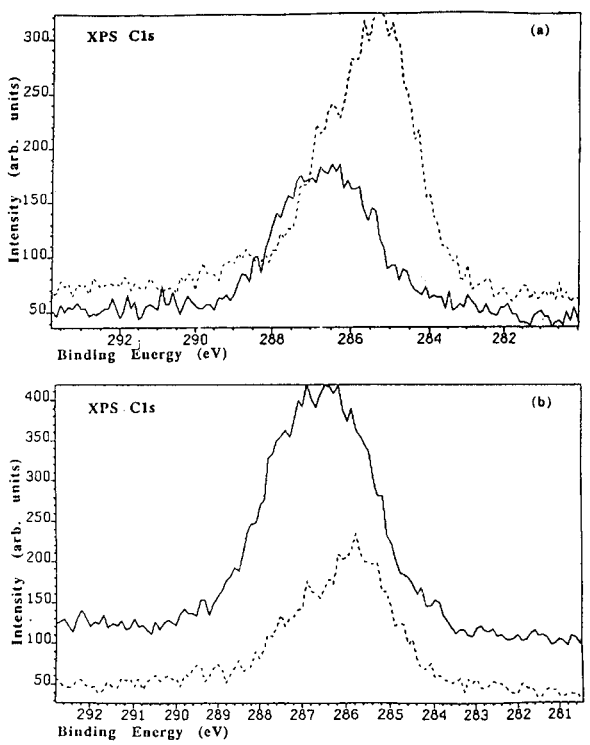

Fig. 8. Angle resolved XPS: C 1s photoelectron spectrum of a high performance electrode, HE (solid line), and a poor performance electrode, PE (dashed line), as a function of take-off angles of (a) 90° and (b) 60°.

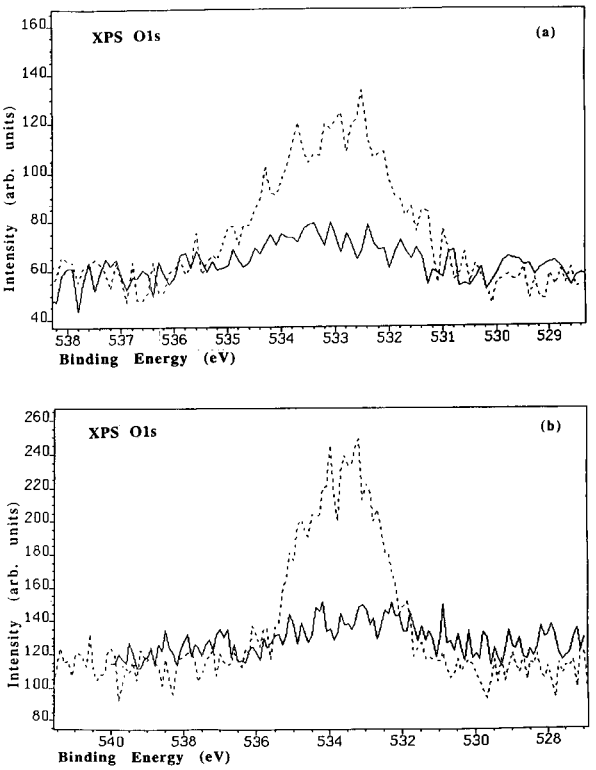

Fig. 9. Angle resolved XPS: O 1s photoelectron spectrum of a high performance electrode, HE (solid line), and a poor performance electrode, PE (dashed line), as a function of take-off angles of (a) 90° and (b) 60°.

the PVC component of the membrane. The C:O:Cl peak area ratio for the coated carbon disc was determined to be 37:12:1. The PVC/QH coating increased peak intensities and shifted peaks to a lower binding energy by between 0.7 to 1.6 eV.

3.3. Correlation of electrode performance and surface structure

Angle-resolved XPS of polymers is especially useful for studying compositional changes that occur very close to the surface (5–10 nm). Angle resolved XPS spectra of the surface of a high performance electrode (slope = 46.9 mV/pH, 25°C) were compared with equivalent spectra for a low performance electrode (slope = 22.0 mV/pH, 25°C) as shown in Figs. 8–10.

At an angle of 90°, the carbon 1s (Fig. 8a) spectrum which includes both the carbon of the bulk (carbon disc) and carbon of the surface (coating) of the poor performance electrode (PE) is greater than the high performance electrode (HE). But, at an angle of 60° (Fig. 8b) in which the contribution of species towards the outer surface are enhanced, the proportion of carbon species coming mostly from PVC and QH coating, is higher in the HE. In the poor performance electrode (Fig. 9a and b), there is a higher oxygen concentration (Fig. 9b), and hence higher QH concentration at the surface. Leaching to the solution may make the electrode QH deficient and therefore more poorly poised. The observed potential therefore would be more sensitive to traces of oxidising and reducing impurities. Hydroquinone comprising 80% of the quinhydrone used is not completely embedded, thus, more susceptible to oxidation. The activity of the hydroquinone will be decreased relative to the quinone and hence the QH electrode will require more time to reach an equilibration potential. In the high performance electrode (HE), the proportion of chlorine species (Fig. 10a and b) and hence PVC, at the surface is higher than the poor performance electrode (PE), as shown in Fig. 10b. This indicates that the high performance electrode membrane is not homogeneous throughout. The PVC serves both as a matrix and as protection for the active species, QH. It is proposed that the key factor for the level of performance of the PVC/QH pH electrode is the distribution of the PVC and QH in the membrane.

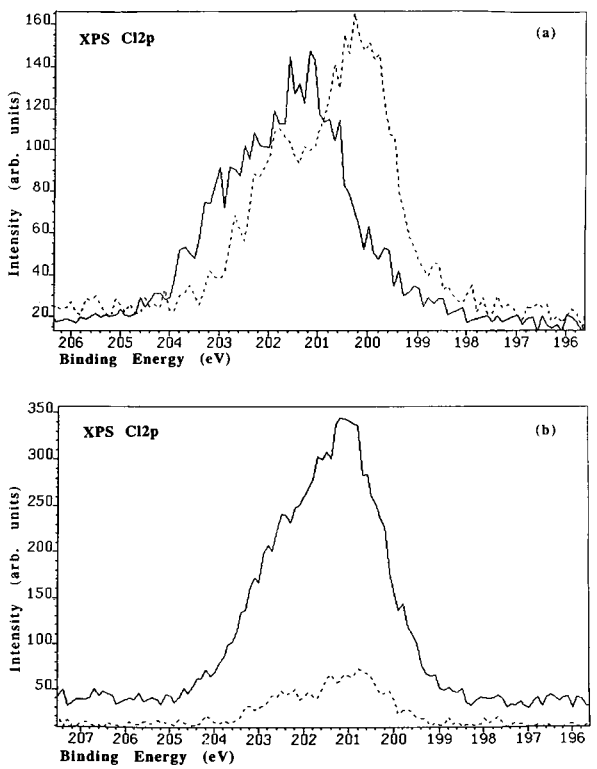

Fig. 10. Angle resolved XPS: Cl 2p photoelectron spectrum of a high performance electrode, HE (solid line), and a poor performance electrode, PE (dashed line), as a function of take-off angles of (a) 90° and (b) 60°.

4. Conclusions

This work demonstrates the analytical utility of the PVC/QH pH electrode as an attractive alternative to the conventional pH glass electrode. It is promising because of its ease of fabrication, low-cost and mechanical stability.

Surface techniques like XPS are important for studying the chemical and physical nature of the membrane coating of the electrode. The concentration of QH increases with depth into the membrane layer, while the concentration of PVC decreases. A good Nernstian responding electrode has a PVC-rich surface layer protecting the under layer of heterogeneously distributed QH electroactive species.

Acknowledgements

C.A.B. wishes to thank the Australian International Development Assistance Bureau for a postgraduate scholarship.

References

[1] G.N. Kamau, W.S. Willis and J.F. Rusling, Anal. Chem., 57 (1985) 545.

[2] L. Meites and H.C. Thomas, Advanced Analytical Chemistry, McGraw-Hill, New York, 1958, Chap. 4.

[3] J.L. Lingane, Electroanalytical Chemistry, Interscience, New York, 1958, Chap. 4.
[4] L. Meites, R.G. Bates and V.E. Bower, Handbook of Analytical Chemistry, McGraw-Hill, New York, 1963, Section 11.
[5] M.J. Rocheleau and W.C. Purdy, Talanta, 37 (1990) 307.
[6] D. Dan and Y. Dong, Talanta, 35 (1988) 589.
[7] L.A. Coury, E.M. Birch and W.R. Heineman, Anal. Chem., 60 (1988) 553.
[8] D.J. Harrison, A. Teclemariam and L.L. Cunningham, Anal. Chem., 61 (1989) 246.
[9] E. Lindner, E. Graf, Z. Niegreisz, K. Toth and E. Pungor, Anal. Chem., 60 (1988) 295.
[10] P.C. Hauser, T.J. Cardwell, R.W. Cattrall, S.S. Tan and I.C. Hamilton, Anal. Chim. Acta, 221 (1989) 139.
[11] H.L. Wu and R.Q. Yu, Talanta, 34 (1987) 577.
[12] F.R. Del Mundo, T.J. Cardwell, R.W. Cattrall, P.J. Iles and I.C. Hamilton, Electroanalysis, 1 (1989) 353.
[13] E.J. Fogt, P.T. Cahalan, A. Jevne and M.A. Schwinghammer, Anal. Chem., 57 (1985) 1155.
[14] U. Oesch, Z. Brzozka and A. Xu, Anal. Chem., 58 (1986) 2285.
[15] P. Schulthess, Y. Shijo and H. Pham, Anal. Chim. Acta, 131 (1981) 111.
[16] T. Cardwell, R.W. Cattrall, L. Deady and K. Murphy, Aust. J. Chem., 45 (1992) 435.
[17] U. Oesch, E. Malinowska and W. Simon, Anal. Chem., 59 (1987) 2131.
[18] V.I. Berestetski and F.M. Tulyupa, J. Anal. Chem. USSR, 44 (1989) 259.
[19] L.G. Bachas and S. Daunert, Anal. Chem., 61 (1989) 499.
[20] G. Arai, T. Koike and I. Yasumori, Chem. Lett. Chem. Soc. Jpn., (1986) 867.
[21] R.W. Cattrall and I.C. Hamilton, Ion-Selective Electrode Rev., 6 (1984) 125.
[22] J. Ruzicka, C.G Lamm and J. Tjell, Anal. Chim. Acta, 62 (1972) 15.
[23] R.J. Bird and T.J. Swift, J. Electron. Spectrosc. Relat. Phenom., 21 (1980) 227.
[24] M.P. Seah, Surface and Interface Analysis, 14 (1989) 488.
[25] I.W. Drummond, L.P. Ogden and F.J. Street, J. Vac. Sci. Technol. A., 9 (1991) 1434.
[26] R. De Marco, R.W. Cattrall, J. Liesegang and G.L. Nyberg, Anal. Chem., 62 (1990) 2339.
[27] Handbook of X-ray Photoelectron Spectroscopy, Perkin Elmer, Physical Electronics Division, Eden Prairie, MN, 1979.
[28] D.T. Clark and H.R. Thomas, J. Polym. Sci.: Polym. Chem. Ed., 16 (1978) 791.

ELSEVIER

Analytica Chimica Acta 291 (1994) 75–80

ANALYTICA CHIMICA ACTA

Study of cathodic stripping of copper in hydrochloric acid medium. Simultaneous determination of cadmium, lead and copper by combined anodic and cathodic stripping voltammetry

T. Nedeltcheva *, L. Costadinnova, M. Athanassova

Department of Analytical Chemistry, Higher Institute of Chemical Technology, Cl. Ohridsky 8, Sofia 1756, Bulgaria

(Received 21st April 1993; revised manuscript received 15th December 1993)

Abstract

The copper cathodic stripping peak obtained in hydrochloric acid medium by fast differential-pulse potential scanning in the negative direction was studied. Conditions for the simultaneous determination of Pb, Cd and Cu by combined stripping voltammetry (anodic for Pb and Cd and cathodic for Cu) were found; copper was actually determined by adsorptive voltammetry. Samples of $CaHPO_4$ and $CaCO_3$ were analysed by the proposed method and the relative standard deviation for 10^{-5}–10^{-4}% metal contents was about 8%. The accuracy of the results was confirmed by extraction flame atomic absorption spectrometry.

Key words: Stripping voltammetry; Cadmium; Copper; Lead

1. Introduction

The voltammetric determination of traces of copper is usually carried out by differential-pulse anodic stripping voltammetry (DPASV) with a hanging mercury drop [1]. The measurements are often made at low pH in hydrochloric acid medium to prevent or decrease adsorption losses and interference by organic matter [2]. Hydrochloric acid is a preferred electrolyte as it is a good solvent for many substances, can be produced with high purity and is less expensive than other acids. However, the determination of low copper concentrations in this medium is hampered by the shape of the anodic peak, which is low, broad and asymmetric [1,2]. Asymmetric copper peaks are observed in nitric acid containing chloride ions [2] and also in 0.1 M KCl [3]. This behaviour of copper in chloride medium is caused by Cu(I) stabilization and the closeness of the copper and mercury oxidation potentials [1,2].

The copper cathodic peak obtained by fast scanning differential-pulse cathodic stripping voltammetry (FSDPCSV) in 0.1 M KCl [the copper is deposited in advance on the mercury drop by reduction of the Cu(II) ions] has been reported [3,4]. This copper peak does not possess the disadvantages of the anodic peak in chloride medium. It could be expected that the behaviour of the copper cathodic peak in hydrochloric acid would be the same. Its study and the conditions for the determination of copper were the subject of this work. As copper is often determined to-

* Corresponding author.

SSDI 0003-2670(94)00020-M

gether with lead and cadmium, the possibility of the simultaneous determination of the three metals was also studied and the determination by combined stripping voltammetry in hydrochloric acid medium is proposed.

2. Study of cathodic copper peak

2.1. Experimental

Apparatus and reagents

Voltammetric measurements were carried out with a Model 646 microprocessor-controlled analyser (Metrohm, Herisau, Switzerland). This device controls a Metrohm Model 647 static mercury drop electrode system (SMDE), mechanical stirrer and x–y recorder. The SMDE is provided with a 50-ml glass cell and a three-electrode system including an Ag/AgCl reference electrode and a graphite rod auxiliary electrode; the mercury working electrode was used in the hanging drop mode (HMDE).

Analytical-reagent grade and Suprapur reagents (Merck, Darmstadt) and ultra-pure water prepared in a Milli-Q water purification unit (Millipore) were used in all experiments. Oxygen was removed from the solutions with 99.99% argon.

Procedure

The test solution (25 ml) was placed in the cell and the oxygen was purged with argon for 5 min. Then a deposition at −350 mV was carried out, and after a 20-s waiting period the potential was scanned from 50 to −350 mV using the differential-pulse modulation (pulse amplitude 50 mV, pulse duration 40 s and different scan rates). During deposition the solution was stirred at 1920 rev min^{-1}. The times of deposition (t_{dep}), oxidation (t_{Cu}^{ox}) and reduction (t_{Cu}^{r}) (see Fig. 1) were varied.

2.2. Results

Effect of copper reduction time

The changes in t_{Cu}^{r} were made in such a way that the potential scan rates varied from 10 to 40

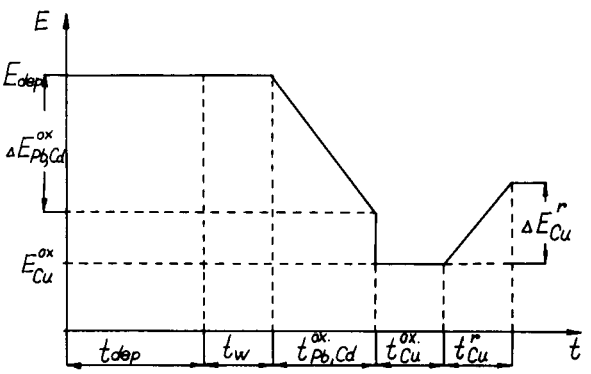

Fig. 1. Change in the working electrode potential (E) with time (t) during combined stripping voltammetry. E_{dep} and t_{dep} = deposition potential and time, respectively; t_w = waiting period; $\Delta E_{Pb,Cd}^{ox}$ and $t_{Pd,Cd}^{ox}$ = potential range and time of lead and cadmium oxidation, respectively; E_{Cu}^{ox} and t_{Cu}^{ox} = potential and time of copper oxidation, respectively; ΔE_{Cu}^{r} and t_{Cu}^{r} = potential range and time of copper ion reduction, respectively.

mV s^{-1}. The i_{Cu}^{c}–V_{Cu}^{c} plots, given in Fig. 2, showed that a decrease in scan rate caused a decrease in current. The higher the copper concentration, the stronger was the dependence. For further investigations a scan rate of 40 mv s^{-1} was chosen because at this value the cathodic

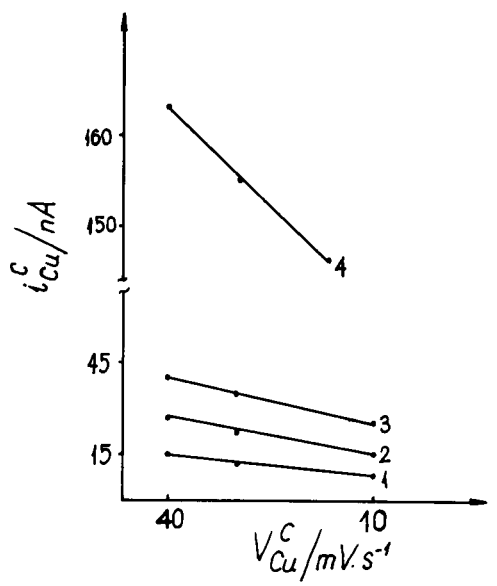

Fig. 2. Influence of V_{Cu}^{c} on i_{Cu}^{c} at copper concentrations of (1) 6, (2) 12, (3) 18 and (4) 68 μg l^{-1}. t_{Cu}^{ox} = 1 s; t_{dep} = 60 s; C_{HCl} = 0.2 M.

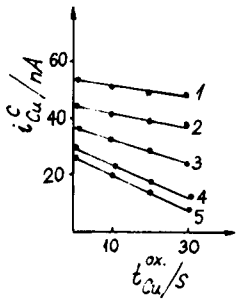

Fig. 3. Influence of t_{Cu}^{ox} on i_{Cu}^{c} at different C_{HCl}: (1) 0.1; (2) 0.2; (3) 0.3, (4) 0.6; (5) 0.9 M. Common parameters: $C_{Cu} = 20$ $\mu g\ l^{-1}$; $V_{Cu}^{c} = 40$ mV s^{-1}; $t_{dep} = 60$ s.

current was the largest and the peak was reproducible.

Effect of copper oxidation time and hydrochloric acid concentration

A decrease in current with increasing t_{Cu}^{ox} and C_{HCl} is observed (see Figs. 3 and 4). The decrease in i_{Cu}^{c} is more effective at higher C_{Cu}. Experiments made at constant pH and different C_{Cl^-} showed that the i_{Cu}^{c}–t_{Cu}^{ox} graph depended on the chloride ion concentration. In conclusion, reproducible and sensitive copper signals were obtained at low copper concentrations, $t_{Cu}^{ox} = 1$–2 s and $C_{HCl} = 0.1$–0.2 M, and these values were selected for use.

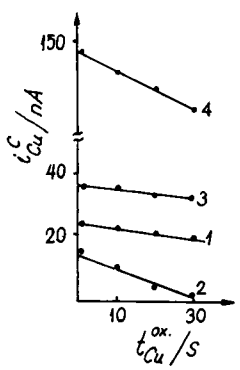

Fig. 4. Influence of t_{Cu}^{ox} on i_{Cu}^{c} at different C_{Cl^-} and C_{Cu}. Curves 1 and 2: $C_{Cu} = 10$ $\mu g\ l^{-1}$ and $C_{HCl} = 0.1$ M; $C_{KCl} =$ (1) 0 and (2) 0.6 M. Curves 3 and 4: $C_{HCl} = 0.2$ M; $C_{Cu} =$ (3) 15 and (4) 58 $\mu g\ l^{-1}$. t_{dep} and V_{Cu}^{c} as in Fig. 3.

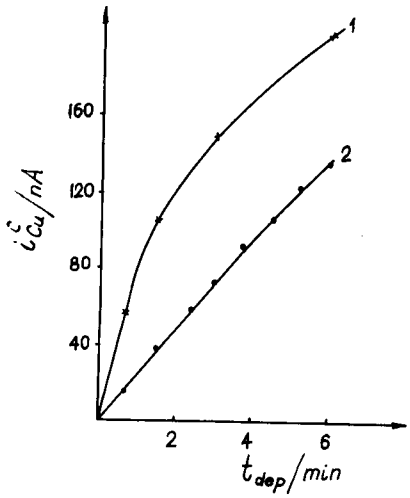

Fig. 5. Influence of t_{dep} on i_{Cu}^{c} at (1) 30 and (2) 10 Cu $\mu g\ l^{-1}$. Common parameters: $V_{Cu}^{c} = 40$ mV s^{-1}; $C_{HCl} = 0.1$ M; $t_{Cu}^{ox} =$ 1 s.

Effect of deposition time

The existence of a proportional relationship between i_{Cu}^{c} and t_{dep} depends on the copper concentration (see Fig. 5). C_{HCl} also affected the i_{Cu}^{c}–t_{dep} graph; an extension of the linear range with increasing C_{HCl} was observed. A value of t_{dep} was chosen at which small cathodic currents were registered (the value of the current after standard additions did not exceed 120 nA). Copper in the concentration range 2–30 $\mu g\ l^{-1}$ was determined at a deposition time of 60 s in 0.1–0.2 M HCl medium. At higher C_{Cu} a higher C_{HCl} has to be used or anodic stripping voltammetry must be applied (the higher copper anodic peaks have a better shape).

Effect of copper concentration

The linearity of the FSDPCSV response (peak height) versus increasing copper concentration was tested. To compare the sensitivity of the method with the sensitivity of DPASV, copper anodic peaks in the same solution were obtained and their heights evaluated. The curves in Fig. 6 show that the linear range of copper cathodic determination was limited. It could be extended using more concentrated hydrochloric acid, a shorter t_{dep} or deposition without stirring. The

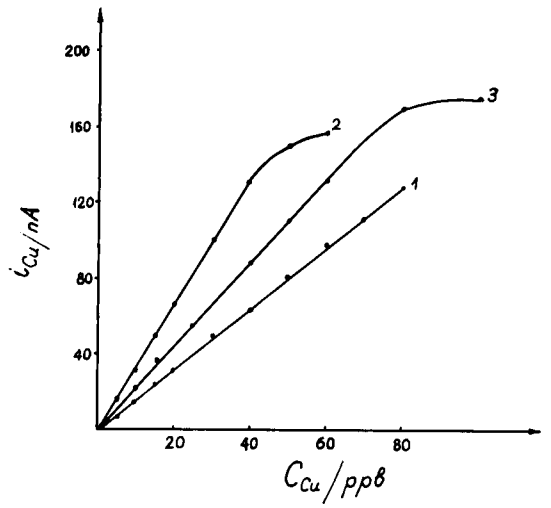

Fig. 6. Plots of (1) $i^{a}_{Cu} = f(C_{Cu})$ and (2 and 3) $i^{c}_{Cu} = f(C_{Cu})$ in (1 and 2) 0.1 M HCl and (1 and 3) 0.3 M HCl. Common parameters: $V^{c}_{Cu} = 40$ mV s^{-1}; $t^{ox}_{Cu} = 1$ s; $t_{dep} = 60$ s; $V^{a}_{Cu} = 20$ mV s^{-1}.

same curves also indicated that the cathodic curves were steeper than the anodic curves; their steepness depended on C_{HCl}.

Table 1
Values of Cu, Bi, Sb and Pb peak potentials and currents obtained by anodic and cathodic stripping voltammetry

C_{HCl} (M)	Metal ion	DPASV		FSDPCSV	
		E_p (mV)	i (nA)	E_p (mV)	i (nA)
0.1	Cu	−140	30	−160	60
	Bi	−10	43	−40	26
	Sb	−120	48	−140	26
	Pb	−360	39	−380	6
0.5	Cu	−180	32	−200	30
	Bi	−50	94	−60	39
	Sb	−150	91	−160	38

$C_{Cu} = C_{Bi} = C_{Sb} = C_{Pb} = 20$ μg l^{-1}; $t_{dep} = 60$ s; oxidation time = 1 s; anodic and cathodic potential scan rates = 20 and 40 mV s^{-1}, respectively.

Effect of foreign metal ions

The interferences caused by metals whose peak potentials are close to that of copper were considered. Experiments with model solutions of Bi, Pb and Sb were carried out. The results for cathodic and anodic peak currents and potentials are given in Table 1. It was established that the cathodic determination of copper in the presence

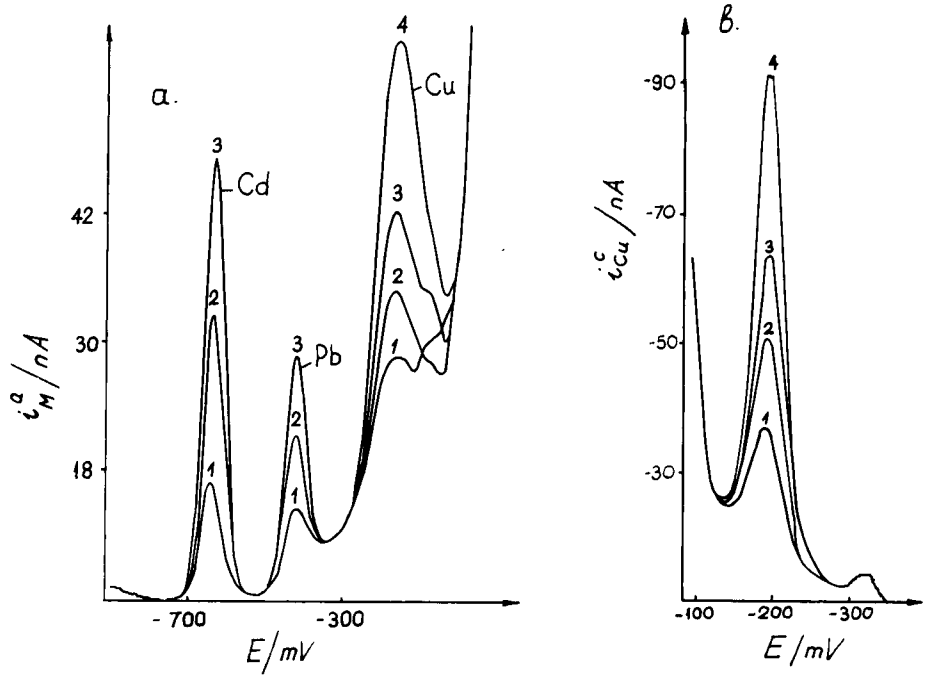

Fig. 7. (a) Anodic and (b) cathodic peaks at $t_{dep} = 180$ s. Standard addition concentrations: (1) 0; (2) 1; (3) 2; (4) 3 μg l^{-1}.

of Pb and Bi was more selective than the anodic determination (20 μg l^{-1} Cu can be determined in the presence of 6 μg l^{-1} Bi using only FSDPCSV), while Sb interfered with both the anodic and cathodic determination of copper. The reason for the Sb interference was the small difference between the peak potentials of the two metals.

The better selectivity of the cathodic determination of copper is seen from the peaks in Fig. 7. The copper anodic peak overlapped with the second peak, identified as the Bi peak. This led to difficulties in the quantitative evaluation of the copper peak height. In contrast to the anodic peak, the cathodic peak showed no overlap and there was no problem in the evaluation of its height.

2.3. Discussion

The study of the copper peak obtained by fast cathodic scanning in hydrochloric acid medium showed that its behaviour could be explained with the occurrence of a copper stripping process, controlled primarily by the one-electron oxidation of the copper and adsorption of the intermediate compounds on the mercury drop surface. The intermediates are assumed to be the insoluble product CuCl [5] or the complex $CuCl_2^-$ [6–8], formed at low or high chloride concentrations, respectively, and adsorbed by the mercury surface to different extents. Proof of these adsorption processes was the more effective decrease in i_{Cu}^c with increase in t_{Cu}^r or t_{Cu}^{ox} observed at higher C_{Cu} and the decrease in i_{Cu}^c with increase in C_{Cl^-} (Figs. 3 and 4). The i_{Cu}^c–V_{Cu}^c (Fig. 2), i_{Cu}^c–t_{dep} (Fig. 5) and i_{Cu}^c–C_{Cu} (Fig. 6) relationships also confirmed the adsorptive nature of the process; they are inherent to adsorptive voltammetry [9,10]. Consequently, a new possibility for the determination of copper was found, according to which copper can be determined by adsorptive voltammetry in hydrochloric acid medium without introducing an additional reagent forming a copper complex or precipitate (adsorptive copper determinations are usually done at pH 6–9 in the presence of a suitable reagent [9]).

3. Determination of lead, cadmium and copper by combined anodic and cathodic stripping voltammetry

3.1. Experimental

The apparatus and reagents were as described in Section 2.1.

Procedure

The solution containing the sample and hydrochloric acid at a 0.1–0.2 M concentration (more precisely the chloride ion concentration varied within the above limits) was placed in the cell, the oxygen was purged with argon and the analytes were deposited on the mercury drop at $E_{dep} = -850$ mV for a few minutes. After a 20-s waiting period the potential was scanned with differential-pulse modulation (scan rates $V_{Pb,Cd}^a = 20$ mV s^{-1} and $V_{Cu}^c = 40$ mV s^{-1}) following the sequence given in Fig. 1. The values of $\Delta E_{Pb,Cd}^{ox}$, ΔE_{Cu}^r and E_{Cu}^{ox} were 600, 400 and 50 mV, respectively. The time values were $t_{Pb,Cd}^{ox} = 26$ s, $t_{Cu}^{ox} = 1$ s and $t_{Cu}^r = 10$ s. The analytes were determined using the three-spike standard addition method.

3.2. Results and discussion

The sequence of the steps in the proposed method is shown in Fig. 1. Cadmium and lead were determined by conventional DPASV as their FSDPCSV currents were very low. The analyses were carried out in 0.2 M HCl as the copper cathodic current was the highest in this medium. The instrumental parameter values (E_{dep} and others) given in the procedure allowed simultaneous metal deposition and stripping peak registration using the same mercury drop. The values related to Cu determination were discussed above. The time $t_{Pb,Cd}^{ox}$ was in conformity with the rate $V_{Pb,Cd}^a$. Both values were found after studying the influence of the scan rate on the anodic (for Pb and Cd) and cathodic (for Cu) currents. Only high rate values were examined to speed up the analysis.

The data in Table 2 show that the slope values of the Pb and Cd calibration graphs and their standard deviations at rates of 10 and 20 mV s^{-1}

did not very much, while there was a tendency for decreasing reproducibility with increasing scan rates up to 40 and 60 mV s^{-1}. The copper current was independent of $V^{a}_{Pb,Cd}$; a rate of 20 mV s^{-1}, i.e., $t^{ox}_{Pb,Cd} = 26$ s, was selected. The t_{dep} value depended on the analyte concentration in the sample solution, and especially on the copper concentration (see *Effect of deposition time*). This sequence of steps was applied to approximately equal metal contents. If the amount of copper in the sample was significantly larger, the copper had to be deposited on a separate mercury drop for shorter t_{dep}.

The method was applied to the determination of Pb, Cd and Cu in technical $CaCO_3$ and $CaHPO_4$. The analyses were carried out by dissolving 0.2-g sample in 20 ml of 0.2 M hydrochloric acid, then following the procedure for the determination of Pb, Cd and Cu with $t_{dep} = 60$ s. The analyte signals in the blank were measured in the hydrochloric acid solution before dissolving the sample and their contents were calculated with the aid of the slopes of the calibration graphs obtained with the sample solution (the presence of phosphates did not change the slope of the calibration graph [11]).

The mean results obtained from five determinations and their relative standard deviations (R.S.D.) are given in Table 3. The same sample was analysed by extraction flame atomic absorption spectrometry (AAS) (three parallel determinations) [12] and the results are also presented in Table 3. A good correlation between the mean values and a better reproducibility with the proposed method were observed.

In conclusion, the proposed method provides a simple approach for the simultaneous determination of Pb, Cd and Cu in hydrochloric acid medium. It maintains the advantages of the determination of Pb and Cd by DPASV and those of the determination of Cu by FSDPCSV.

Table 2
Slopes of the cadmium and lead calibration graphs and their standard deviations at different $V^{a}_{Pb,Cd}$ for concentration ranges 5–76 $\mu g\ l^{-1}$ (Cd) and 5–70 $\mu g\ l^{-1}$ (Pb) with $t_{dep} = 2$ min

$V^{a}_{Pb,Cd}$ (mV s^{-1})	Slope (nA μg^{-1} l)		Standard deviation (nA μg^{-1} l)	
	Pb	Cd	Pb	Cd
10	3.6	4.0	0.031	0.043
20	3.6	4.1	0.036	0.036
40	3.7	4.5	0.052	0.210
60	3.8	5.0	0.073	0.491

Table 3
Results obtained by the combined voltammetric method and extraction flame AAS

Method	Metal	$\bar{x}$ (10^{-5}%)		R.S.D. (%)
		$CaHPO_4$	$CaCO_3$	
Voltammetry	Cd	2.5	6.8	7
	Pb	5.2	8.9	9
	Cu	4.6	11	8
AAS	Cd	2.3	7.2	14
	Pb	4.8	9.2	17
	Cu	5.1	10	5

References

[1] F. Vydra, K. Stulik and E. Julakowa, Inversionna Voltamperometria, Mir, Moscow, 1980, p. 226.
[2] Z. Komy, E. Roekens and R. Van Grieken, Anal. Chim. Acta, 204 (1988) 179.
[3] Ch. Yarnitsky and M. Ariel, J. Electroanal. Chem., 10 (1965) 110.
[4] M. Copanica and V. Stara, J. Electroanal. Chem., 127 (1981) 255.
[5] Z.L. Ermakova and V.V. Puzakov, Zvetni Metali, (1986) 25.
[6] A. Nelson and R.F.C. Matatoura, J. Electroanal. Chem., 164 (1984) 237.
[7] A. Nelson, Anal. Chim. Acta, 169 (1985) 273.
[8] B.E. Batley, Anal. Chim. Acta, 189 (1986) 371.
[9] C.M.G. van der Berg, Analyst, 114 (1989) 1527.
[10] C.M.G. van der Berg, J. Electroanal. Chem., 215 (1986) 111.
[11] T. Nedeltcheva, N. Elenkova, L. Costadinnova, M. Atanassova and K. Minnea, Hem. Ind., in press.
[12] S. Arpadjan, I. Karadjova, S. Alexandrov and D. Tsalev, Fresenius' Z. Anal. Chem., 320 (1985) 581.

ELSEVIER

Analytica Chimica Acta 291 (1994) 81–87

ANALYTICA CHIMICA ACTA

Mercury(II) acetate–Nafion modified electrode for anodic stripping voltammetry of lead and copper with flow-injection analysis

Ruelito R. Dalangin, Hari Gunasingham *

Department of Chemistry, National University of Singapore, Kent Ridge Crescent, 0511, Singapore

(Received 11th October 1993; revised manuscript received 22nd November 1993)

Abstract

A new method for the preparation of mercury film electrodes used in anodic stripping voltammetry is introduced. This method is simple, rapid and eliminates the need for a mercury plating step. In this alternative method, Hg^{2+} (as in mercury(II) acetate) is incorporated into a Nafion perfluorosulfonate formed on top of a glassy carbon electrode. When a negative potential is applied to the electrode, the Hg^{2+} is reduced to Hg^0 forming a three dimensional mercury film within a Nafion coating. The modified electrode is very stable in flowing solutions and has several advantages over a conventional preplated mercury film. The modified electrode was used to determine Pb^{2+} (0.07–2.8 $\mu g\ ml^{-1}$) and Cu^{2+} (0.5–2.3 $\mu g\ ml^{-1}$) in industrial effluents.

Key words: Flow injection; Anodic stripping voltammetry; Copper; Lead; Mercury(II) acetate–Nafion modified electrode

1. Introduction

Despite the development of many chemically modified electrodes over the past decade [1–12], there has been no perfect substitute for mercury electrodes – both hanging mercury and mercury film – for trace metal analysis using anodic stripping voltammetry. Its ability to form amalgams with metal ions during the preconcentration step [13] is unique.

Whereas other workers have used mercury films in conjunction with polymer modified glassy carbon electrodes, most, however, employed a preplated film. The mercury film was formed either before or after the polymer coating. For example, Wang and Hutchins-Kumar [14] placed a cellulose acetate film over a preplated mercury-film glassy carbon electrode. Hoyer et al. [15,16] preplated mercury onto a glassy carbon electrode that had been previously coated with Nafion. Stewart and Smart [17] coated a glassy carbon rotating disk electrode with a dialysis membrane and then plated it with a thin mercury film. Ge et al. [18] also used a preplated film to produce a polypyrrole-dispersed mercury film modified electrode. In most cases, the added polymer is mainly for circumventing organic in-

* Corresponding author.

SSDI 0003-2670(94)00026-I

terferences which are usually present in sample matrix.

In this work, another way of preparing a glassy carbon electrode with mercury film and Nafion coating is introduced. Here, mercury(II) acetate is incorporated into the Nafion perfluorosulfonate resin by mixing ethanolic solutions of the two. The mixture is then used to coat the newly polished glassy carbon surface. Because the mercury is already on the surface of the electrode within the Nafion framework, the use of mercury preplating solution is no longer needed. The exposure of the coated electrode surface to the supporting electrolyte in the electrochemical cell with the application of a negative potential reduces the mercury(II) ions to mercury atoms. This modified electrode is used in the determination of trace metals using flow-injection analysis with a wall-jet detector. With this electrode, the use of another pump to deliver the mercury plating solution as well as possible cross contamination due to the switching of solutions are eliminated.

2. Experimental

2.1. Instrumentation

A PAR Model 174A polarographic analyzer together with a PAR X–Y recorder (Model RE0089) was used for all voltammetric experiments. Analyses using atomic absorption spectrometry and inductively coupled plasma atomic emission spectrometry were carried out using a Shimadzu atomic absorption/flame emission spectrometer Model AA-670 and a Labtam inductively coupled spectrophotometer (Plasmascan 710), respectively. Scanning electron micrographs of the electrode surface were taken using a JEOL 100 CX II scanning transmission electron microscope with a LINK EDX and a JEOL T220 A scanning electron microscope. A Corning pH meter was used for pH measurements.

The wall-jet cell used in the experiment is made of Perspex with a geometric cell volume of about 4 ml and a jet-nozzle inside diameter of 0.3 mm. The working electrode was a 3-mm diameter glassy carbon disk (Tokai, Tokyo) embedded into a PTFE holder. The reference electrode was Ag–AgCl saturated with KCl. The graphite counter electrode was from Johnson Matthey. The wall-jet cell was connected in such a way that the outlet was at the highest point (at 45° elevation).

Peristaltic pumps (Eyela Model MP-3) with pulse dampers were used to deliver the supporting electrolyte and the mercury plating solution to the cell. The 0.5-ml loop was controlled by a pneumatically actuated six-port PTFE stream selector valve (Model 5701, Rheodyne). The switching of the delivery of sample and mercury plating solutions was controlled by a PTFE two-way switching valve. When the voltammetric analysis was done using the modified electrode, the pump for mercury plating solution was disconnected from the set-up. The differential pulse anodic stripping voltammetry (DPASV) experimental conditions with a wall-jet detector previously optimized by Gunasingham et al. [19] were employed: modulation amplitude, 50 mV; clock, 0.5 s; low pass filter time constant, 0.3 s.

2.2. Chemicals

50 ml of stock mercury(II) acetate solution (ca. 10 mg ml^{-1}) was prepared by dissolving the required amount of salt (extra pure, Merck) in absolute ethanol and acidifying it with 100 μl of concentrated acetic acid. Nafion in its solution form (5 wt.% solution in a mixture of lower aliphatic alcohols +10% water) was obtained from Aldrich (Catalog No. 27,470-4). Stock solutions (1000 $\mu g\ ml^{-1}$) of copper (Merck), lead (BDH) and mercury (BDH) in nitrate form were used to prepare the standard solutions. The supporting electrolyte, 0.1 M KNO_3–0.005 M HNO_3, was prepared from analytical grade reagents. It was purged with oxygen free nitrogen for at least 20 min prior to use.

Stock solutions of organic surfactants (1000 $\mu g\ ml^{-1}$) were prepared by dissolving the required amount in water. In the case of *n*-octanol, absolute ethanol (10%, v/v) was added to enhance dissolution.

The water used in all analysis was purified using a Millipore Milli-Q system.

2.3. Procedures

Preparation of the modified electrode

Using microliter pipets, required volumes of stock mercury(II) acetate and Nafion solutions were mixed in a vial with a screw cap. The mixture was sonicated in an ultrasonic bath for 5 min to produce a homogeneous mixture. 5 μl of this stock mixture was used to coat the newly polished glassy carbon electrode. The coating was allowed to dry gradually without a flow of air (inside an inverted 1000-ml beaker) at room temperature for at least 20 min.

Flow-injection analysis

At the beginning of each experiment with the modified electrode, the wall-jet cell was filled with supporting electrolyte using a moderately low flow rate (ca. 1.2 ml min^{-1}). As soon as all the three electrodes were submerged in the electrolyte, the pump was switched off and a potential of -1.0 V was applied for 5 min. Afterwards, the electrolyte was allowed to flow again using a moderately fast flow rate (ca. 1.5 ml min^{-1}) while holding the potentials at 0.0 V for 2 min. The electrode was then ready for analysis.

The 0.5 ml sample was delivered to the cell for 45 s and a hold time of 15 s was observed before stripping the metals in stationary solution at 20 mV s^{-1}. The cell was flushed with the supporting electrolyte for 2.5 min before the injection of the next sample to avoid possible cross-contamination.

For studies using preplated films, the mercury film was obtained by electrodeposition of 40 μg ml^{-1} Hg^{2+} using a flow rate of about 2.0 ml min^{-1} for 5 min and a deposition potentials of -1.0 V.

3. Results and discussion

Initial studies using the above-mentioned method were carried out by coating the glassy carbon surface with a mixture of 60% (v/v) Nafion stock solution and 40% (v/v) mercury(II) acetate solution. At this ratio, the actual concentration of Nafion is about 3% (w/v) which is very much thicker than that reported by Hoyer et al. [15].

Even if the evaporation of the 5 μl coating mixture on the glassy carbon surface was done inside an inverted 1000-ml beaker (to avoid contamination with dust particles in air), within 20 min the electrode was found to be dry with a very transparent coating. Under the scanning electron microscope, the dry coating appeared to be homogeneous. The mapping of the electrode surface for Hg using a scanning electron microscope with an x-ray microanalyzer shows that mercury (II) ions are well dispersed. This means that mercury(II) acetate is well dispersed within the Nafion matrix.

In some cases, cracks were also found in the coating which extends down to the glassy carbon, but the exposed surface is very small compared to the coated part and this does not affect the voltammetric peaks, as previously noted [15].

When the coated surface gets in contact with the supporting electrolyte, the supporting electrolyte diffuses into the coating and hydrolyses the mercury ions suspended in the Nafion framework. Stopping the flow of the supporting electrolyte and the immediate application of a negative potential prevents the migration of the Hg^{2+} ions away from the glassy carbon surface resulting in the formation of mercury film. Although the dissolution/reduction process was held for 5 min in most experiments, it was found that 1 min was sufficient to obtain good voltammetric signals.

3.1. Effect of mercury loading

The effect of mercury loading on the stripping peaks of lead and copper was studied by decreasing the volume of the stock mercury(II) acetate solution in the coating solution (from 40%, v/v). The volume of Nafion stock solution was held constant (at 60%, v/v) of the coating solution) while the remaining volume was compensated by adding absolute ethanol.

Although the peak currents of the metals vary from one electrode to another using the same

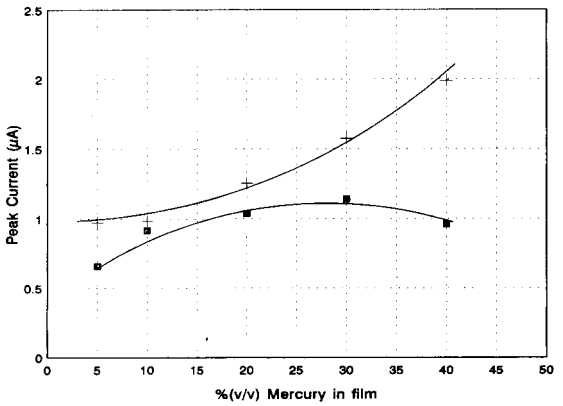

Fig. 1. Effect of Hg loading on peak currents of (■) lead and (+) copper. $[Pb^{+2}] = 4.83 \times 10^{-7}$ M, $[Cu^{+2}] = 1.57 \times 10^{-6}$ M; Deposition flow rate = 1.52 ml min^{-1}. Nafion loading = 60% (v/v) of stock solution. Deposition potentials for Pb and Cu = −1.0 V.

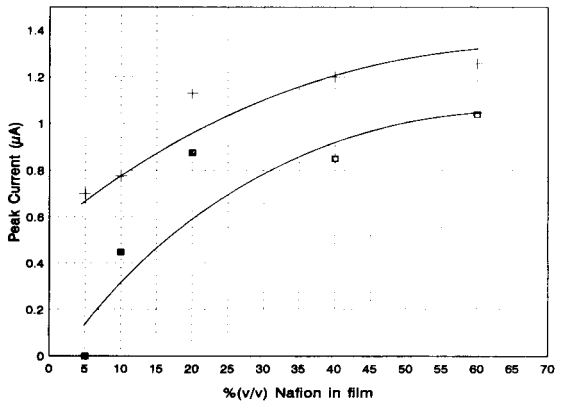

Fig. 2. Effect of Nafion loading on peak currents of (■) lead and (+) copper. Same experimental conditions as Fig. 1. Hg loading = 20% (v/v) of stock solution.

coating solution, the general trend of the peaks is a decline as the concentration of mercury in the coating solution decreases. The effect is greater for copper peaks than for lead peaks as shown in Fig. 1. At high mercury loadings (40%), however, it was noticed that white precipitates are formed when the coating solution was stored for some days. Thus, a lower mercury loading (30 or 20%) was used for the remaining experiments.

3.2. Effect of Nafion loading

The dependency of peak currents on the amount of Nafion present was determined by varying the volume of the Nafion stock solution in the coating mixture while holding the mercury concentration at 20% (v/v). In general, decreasing the Nafion concentration in the coating mixture beyond 20% (v/v) resulted in a decline in the stripping peaks of both metals (Fig. 2). The background current was also observed to be very high at low Nafion thickness (especially at 5 and 10%). Also, at the latter condition cracks were more evident and the previously transparent film became cloudy due to the precipitation of mercury(II) acetate on the glassy carbon surface. Except for the first two highest Nafion coating mixture, precipitates occurred when the coating mixtures are kept for several days.

3.3. Effect of pH

pH greatly affects the stripping peaks of lead and copper using the modified film. In this study, the pH of the sample solution was adjusted by adding volumes of 0.1 M NaOH to the sample solution. Fig. 3 shows similar effects for both lead and copper. This decreasing trend is related to the fact that these metals form insoluble hydroxides.

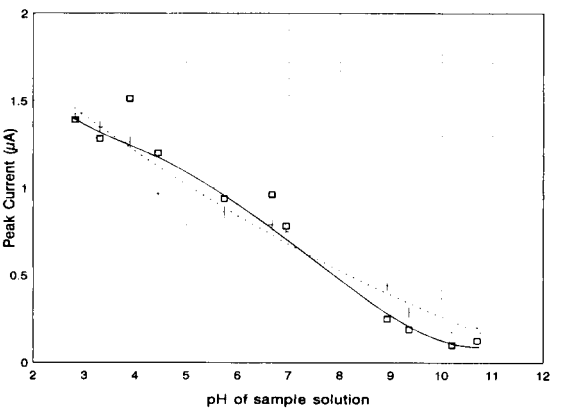

Fig. 3. Effect of pH using Hg incorporated film for (■) lead and (+) copper. Same experimental conditions as Fig. 1 with Hg loading = 30% (v/v) of stock solution.

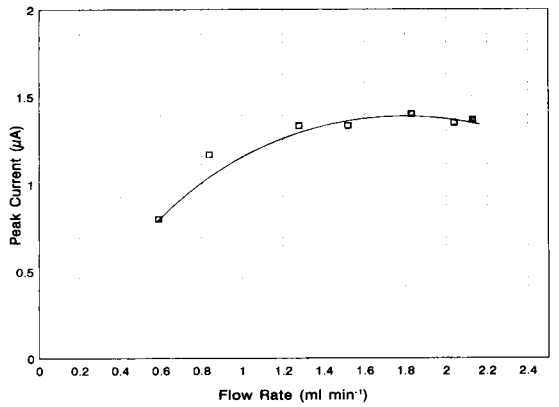

Fig. 4. Effect of deposition flow rate on the stripping peaks of (■) lead. $[Pb^{+2}] = 4.826 \times 10^{-7}$ M; Deposition flow rate = 1.52 ml min^{-1}. Hg loading = 30% (v/v) of stock solution. Nafion loading = 60% (v/v) of stock solution. Deposition potentials for Pb = −1.0 V.

3.4. Effect of flow rate

The effect of deposition flow rate on the stripping peak current of lead using the modified electrode is shown in Fig. 4. The peak height increases reaching a limiting value at about 1.7 ml min^{-1}.

3.5. Effect of electrode-inlet distance

Though the equation for the limiting current using a wall-jet detector does not include the inlet-electrode distance, a significant dependency exists between the two [20–22]. Fig. 5 shows that the peak heights for both metals decreased as the electrode gets closer to the inlet nozzle. When the distance is between 2–4 mm, the peak heights are constant. Increasing the distance further decreases the peak currents due to the break-up of the jet.

3.6. Effect of organic surfactants

As previously mentioned, one of the main reasons for modifying the mercury film electrode is to minimize, if not eliminate, organic interferences. In this study, the effects of different surfactants with concentrations ranging from 1 μg ml^{-1} to 100 μg ml^{-1} on the stripping peak currents of lead and copper were observed. Each of the five surfactants chosen was studied using newly prepared modified electrode. Blank sample solution (without the surfactant) was injected at the beginning and at the end of the analysis to see if there is electrode surface deterioration. The results were compared to those obtained using a preplated film under the same experimental conditions. Each sample solution was injected three times in increasing surfactant concentration. Values were reported as the ratio of the average peak current of the sample solution (i_p) to the average peak current of the blank sample solution obtained before the analysis (i_o).

From the results in Table 1, it can be seen that for the modified electrode, the presence of gelatin, *n*-octanol and sodium dodecyl sulfate in the sample solution did not suppress the lead stripping peaks but even gave higher peaks than the blank sample peaks in certain cases. For the preplated film, a decreasing trend was observed with increasing concentration of these surfactants. In the presence of 50 μg ml^{-1} and 100 μg ml^{-1} Triton X-100, the lead peak was completely suppressed when a bare mercury film electrode (MFE) is used. A gradual decline, however, was observed for the modified electrode. In the case of solutions containing with albumin, the preplated film gave better results for lead than the modified electrode.

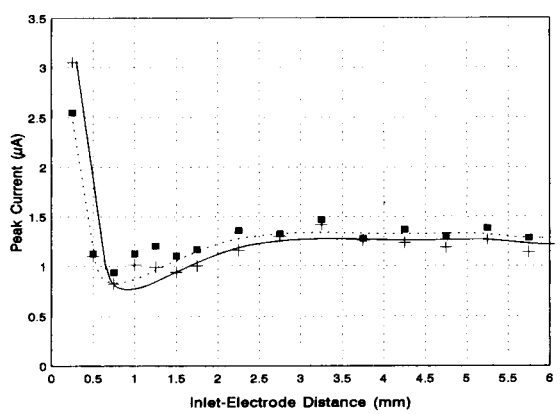

Fig. 5. Effect of inlet-electrode distance on the stripping peaks of (■) lead and (+) copper. Same conditions as Fig. 3.

Table 1
Effect of organic surfactants

$\mu g\ ml^{-1}$	Lead		Copper	
	MFE (i_p/i_o)	MNME (i_p/i_o)	MFE (i_p/i_o)	MNME (i_p/i_o)
Gelatin				
1	1.065	0.989	1.078	0.894
5	0.931	0.970	0.989	0.829
10	0.750	1.128	0.820	0.887
50	0.655	1.030	0.506	0.887
100	0.576	0.970	0.449	0.469
blank	0.678	1.039	0.829	0.599
n-Octanol				
1	0.991	1.035	0.985	0.952
5	0.946	1.067	0.779	0.869
10	0.893	1.123	0.705	0.857
50	0.812	1.147	0.627	0.809
100	0.723	1.140	0.561	0.714
blank	0.812	1.182	0.731	0.920
Sodium dodecyl sulfate				
1	1.012	1.107	1.136	1.088
5	0.868	1.079	0.964	1.003
10	0.776	1.073	0.854	0.784
50	0.615	1.045	0.869	0.859
100	0.539	0.949	0.734	0.818
blank	0.767	1.169	0.771	0.825
Triton X-100				
1	1.041	0.885	0.883	0.770
5	0.537	0.882	0.532	0.653
10	0.454	0.868	0.500	0.653
50	0.000	0.700	0.494	0.643
100	0.000	0.488	0.352	0.570
blank	0.361	0.499	0.486	0.660
Albumin				
1	0.858	0.855	0.616	0.761
5	0.764	0.885	0.384	0.779
10	0.663	0.548	0.270	0.303
50	0.639	0.327	0.285	0.225
100	0.651	0.272	0.316	0.084
blank	0.764	0.378	0.487	0.122

MFE = Mercury film electrode. MNME = Mercury (incorporated into/) Nafion modified electrode. i_p = Average peak current of sample solution. i_o = Average peak current of blank solution (without surfactant). Hg plating flow rate = 2.24 ml min^{-1}. Hg deposition potentials = −1.0 V. Other experimental conditions as Fig. 5. See text.

For copper, the voltammetric signals obtained using the modified electrode were also better than the ones obtained using the preplated MFE except for solutions with high concentrations of albumin.

From the peak currents obtained for the blank sample solution after the analysis, it is of interest to note that the modified electrodes show a memory effect after the injections of high concentrations of Triton X-100 and albumin.

3.7. Reproducibility

The reproducibility of the peak currents for 55 successive injections of 4.83×10^{-7} M Pb^{2+} and 1.57×10^{-6} M Cu^{2+} using the modified film gave average peak currents of 1.43 μA (R.S.D. = 7.16%) and 1.45 μA (R.S.D. = 8.10%), respectively.

3.8. Limit of detection

The limit of detection (c_L) was calculated using the IUPAC model [23] with $k = 3$. The simultaneous determination of lead and copper from 0.10 $\mu g\ ml^{-1}$ to 1.0 $\mu g\ ml^{-1}$ ($n = 4$) using the experimental conditions (60% Nafion and 30% Hg loadings, 0.50 ml sample volume loop) yielded calibration plots with the following regression equations: for lead, $Y(\mu A) = 12.53X(\mu g\ ml^{-1}) - 0.22$ with $r = 0.9995$ and for copper, $Y(\mu A) = 13.01X(\mu g\ ml^{-1}) + 0.06$ with $r = 0.9995$. 13 successive determinations of the blank solution resulted in $s_B = 0.021$ and $s_B = 0.017$ μA for lead and copper signals, respectively. Hence, $c_L = 5$ ng ml^{-1} for lead and $c_L = 4$ ng ml^{-1} for copper. Using a similar approach, the limits of detection for lead and copper using a conventional MFE were found to be 3 and 2 ng ml^{-1}, respectively. In the latter case, the MFE was obtained by electrodeposition of 40.0 $\mu g\ ml^{-1}$ Hg^{+2} at −1.0 V for 5 min using a flow rate of 2.5 ml min^{-1}.

3.9. Analysis of industrial effluents

The suitability of the mercury(II) acetate–Nafion modified electrode for real analysis was demonstrated by using it for the determination of lead and copper in waste water samples from a plating bath. After collection, the only pretreatment steps done on the samples were filtration and acidification by adding 0.05 M HNO_3 (10%, v/v). Results are compared with those obtained using flame atomic absorption spectrometry

Table 2
Comparison of results for the determination of Pb and Cu on waste water samples (Experimental conditions as in Table 1)

	ICP ($\mu g\ ml^{-1}$)	AAS ($\mu g\ ml^{-1}$)	MFE ($\mu g\ ml^{-1}$)	MNME ($\mu g\ ml^{-1}$)
Lead				
S1	0.185	0.019	0.137	0.175
S2	0.077	nd[a]	0.065	0.070
S3	0.073	nd	0.062	0.070
S4	0.186	0.177	0.100	0.129
S5	0.275	0.212	0.090	0.135
Copper				
S1	2.025	1.990	1.202	2.374
S2	0.531	0.522	0.171	0.389
S3	1.323	1.708	0.821	1.360
S4	2.331	2.412	0.925	2.248
S5	1.521	1.618	1.045	1.595

[a] nd = not detected.

(FAAS), inductively coupled plasma atomic emission spectrometry (ICP-AES) and ASV with a preplated Hg film (MFE). For all these methods, the concentrations were obtained using calibration plots. Table 2 summarizes the results obtained using these four techniques. Only one analysis was carried out for each spectroscopic technique while the average of peak currents of three consecutive injections was used for ASV determinations.

Aside from the fact that the values obtained using the modified electrode are higher than that of preplated film, the results using the former technique are very close to those obtained using ICP-AES. Flame AAS results for Pb at low concentrations were inconsistent, as can be seen from Table 2. Thus the accuracy of the ASV technique can be greatly improved if the modified electrode is used rather than the conventional mercury film electrode.

Acknowledgements

We are grateful for the Research Studentship granted by the National University of Singapore to R.R. Dalangin. The technical assistance of Madam Loy of the Department of Zoology and Mr. Christopher Tan Tzy Yung of the Department of Chemistry is also acknowledged.

References

[1] H. Gunasingham and R.R. Dalangin, Anal. Chim. Acta, 246 (1991) 309.
[2] J. Wang, B. Greene and C. Morgan, Anal. Chim. Acta, 158 (1984) 15.
[3] J. Wang and M. Bonakdar, Talanta, 35 (1988) 277.
[4] P. Li, Z. Gao, Y. Xu, G. Wang and Z. Zhao, Anal. Chim. Acta, 229 (1990) 213.
[5] S. Tanaka and H. Yoshida, Talanta, 36 (1989) 1044.
[6] Z. Gao, P. Li, S. Dong and Z. Zhao, Anal. Chim. Acta, 232 (1990) 367.
[7] S.V. Prabhu, R.P. Baldwin and L. Kryger, Anal. Chem., 59 (1987) 1074.
[8] R.P. Baldwin, J.K. Christensen and L. Kryger, Anal. Chem., 58 (1986) 1790.
[9] Z. Gao, P. Li, G. Wang and Z. Zhao, Anal. Chim. Acta, 241 (1990) 137.
[10] S. Dong and Y. Wang, Fenxi Huaxue, 16 (1988) 216.
[11] S. Dong and Y. Wang, Anal. Chim. Acta, 212 (1988) 341.
[12] S. Dong and Y. Wang, Talanta, 35 (1988) 819.
[13] J. Wang, Stripping Analysis: Principles, Instrumentations and Applications, VCH, Deerfield Beach, FL, 1985.
[14] J. Wang and L.D. Hutchins-Kumar, Anal. Chem., 58 (1986) 402.
[15] B. Hoyer, T.M. Florence and G.E. Batley, Anal. Chem., 59 (1987) 1608.
[16] B. Hoyer and T.M. Florence, Anal. Chem., 59 (1987) 2839.
[17] E.E. Stewart and R.B. Smart, Anal. Chem., 1984 (56) 1131.
[18] H. Ge, H. Zhao and G.G. Wallace, Anal. Chim. Acta, 238 (1990) 345.
[19] H. Gunasingham, K.P. Ang, C.C. Ngo and P.C. Thiak, Anal. Chim. Acta, 198 (1986) 27.
[20] W.J. Albery and C.M.A. Brett, J. Electroanal. Chem. Interfacial Electrochem., 148 (1983) 211.
[21] C.C. Ngo, Ph.D. Thesis, National University of Singapore, 1985.
[22] H. Gunasingham and B. Fleet, Anal. Chem., 55 (1983) 1409.
[23] J.D. Winefordner and G.L. Long, Anal. Chem., 55 (1983) 712A.

ELSEVIER

Analytica Chimica Acta 291 (1994) 89–105

ANALYTICA CHIMICA ACTA

Review

Vapour generation atomic absorption spectrometry

Xiu-Ping Yan *, Zhe-Ming Ni

Research Centre for Eco-Environmetal Sciences, Academia Sinica, P.O. Box 2871, Beijing 100085, China

(Received 22nd February 1993)

Abstract

Vapour generation atomic absorption spectrometry has been systematically described as a technique for the determination of trace elements, including hydride generation, cold vapour generation and other chemical vapour generation AAS. Emphasis has been placed on the principle, instrumentation and applications of hydride generation AAS. Recent advances in other vapour generation techniques are also reviewed.

Key words: Atomic absorption spectrometry; Hydride generation; Review; Speciation; Trace metals; Vapour generation

1. Introduction

Vapour generation atomic absorption spectrometry (VG-AAS) is a technique for the determination of trace elements that provides an ideal sample introduction procedure in the gas phase for atomic absorption spectrometry. It has been applied to the determination of trace elements in a wide range of matrices. Its popularity arises from the following advantages: separation of the analyte from the matrix leads to good accuracy in many instances; high efficiency of sample introduction results in very good sensitivity; a large sample volume can be used and yields excellent relative detection limits; the method can easily be automated; and chemical speciation determination is possible in some instances.

There are several vapour generation methods. The hydride generation technique is the most widely used and is typical of gas-phase sample introduction methods for AAS. Cold mercury vapour generation is also widely used to determine traces of mercury in various samples [1–5]. Attempts to generate volatile compounds of other elements that do not form volatile hydrides may be expected in the future, as has already been done with the generation of nickel carbonyl [6–8], volatile metal chelates [9–13], gaseous fluorides [10–13], chlorides [14–17] and oxides [18,19].

2. Hydride generation

Hydride generation AAS (HG-AAS) was introduced around 1970 [20–22] to overcome problems associated with the flame AAS determination of arsenic and selenium. Now the determinations have been extended to include As, Bi, Ge, Pb, Sn, Sb, Te, Se and even Tl and In [23–27]. The hydrides of the first six elements are usually called arsine, bismuthine, germane, plumbane,

* Corresponding author.

SSDI 0003-2670(93)E0671-S

Table 1
Physical properties of covalent hydrides of practical analytical importance

Element	Hydride	ΔH_f^0 at 25°C (kcal mol^{-1})	M.p. (°C)	B.p. (°C)
As	AsH_3	15.9	−116.9	−62.5
Bi	BiH_3	66.4		−22
Ge	GeH_4	21.6	−165.9	−88.5
Pb	PbH_4	59.7		−13
Sb	SbH_3	34.7	−88	−18.4
Se	H_2Se	20.5	−65.7	−41.3
Sn	SnH_4	38.9	−150	−51.8
Te	H_2Te	36.9	−51	−2.3

stannane and stibine, respectively. Table 1 gives some physical properties of the hydride-forming elements [24].

The basic design of a hydride generation system, with subsequent AAS detection, may conveniently be considered as four steps [23]: First, generation of the hydride; second, collection of the hydride (if necessary); third, transfer of the hydride; and fourth, atomization of the hydride. In order to increase the signal it is necessary to generate the hydride quickly or to collect it and then transfer it as quickly as possible to the atomizer. This minimizes dilution of the hydride by the carrier gas.

3. Reagents

Several reagents have been used to convert the analyte element into its hydride for analytical purposes. In most of the early work, a metal–acid reducing system was employed, such as $SnCl_2$–HCl–KI–Zn and $TiCl_3$–HCl–Mg [23,24]. However, the most convenient and currently almost exclusively used method is the $NaBH_4$–acid system. Reduction is effected according to the following equation:

$$NaBH_4 + 3H_2O + HCl \longrightarrow H_3BO_3 + NaCl + 8H \xrightarrow{E^{m+}} EH_n + H_2 \text{ (excess)} \quad (1)$$

where E is the analyte of interest and m may or may not equal n. The solid $NaBH_4$ in pelletized form was initially favoured but introduction of a solid into a reaction gives undesirable highly localized reagent concentrations. A freshly prepared solution of $NaBH_4$ is more efficient and now preferred and also is the obvious reagent for continuous-flow systems. The concentration of $NaBH_4$ must be optimized for the particular analyte element and for the equipment concerned. A variety of $NaBH_4$ concentrations are recommended, usually 0.5–10% aqueous solutions stabilized by 0.1–2% KOH or NaOH [24].

In the $NaBH_4$–acid system, hydrochloric acid is most often used, although sulphuric and nitric acid are equally suitable in some instances. The optimum acidity ranges appear to be dependent on the element of interest and the type of hydride generators, and were reported to be 1–9 M for As, Bi and Sb, 0.1–3 M for Ge, 0.1–0.2 M for Pb and Sn, 2.5–5 M for Se, 2.5–3.6 M for Te, 1–3 M for In and 1–1.5 M for Tl [24–29]. Some organic acids such as tartaric, malic and oxalic acid or acetate buffer solutions [24] can also be employed as an alternative to hydrochloric acid in the determination of Ge, Pb and Sn. For the generation of plumbane, to achieve high sensitivity, some oxidizing reagents should be used to convert Pb(II) in the sample solution into Pb(IV), such as $K_2Cr_2O_7$, $(NH_4)_2S_2O_8$, H_2O_2, $Ce(SO_4)_2$, $KMnO_4$ or $Ce(NH_4)_2(NO_3)_6$ [28,30] before hydride generation. Hydrides of Sb, Pb and Sn were even released from non-aqueous media acidified with sulphuric acid [31–33].

The rapid reaction between sodium tetrahydroborate and hydrochloric acid may generate a troublesome foam, particularly when undigested biological fluids such as urine or blood plasma are being analysed. In these instances the addition of an antifoaming compound such as Antifoam 110A Emulsion is useful [34].

4. Instrumentation

One of the attractions of the original hydride generation method is the simplicity of the equipment, which allows the method to be used with a conventional atomic absorption spectrometer. Subsequently, the design of most apparatus has undergone modification to automate the system,

to facilitate the addition of reagents, to decrease the duration of analysis, to diminish errors due to numerous manipulations in the course of the analysis and to overcome interferences.

There are three variations of the batch-type operation. In its simple form, the generated hydride and hydrogen are transported immediately into the atomizer, normally in a carrier gas. In equipment of the "stopped-flow" type [35], the sweep of the hydride from the reaction vessel is delayed for a few seconds to allow the generation reaction to proceed to completion, but inherent instability of the hydride must be taken into consideration when this technique is contemplated. Others use a low-temperature trapping device to concentrate the hydride so that it may be transported to the atomizer without dilution with the large volume of generated hydrogen [36].

In continuous-flow equipment both sample solution and borohydride solution are delivered continously at a constant rate to the generator using a peristaltic pump. This type of equipment has been used for hydride generation both with [37] and without [38] air segmentation and the hydride has been separated with conventional gas–liquid separators [37] or by membrane separation [39]. These systems have the advantages of intimate mixing of reagents with better pH control and also they appear to be much more tolerant of elements that normally interfere in the hydride generation. Moreover, they usually have a lower detection limit than batch systems. A special gas–liquid separator was designed for an automated system in which sample, acid and sodium tetrahydroborate(III) are mixed continuously using a peristaltic pump [38]. This method has been shown to tolerate nitric acid in the sample digest system when applied to the determination of As and Se in a variety of matrices [40], and to give good analyte recoveries in the presence of many metals that normally interfere in the hydride generation. An oblique section hydride generator has been developed [41,42], in which the sample solution and borohydride solution are conveyed by the peristaltic pump through two separate polyethylene tubes, while the mixing and reaction of these solution and the separation of gaseous hydrides and liquid are accomplished simultaneously in the oblique section. There is no mixing tube, which was widely used in the conventional hydride generator.

In a flow-injection system, acid and $NaBH_4$ solutions flow continuously at a constant rate into the generator and a limited volume of sample is injected into the acid stream. Use of the very successful and readily available flow-injection type of equipment has led to methods in which discrete sample are introduced repeatedly with a resultant transition signal. Flow-injection techniques have been shown to be capable of significantly enhancing the performance of HG-AAS by providing higher sample throughputs, better selectivities, higher absolute sensitivities and large savings in reagent consumption [43,44].

5. Hydride transportation

The hydride evolved has been transferred in two principal ways: either the hydride is conveyed directly into the atomizer as it is generated, or some form of storage is used before the transfer to the atomizer. In the latter mode, the hydride is collected in a collection device until the evolution is completed and then is transported to the atomizer all at once.

The generated hydride has been collected in a closed vessel under pressure (pressure collection) [23,24,45–49], in a U-tube immersed in liquid nitrogen [23,24,50–62] through which hydrogen passes freely and is not collected (cold-trap collection) and in an absorbing solution of silver nitrate [63–65], mercury(II) chloride–sulphuric acid–potassium permanganate [66], silver diethyldithiocarbamate–ephedrine [67], potassium iodide and iodine [68–70], cerium(IV) and potassium iodide [71,72] or iodine [73] and subsequently determined by AAS.

Several direct transfer methods are currently employed: the continuous-flow mode [23,24,38, 74–83], the flow-injection mode [74,84–89] and the batch mode [31,32,60,74,90–104]. With the batch mode, a limited volume of sample is reduced all at once.

Hydride stability is of primary importance for choosing the transfer method. Collection meth-

ods, namely the pressure collection and cold-trap collection with closed system heating, cannot be used for unstable hydrides. However, the collection step is expected to eliminate the possible influence of the hydride generation kinetics.

6. Hydride atomization

The following atomizer have been used in HG-AAS.

6.1. Flames

Holak [20] used a conventional air–acetylene flame supported on a three-slot Boling burner. The air–acetylene flame was used by many workers in the early stages of the development of the technique, but it was soon replaced by the argon–hydrogen–entrained air flame (usually called the argon–hydrogen diffusion flame) [23].

The use of an argon–hydrogen diffusion flame for the determination of arsenic in aqueous solution was first described by Kahn and Schallis [105]. Dalton and Malanoski [22] introduced arsenic directly into the argon–hydrogen flame and Fernandez and Manning [21] collected arsine in a balloon before releasing arsine into argon–hydride flame. Since then, this relatively cool and low-background flame supported on a conventional slot burner has been used by many workers, as has the nitrogen–hydrogen flame [24].

It should be noted that diffusion flames were used mainly in the past, and they are inferior to the other atomizers. The sensitivity is lower owing to the pronounced dilution of hydride with flame gases. The flame also has a high background absorption and its flicker noise adversely affects the limit of detection. As a result, diffusion flames have not often been employed in recent years [74,82].

6.2. Flame-in-tube atomizers

Flame-in-tube atomizers are most often externally unheated quartz tubes with a flame burning inside. This type of atomizer, in which the excess hydrogen generated was used to carry the released hydride to a T-shaped quartz tube and a small amount of oxygen was added to support combustion and atomization of the hydride, was first described by Siemer and Hagemann [106]. Their design, combined with an oxygen–hydrogen flame [98,107] or air–hydrogen flame [50,54,108], has subsequently been adopted either without change [74,98,109,110] or with some modifications [54,58,59,61,111–116]. Nakashima [117] modified the flame-in-tube atomizer in which a long absorption tube, aligned in the optical path, was used as an extension of a Beckman burner with argon (or nitrogen)–air–hydrogen flame. The Dedina flame-in-tube atomizer [74] consists of two parts: an intake part and a T-tube, both made of quartz, connected by a standard joint.

6.3. Externally heated quartz tubes

The earliest reported use of an electrically heated or a flame heated quartz tube for hydride atomization was by Chu et al. in 1972 [118] and Thompson and Thomerson in 1974 [119], respectively. Since then, externally heated quartz tubes have become the most commonly used atomizers [23,24,74].

The design is usually very similar to the flame-in-tube atomizer, consisting of a T-tube with its bar-tube aligned in the optical path and the central arm of the T serving for delivery of hydrides carried by a flow of gas from a generator. The bar-tube is heated either by a chemical flame or, more often and more conveniently electrically, either by a resisitance wire wound around it or by a tailored furnace. The two outlets of the bar tube are either open or closed with optical windows. If closed, two outlet arms are fused to the bar-tube near its end. To prevent ignition of hydrogen at the ends of the open-ended system, which leads noisy signals, an auxiliary inert gas stream can be injected into a pair of auxiliary inlets [23,45,46,60,119]. The other way to prevent ignition is to leave the ends of the tube unheated and uninsulated [85,89] or even to provide them with graphite rings [120,121].

Oxygen or air is often introduced into the atomizer mainly because of the beneficial effect on sensitivity. For optimum sensitivity, there is a

need for a minimum oxygen concentration which depends on, apart from the hydride identity, temperature: the higher the temperature, the lower is the oxygen concentration needed. At lower temperatures oxygen present in the system as a contaminant may not be sufficient for optimum sensitivity and thus additional extra oxygen may be required [74].

There is a marked effect of the quality of the inner quartz surface on sensitivity [89,91,120,122–128], most often manifesting itself as a gradual deterioration of sensitivity and/or precision. Optimum performance is most conveniently kept by rinsing the tube in 40% hydrofluoric acid. Grinding the inner atomizer surface with alumina has also been employed [129].

Compared with flame atomizers, externally heated quartz tubes have the following advantages: the flame background is virtually eliminated and better sensitivity is achieved owing to the longer residence time of the atom cloud in the optical path, the lower dilution and the much lower noise levels.

6.4. Graphite furnace atomizers

The first report on the use of the graphite furnace atomizer for atomization of hydrides was by Knudson and Christian in 1974 [130]. Since then, atomization of hydrides in a heated graphite furnace has been carried out by other workers [23,24,74]. There are two approaches to using graphite furnaces: on-line atomization and in situ trapping of hydrides in the furnace.

The on-line atomization approach utilizes a direct transfer of the hydride from the generator to the furnace, which is preheated to a temperature usually over 2200°C [36,58,59,62,74,131–143]. Although the continuous-flow generation of hydrides was recently shown to work in connection with graphite furnaces, batch or cold-trap collection methods have so far invariably been applied [74,144].

The generated hydrides are almost exclusively introduced to the internal gas line of commercial furnaces. This method is simple but the hydride can be captured on cooler metal or graphite parts. A similar drawback, hydride capture in the connecting tube, can result from introduction of hydrides to the sampling port of the graphite furnace by a sealed graphite tube [132,141]. There is a viable alternative for introducing hydrides to the furnace using a quartz tube interfaced to the sampling port, which does not retain hydrides and can withstand temperatures above 2300°C, for a reasonable time, if cooled by a gas flow [144].

Naturally, the sensitivity for on-line atomization is generally lower than with in situ trapping. It is also lower than in quartz tube atomizers as the small dimensions of commercial graphite furnaces and their high atomization temperatures decrease the residence time of free analyte atoms and subsequently the sensitivity [74].

The in situ trapping technique uses the graphite furnace as both the hydride trapping medium and the atomization cell. The hydride purged from the generator is trapped in the preheated graphite furnace, usually in the range 300–600°C, until the evolution of hydride is completed. The trapped analyte is subsequently atomized at temperatures generally over 2200°C. This technique has been shown to enhance the sensitivity significantly and to eliminate effectively the possible influence of the hydride generation kinetics on the signal shape. The first use of this technique was reported by Lee [145]. Since then, work on the determination of As [41,146–153], Bi [139,152,154–157], Sb [41,152,154–158], Se [41, 147,150–152,159,160], Sn [145,150–152,156,161] Te [152,157,162], Pb [28,150,163,164] and Ge [152,157] has been published.

The nature of the graphite tube is expected to affect greatly the efficiency of hydride adsorption. It has been shown that the efficiency of adsorption increases in the order new normal graphite tubes < old pyrolytic graphite tubes < old normal graphite tubes [163]. The trapping efficiency on a conventional graphite tube has been shown to be relatively low, less than 72% for bismuthine [145] and only 24% for arsine [153]. The use of a palladium-coated graphite tube for the adsorption of hydrides has been shown to improve the sensitivity and precision significantly [41,151,152, 157]. Similar results has been obtained with the use of a Zr-coated graphite tube as both the

trapping medium and the atomization cell for the hydrides of lead [28] and tin [161].

Interfacing of the hydride generator is critical for the proper functioning of an in situ trapping apparatus. Generated hydrides are introduced either via the internal gas line of commercial furnaces [147,149,158,162] or to the sample port of the graphite tube through an interface made of graphite [145], quartz [28,41,146,147,159] or PTFE [163]. Graphite interfaces are apt to capture hydride partially during the trapping stage, leading to a relatively low overall efficiency. Similar difficulties can be encountered with hydrides introduced into the internal gas line, because there the hydride comes into contact with metal components with graphite tube ends and with graphite cylinders, which are cold during both the trapping and the atomization stages. The PTFE device used to connect the transport tube to the furnace begins to deteriorate at 600°C and cannot withstand higher temperatures [163].

7. Interferences and their eliminations

The interferences associated with HG-AAS may be conveniently divided into three groups: spectral interferences, liquid-phase interferences and gas-phase interferences.

7.1. Spectral interferences

Spectral interferences are usually insignificant in this technique owing to the separation of the analyte from the matrix. Only background absorption can occur, most often in diffusion flame atomization owing to changes in the flame transparency that may take place when hydride is purged into the flame. The structured absorbance by molecular oxygen has been shown to be responsible for the well known background absorption by oxygen on the selenium 196-nm line [165]. The background interference by hydrides of arsenic, antimony and tin on the selenium 196-nm line is pronounced in the flame-in-tube atomizer [106,111]. Even so, background correction is usually considered unnecessary for externally heated quartz tube atomization [78,91,93,120] and also for in situ trapping and on-line atomization in the graphite furnace [138,145,162]. However, in a significant number of studies background correction has been employed, most often in connection with flame-in-tube or graphite furnace atomization [74].

7.2. Liquid-phase interferences

Liquid-phase interferences can occur in the liquid phase either during hydride formation or its transfer from the solution due to changes in the hydride release rate (release kinetic interferences) and/or decrease in hydride release efficiency (release efficiency interferences). In general, there are numerous interferences in the liquid phase but all can be divided into two basic groups: compound interferences and matrix interferences [74].

Compound interferences may arise if the oxidation state or chemical environment of the analyte in the sample is not the same as in the standard solution employed owing to the different rates of hydride formation. It is well known that arsenic, antimony, selenium and tellurium each commonly exist in solution in two oxidation states: As(III) and As(V), Sb(III) and Sb(V), Se(IV) and Se(VI) and Te(IV) and Te(VI). Even when using $NaBH_4$ reaction, the effect of the oxidation state of the elements in the sample on the rate of hydride formation has been observed. In order to determine the total concentration for arsenic and antimony, potassium iodide has been employed as a prereductant [54,88,166–170]. Additionally, NaI [171,172], KBr [173,174] and a mixture of KI and ascorbic acid [140,175,176] have been used as prereductants in the determination of As and Sb. For selenium, a prereduction with KBr [45,54], $SnCl_2$ [177] or by boiling the sample in 4–5 M HCl [51,57,61,178–180] has been performed to determine the total selenium. Similarly, Te(VI) could be prereduced to Te(IV) by boiling the sample in 2–6 M HCl for 10–20 min during sample preparation [69,162]. Since many hydride-forming elements in environmental and biological samples exist in various organic forms, it is necessary to decompose organic bonds of the analyte completely during sample pretreatment for determination of the total analyte.

Compound interferences should be eliminated when only the total analyte concentration in the sample is required to be determined. However, they are useful for chemical speciation determination. For example, selective determinations of As(III) and As(V) [37,168,169], Sb(III) and Sb(V) [37,54,55], Se(IV) and Se(VI) [51,61], and Te(IV) and Te(VI) [162] can be carried out by measuring their total amount after prereduction of their higher to the lower oxidation states and separately by hydride generation of the lower oxidation state alone without any prereduction step. Determinations of various organic forms of hydride-forming elements in environmental and biological samples can also be performed. The procedure involves generating inorganic and organic hydrides of the element concerned with sodium tetrahydroborate and collection of the hydrides in a liquid nitrogen trap. Subsequently the various hydride species are separated by selective volatilization and analysed to determine arsenic [181–183], germanium [52], lead [184] and tin [59,125,184–188] by AAS.

Matrix interferences occur when the matrix affects the hydride release efficiency. The influences of inorganic acids usually used in sample digestion procedures have been studied systematically [120,121,127,189–192]. The strongly suppressing effect of nitric and sulphuric acid has been recognized. These acid interferences are more pronounced in a closed-ended than in an open-ended quartz tube atomizer [120,127]. Nearly all of the volatile hydride-forming elements interfere with the determination of all other hydride-forming elements [111]. This is generally considered to be the result of a competitive reaction where an accompanying material uses up most of the reducing agent and only a small portion is left for the analyte. Alkali and alkaline earth metals cause no interferences with the generation of hydrides, but those metal ions which can be reduced easily by sodium tetrahydroborate, under the experimental conditions, have been found to interfere with hydride generation, e.g., cobalt and nickel, the elements of the copper group and the noble metals [193]. The mechanism of this and of most other interferences is due to a preferential reduction of interfering ion to the metal. It is possible that the finely dispersed precipitated metal then adsorbs and decomposes the gaseous hydride (nickel and other Group VIII elements are effective hydrogenation catalysts and can absorb hydrogen in large amounts). Insoluble nickel arsenide or similar compounds may then be formed in a secondary reaction [93]. The interference of copper, nickel and cobalt with the generation of selenium hydride may be explained by the high decomposition rate of sodium tetrahydroborate in acidic media and the catalytic effect of transition metal ions on this decomposition [194]. The above-mentioned catalytic effect may be due to the metal ion itself or the finely divided metallic particles formed by reduction of the metal ion by sodium tetrahydroborate or metal borides formed by the reduction of metal ion and sodium tetrahydroborate [194]. Organic matrix constituents should also be regarded as potential interferences: Se(IV) is extracted very effectively by a wide range of organic compounds from hydrochloric acid media [195,196] and arsine forms stable adducts with some organic compounds [67]. Humic acid [197] and non-specified organic compounds dissolved in natural waters [141] has been found to interfere with selenium hydride release from the sample solution.

7.3. Gas-phase interferences

Gas-phase interferences are caused by an interferent in either volatile form or as a liquid spray. These interferences can occur on the surface or in the dead volume of the generator, the connective tubing and/or the atomizer. They could have either a direct effect (if observed only simultaneously with generation of the interferent) or a memory effect (if they persist after the cessation of the interferent generation). Two groups of gas-phase interferences can be distinguished according to the locality of their origin: "transport interference" takes place along the route of the hydride from the generator to the atomizer, causing delay (transport kinetics interferences) and/or loss (transport efficiency interferences) of the analyte hydride; "interferences in the atomizer" depend on the mechanism of hydride atomization and on analyte transfer in

the given type of atomizer. However, there is no direct evidence of transport interferences in the literature [74].

The usual source of interferences in the atomizer is other hydrides. Taking into account the mechanism of hydride atomization and free analyte atom transfer in the atomizer bar-tube, two types of interferences in the atomizer emerge [74]: a radical population interference occurs when an interferent changes the H · atom population in the radical cloud; and an analyte decay interference takes place when an interferent speeds the decay of free analyte atoms in the bar-tube via analyte–interferent reactions in the gas phase. The mechanism of interferences in externally heated quartz tubes is still largely unknown. Mutual interferences in this type of atomizer may result from the formation of stable diatomic molecules such as AsSb [198]. By thermodynamic calculations, the formation of diatomic molecules between the analyte and matrix has been proposed as a major source of matrix interferences in the gas phase within the graphite furnace atomizer [143,198].

7.4. Interference elimination and control

Many methods have been developed to eliminate or minimize interferences. One of the simplest methods is the technique of increasing the acidity of reaction solution and/or the concentration of a reducing agent [93,94,96,115,121,127, 199,200]. Various reagents have been used to minimize or eliminate the interferences; most of them are Lewis bases and could behave as: ligands, and some are also reducing agents, such as EDTA [133,201–205], KI [98,206–208], KCN [209,210], thiourea [122,206,211–215], ascorbic acid [122,206,207,211], malic acid [214], 1,10-phenanthroline [81,84,136,138,216], thiosemicarbazide [217] and L-cystine [218]. The addition of interference-releasing elements such as iron [95,101,219], copper [98], tellurium [97] and mercury [215] has been employed to minimize interferences from some metal ions. Additionally, several separation techniques including liquid–liquid extraction [31,220], coprecipitation [69,70,162, 167,221–223], adsorbing colloid flotation [224] and ion exchange [135,141,224–227] have been used. Although there have been some successful minimizations or eliminations of interferences as described above, use of the method of standard additions is essential in many instances [23,212, 213,228–231].

It should be noted that the presence and severity of these interference effects depend to some extent on the experimental conditions, the hydride generator and/or the atomizer used. The mechanism of interference is not yet fully understood and needs further study.

8. Atomization mechanisms

Two types of atomization mechanisms have been proposed for HG-AAS: a free hydrogen radical mechanism and a thermal decomposition mechanism.

Atomization of gaseous hydrides in the heated quartz tube has been thought to be caused by free hydrogen atoms rather than a thermal decomposition because according to thermodynamic calculations the only species that can be expected at temperatures below 1000°C are the dimeric molecules and not atoms. It has also been shown that no atomization signal is obtained for arsenic when it is introduced into a heated quartz cell in an inert gas atmosphere, i.e., in the absence of hydrogen [124]. Although the mechanism of radical formation is not fully understood, traces of oxygen appear to play an important role in the generation of radicals according to the following reactions [74]:

$$H + O_2 \rightleftharpoons OH + O \quad (2)$$

$$O + H_2 \rightleftharpoons OH + H \quad (3)$$

$$OH + H_2 \rightleftharpoons H_2O + H \quad (4)$$

The actual mechanism of hydride atomization probably proceeds via interaction of hydride species with H atoms. For selenium, two consecutive reactions take place:

$$SeH_2 + H \longrightarrow SeH + H_2 \quad (5)$$

$$SeH + H \longrightarrow Se + H_2 \quad (6)$$

Analogous reactions take place for arsenic hydride and probably for other hydrides also [74].

However, on the basis of the equilibrium concentration of free radicals at temperatures prevailing in the heated quartz tubes, it is concluded that the radicals are not present in sufficient concentrations for reactions of type in Eqs. 5 and 6 to take place. Thus, the following mechanisms have been proposed for AsH_3 atomization [75]:

$$2AsH_3 \longrightarrow 2As + 3H_2 \quad (7)$$

$$4AsH_3 + 3O_2 \longrightarrow 4As + 6H_2O \quad (8)$$

which are catalysed by H and OH radicals. A similar mechanism has been suggested for the decomposition of SeH_2 [232].

The positive effect of oxygen and hydrogen on the atomization of hydride-forming elements in an electrically heated quartz atomizer has been indicated in the determination of As, Se, Bi, Sb and Sn [79,91,125,233]. Probably the role of both gases is to form radicals, which may participate in reactions such as those in Eqs. 2–8.

The mechanism of hydride atomization in graphite tubes is not usually addressed. For arsenic, it has been thought that arsine is decomposed in the graphite tube, the resulting arsenic is deposited on the surface and then volatilized and atomized [62,132], or the elemental arsenic is vaporized as As_4, which is then decomposed to As_2 and atomized by gas-phase dissociation [149]. The fact that the influence of hydrogen on the atomization of arsenic hydride is less at higher temperatures in the graphite furnace suggested that the thermal decomposition atomization mechanism plays the main role in the graphite furnace [234]. Dedina et al. [144] suggested two independent mechanisms of selenium hydride atomization in the graphite furnace: a low-temperature mechanism, similar to that in quartz tube atomizers due to collisions with H atoms formed in the furnace by reactions of oxygen with hydrogen, which is effective only in the presence of traces of oxygen at temperatures above 1200°C; and a high-temperature mechanism, involving thermal decomposition of hydride in the gas phase and/or on the graphite surface, which becomes effective at temperatures above 1600°C and which is independent of oxygen supply to the atomizer.

The hydride trapping and analyte atomization mechanism for arsenic, antimony, selenium, tin and lead has been investigated by Sturgeon et al. [150]. Hydride is deposited in the preheated graphite furnace via thermal decomposition. A porous surface increases the efficiency of trapping. The deposited metal may subsequently be reoxidized during the trapping stage. Atomization of As, Sb, Se, and Sn is identical with that occurring when these elements are injected directly in an aqueous solution, while atomization of Pb and Bi deposits is distinctly different from their aqueous counterparts. The effective adsorption of hydrides in the palladium-coated graphite tube may result from the catalytic decomposition of hydrides by palladium metal [151].

The process of determination of elements that form volatile hydrides by AAS can be considered: as two completely independent steps: hydride generation, followed by atomization. The theoretical peak shapes (absorbance vs. time profile) have been obtained by developing a kinetic model and compared with experimental results [107,235] the kinetic factors that control the peak shapes can be employed to optimize any configuration of a hydride generator used in AAS [235]. Although the atomization of hydrides has been investigated as described above, its exact mechanism is still unclear and needs further study.

9. Analytical figures of merit

The analytical performance of HG-AAS is characterized by figures of merit such as detection limit, linear dynamic range and precision and accuracy of measurements.

By comparing a large number of literature reports, Nakahara [24] discussed the analytical performance of this technique. Relative to solution nebulization, detection limits achieved in hydride generation methods are better by up to a factor of 1000 for certain elements. The precision reported as relative standard deviation (R.S.D.) usually ranges from 1 to 5% and occasionally 10%. Thus, in general, the hydride-forming elements can be detected at concentrations below 1 ng ml^{-1}, particularly at pg ml^{-1} levels when the palladium-coated graphite tube is used both for hydride trapping and atomization, and concentra-

tions that are ten or more times the detection limit can be measured with R.S.D.s $\leqslant 5\%$. The linear dynamic ranges vary from two to four orders of magnitude.

10. Practical applications

HG-AAS has successfully been applied to the determination of trace elements such as As, Bi, Sb, Se, Te, Pb, Sn and Ge in a wide range of matrices. Examples of these applications are given in Table 2.

11. Cold vapour generation

Cold vapour generation atomic absorption spectrometry (CV-AAS) has received great attention for the determination of mercury because of its simplicity, high sensitivity and relative freedom from interferences [1,2]. The basic design of a CV-AAS system, which is similar to that of an HG-AAS system, usually consists of four steps: mercury vapour generation, collection, transfer and detection with AAS. Reduction of mercury compounds in solution into mercury vapour can be performed either by using $SnCl_2$ [264] or $NaBH_4$ [265] solution as a reducing agent.

As the high toxicity of mercury and some of its compounds requires its determination at very low concentrations, particularly in water, several enrichment techniques have been developed for mercury. Preconcentration is usually facilitated by passing the mercury vapour generated by reduction through an amalgamating medium [2,266–270]. Copper, silver, gold and platinum metals are often used for this purpose [268]. Once all the mercury has been generated from the sample and collected, the amalgamating medium is heated and the mercury is transported by a gas stream into an absorption cell. Atmospheric Hg can effectively trapped on MnO_2-[271] and $KMnO_4$-coated [272] glass beads prior to elution and electrothermal atomization AAS (ETAAS) detection. Electrochemical preconcentration prior to CV-AAS has been reported as a technique for the speciation determination of inorganic and organic mercury [273]. In principle there are two disadvantages with the amalgamation technique [272]. First, the efficiency of mercury collection may be impaired by moisture [274] or other gaseous reaction products which poison the surface of the amalgamating medium [275],

Table 2
Applications of HG-AAS

Element	Matrix
Se	Biological fluids: human serum and serum proteins [57], blood [236], faeces [237]
	Biological tissues: bovine liver [50,85,237], fingernail and hair [57], marine tissues [147,159,238], biological reference materials [180], oyster tissue [45]
	Environmental samples: biogenic particles and sediments [61], marine sediments [147,159, coal [167], coal fly ash [37]
	Food stuffs: grape berries [179], flour [37,45, 236,237], mixed diet [237]
	Geological samples: geological references [63,84], rocks [81]
	Metallurgical samples: Cu alloys and Ni sponge [87], steel [37]
	Plant material: orchard leaves [37,45,50,62,90]
	Water samples: water and wastewater [178], natural water [51,54], sea water [147,150]
As	Biological fluids: urine [236,237,238, oyster tissue [45], bovine liver [62]
	Environmental samples: sediments [146,221,240], airborne particulate matter [182], marine sediments [147], soils [71,71,100]
	Food stuffs: flour samples [37,45], food materials [241]
	Geological samples: silicate materials [221], geological references [63], ores and concentrates [170]
	Matallurgical samples: steel [37,122]
	Plant material: plant tissues [71], orchard leaves [37, 45,122,62], pine needles [45], tomato leaves [62].
	Water samples: river water [45,181], environmetal waters [15, mineral water [71,72], sea water [39,146,147,242,243], soil water and commerical bottle waters [244], thermal water [37], Canadian drinking water supplies [177], interstitial waters [240], soil-pore waters [245]

Table 2 (continued)

Element	Matrix
Sn	Biological tissues: oyster [188], marine biological tissues [246]
	Environmental samples: marine sediments [246], atomspheric particulate matter [247], sediments and sewage sludges [248]
	Metallurgical samples: Al-based alloy [136], steels [249]
	Water samples: sea water [185,250], marine and estuarine waters [187], river water [250]
Pb	Biological fluids: urine [251]
	Biological tissues: mussel and eggs [252], oyster tissue [253]
	Environmental samples: atomspheric particulates [31]
	Food stuffs; food [252]
	Geological samples: gasolines [33]
	Metallurgical samples: steel [31]
	Plant material: tea leaves [28]
	Water samples: tap water [28], drinking waters [254,255]
Sb	Biological fluids: blood [256], whole blood [257], urine [256]
	Biological tissues: biological samples [258]
	Environmental samples: atomspheric particulate matter [166], soil [72], coal fly ash [37]
	Food stuffs: foods [259].
	Geological samples: ores and pyrites [206]
	Metallurgical samples: steel [37,122], solder alloy [136]
	Plant material: orchard leaves [37,122,171]
	Water samples: sea water [158], thermal water [37], natural waters [54,55]
Bi	Biological fluids: blood and urine [260]
	Biological tissues; shells, marine algae [145]
	Environmental samples: soil [72], water sediments [145]
	Geological samples: ores and pyrites [206], geological reference samples [76,211]
	Metallurgical samples: steel [37]
	Plant material: orchard leaves [37]
	Water samples: natural water [145], sea water [261]
Te	Biological tissues: liver and tuna [171]
	Environmental samples: coal and ash samples [262]
	Metallurgical samples: steel [37]
	Plant material: orchard leaves [37]
	Water samples: sea water and rain water [162]
Ge	Environmental samples: coal ash [263]
	Geological samples: rocks [202]
	Metallurgical samples: steel [37]
	Plant material: orchard leaves [37]
	Water samples: sea water [224], natural water [112]

necessitating occasional cleaning [2]. Second, during heating of the collector to release the mercury, a gas flow is used to transport the vapour to the absorption cell, which means that the sensitivity is flow-rate limited. Slight changes in the flow-rate will also impair the reproducibility [276]. To overcome these problems, in situ trapping techniques have been developed, in which the generated mercury vapour is collected in a porous gold-plated graphite minitube [3] or in a gold-coated [4,5], platinum-lined [276] or palladium-coated graphite tube [277], followed by ETAAS detection.

12. Other vapour generation techniques

The generation of volatile chlorides and fluorides has been carried out by using halogenating reagents [10–17]. The analyte reacted with hydrogen chloride gas at a certain temperature to form the volatile metal chloride, which was swept into

the atomizer by a carrier gas [14,15]. Solid $CuCl_2$ was used for reaction with Si in high-purity indium at 470°C, and the resulting $SiCl_4$ was delivered to a graphite furnace for AAS detection [16]. $AsCl_3$ was produced in a flow system by the reaction of concentrated hydrochloric acid with a solution of As(III) and transported to an O_2–H_2 flame-in-tube atomizer [17]. The interferences of cobalt, copper, iron and nickel observed with the $NaBH_4$ generation of AsH_3 were considerably decreased in this procedure.

Volatile oxides were generated from analyte solution. The use of Ce(IV) as the oxidant to produce RuO_4 from Ru(III) solutions improved the flame AAS sensitivity by a factor of 60 owing to the increased volatility of the analyte in the spray chamber [18]. A similar method was employed to generate the volatile OsO_4 using $K_2Cr_2O_7$ as the oxidant [19].

The chemical generation of volatile metal carbonyls was employed as a means of sample introduction for the determination of nickel by AAS [6–8]. A procedure was devised based on the on-column ethylation of Ge, Hg, Pb, Sb and Sn using $NaBH_4$ [278]. The ethylated species were separated chromatographically and detected by AAS. $NaBH_4$ was also used as a reagent for the generation of an unidentified volatile species of Cd [279]. Tetraethyllead was generated by reaction with tetraethylborate, and preconcentrated in a graphite furnace [164]. There has been revived interest in the generation of methoxyboric ester for the determination of boron by flame AAS [280].

The preparation of volatile chelates allows gaseous sample introduction to be extended to metals other than Hg and the hydride-forming elements and often provides improved sensitivity compared with conventional liquid sample introduction into flames [9–13,281–283]. Determinations of Cr, Co and Fe have been carried out by the formation of the trifluoroacetylacetonates and sweeping the chelates into a heated silica tube for AAS detection [281]. A sixteen-fold sensitivity improvement for Fe has been reported, compared with conventional flame AAS [282]. Several chelating agents have been examined for the determination of Co by flame AAS [283]. Chromatographic separation prior to determination by AAS has been used either for speciation determination of organometallic compounds present in the sample or as a means of separating organometallic compouns [284–287].

Acknowledgement

This work was supported by the National Natural Science Foundation of China.

References

[1] G. Topping and J.M. Pirie, Anal. Chim. Acta, 62 (1972) 200.
[2] B. Welz, M. Melcher, H.W. Sinemus and D. Maier, At. Spectrosc., 5 (1984) 37.
[3] D.D. Siemer and L. Hagemann, Anal. Chem., 52 (1980) 105.
[4] S.H. Lee, K.H. Jung and D.S. Lee, Talanta, 36 (1989) 999.
[5] Z. Hladky, J. Risova and M. Fisera, J. Anal. At. Spectrom., 5 (1990) 691.
[6] D.S. Lee, Anal. Chem., 54 (1982) 1182.
[7] P.N. Vijan, At. Spectrosc., 1 (1980) 143.
[8] J. Alary, J. Vandaele, C. Escrient and R. Haran, Talanta, 33 (1986) 748.
[9] D.C. Hilderbrand and E.E. Pickett, Anal. Chem., 47 (1975) 424.
[10] V.I. Rigin, Zh. Anal. Khim., 40 (1985) 630.
[11] V.I. Rigin, Zh. Anal. Khim., 40 (1985) 1399.
[12] V.I. Rigin, Zh. Anal. Khim., 41 (1986) 581.
[13] V.I. Rigin, Zh. Anal. Khim., 41 (1986) 788.
[14] R.K. Skogerboe and D.L. Parlica, Anal. Chem., 47 (1975) 568.
[15] Y.-M. Liu, B.-L. Gong and T.-Z. Lin, Fenxi Huaxue, 12 (1984) 21.
[16] L.B. Kuznetsov, L.N. Kolonina and V.N. Belyaev, Zh. Anal. Khim., 41 (1986) 80.
[17] S. Tesfalidet and K. Irgum, Anal. Chem., 60 (1988) 2031.
[18] K. Motojima, K. Tatenuma, Z. Yoshida, H. Takeishi and E. Akatsu, Anal. Chim. Acta, 183 (1986) 217.
[19] H. Tao, A. Miyazaki and K. Bansho, Anal. Chem., 60 (1988) 1762.
[20] W. Holak, Anal. Chem., 41 (1969) 1712.
[21] F.J. Fernandez and D.C. Manning, At. Absorpt. Newsl., 10 (1971) 86.
[22] E.F. Dalton and A.J. Malanoski, At. Absorpt. Newsl., 10 (1971) 92.
[23] R.G. Godden and D.R. Thomerson, Analyst, 105 (1980) 1137.

[24] T. Nakahara, Prog. Anal. At. Spectrosc., 6 (1983) 163.
[25] I.S. Busheina and J.B. Headridge, Talanta, 29 (1982) 519.
[26] D. Yan, Z. Yan, G.-S. Cheng and A.-M. Li, Talanta, 31 (1984) 133.
[27] J.R. Castillo, J.M. Mir and M.T. Gomz, Microchem. J., 38 (1982) 387.
[28] X.-P. Yan and Z.-M. Ni, J. Anal. At. Spectrom., 6 (1991) 483.
[29] S.-Z. Zhang, H.-B. Han and Z.-M. Ni, Anal. Chim. Acta, 221 (1989) 85.
[30] J.-X. Li, Y.-M. Liu and T.-Z. Lin, Anal. Chim. Acta, 231, (1990) 151.
[31] J. Aznarez, F. Palacios, M.S. Ortega and J.C. Vidal, Analyst, 109 (1984) 123.
[32] J. Aznarez, J.M. Rabadan, A. Ferrer and P. Cipres, Talanta, 33 (1986) 458.
[33] J. Aznarez, J.C. Vidal and R. Carnicer, J. Anal. At. Spectrom., 2 (1987) 55.
[34] B. Welz and M. Melcher, At. Absorpt. Newsl., 18 (1979) 121.
[35] B. Welz and M. Melcher, Anal. Chim. Acta, 131 (1981) 17.
[36] M. McDaniel, A.D. Shendrikar, K.D. Reiszner and P.W. West, Anal. Chem., 48 (1976) 2240.
[37] M. Yamamoto, M. Yasuda and Y. Yamamoto, Anal. Chem., 57 (1985) 1382.
[38] B.T. Sturman, Appl. Spectrosc., 39 (1985) 48.
[39] M. Yamamoto, K. Takada, T. Kumamaru, M. Yasuda and S. Yokoyama, Anal. Chem., 59 (1987) 2446.
[40] L.M. Voth-Beach and D.E. Shrader, Spectroscopy, 1 (1985) 60.
[41] L. Zhang, Z.-M. Ni and X.-Q. Shan, Spectrochim. Acta, Part B, 44 (1989) 339.
[42] L. Zhang, X.-Q. Shan and Z.-M. Ni, Fresenius' Z. Anal. Chem., 332 (1988) 764.
[43] Z.-L. Fang, in J.L. Burguera (Ed.), Flow Injection Atomic Spectroscopy, Dakkar, New York, Chap. 4, 1989.
[44] J.F. Tyson, Spectrochim. Acta Rev., 14 (1991) 169.
[45] H. Narasaki and M. Ikeda, Anal. Chem., 56 (1984) 2059.
[46] H. Narasaki, Fresenius' Z. Anal. Chem., 321 (1985) 464.
[47] K. Fujita and T. Takada, Talanta, 33 (1986) 203.
[48] M. Yamamoto and Y. Yamamoto, Analyst, 109 (1984) 1461.
[49] T. Yamashige, M. Yamamoto, Y. Shigetomi and Y. Yamamoto, Bunseki Kagaku, 34 (1985) 646.
[50] A. Tsunoda, K. Matsumoto and K. Fuwa, Anal. Sci., 2 (1986) 119.
[51] S.C. Apte and A.G. Howard, J. Anal. At. Spectrom., 1 (1986) 379.
[52] G.A. Hambrick III, P.N. Froelich, Jr., M.O. Anreae and B.L. Lewis, Anal. Chem., 56 (1984) 421.
[53] S. Tanaka, M. Kaneko, Y. Konno and Y. Hashimoto, Bunseki Kagaku, 32 (1983) 535.
[54] S. Tanaka, M. Nakamura, H. Yokoi, M. Yumura and Y. Hashimoto, Bunseki Kagaku, 35 (1986) 116.
[55] S.C. Apte and A.G. Howard, J. Anal. At. Spectrom., 1 (1986) 221.
[56] M. McDaniel, A.D. Shendrikar, K.D. Reiszner and P.W. West, Anal. Chem., 48 (1976) 2240.
[57] J. Piwonka, G. Kaiser and G. Tolg, Fresenius' Z. Anal. Chem., 321 (1985) 225.
[58] M.O. Andreae, J.-F. Asmode, P. Foster and L. Van't dack, Anal. Chem., 53 (1987) 1766.
[59] M.O. Andreae and J.T. Byrd, Anal. Chim. Acta, 156 (1984) 147.
[60] B. Welz and M. Schubert-Jacobs, Fresenius' Z. Anal. Chem., 324 (1986) 832.
[61] G.A. Cutter, Anal. Chem., 57 (1985) 2951.
[62] W.J. Wang, S. Hanamura and J.D. Winefordner, Anal. Chim. Acta, 184 (1986) 213.
[63] C.H. Branch and D. Hutchison, Analyst, 110 (1985) 163.
[64] R.E. Madsen, At. Absorpt. Newsl., 10 (1971) 57.
[65] R.F. Sanzolone, T.T. Chao and E.P. Welsch, Anal. Chim. Acta, 108 (1979) 357.
[66] W.L. Hoover, J.R. Melton, P.A. Howard and J.W. Bassett, Jr., J. Assoc. Off. Anal. Chem., 57 (1974) 18.
[67] A.U. Shaikh and D.E. Tallman, Anal. Chem., 49 (1977) 1093.
[68] W.A. Maher, At. Spectrosc., 8 (1987) 88.
[69] W.A. Maher, Analyst, 108 (1983) 305.
[70] W.A. Maher, Anal. Lett., 16 (1983) 801.
[71] D.L. Tsalev, P.B. Mandjukov and J.A. Stratis, J. Anal. At. Spectrom., 2 (1987) 135.
[72] D.L. Tsalev and P.B. Mandjukov, Microchem. J., 35 (1987) 83.
[73] J.A. Hagen and R.J. Lovett., At. Spectrosc., 7 (1986) 69.
[74] J. Dedina, Prog. Anal. Spectrosc., 11 (1988) 251.
[75] J. Agterdenbos and D. Bax, Fresenius' Z. Anal. Chem., 323 (1986) 783.
[76] J.G. Crock, Anal. Lett., 19 (1986) 1367.
[77] J. Agterdenbos, J.T. van Elteren, D. Bax and J.P. Heege, Spectrochim. Acta, Part B, 41 (1986) 303.
[78] J. Agterdenbos, J.P.M. van Noort, F.F. Peters, D. Bax and J.P. Ter Heege, Spectrochim. Acta, Part B, 40 (1985) 501.
[79] D. Bax, F.F. Peters, J.P.M. van Noort and J. Agterdenbos, Spectrochim. Acta, Part B, 41 (1986) 275.
[80] J. Agterdenbos, J.P.M. van Noort, F.F. Peters and D. Bax, Spectrochim. Acta, Part B, 41 (1986) 283.
[81] C.C.Y. Chan and M.W.A. Baig, Anal. Lett., 17 (1984) 143.
[82] J.W. Hershey and P.N. Keliher, Spectrochim. Acta, Part B, 41 (1986) 713.
[83] N. Imai, S. Terashima and A. Ando, Bunseki Kagaku, 33 (1984) 288.
[84] C.C.Y. Chan, Anal. Chem., 57 (1985) 1482.
[85] J. Pettersson, L. Hansson and A. Olin, Talanta, 33 (1986) 249.
[86] M. Ikeda, Anal. Chim. Acta, 167 (1985) 289.
[87] M. Ikeda, Anal. Chim. Acta, 170 (1985) 217.
[88] M. Yamamoto, M. Yasuda and Y. Yamamoto, Anal. Chem., 57 (1985) 1382.
[89] O. Astrom, Anal. Chem., 54 (1982) 190.
[90] C. Boampong, I.D. Brindle and C.M. Ceccarelli Ponzoni, J. Anal. At. Spectrom., 2 (1987) 197.

[91] N.E. Parisis and A. Heyndrickx, Analyst, 111 (1986) 281.
[92] J.R. Castillo, J.M. Mir, J. Val, M.P. Colon and C. Martinez, Analyst, 110 (1985) 1219.
[93] B. Welz and M. Melcher, Analyst, 109 (1984) 569.
[94] B. Welz and M. Melcher, Analyst, 109 (1984) 573.
[95] B. Welz and M. Melcher, Analyst, 109 (1984) 577.
[96] B. Welz and M. Schubert-Jacobs, J. Anal. At. Spectrom., 1 (1986) 23.
[97] R. Bye, L. Engvik and W. Lund, Fresenius' Z. Anal. Chem., 318 (1984) 349.
[98] L.H.J. Lajunen, T. Merkkiniemi and H. Hayrynen, Talanta, 31 (1984) 709.
[99] R. Bye, Anal. Chem., 57 (1985) 1481.
[100] N.G. van der Veen, H.J. Keukens and G. Vos., Anal. Chim. Acta, 171 (1985) 285.
[101] R. Bye, Analyst, 111 (1986) 111.
[102] R. Bye, Analyst, 110 (1985) 85.
[103] T.W. May and J.L. Johnson, At. Spectrosc., 6 (1985) 9.
[104] B. Vanloo, R. Dams and J. Hoste, Anal. Chim. Acta, 175 (1985) 325.
[105] H.L. Kahn and J.E. Schallis, At. Absorpt. Newsl., 7 (1968) 5.
[106] D.D. Siemer and L. Hagemann, Anal. Lett., 8 (1975) 323.
[107] J. Dedina, Fresenius' Z. Anal. Chem., 323 (1986) 771.
[108] P.W. Balls, Anal. Chim. Acta, 197 (1987) 309.
[109] D.D. Seimer, P. Koteel and V. Jariwala, Anal. Chem., 48 (1976) 836.
[110] D.D. Seimer and P. Koteel, Anal. Chem., 49 (1977) 1096.
[111] J. Dedina, Anal. Chem., 54 (1982) 2097.
[112] M.O. Andreae and P.N. Froelich, Jr., Anal. Chem., 53 (1981) 287.
[113] G.A. Cutter, Anal. Chim. Acta, 98 (1978) 59.
[114] G.A. Cutter, Anal. Chim. Acta, 149 (1983) 391.
[115] M.O. Andreae, Anal. Chem., 49 (1977) 820.
[116] V.F. Hodge, S.L. Seidel and E.D. Goldberg, Anal. Chem., 51 (1979) 1256.
[117] S. Nakashima, Analyst, 103 (1978) 1031.
[118] R.C. Chu, G.P. Barron and P.A.W. Baumgarner, Anal. Chem., 44 (1972) 1476.
[119] K.C. Thompson and D.R. Thomerson, Analyst, 99 (1974) 595.
[120] M. Verlinden, J. Baart and H. Deelstra, Talanta, 27 (1980) 633.
[121] B. Welz and M. Melcher, Spectrochim. Acta, Part B, 36 (1981) 439.
[122] P. Hon, O. Lau and S. Tsui, J. Anal. At. Spectrom., 1 (1986) 125.
[123] J.F. Chapman and L.S. Dale, Anal. Chim. Acta, 111 (1979) 137.
[124] B. Welz and M. Melcher, Analyst, 108 (1983) 213.
[125] O.F.X. Donard, S. Rapsomanikis and J.H. Weber, Anal. Chem., 58 (1986) 772.
[126] W.H. Evans, F.J. Jackson and D. Dellar, Analyst, 104 (1979) 16.
[127] A. Meyer, C. Hofer, G. Tolg, S. Raptis and G. Knapp, Fresenius' Z. Anal. Chem., 296 (1979) 337.
[128] M. Verlinden, Anal. Chim. Acta, 140 (1982) 229.
[129] J.G. Crock and F.E. Lichte, Anal. Chim. Acta, 144 (1982) 223.
[130] E.J. Knudson and G.D. Christian, At. Absorpt. Newsl., 13 (1974) 74.
[131] M.O. Andreae and P.N. Froelich, Anal. Chem., 53 (1981) 287.
[132] A.U. Shaikh and D.E. Tallman, Anal. Chim. Acta, 98 (1978) 251.
[133] E.O. Uthus, M.E. Collings, W.E. Cornatzer and F.H. Nielsen, Anal. Chem., 53 (1981) 2221.
[134] T. Inui, S. Terada and H. Tamura, Fresenius' Z. Anal. Chem., 305 (1981) 189.
[135] T. Inui, S. Terada, H. Tamura and N. Ichinose, Fresenius' Z. Anal. Chem., 311 (1982) 492.
[136] T. Inui, S. Terada, H. Tamura and N. Ichinose, Fresenius' Z. Anal. Chem., 318 (1984) 502.
[137] E.J. Knudson and G.D. Christian, Anal. Lett., 6 (1973) 1039.
[138] T. Inui, S. Terada, H. Tamura and N. Ichinose, Fresenius' Z. Anal. Chem., 315 (1983) 598.
[139] W.A. Maher, Anal. Chim. Acta, 126 (1981) 157.
[140] W.A. Maher, Talanta, 29 (1982) 532.
[141] D.R. Roden and D.E. Tallman, Anal. Chem., 54 (1982) 307.
[142] K. Dittrich and R. Mandry, Analyst, 111 (1986) 277.
[143] K. Dittrich and R. Mandry, Analyst, 111 (1986) 269.
[144] J. Dedina, W. Frech, E. Lundberg and A Cedergren, in Kurzreferate IX CANAS, 15–19 September, Neubrandenburg, East Germany, 1986, p. 234.
[145] D.S. Lee, Anal. Chem., 54 (1982) 1682.
[146] R.E. Sturgeon, S.N. Willie and S.S. Berman, J. Anal. At. Spectrom., 1 (1986) 115.
[147] R.E. Sturgeon, S.N. Willie and S.S. Berman, Fresenius' Z. Anal. Chem. 323 (1986) 788.
[148] G. Drasch, L.V. Meyer and G. Kauert, Fresenius' Z. Anal. Chem., 304 (1980) 141.
[149] S. Akman, O. Genc and T. Balkis, Spectrochim. Acta, Part B, 37 (1982) 903.
[150] R.E. Sturgeon, S.N. Willie, G.I. Sproule and S.S. Berman, J. Anal. At. Spectrom., 2 (1987) 719.
[151] R.E. Sturgeon, S.N. Wllie, I. Sproule, P.T. Robinson and S.S. Berman, Spectrochim. Acta, Part B, 44 (1989) 667.
[152] P.S. Doidge and B.T. Sturman, T.M. Rettberg, J. Anal. At. Spectrom., 4 (1989) 251.
[153] J.E. Whitley, R. Hannah and D. Littlejohn, Anal. Proc., 25 (1988) 246.
[154] I.A. Brovko, A. Tursunov, M.A. Rish and A.D. Davirov, Zh. Anal. Khim., 39 (1984) 1768.
[155] Y.K. Lee, D.S. Lee, B.M. Yoon and H. Hwang, Bull. Korean Chem. Soc., 12 (1991) 290.
[156] I.A. Brovko, R.I. Sharibdzhanov and B.N. Vasiev, Vysokochist Veshchestva, 4 (1989) 177.

[157] L. Zhang, Z.-M. Ni and X.-Q. Shan, Spectrochim. Acta, Part B, 44 (1985) 751.
[158] R.E. Sturgeon, S.N. Willie and S.S. Berman, Anal. Chem., 57 (1985) 2311.
[159] S.N. Willie, R.E. Sturgeon and S.S. Berman, Anal. Chem., 58 (1986) 1140.
[160] L. Zhang, Z.-M. Ni and X.-Q. Shan, Can. J. Appl. Spectrosc., 36 (1991) 47.
[161] Z.-M. Ni, H.-B. Han, A. Li, B. He and F.-Z. Xu, J. Anal. At. Spectrom., 6 (1991) 385.
[162] M.O. Andreae, Anal. Chem., 56 (1984) 2064.
[163] I. Aroza, M. Bonilla, Y. Madrid and C. Camara, J. Anal. At. Spectrom., 4 (1989) 163.
[164] R.E. Sturgeon, S.N. Willie and S.S. Berman, Anal. Chem., 61 (1989) 1867
[165] M.S. Droessler and J.A. Holcombe, Can. J. Spectrosc., 31 (1986) 6.
[166] K. De Doncker, R. Dumarey, R. Dams and J. Hoste, Anal. Chim. Acta, 153 (1983) 33.
[167] L. Ebdon and J.R. Wilkinson, Anal. Chim. Acta, 194 (1987) 177.
[168] S.A. Amankwah and J.L. Fasching, Talanta, 32 (1985) 111.
[169] G.E. Pacey, M.R. Straka and J.R. Gord, Anal. Chem., 58 (1986) 502.
[170] E.M. Donaldson and M.E. Leaver, Talanta, 35 (1988) 297.
[171] J.A. Fiorino, J.W. Jones and S.G. Capar, Anal. Chem., 48 (1976) 120.
[172] D.R. Corbin and W.M. Barnard, At. Absorpt. Newsl., 15 (1976) 116.
[173] B. Pahlavanpour, J.H. Pullen and M. Thompson, Analyst, 105 (1980) 274.
[174] M. Thompson, B. Pahlavanpour and L.T. Thorne, Water Res., 15 (1981) 407.
[175] F.J. Schmidt and J.L. Royer, Anal. Lett., 6 (1973) 17.
[176] B.J.A. Haring, W. van Delft and C.M. Bom, Fresenius' Z. Anal. Chem. 310 (1982) 217.
[177] K.S. Subramanian and J.C. Meranger, At. Spectrosc., 5 (1984) 34.
[178] V. Krivan, K. Petrick, B. Welz and M. Melcher, Anal. Chem., 57 (1985) 1703.
[179] F. Alt, J. Messerschmidt and G. Tolg, Fresenius' Z. Anal. Chem., 327 (1987) 233.
[180] F. Nakata, Y. Yasui, H. Matsuo and T. Kumamaru, Anal. Sci., 1 (1985) 417.
[181] S. Tanaka, M. Nakamura, Y. Kishi and Y. Hashimoto, Nippon Kagaku Kaishi, (1986) 727.
[182] H. Mukai and Y. Ambe, Anal. Chim. Acta, 193 (1987) 219.
[183] R.J.A. Van Cleuvenbergen, W.E. Van Mol and F.C. Adams, J. Anal. At. Spectrom., 3 (1988) 169.
[184] O.F.X. Donard, L. Randall, S. Rapsomanikis and J.H. Weber, Int. J. Environ. Anal. Chem., 27 (1986) 55.
[185] P.W. Balls, Anal. Chim. Acta, 197 (1987) 309.
[186] L. Randall, O.F.X. Donard and J.H. Weber, Anal. Chim. Acta, 184 (1986) 197.
[187] A.O. Valkirs, P.F. Seligman, G.J. Olson, F.E. Brinckman, C.L. Matthias and J.M. Bellama, Analyst, 112 (1987) 17.
[188] J.S. Han and J.H. Weber, Anal. Chem., 60 (1988) 316.
[189] H.D. Fleming and R.G. Ide, Anal. Chim. Acta, 83 (1976) 67.
[190] H.K. Kang and J.L. Valentine, Anal. Chem., 49 (1977) 1829.
[191] M. Thompson, B. Pahlavanpour, S.J. Walton and G.F. Kirkbright, Analyst, 103 (1978) 568.
[192] F.D. Pierce and H.R. Brown, Anal. Chem., 49 (1977) 1417.
[193] A.E. Smith, Analyst, 100 (1975) 300.
[194] D. Bax, J. Agterdenbos, E. Worrell and J. Beneken Kolmer, Spectrochim. Acta, Part B, 43 (1988) 1349.
[195] S. Landsberger and G.G.J. Boswell, Anal. Chim. Acta, 89 (1977) 281.
[196] L. Futekov, G. Angelova and H. Specker, Fresenius' Z. Anal. Chem., 294 (1979) 262.
[197] S.M. Workman, P.N. Soltanpour, Soil. Sci. Soc. Am. J., 44 (1980) 1331.
[198] K. Dittrich and R. Mandry, Analyst, 111 (1986) 277.
[199] P.N. Vijan and D. Leung, Anal. Chim. Acta, 120 (1980) 141.
[200] H. Berndt, P.G. Willmer and E. Jackwerth, Fresenius' Z. Anal. Chem., 296 (1979) 377.
[201] A. D'ulivo and P. Papoff, Talanta, 32 (1985) 383.
[202] K. Jin, H. Terada and M. Taga, Bull. Chem. Soc. Jpn., 54 (1981) 2934.
[203] J.E. Drinkwater, Analyst, 101 (1976) 672.
[204] D.C. Reamer and C. Veillon, Anal. Chem., 53 (1981) 1192.
[205] E. Henden, Analyst, 107 (1982) 872.
[206] X.-A. Yu, G.-X. Dong and C.-X. Li, Talanta, 31 (1984) 367.
[207] Y. Yamamoto, T. Kumamaru, T. Edo and J. Takemoto, Bunseki Kagaku, 25 (1976) 770.
[208] M. Burguera and J.L. Burguera, Analyst, 111 (1986) 171.
[209] R.M. Brown, Jr., R.C. Fry, J.L. Moyers, S.J. Northway, M.B. Denton and G.S. Wilson, Anal. Chem., 53 (1981) 1560.
[210] R. Smith, At. Spectrosc., 2 (1981) 155.
[211] S. Terashima, Anal. Chim. Acta, 156 (1984) 301.
[212] T. Nakahara and N. Kikui, Anal. Chim. Acta, 172 (1985) 127.
[213] T. Nakahara, K. Nakanishi and T. Wasa, Spectrochim. Acta, Part B, 42 (1987) 119.
[214] T. Nakakara, Appl. Spectrosc., 37 (1983) 539.
[215] I.D. Brindle and C.M. Ceccarelli Ponzoni, Analyst, 112 (1987) 1547.
[216] P. Ek and S.G. Hulden, Talanta, 34 (1987) 495.
[217] G.F. Kirkbright and M. Taddia, Anal. Chim. Acta, 100 (1979) 145.
[218] C. Boampong, I.D. Brindle, X. Le, L. Pidwerbesky and C.M. Ceccarelli Ponzoni, Anal. Chem., 60 (1988) 1185.
[219] R. Bye, Anal. Chim. Acta, 192 (1987) 115.

[220] L. Halicz, Analyst, 110 (1985) 943.
[221] W.A. Maher, Chem. Geol., 45 (1984) 173.
[222] T. Dorado Lopez, M.T. Larrea and A. Gomez Coedo, J. Anal. At. Spectrom., 3 (1988) 447.
[223] L. Halicz and G.M. Russell, Analyst, 111 (1986) 15.
[224] S. Nakashima and M. Yagi, Anal. Chim. Acta, 157 (1984) 187.
[225] T. Yamashige, Y. Ohmoto and Y. Shigetomi, Bunseki Kagaku, 27 (1978) 607.
[226] J.W. Jones, S.G. Capar and T.C. O'Haver, Analyst, 107 (1982) 353.
[227] T. Nakahara, T. Wakisaka and S. Musha, Spectrochim. Acta, Part B, 36 (1981) 661.
[228] S. Kobayashi, T. Nakahara and S. Musha, Talanta, 26 (1979) 951.
[229] T. Nakahara, S. Kobayashi and S. Musha, Anal. Chem., 51 (1979) 1589.
[230] T. Nakahara, S. Kobayashi, T. Walkisaka and S. Musha, Appl. Spectrosc., 34 (1980) 194.
[231] T. Nakahara and T. Wasa, J. Anal. At. Spectrom., 1 (1986) 473.
[232] D. Bax, J.T. van Elteren and J. Agterdenbos, Spectrochim. Acta, Part B, 41 (1986) 1007.
[233] Narsito and J. Agterdenbos, Anal. Chim. Acta, 197 (1987) 315.
[234] K. Dittrich, R. Mandry, C. Udelnow and A. Udelnow, Fresenius' Z. Anal. Chem., 323 (1986) 793.
[235] S. Van Wagen, D.E. Carter, A.G. Ragheb and Q. Fernando, Anal. Chem., 59 (1987) 891.
[236] L. Hanson, J. Petterson and A. Olin, Talanta, 34 (1987) 829.
[237] V.W. Bunker and H.T. Delves, Anal. Chim. Acta, 201 (1987) 331.
[238] B. Welz and M. Melcher, Anal. Chem., 57 (1985) 427.
[239] B.S. Chana and N.J. Smith, Anal. Chim. Acta, 197 (1987) 177.
[240] J. Aggett and M.R. Kriegman, Analyst, 112 (1987) 153.
[241] H. Münz and W. Lorenzen, Fresenius' Z. Anal. Chem., 319 (1984) 395.
[242] S.A. Amankwah and J.L. Fasching, Talanta, 32 (1985) 111.
[243] A.G. Howard, M. Volkan and D.Y. Ataman, Analyst, 112 (1987) 159.
[244] C.T. Tye, S.J. Haswell, P. O'Neill and K.C.C. Bancroft, Anal. Chim. Acta, 169 (1985) 195.
[245] S.J. Haswell, P. O'Neill and K.C.C. Bancroft, Talanta, 32 (1985) 69.
[246] R.E. Sturgeon, S.N. Willie ans S.S. Berman, Anal. Chem., 59 (1987) 2441.
[247] K. De Doncker, R. Dumarey R. Dams and J. Hoste, Anal. Chim. Acta, 187 (1986) 163.
[248] M. Legret and L. Divet, Anal. Chim. Acta, 189 (1986) 313.
[249] H. Tao, A. Miyazaki and K. Bansho, Bunseki Kagaku, 34 (1985) 188.
[250] A. Clark and P.J. Craig, Appl. Organomet. Chem., 2 (1988) 33.
[251] H. Yamauchi, F. Arai and Y. Yamamura, Ind. Health., 19 (1981) 115.
[252] M. Bonilla, L. Rodriguez and C. Cámara, J. Anal. At. Spectrom., 2 (1987) 157.
[253] K. Jin and M. Taga, Anal. Chim. Acta, 143 (1982) 229.
[254] P.N. Vijan and R.S. Sadana, Talanta, 27 (1980) 321.
[255] R. Smith, At. Spectrosc., 2 (1981) 155.
[256] D.L. Collett, D.E. Fleming and G.A. Taylor, Analyst, 103 (1978) 1074.
[257] K. Bencze, Aerztl. Lab., 27 (1981) 347.
[258] A. Dornemann and H. Kleist, Fresenius' Z. Anal. Chem., 294 (1979) 402.
[259] H. Woidich and W. Pfannhauser, Nährung, 24 (1980) 367.
[260] R.C. Rooney, Analyst, 101 (1976) 749.
[261] J. Ohyama, F. Maruyama and Y. Dokiya, Anal. Sci., 3 (1987) 413.
[262] R.A. Nadkarni, Anal. Chim. Acta, 135 (1982) 363.
[263] J.R. Castillo, J. Lanaja and J. Aznárez, Analyst, 107 (1982) 89.
[264] N.S. Polucktov and R.A. Vitkun, Zh. Anal. Khim., 18 (1963) 83.
[265] L. Lopez-Escobar and D.N. Hume, Anal. Lett., 6 (1973) 343.
[266] W.F. Fitzgerald and G.A. Gill, Anal. Chem., 51 (1979) 1714.
[267] R. Dumarey, R. Dams and J. Hoste, Anal. Chem., 57 (1985) 2638.
[268] W.H. Schroeder, Environ. Sci. Technol., 16 (1982) 394A.
[269] N.S. Bloom and E.A. Crecelius, Mar. Chem., 14 (1983) 49.
[270] G.A. Gill and W.F. Fitzgerald, Mar. Chem., 20 (1987) 227.
[271] E. Nakamura and H. Namiki, Bunseki Kagaku, 35 (1986) 27.
[272] E. Nakamura and H. Namiki, Bunseki Kagaku, 35 (1986) 499.
[273] C. Ergucyener, S. Aygun, O.Y. Ataman and A. Temizer, J. Anal. At. Spectrom., 3 (1988) 177.
[274] B. Welz and M. Schubert-Jacobs, Fresenius' Z. Anal. Chem., 331 (1988) 324
[275] B. Welz, Atomic Absorption Spectrometry, VCH, Weinheim, 2nd edn., 1985.
[276] D.C. Baxter and W. Frech, Anal. Chim. Acta, 225 (1989) 175.
[277] X.-P. Yan, Z.-M. Ni and Q.-L. Guo, Anal. Chim. Acta, 272 (1993) 105.
[278] J. Ashby, S. Clark and P.J. Craig, J. Anal. At. Spectrom., 3 (1988) 735.
[279] A. D'Ulivo and Y.-W. Chen, J. Anal. At. Spectrom., 4 (1989) 319.
[280] J.R. Castillo, J.M. Mir, C. Bendicho and C. Martinez, At. Spectrosc., 6 (1985) 152.
[281] J.R. Castillo, E. Garcia, J. Delfa, J.M. Mir and C. Bendicho, Microchem. J., 42 (1990) 103.
[282] J.R. Castillo, J.M. Mir, M.E. Garcia-Ruiz, C. Bendicho, Fresenius' J. Anal. Chem., 338 (1990) 721.

[283] J.R. Castillo, J. Delfa, J.M. Marin, C. Bendicho, M. de la Guardia, A.R. Mauri, C. Mongay and E. Martinez, J. Anal. Spectrom., 5 (1990) 325.
[284] L. Ebdon, S. Hill and R.W. Ward, Analyst, 111 (1986) 1113.
[285] L. Ebdon, S. Hill and R.W. Ward, Analyst, 112 (1987) 1.
[286] S.J. Hill, J.B. Dawson, W.J. Price, I.L. Shuttler and J.F. Tyson, J. Anal. At. Spectrom., 6 (1991) 187R.
[287] S.J. Hill, J.B. Dawson, W.J. Price, I.L. Shuttler and J.F. Tyson, J. Anal. At. Spectrom., 7 (1992) 215R.

ELSEVIER

Analytica Chimica Acta 291 (1994) 107–113

ANALYTICA CHIMICA ACTA

Metal ion interferences in determination of sulphur by flame molecular emission spectrometry

Sverre Hauge [a], Kjartan Marøy [a], Arngrímur Thorlacius *[,b]

[a] *Department of Chemistry, University of Bergen, Allégaten 41, 5007 Bergen, Norway*
[b] *Agricultural Research Institute, Keldnaholt, 112 Reykjavík, Iceland*

(Received 9th May 1993; revised manuscript received 14th December 1993)

Abstract

The well known interference from metal ions on disulphur emission in flames was investigated. Sulphite was introduced by flow-injection through a cation-exchange column into a hydrogen–nitrogen diffusion flame. The effects of sodium, potassium, magnesium, calcium, nickel and copper ions were investigated. Cooling of the flame, metal catalyzed oxidation, solubility differences and the formation of metal disulphites have been suggested to explain the variation of the observed interferences.

Key words: Flow injection; Flame molecular emission spectrometry; Metals; Sulphur

1. Introduction

We have recently reintroduced the measurement of disulphur (S_2) emission in a hydrogen–nitrogen diffusion flame for the detection of mainly inorganic sulphur compounds [1,2]. The interference from metal cations on this emission as well as on the related phenomenon of HPO emission from phosphorous compounds is well known, but its cause is not fully established. In the literature there is a general agreement, that the effect is related to the stability of analyte salts in the flame. The degree of interference depends on the temperature of the flame and the reducing effect of the flame gases.

Veillon and Park [3] observed no interference on aspirating one of several sulphur compounds into a separated hydrogen–nitrogen flame where the analyte travels across the hot combustion zone before producing the disulphur emission. However, they measured only solutions with the cations and sulphur anions in equivalent amounts. Syty and Dean [4] observed no interference on phosphorus emission from molybdenum, cadmium, silver or arsenic. They measured an increase in the background emission with the alkali metals, but a depressive interference from alkaline earth elements. As in the first case, a separated flame was used, but the green HPO emission was observed on both sides of the combustion zone. Dagnall et al. [5] found interference from all (ten) metal ions they tested, aspirating phosphate into a cooler hydrogen–nitrogen diffu-

* Corresponding author.

SSDI 0003-2670(94)00006-8

sion flame. The degree of interference was not related to the thermal stability of the metal phosphates, but it could be correlated with the ease with which the compounds could be reduced with hydrogen. Everett and West [6] excited sulphur and phosphorus from a carbon filament inside a hydrogen–nitrogen diffusion flame. The magnitude of the interference from Na, K, Ca and Zn was in the same order as the thermal stability of their sulphates and phosphates, respectively, whereas transition metals showed no such trends.

With molecular emission cavity analysis (MECA), approximate temperatures corresponding to maximum emission can be estimated from the cavity temperature–time curve. Belcher et al. [7] observed for several sulphates and thiourea, that the temperatures producing maximum emission were generally lower than reported values for thermal decomposition. They attributed this difference to the reducing nature of the flame gases. Moreover they concluded, that aside from slow breakdown of analyte salts the interference might be caused by radical reactions such as:

$$H + H + Na = H_2 + Na^*$$

In the present work, we try to explain this interference phenomenon by measuring the emission from sulphite, in the presence of several metal salts. We have shown earlier that sulphite can be introduced into the flame either in solution or as free sulphur dioxide gas [2].

2. Experimental

The flame and spectrophotometer setup were as described previously [1], except for the following details. 99.99% nitrogen was used as a diluent gas for the flame. Instead of shielding the burner compartment door a rectangular brass shield was attached to the 3-slot burner head, surrounding the flame on three sides. The shield, which is made from a 1 mm thick plate, is 4 cm high and its lower edge is ca. 2 mm below the top of the burner head. The two parallel sides are 2 cm apart and cover the entire length of the burner. The cation-exchange column was packed with Dowex 50W-X10, 20–50 mesh, Na^+ form, with a bed height of ca. 4 cm. The bed was saturated with ammonium or hydronium ions by pumping 0.5 M ammonium nitrate or nitric acid, respectively, through the column for ca. 15 min.

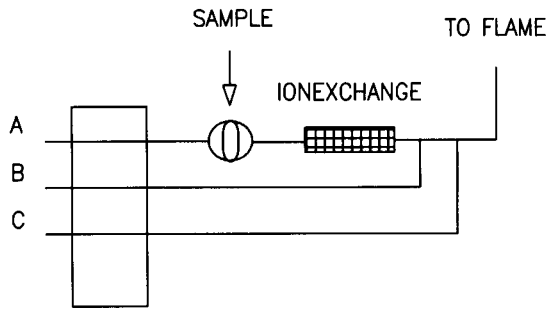

Fig. 1. Flow diagram of the flow-injection system. A, deionized water; B, metal acetate; C, deionized water (ammonium exchange), nitric acid, hydrochloric acid or ammonium nitrate (hydronium exchange). Relative flow rates for channels A, B, and C are 4:4:1 with a total flow of ca. 6 ml/min.

Samples were introduced into the flame by flow-injection as shown in Fig. 1. The relative flow rates through channels A, B and C were 4:4:1, with a total throughput of ca. 6 ml/min. With this setup one can easily combine different metal ions and acids and vary their concentrations independently. The carrier stream, A, was deionized water throughout. The metals Na, K, Mg, Ca, Ni and Cu were introduced as their dissolved acetates of varying concentrations through channel B. Stock solutions were prepared from $NaAc \cdot 3H_2O$, KAc, $Mg(Ac)_2 \cdot 4H_2O$, $Ca(Ac)_2 \cdot H_2O$, $Ni(Ac)_2 \cdot 4H_2O$ and $Cu(Ac)_2 \cdot H_2O$, respectively. From each metal stock solution a series of diluted solutions was made, all series being equivalent with respect to the concentration of acetate ions. Channel C carried deionized water in all experiments involving ammonium exchange, but 0.9 M nitric acid with hydronium exchange experiments, except for nickel and copper where, in addition, hydrochloric acid, ammonium chloride and nitric acid were tried in different combinations. Sulphite was always injected as a 15 mM solution of sodium sulphite, which was prepared by dissolving the salt in 0.1% sodium hydroxide. The base was first flushed with nitrogen gas for at least 5 min and the flushing was continued until the salt was

completely dissolved. Signals were estimated as the square root of the average peak heights from 3 or 4 injections.

3. Results and discussion

The position of the diffusion flame, optimized for disulphur emission, is sensitive to movements in front of the burner compartment, which therefore has to be partially shielded [1]. We have found, working with another instrument (PE 2380), that the optimal shield construction depends on the form of the burner compartment and its ventilation. Moreover, we find that one can change the shields within certain limits, to obtain different sets of optimal conditions, without altering the sulphur detection significantly. With powerful ventilation, the emission intensity is decreased. By attaching to the burner head a metal shield, as described above, rather than shielding the burner compartment, the flame becomes less sensitive to external factors and a more reproducible set of optimal conditions is obtained. The arrangement was optimized with a simplex program [1] varying the sample uptake rate, the burner height and the flow rate of hydrogen, but keeping the nitrogen flow rate constant (and close to the lowest attainable). This produced very similar sensitivity and noise as was obtained with the external shield, but the factor values were significantly different. The optimal observation height is lowered from 20 to 15 mm and the hydrogen content is lowered from 18 to 9%. These values are in fact quite close to optimal conditions obtained with a bit more open (and irregular) external shield which was tried in our early studies with this flame. Lessening the purity grade of the nitrogen to 99.99% and reoptimizing changed only the optimal hydrogen content from 9 to 7%, counteracting the heating effect of the increased oxygen content. Comparing univariate profiles of the observation height for the temperature and the emission intensity (with restricted lightpath [1]) gives an optimal temperature of ca. 300°C, which is ca. 100°C higher than obtained earlier with external shielding and nitrogen of higher purity. The less pure nitrogen and the corresponding optimal conditions were used for all measurements discussed below. Two narrower shields, 1.0 and 1.5 cm wide were also tried. When the flame had been lit for several minutes, both shields produced unstable green emission from copper in the metal walls and the background emission at 374 nm was increased. Sulphur detection was not improved by the narrower shields.

Our previous results with acidic solutions of sulphite indicated that sulphur dioxide is completely transferred from the aerosol droplets to the surrounding gas stream inside the nebulizer, whereas with ammonium sulphite the analyte is strictly confined to the droplets [2]. This enables us to study separately the effect of metal ions on decomposition processes and on the chemiluminescent reaction sequence, respectively. When sulphite is introduced in a strongly acidic solution, any interference from metal cations will be due to recombination reactions between sulphur species on one side and the metal or some flame constituent affected by the metal on the other hand. Conversely, by introducing ammonium sulphite along with the same metal, the emission will also be affected by decomposition processes in the particles, that are generated by evaporation of the aerosol droplets.

To see the effect of metal ions during decomposition of aerosol particles it is important to choose a counter ion for the metal ions that does not interfere with the disulphur emission. It is also important that the counter ion forms thermally labile salts so that decomposition of the added metal salt is not a dominating process. The acetate ion was found suitable for this purpose. 50 mM ammonium acetate had no effect on the response from sulphite with ammonium exchange nor did the same concentration of acetic acid with hydronium exchange. This confirms that neither acetate nor ammonium ions interfere at this level. It also supports the theory that the constructive interference from ammonium on the emission from sulphate is a volatilization effect [1]. Both the acidic and ammonium forms of sulphite are readily decomposed and consequently, no interference is observed.

We investigated the effect of sodium, potassium, magnesium, calcium, nickel and copper representing the alkali metals, the alkaline earth metals and the transition metals. All six metals are available as reasonably well-defined acetate salts. The first four frequently occur as major matrix constituents and the remaining two are also found in many sample matrices. To be able to compare gas phase interferences from the metal ions, sulphite was introduced through hydronium exchange and 0.9 M nitric acid added through channel C (0.1 M after mixing in the manifold) to ensure that all the sulphite was released from the aerosol droplets as sulphur dioxide. We already know that this acid has very little effect on the emission from sulphate [1]. It is easily evaporated and the nitrate ion does not form stable metal precipitates. With the pumping rate used, the distance from the mixing point of channel C to the nebulizer corresponds to ca. 2 s travel time for the analyte. This was found to be short enough to practically prevent oxidation of sulphite to sulphate by the nitric acid in the absence of a catalyst. All six metal acetates were introduced in coinciding series, with concentrations at the nebulizer inlet, ranging from 3 to 53 mM with respect to acetate ions. Having corrected the concentration of sulphite for dispersion in the manifold as previously described [2], the metal concentrations can be expressed as sulphite equivalents. It must be noted though, that this equivalent concentration is only valid, while the metal ions and sulphite are contained in the aerosol. With hydronium exchange all the sulphite is transferred to the flame gases inside the nebulizer, whereas only about 10% of the metal ions reach the flame. With ammonium exchange, fewer points were measured since the emission from ammonium sulphite is much less intense and the background noise becomes increasingly dominating with increasing metal concentration. The results are depicted in Fig. 2. The intensity values have been corrected for metal ion background by subtracting the emission obtained from the metal salt alone, pumping deionized water instead of the sulphite solution. The square root was used to give a response that is directly proportional to the concentration of emitting sulphur. In addition, the values are scaled by division with the corresponding value obtained with zero metal concentration (an intensity value of one corresponds to no interference, except background elevation). This scaling enables us to view in a single graph the two sets of results for each

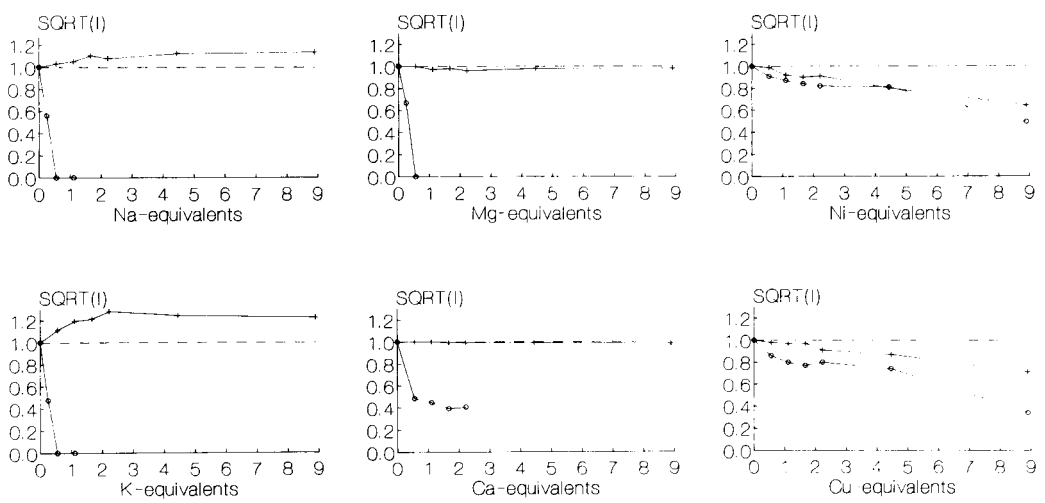

Fig. 2. The effect of varying concentrations of several metal acetates on the disulphur emission from sulphite. The amount of injected sulphur is the same in all cases. The emission signal, I, is calculated as a fraction of the intensity measured, when no metal is present. The square root of I varies linearly with the concentration of emitting sulphur. (+) hydronium exchange, (○) ammonium exchange

metal, even though the emission from ammonium sulphite is only about 1% that of the free sulphur dioxide [2]. The background emission intensity from the six metals at 374.9 nm, was in the order: Cu < Ni < Ca ≪ Na < K < Mg.

When sulphite is introduced as an aerosol, sodium, potassium and magnesium have identical effects, totally quenching the emission when the metal concentration reaches one half equivalent of the sulphite. The extra point found on each of these three curves (0.25 equivalents) was obtained by approximately doubling the sulphite concentration through the use of a larger sample loop. The curves indicate the formation of thermally stable salts. The concentration ratio could indicate the formation of metal hydrogen sulphites or metal ammonium sulphites but, for these metals, the former are not stable even at room temperature and the latter probably lack the thermal stability to totally quench the emission in the flame. We suggest the formation of metal disulphites during the drying of aerosol droplets, since the disulphite ion, $S_2O_5^{2-}$, is an equilibrium component of sulphite solutions, and its fraction will increase with increasing total sulphite concentration [8]. The sodium, potassium, magnesium and calcium salts of sulphite and disulphite have been studied by Foerster et al. [9,10] and found to be thermally rather stable. Calcium shows a behaviour similar to that mentioned above, except that the emission is not quenched but the efficiency is sharply decreased to about 50% at the half-equivalent level. The shape of the curve could suggest that a similar salt is formed, but that it is less thermally stable. Of the ions studied here, calcium forms the most stable sulphite and the transformation of calcium disulphite to calcium sulphite inside the flame would explain the form of the curve for calcium.

The situation is clearly more complicated with copper and nickel, which both produce a relatively even fall in the intensity over the whole concentration range. At nine equivalents, emission is still detected with appreciable intensity. Both metal sulphites are insoluble in water and if no other metal sulphur compounds were formed during evaporation or decomposition of the thus formed particles, the curves should level off to a plateau, where the metal ion concentration reaches that of the sulphite. The curves thus suggest that more than one compound is formed in both cases. Formation of complex compounds or double salts may occur [11,12].

Turning to the curves for hydronium exchange, calcium and magnesium produce no interference in the gas phase, whereas sodium and potassium clearly increase the emission efficiency, the latter by as much as 30%. With both transition metals a steady fall in the intensity is observed over the entire concentration range. Neither of the metals form precipitates or complexes with sulphite which could withhold sulphur dioxide in the strongly acidic aerosol phase during nebulization. The interference was suspected to be the oxidation of sulphite to sulphate, before nebulization, by nitric acid, catalyzed by the transition metal ions. To investigate this, we repeated the study with different acids in channel C. The results are depicted in Fig. 3. Increasing the concentration of nitric acid from 0.1 to 0.5 M magnifies the interference with both metals, whereas with 0.1 M hydrochloric acid no or very little interference is observed. This supports the idea of catalyzed oxidation by nitrate. 0.1 M nitric acid and 0.1 M ammonium chloride together give much less interference than 0.1 M nitric acid alone, suggesting that catalysis with chloro complexes of the two metals is less effective than with the aqua complexes.

An enhancement of disulphur emission is observed with orthophosphoric acid and cooling of the flame has been proposed as an explanation [1]. The flame temperatures in the presence of each of the six metals were measured in the flame centre with a thermocouple probe positioned in the optimal observation height. The metal ions were introduced as acetates by direct aspiration of solutions 120 mM with respect to acetate ions. Following temperature equilibration of at least 30 s for each solution, a temperature value was taken as an average from 12 consecutive readings. Deionized water was aspirated in-between the metal ion solutions and the temperature measured in the same way. To detect a significant fall in temperature, one-sided *t*-tests with 99% confidence were performed, comparing

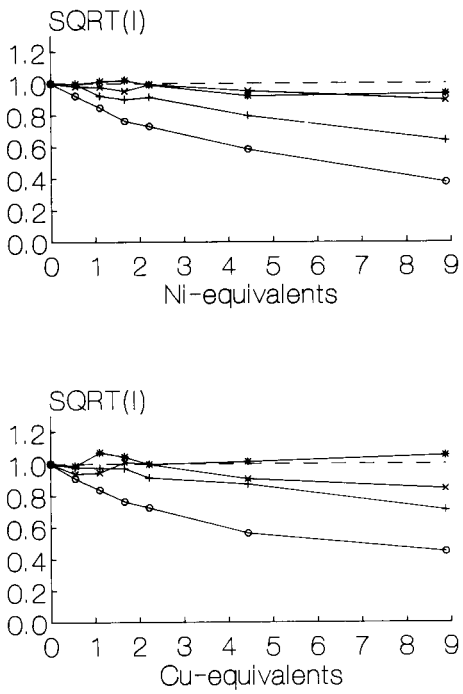

Fig. 3. The effect of copper and nickel ions on the emission from sulphite with hydronium exchange introducing different solutions through channel C. The sulphur concentration and scaling are the same as in Fig. 2. (*) 0.9 M hydrochloric acid, (×) 0.9 M nitric acid and 0.9 M ammonium chloride, (+) 0.9 M nitric acid, (○) 4.5 M nitric acid.

the mean for each metal with the mean of the corresponding 24 readings for water (12 before and 12 after). Magnesium and calcium did not cool the flame significantly, but sodium and potassium produced a fall of 6°C and 9°C, respectively, which is in the same order as their emission enhancement. The intensity enhancement of 0.05 M orthophosphoric acid is about twice the maximum enhancement of potassium and the corresponding temperature change was ca. 15°C [1]. These temperature differences are, however, not directly comparable, since the phosphate effect was measured with somewhat different flame conditions, due to the use of purer nitrogen. Nickel and copper also decrease the flame temperature significantly, by 6°C and 8°C, respectively. This cooling should enhance the emission, which suggests that the catalyzed oxidation of sulphite is even more pronounced than indicated by the observed fall in the intensity. A temperature measurement aspirating the same concentrations of nickel and copper acetates in 0.1 M hydrochloric acid revealed a significant fall, but of only 3°C and 5°C, respectively. This more modest cooling of the flame along with the fact, that in the presence of a catalyst sulphite may be oxidized to some extent by dissolved oxygen and in the case of copper by copper ions, may explain why a distinct intensity enhancement is not observed with either of the metal ions in this acid.

To cool the flame, the decomposition of a metal salt must either compete with the combustion for one of the two flame gases, as has been suggested with phosphate [1] or more likely, it has to consume some of the released heat. In this study we have equal amounts of both acetate and nitrate in all six cases and, in the absence of a catalyst, neither ion effects disulphur emission as discussed above. The metal ions will be surrounded by oxygen in the dried aerosol particles so their decomposition is likely to produce either oxides or free metal atoms. Calcium and magnesium form excessively stable oxides which may explain their minute effect on the flame temperature, but potassium, which has the greatest cooling effect, forms the least stable oxide and this can be decomposed, even in this cool flame. The flame is not hot enough to decompose the three remaining oxides, so reduction with hydrogen would be needed, but nickel, which has the most stable oxide, is the one producing the least cooling effect of the three metals.

4. Conclusions

From the results above, there is nothing that supports the idea of Belcher et al. [7] that metal atoms depress the emission by decreasing the availability of hydrogen radicals through competing radical reactions. When sulphur is introduced into the flame unbound by metals, the metals tested here either had no effect or actually enhanced the disulphur emission. The concurrent cooling effect and intensity enhancement of the alkali metal salts supports the explanation given earlier for the constructive interference by phos-

phate on the emission from sulphate [1]. The present data do in general support the idea that the release of sulphur from analyte salts is the major rate determining effect in the disulphur emission process. Once sulphur has been released to the gas phase, other substances seem to interfere only indirectly by altering the temperature of the flame. This cool flame will not thermally decompose the oxides of sodium, copper or nickel, yet their acetates significantly affect its temperature. This indicates that the effect of reduction is important as was pointed out for phosphorus by Dagnall et al. [5] and in the MECA study on sulphur by Belcher et al [7].

The present work was meant to improve our understanding of disulphur emission and related phenomena in hydrogen diffusion flames. It has in addition suggested to us a possible means of dealing with the inevitable interferences from sulphate and phosphate when detecting sulphur dioxide or hydrogen sulphide for the measurement of sulphite, thiosulphate or sulphide. Calcium, which produces relatively modest background emission at the relevant wavelength may be useful in masking the interfering emission from both ions without effect on the emission from the analytes when they are introduced in strongly acidic solutions. Furthermore, adding copper(II) ions when determining sulphite, may be useful in masking sulphide ions.

References

[1] S. Hauge, K. Marøy and A. Thorlacius, Anal. Chim. Acta, 243 (1991) 227.
[2] S. Hauge, K. Marøy and A. Thorlacius, Anal. Chim. Acta, 251 (1991) 197.
[3] C. Veillon and J.Y. Park, Anal. Chim. Acta, 60 (1972) 293.
[4] A. Syty and J.A. Dean, Appl. Opt., 7 (1968) 1331.
[5] R.M. Dagnall, K.C. Thompson and T.S. West, Analyst, 93 (1968) 72.
[6] G.L. Everett and T.S. West, Anal. Chim. Acta, 68 (1974) 387.
[7] R. Belcher, S.L. Bogdanski and A. Townshend, Anal. Chim. Acta, 67 (1973) 1.
[8] N.N. Greenwood and A. Earnshaw, Chemistry of the Elements, Pergamon, Oxford, 1984, p. 853.
[9] F. Foerster and K. Kubel, Z. Anorg. Chem., 139 (1924) 261.
[10] F. Foerster and G. Hamprecht, Z. Anorg. Chem., 158 (1926) 277.
[11] Gmelin's Handbuch der anorganischen Chemie, 8. Auflage, Kupfer, Teil B – Lieferung 1, System-nummer 60, seite 486, Verlag Chemie, Weinheim, 1958.
[12] Gmelin's Handbuch der anorganischen Chemie, 8. Auflage, Nickel, Teil B – Lieferung 2, System-nummer 57, seite 678, Verlag Chemie, Weinheim, 1966.

ELSEVIER

Analytica Chimica Acta 291 (1994) 115–120

ANALYTICA CHIMICA ACTA

Determination of aluminium in biological materials by electrothermal atomic absorption spectrometry with a tungsten tube atomizer

Kiyohisa Ohta *, Masayosi Yokoyama, Syn-ichi Itoh, Satoshi Kaneco, Takayuki Mizuno

Department of Chemistry for Materials, Faculty of Engineering, Mie University, Tsu, Mie 514, Japan

(Received 8th October 1993; revised manuscript received 30th November 1993)

Abstract

Electrothermal atomic absorption spectrometry (ETA-AAS) of aluminium with a tungsten tube atomizer was investigated. By the addition of hydrogen to the argon purge, a sensitive ETA-AAS method was developed. The optimum gas flow-rates were argon 300 ml min^{-1} and hydrogen 200 ml min^{-1}. The absolute characteristic mass (the mass of element giving 0.0044 absorbance) of aluminium by the atomizer was 0.98 pg and the detection limit was 52 pg ml^{-1}. These values were more than ten times better than those obtained using a graphite atomizer, inductively coupled plasma (ICP), flame AAS, neutron activation analysis, x-ray fluorescence spectrometry and ICP mass spectrometry. The interferences caused by large amounts of interferents were evaluated. For severe interferences, the standard additions method was applied to the determination. The analytical results were in good agreement with the certified values.

Key words: Atomic absorption spectrometry; Aluminium; Biological materials

1. Introduction

Aluminium has been found to be toxic to haemodialysis patients and has been suggested as a cause of Alzheimer's disease [1–3]. Therefore, interest in the possible biological function of aluminium continues to increase. Several methods have been used to determine the aluminium concentration, including graphite furnace atomic absorption spectrometry (GFAAS) [4–23], inductively coupled plasma atomic emission spectrometry (ICP-AES) [24], flame AAS [25], neutron activation analysis [9,26] and x-ray fluorescence spectrometry [27]. However, these methods, except for GFAAS, show poor sensitivity for measuring trace levels of aluminium in biological materials or are time consuming and the facilities are not always readily available. ETAAS is in much more general use.

In recent years, metal tubes as atomizers in ETA-AAS have been developed [28–31]. This type of atomizer has been found to be superior to graphite atomizers because of the higher sensitivity, the ability to use smaller sample sizes, the relatively low power consumption and the low

* Corresponding author.

SSDI 0003-2670(93)E0684-Y

cost. There is, however, little information on the application of metal tube atomizers in ETAAS.

This paper describes the determination of aluminium in biological samples by ETAAS with a tungsten tube atomizer. Atomization characteristics for aluminium in the atomizer were evaluated. Interference studies on the aluminium absorption signal were also performed.

2. Experimental

2.1. Apparatus

Atomic absorption was measured at 328.1 nm (Al hollow-cathode lamp; Hamamatsu Photonics) using a monochromator (Nippon Jarrell-Ash 0.5-m Ebert-type), an amplifier, a storage oscilloscope (Iwatsu MS-5021) and a microcomputer (Sord M223). The tungsten tube atomizer (25 mm long × 1.8 mm i.d. with 0.05-mm wall thickness) was made from high-purity tungsten foil (99.95% purity; Rembar). A 0.3-mm diameter hole was drilled at the mid-point of the tube to inject sample solution. The electric power for heating the atomizer was supplied by a step-down transformer and a transformer (Yamabishi volt-slider, S-130-30, capacity 3 kV A). Two pinhole apertures were placed in front of and at the rear of the atomizer, in order to collimate the light beam and eliminate the radiation from the atomizer surface. Background absorption was checked with a deuterium lamp (Original Hanau D200F). The absorption signal from the amplifier and the output signal from a photodiode for the measurement of atomizer temperature were simultaneously fed into the microcomputer. Calibration of the temperature of the atomizer was done against the photodiode voltage with an optical pyrometer (Chino Works) and a microcomputer [29].

2.2. Reagents

A stock standard solution (1 mg ml^{-1}) of aluminium was prepared as the nitrate in 0.1 M HNO_3 after dissolving the high-purity metal in 7 M HNO_3. Solutions of the matrix elements for the interference study were prepared as nitrates or chlorides in 0.1–6 M nitric acid. Working standard solutions with concentrations appropriate to the atomic absorption measurements were prepared by diluting the stock standard solutions with water immediately before use. All chemicals used were of analytical-reagent grade.

2.3. Procedures

For the interference study, a 1-μl portion of the sample solution containing Al (0.2 ng ml^{-1}) and interferent (20–200 μg ml^{-1}) was pipetted into the tungsten tube atomizer. The sample was dried at 90°C for 10 s and 1200°C for 10 s and heated to atomize at 2410°C for 3 s. The atomization temperature corresponded to a heating rate of 5.1°C ms^{-1}.

An accurately weighed biological sample (about 0.5 g) was treated with 3 ml of nitric acid (14 M) and 1 ml of hydrogen peroxide (30%) in a Uni-seal decomposition vessel and heated for 3 h in an electric oven at 120°C. After the decomposition, the solution was evaporated in a Teflon beaker by heating in a polyethylene glycol bath (110°C) and then the wet residue was dissolved in 5 ml of 1 M nitric acid on the bath. Finally, the solution was transferred into a 50-ml volumetric flask and, after the addition of standard aluminium solution, diluted to volume with water. ETAAS measurements were performed in the same manner as described for the interference study.

3. Results and discussion

3.1. Effect of heating rate

As some elements are affected by the atomization rate of the atomizer, as reported in a previous paper [29], for aluminium also it is important to investigate the effect of the atomization rate on the aluminium AA profile. Therefore, the AA signals were measured at various heating rates of the atomizer (6.3, 5.1 and 3.3°C ms^{-1}). The absorption profile of aluminium was characterized by a sharper and narrower peak with increase in heating rate, as shown in Fig. 1. The appearance temperature of the aluminium signal (1450°C),

which is defined as the temperature of the atomizer giving an absorbance of 0.0044, was independent of the heating rate. Aluminium nitrate is converted into amorphous alumina at 500–700°C [32]. The appearance temperature of aluminium in the tungsten atomizer is too low compared with the melting and boiling points of aluminium oxide (2072 and 2980°C, respectively [33]). As aluminium produces an intermetalic compound with tungsten [32], it seems reasonable to assume that aluminium oxide reduced at < 1450°C (during the pyrolysis stage) in an argon–hydrogen atmosphere is adsorbed as aluminium metal on the surface of the tungsten and then atomized (the melting and boiling points of aluminium are 660.37 and 2467°C, respectively [33]). The temperature at the maximum of the AA signal (peak temperature) was 2100°C at 6.3°C ms^{-1}, 1880°C at 5.1°C ms^{-1} and 1560°C at 3.3°C ms^{-1}, and thus the peak temperature of the signal was found to be dependent on the heating rate. These phenomena are the same as those observed for the absorption of silver, etc. [29]. Although the highest AA signal of aluminium was obtained at a heating rate of 6.3°C ms^{-1}, a rate of 5.1°C ms^{-1} was adopted in view of the lifetime of the metal atomizer.

3.2. Effect of hydrogen

A small amount of hydrogen has been found to be very effective for the atomization of some

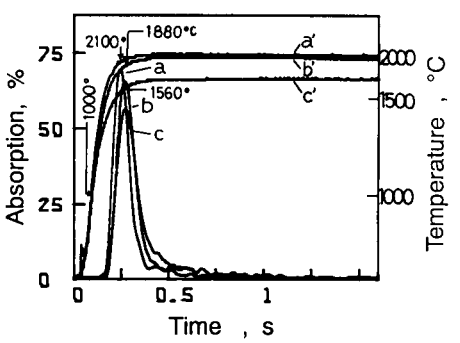

Fig. 1. Effect of heating rate of the tungsten atomizer on atomic absorption of aluminium. (a,a') 6.3°C ms^{-1}; (b,b') 5.1°C ms^{-1}; (c,c') 3.3°C ms^{-1}; (a–c) atomization profiles; (a'–c') temperature increase. Al, 200 pg; purge gas, 480 ml min^{-1} Ar + 20 ml min^{-1} H_2.

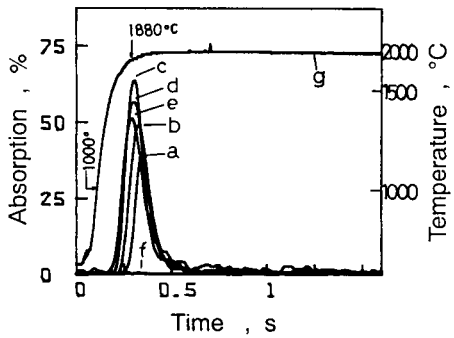

Fig. 2. Effect of hydrogen on atomic absorption of aluminium. (a) 500 ml min^{-1} Ar; (b) 480 ml min^{-1} Ar + 20 ml min^{-1} H_2; (c) 400 ml min^{-1} Ar + 100 ml min^{-1} H_2; (d) 300 ml min^{-1} Ar + 200 ml min^{-1} H_2; (e) 200 ml min^{-1} Ar + 300 ml min^{-1} H_2; (f) 500 ml min^{-1} H_2; (g) temperature increase. Al, 200 pg; heating rate, 5.1°C ms^{-1}.

elements in ETAAS with a metal tube atomizer [28,30,34]. Therefore, the absorption signal for aluminium (200 pg) was evaluated in an argon–hydrogen purge gas at a heating rate of 5.1°C ms^{-1}. A small addition of hydrogen (< 100 ml min^{-1}) to the argon purge gas provided higher peaks than obtained in pure argon, but above 100 ml min^{-1} of hydrogen the peak height of the aluminium signal decreased and in pure hydrogen the AA signal became very small and shifted to the lower temperature region, as shown in Fig. 2. It seems likely that the effect of hydrogen on the aluminium AA signal is due to the high specific heat of hydrogen. This phenomenon was similar to that observed with titanium [31]. The optimum purge gas flow-rates for the absorption signal were argon 400 ml min^{-1} and hydrogen 100 ml min^{-1}.

3.3. Effect of pyrolysis temperature

In order to achieve the sensitive absorption of aluminium, it is important to select the appropriate pyrolysis temperature for the analysis. The effect of pyrolysis temperature on the absorbance of aluminium in the tungsten tube atomizer is shown in Fig. 3. For the atomization of aluminium, the sensitive pyrolysis temperatures are > 1200°C (about 1450°C, high-frequency temper-

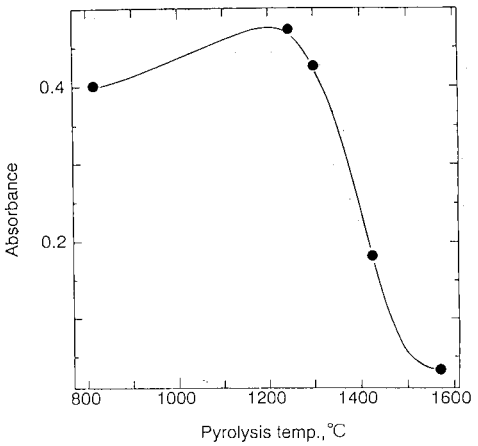

Fig. 3. Effect of pyrolysis temperature on atomic absorption signal of aluminium. Al, 200 pg.

ature) in a graphite furnace atomizer [4–23] and > 1600°C in a slotted graphite tube atomizer [5]. In the metal atomizer, the highest absorbance was obtained at a pyrolysis temperature of about 1200°C. Above 1300°C, the absorbance decreased significantly. The trend of the curve with the tungsten atomizer was similar to that with a graphite furnace atomizer [4]. However, the optimum pyrolysis temperature with the metal atomizer was lower than that in GFAAS. The difference may arise because there is no formation of aluminium carbide in the metal tube. Finally, with the tungsten atomizer, it was found that the optimum pyrolysis temperature was in the range 1000–1250°C.

3.4. Detection limit, characteristic mass and reproducibility

The characteristic mass of aluminium with the atomizer was 0.98 pg. The detection limit, calculated as the weight of analyte that gave an atomic absorption signal equal to three times the standard deviation of the background (obtained from the measurement of a solution blank), was calculated from the height of the aluminium absorption signal. The detection limit of aluminium with the use of the tungsten tube atomizer was 0.52 pg (corresponding to 52 pg ml^{-1}, 10 μl taken). These values were more than ten times better than the characteristic mass (5.6 pg [7]) and detection limit (1300 pg ml^{-1} [23]) obtained with graphite atomizers and those obtained with ICP (20 ng ml^{-1} [24]) and ICP-MS (600 pg ml^{-1} [24]). The better sensitivity with the tungsten atomizer may be due to the non-porous atomizer wall differing from a graphite furnace [34], the lack of formation of the carbide [35], the difference in the adsorptivity of aluminium nitrate on tungsten and carbon and the much smaller volume compared with graphite furnaces. Although it has been reported that when heated at 100–150°C 75% of aluminium nitrate is eliminated [32], the nitrate in the tungsten atomizer and the reducing atmosphere may make vaporization difficult at the temperature used owing to the Al–W affinity.

The reproducibility with the use of the tungsten atomizer was investigated. The relative standard deviation for 200 pg of aluminium was 3.8% for ten measurements.

3.5. Interference study

In the determination of aluminium in biological materials by GFAAS, interferences by some matrix elements have been observed [4–22]. Therefore, the influences of Ca, Cu, Fe, K, Mg, Na, Pb and Zn, which are included as matrix elements in biological materials, on the aluminium absorption signal were investigated in the tungsten tube atomizer. The aluminium signal in the presence of these elements (200 ng) was measured using both the peak-height and the peak-area methods. The trends of the interferences by these methods were similar, as summarized in Table 1. The peak-height measurement method was adopted for of the convenience. The aluminium signal (200 pg) was influenced by Ca, Fe and Mg, but the reason is unclear. With graphite furnace atomizers, interferences of Ca, Fe, Na, K and Mg on the aluminium signal have been reported [12,22,26]. In order to eliminate the interferences in GFAAS, many chemical modification methods [3,6,7,11,12,14,15,17] have been proposed for the accurate determination of aluminium in biological materials. $Mg(NO_3)_2$, $Ca(NO_3)_2$, CuF_2, Triton X-100, orthophosphoric acid, phosphate, carbon black, nitric acid, etc.,

Table 1
Interferences on the atomic absorption signal of aluminium

Interferent		Peak-height (absorbance)	Peak-area (absorbance s)
Element	Amount (ng)		
Al	0.2	0.397 ± 0.021	9.97 ± 0.24
Ca	200	0.325 ± 0.010	7.03 ± 0.29
Cu	200	0.401 ± 0.022	10.15 ± 0.52
Fe	200	0.219 ± 0.015	6.79 ± 0.28
K	200	0.395 ± 0.019	9.98 ± 0.63
Mg	200	0.264 ± 0.015	5.74 ± 0.29
Na	200	0.408 ± 0.020	10.38 ± 0.14
Pb	200	0.358 ± 0.026	9.61 ± 0.28
Zn	200	0.411 ± 0.015	9.64 ± 0.22

Number of measurement > 5.

have been reported as chemical modifiers. All the chemical modifiers reported in the literatures were therefore tested in the determination of aluminium with the metal tube atomizer. However, none of them could eliminate the interferences completely.

3.6. Determination of aluminium

As a suitable chemical modifier could not be found for the tungsten atomizer, a standard additions method was applied to the determination of aluminium in biological materials. Following the digestion of biological samples, the samples were analysed by the standard additions method under the optimum conditions. Volumes of 0.2–1 ml of aluminium standard solutions (0.1 ng Al ml^{-1}) were added to the sample solutions and then the calibration graph was constructed. Table 2 gives the results obtained for some biological Standard Reference Materials (NIST), compared with the certified values. The relative standard deviations were better than 13.6% for three replicate analyses. The average value found for the standards lies within the limits of the certified values. The results obtained with the standard additions technique can be considered satisfactory for the determination of aluminium in biological materials, whereas it has been reported that GFAAS did not yield accurate results [6].

Table 2
Determination of aluminium in NIST SRM in biological materials

Sample	Concentration of aluminium ($\mu g\ g^{-1}$)	
	Found [a]	Certified value
SRM 1577a Bovine Liver	1.91 ± 0.26	2 [b]
SRM 1549 Non-Fat Milk	2.05 ± 0.09	2 [b]
SRM 1572 Citrus Leaves	99.4 ± 4.4	92 ± 15

[a] Number of analyses = 3.
[b] Information value (uncertified).

As described above, for the determination of aluminium the major benefits of the tungsten tube atomizer in an argon–hydrogen atmosphere are the high sensitivity and the longer lifetime (more than 5000 firings) than that of a graphite furnace (200–250 firings) [16]. The performance characteristics of the tungsten tube atomizer will serve for the accurate and sensitive determination of aluminium in complex samples.

Acknowledgement

This work was supported financially by the Ministry of Education, Science and Culture of Japan.

References

[1] A.J. Wing, Lancet, ii (1980) 190.
[2] M.R. Wills and J. Savory, Lancet, ii (1983) 29.
[3] D.P. Perl and A.R. Brody, Science, 208 (1980) 297.
[4] E. Bulska, K. Wrobel and A. Hulanicki, Fresenius' Z. Anal. Chem., 342 (1992) 740.
[5] K. Nordahl, B. Radziuk, Y. Thomassen and R. Weberg, Fresenius' Z. Anal. Chem., 337 (1990) 310.
[6] P.C. D'Haese, L. Liang, L.V. Lamberts and M.E. De-Broe, Fresenius' Z. Anal. Chem., 342 (1992) 714.
[7] E.A. Nater, R.G. Burau and M. Akeson, Anal. Chim. Acta, 225 (1989) 233.
[8] A. Cedergren and W. Frech, Pure Appl. Chem., 59 (1987) 222.
[9] B. Kratochvil, N. Motkosky, M.J.M. Duke and D. Ng, Can. J. Chem., 65 (1987) 1047.
[10] W. Frech and D.C. Baxter, Fresenius' Z. Anal. Chem., 328 (1987) 400.
[11] F. Fagioli and C. Locatelli, Analyst, 112 (1987) 1229.

[12] A.D. Woolfson and G.M. Gracey, Analyst, 112 (1987) 1387.
[13] K.B. Pierson and M.A. Evenson, Anal. Chem., 58 (1986) 1744.
[14] C.C. Craney, K. Swartout, F.W. Smith, III, and C.D. West, Anal. Chem., 58 (1986) 656.
[15] T. Yoshimura and N. Shinya, Nihon Kagakukaishi, 1986 (1986) 1363.
[16] M. Bettinelli, U. Baroni, F. Fontana and P. Poisetti, Analyst, 110 (1985) 19.
[17] D.J. Halls and G.S. Fell, Analyst, 110 (1985) 243.
[18] P.E. Gardiner, M. Stoeppler and H.W. Nurnberg, Analyst, 110 (1985) 611.
[19] L. Lian, Spectrochim. Acta, Part B, 47 (1992) 239.
[20] B.V. L'vov, N.P. Romanova and L.K. Polzik, Spectrochim. Acta, Part B, 46 (1991) 1001.
[21] T. Yoshimura and N. Shinya, Bunseki Kagaku, 31 (1982) E311.
[22] J.A. Persson, W. Frech, G. Pohl and K. Lundgrem, Analyst, 105 (1980) 1163.
[23] G.B. van der Voet, J.M. de Haas and F.A. de Wolff, J. Anal. Toxicol., 9 (1985) 100.
[24] L.H.J. Lajunen, Spectrochemical Analysis by Atomic Absorption and Emission, Royal Society of Chemistry, Cambridge, 1992, pp. 186–189, 231.
[25] T.V. Ramakrishna, P.W. West and J.W. Robinson, Anal. Chim. Acta, 39 (1967) 81.
[26] K. Garmestani, A.J. Blotcky and E.P. Pack, Anal. Chem., 50 (1978) 144.
[27] J.R.J. Sorenson, I.R. Campbell, L.B. Tepper and R.D. Lingg, in Proceedings of Conference on Aluminium Analysis in Biological Materials, Charlottesville, Virginia, 1983, p. 76.
[28] K. Ohta and T. Mizuno, Anal. Chim. Acta, 217 (1989) 377.
[29] K. Ohta, S. Kaneco, S. Itoh and T. Mizuno, Anal. Chim. Acta, 267 (1992) 131.
[30] K. Ohta, S.Y. Su and T. Mizuno, Anal. Lett., 20 (1987) 1399.
[31] K. Ohta, S. Itoh and T. Mizuno, Anal. Sci., Suppl., 7 (1991) 457.
[32] K. Wade and A.J. Banister, in J.C. Bailar, H.J. Emeleus, R. Nyholm and A.F. Trotman-Dickenson (Eds.), Comprehensive Inorganic Chemistry, Vol. 1, Pergamon, Oxford, 1973, pp. 1004, 1052.
[33] D.R. Lide (Ed.), Handbook of Chemistry and Physics, 72nd edn., CRC Press, Boca Raton, FL 1991, pp. 4–36,37.
[34] Y. Zheng, R. Woodriff and J.A. Nichols, Anal. Chem., 56 (1984) 1388.
[35] D.A. Katskov, A.M. Shtepan, I.L. Grinshtein and A.A. Pupyshev, Spectrochim. Acta, Part B, 47 (1992) 1023.

ELSEVIER

Analytica Chimica Acta 291 (1994) 121–126

ANALYTICA CHIMICA ACTA

Indirect determination of polychlorinated organic compounds in environmental samples by molecular emission cavity analysis

Vladimir I. Rigin

Research and Design Institute for Problems of Development of the Kansk–Achinsk Coal Basin, 87 Kirensky Street, Krasnoyarsk 660041, Russian Federation

(Received 22nd June 1993; revised manuscript received 1st October 1993)

Abstract

A simplified indirect method for the determination of the total content of polychlorinated organic compounds in waters, soils and plants was developed using adapted versions of molecular emission cavity analysis based on measurements of the intensity of the emission band of indium monochloride at 359.9 nm. The compounds of interest were separated from the matrix by liquid–liquid extraction. The detection limit was 0.05 ng of chlorine. The proposed technique is suitable for the evaluation of the level of contamination of some environmental samples with polychlorinated organic pesticides and other similar pollutants.

Key words: Atomic emission spectrometry; Molecular emission cavity analysis; Pesticides; Plants; Polychlorinated organic compounds; Waters

1. Introduction

The presence of polychlorinated organic compounds in environmental samples indicates contamination with pesticides, herbicides and their residues [1], which is why the permanent control of the total content of these compounds in waters, soils and plants is of great importance in ecological analytical services.

Simple, inexpensive and accessible analytical methods for routine laboratories include potentiometry [2], coulometry [3], inverse polarography [4] and spectrophotometry [5]. However the practical applicability of these methods is questionable because of the serious interferences arising from other halogenated compounds and high limits of determination that prevent the determination of the pollutants at tolerable concentration levels. The most reliable method is chromatography combined with mass spectrometry [6], but it is very expensive and requires skilled operators.

Molecular emission cavity analysis (MECA) is a reliable technique for the determination of halogen-containing compounds [7,8], in view of the high selectivity and the simplicity of the apparatus. This method is based on measuring the intensity of emission bands of volatile monohalides of some metals (Cu, Ge, In, Ga, Sn and certain others) in cool diffusion-type hydrogen-containing flames. The halogens alone do not emit in such flames, and it is therefore necessary to convert the halides into a metal halide to obtain the metal halide emission. In one method halide-containing solutions were injected into a

SSDI 0003-2670(94)00005-7

cavity coated with the required metal and heated in an appropriate flame, so that the halogen atoms reacted with the metal coating of the inner surface of the cavity to form corresponding monohalides.

Indium offers the greatest promise for the determination of chlorine, because the molecular emission band of indium monochloride at 359.9 nm has a very high intensity and does not overlap significantly with the molecular emission bands of the other indium monohalides or other indium compounds [9].

It has been found that this simple version of MECA does not ensure the required sensitivity of determination as only a small proportion of the compound of interest has an opportunity to react with indium atoms to yield indium monochloride molecules, owing to the fairly low concentration of indium atoms in the gas phase in the cavity. To increase the sensitivity, various modifications of MECA can be used. One means of improving the reaction conditions consists in adding a preassigned amount of an indium compound to the sample solution. Thus, a high concentration of indium atoms is generated in the gas phase in the cavity. In another approach, one can feed into the cavity an excess of the vapour of a volatile chelate of indium, and thus the effective concentration of indium atoms in the gas phase increases by several orders of magnitude.

In this work, modified MECA methods for the determination of chlorine in combination with extraction recovery of the compounds of interest was used for a rapid, rough evaluation of the total contents of polychlorinated organic compounds in waters, soils and plants.

2. Experimental

2.1. Instrumentation

The basic design of the laboratory-built MECA spectrometer has been described elsewhere [10]. As a preselected spectral band (360 nm) is recorded, instead of an expensive monochromator a narrow-band interference filter was used (type UIFS-75 with maximum transmittance at 360 nm and a half-width of about 6 nm; Russian manufacture) in combination with a diffraction grating with 600 lines mm^{-1}. Such a combination eliminates any stray radiation in the analytical signal and ensures a wide linear dynamic range of measurements. For detection of radiation, an FEU-79 photomultiplier tube, installed in a cold housing that was thermostated at −60°C by dry-ice–acetone, was used. The anodic current of the photomultiplier was recorded by using a linear amplifier interfaced with an Elekzronika-60 microprocessor equipped with an I-5 integrator (all equipment of Russian manufacture). Such construction is compact and allows rapid determinations in the field.

As the analytical signal, the integral value of the intensity of the molecular emission, I_e, was used. It was calculated by integration of the anodic current of the photomultiplier for a period from the moment of appearance of the current signal until the anodic current returned to the conditional zero ("idling" value), and expressed in arbitrary units. As a calibration function, the specific integral value of the intensity of molecular emission, $(I_e)_s$, expressed in arbitrary units per nanogram of chlorine in an analysed aliquot of sample solution, was used.

For grinding and homogenization of solid samples (soils and plants), a Mikro-Dismembrator Type II (Braun, Melsungen, Germany) equipped with PTFE-lined grinding parts was used. The sample was cooled with liquid nitrogen and then ground for 15 min at an amplitude of vibration of about 1.5 cm.

A radiotracer study was carried out by using a 40-cm^3 Ge–Li detector interfaced with a B-2 count-rate digital integrator (Russian manufacture).

2.2. Procedures

Water samples are first filtered through a Type UAM-500 membrane filter (Russian manufacture) to remove suspended particles. The components to be determined are extracted from 500-ml samples with hexane using a device and technique as described by Murray [11]. Extraction is

carried out sequentially with three 2-ml portions of hexane. The obtained extracts are combined in a conical flask and dried with sodium wire. This treatment frees the extract from the last traces of inorganic chlorides that may pass into the hexane from the water sample.

In the first version of the modification of MECA measurements, the dry extract is introduced into a 10-ml volumetric flask, then a known amount of an organic indium compound in hexane is added and the solution is diluted to volume with dry hexane. This final hexane solution serves as the analytical concentrate for spectral measurements. An aliquot of the hexane analytical concentrate (0.20 ml) is smeared on the inner surface of the MECA cavity, the cavity is introduced into the flame and the analytical signal is measured.

In the second version of modification of MECA measurements, the dry extract is introduced into a 10-ml volumetric flask and diluted to volume with dry hexane. An aliquot of this solution (0.20 ml) is smeared on the inner surface of the MECA cavity and then, while a flow of vapour of indium chelate is fed into the cavity, the cavity is introduced into the flame and the analytical signal is recorded simultaneously.

Solid samples (plants and soils) are ground and analysed under conditions of natural moisture without preliminary drying in order to avoid any losses of compounds of interest. The required weight (about 5 g) of the ground sample material is placed in the sleeve of a Soxhlet extractor and polychlorinated organic compounds are extracted with 20 ml of hexane for 30 min. After cooling and separation of the phases, the hexane extract is treated as described above, using a 25-ml volumetric flask.

2.3. Recovery studies and reference samples

The completeness of the recovery of the analyte compounds from the investigated samples into the analytical concentrate was studied by a radiotracer method. In water analysis, synthetic reference samples containing polychlorinated organic compounds labelled with ^{36}Cl were used. As model compounds octachloronaphthalene, hexachlorobiphenyl and heptachlor (1,4,5,6,7,8,9-heptachloro-3a,4,7,7a-tetrahydro-4,7-methanindene, $C_{10}H_7Cl_7$) were used. Experiments with water samples spicked with these compounds demonstrated that triple extraction with hexane ensures a mean recovery of $93 \pm 5\%$. It was also established that polychlorinated organic compounds display no noticeable interaction with sodium wire.

The preparation of reference samples of plants follows the method of hydroponic cultivation of fast-growing plants using a feed solution that contains the above labelled compounds. By changing the concentrations of these compounds in the feed solution, plant samples with various contents of the compounds of interest can be obtained. It is important that the concentrations of contaminants in such samples should correspond to those occuring in natural plants. The synthetic sample obtained is treated as described above; the radioactivity levels in the starting material, the ultimate analytical concentrate and the residue in extractor after completion of the recovery procedure were measured. Using these results the recoveries were calculated to be $95 \pm 7\%$.

To verify the validity of the results obtained by the proposed technique, some samples were analysed by means of chromatography–mass spectrometry using the method recommended by the US EPA [12].

The two modifications of spectrometric measurement described above, which ensure the efficient concentration of indium atoms in the gas phase in the cavity, were used, one consisting of addition of any easily decomposed indium compound to the analytical concentrate before injection into the cavity, and the other the immediate feed of vapour of a volatile chelate of indium inside the cavity while measuring the molecular emission.

Performance of the first method presents no special problems because indium forms many hexane-soluble salts that are readily obtainable. It was established that the nature of such compounds has no effect on the intensity of the analytical signal, and the total concentration of indium in the analytical concentrate must be not

less than five times the expected concentration of chlorine.

A severe experimental difficulty is the choice of the indium chelate for obtaining a suitable vapour to feed into the cavity. The chelate to be used should have conflicting characteristics: it must be stable enough in the gas phase and yet be decomposed rapidly and easily on heating in the cavity. Preliminary experiments indicated that indium acetylacetonate and pivaloylmethanate are best suited for this purpose.

3. Results and discussion

Tables 1 and 2 give the values of the specific integral intensity of molecular emission, $(I_e)_s$, obtained under given experimental conditions for reference samples containing different combinations of labelled polychlorinated organic compounds, using the two modifications of MECA measurements. The emission intensities are independent of the nature of the compounds used but show considerable variations between the two methods. With direct feeding of indium chelate vapour into the cavity, the emission intensity is much stronger than when indium salt is introduced in the final analytical concentrate.

The instrumental detection limit found for pure hexane solutions of polychlorinated organic compounds averages about 0.05 ng of chlorine introduced into the cavity. The determination range (with a relative standard deviation of not more than 0.1%) is 0.2–500 of chlorine in aliquot.

Most of usual pesticides have chlorine contents between 30 and 60%, and therefore one can calculate the approximate content of polychlorinated compounds by doubling of found content of chlorine. If the nature of the pesticide to be determined is known, then its content may be determined more precisely.

Contents of polychlorinated organic compounds in samples of plants and soils taken from fields that had been treated with various individual pesticides are given in Tables 3 and 4. The same samples were also analysed independently by chromatography–mass spectrometry according to the US EPA method [12]. The good agreement between the results for the two methods is evidence for the reliability of the proposed method.

Table 5 contains results for the determination of polychlorinated organic compounds in waters from various springs. It should be particularly emphasized that the analyses were performed under field conditions, at the sampling sites, which obviates the need to conserve samples and eliminates the risk of losses of analytes and uncontrollable contamination of samples.

Table 1
Values of $(I_e)_s$ ($\bar{x} \pm ts/\sqrt{n}$), in arbitrary units per nanogram of chlorine, for various reference compounds and their combinations in plant and water samples, obtained by spectrometric measurements with addition of indium salt to the analytical concentrate ($n = 10$; $P = 0.95$)

Reference compound [a]	Sample	
	Plant	Water
A	75±5	77±5
B	73±5	82±6
C	81±6	74±5
A+B	75±4	81±5
A+C	71±5	81±4
A+B+C	81±6	82±6

Mean value of $(I_e)_s$, accepted for computation of results of analyses is equal to 78 arbitrary units per nanogram of chlorine in the measuring cavity.
[a] A = octachloronaphthalene; B = hexachlorobiphenyl; C = heptachlor.

Table 2
Values of $(I_e)_s$ ($\bar{x} \pm ts/\sqrt{n}$), in arbitrary units per nanogram of chlorine, for various reference compounds and their combinations in plant and water samples, obtained by spectrometric measurements with direct feed of indium chelate vapour into the cavity ($n = 10$; $P = 0.95$)

Reference compound [a]	Sample	
	Plant	Water
A	92±6	96±5
B	93±5	95±5
C	94±5	95±4
A+B	96±5	95±4
A+C	97±6	96±6
A+B+C	93±6	95±7

Mean value of $(I_e)_s$, accepted for computation of results of analyses is equal to 95 arbitrary units per nanogram of chlorine in the measuring cavity.
[a] A = octachloronaphthalene; B = hexachlorobiphenyl; C = heptachlor.

Table 3
Contents of pesticides in plants sampled from fields treated with individual pesticides ($n = 5$; $P = 0.95$)

Pesticide	Plant	Found ($\mu g\ g^{-1}$) [a]	
		Proposed method	Chromatography–mass spectrometry
Bayer 13/59	Beans	0.15 ± 0.02 [a]	0.13 ± 0.01
	Wheat corn	0.09 ± 0.01 [a]	0.08 ± 0.01
Heptachlor	Cucumber	0.08 ± 0.01 [a]	0.07 ± 0.01
	Potatoes	0.11 ± 0.02 [a]	0.12 ± 0.01
	Tomato	0.15 ± 0.03 [b]	0.11 ± 0.01
Lindane	Cabbage	0.46 ± 0.08 [b]	0.41 ± 0.03
	Potatoes	0.71 ± 0.13 [a]	0.57 ± 0.08
Polychloro-pinene	Peas	0.09 ± 0.02 [b]	0.08 ± 0.005
	Potatoes	0.05 ± 0.01 [b]	0.04 ± 0.01
	Sugar-beet	0.03 ± 0.01 [a]	0.01 ± 0.005
Trichlorometh-aphos-3	Cabbage	0.95 ± 0.11 [a]	0.96 ± 0.07
	Cucumber	1.14 ± 0.13 [b]	1.05 ± 0.09

[a] $\bar{x} \pm ts/\sqrt{n}$.
[b] Method: addition of indium salt to analytical concentrates.
[c] Method: direct feeding of indium chelate vapour into cavity.

In most instances there is no need to know the precise values of the concentrations of polychlorinated organic compounds in the investigated samples, as it is sufficient to estimate level of pollution in relation to tolerable levels. The proposed technique allows this to be achieved by using inexpensive and simple apparatus, with a mean duration of analysis of less than 1 h.

Table 4
Results of analysis of soils treated with individual pesticides ($n = 5$; $P = 0.95$)

Pesticide	Found ($\mu g\ g^{-1}$) [a]	
	Proposed method	Chromatography–mass spectrometry
Bayer 13/59	1.12 ± 0.18 [b]	1.05 ± 0.08
	1.09 ± 0.11 [c]	
Heptachlor	0.27 ± 0.02 [b]	0.17 ± 0.01
Lindane	0.85 ± 0.15 [c]	0.81 ± 0.06
Polychloropinene	0.44 ± 0.09 [b]	0.47 ± 0.04
	0.45 ± 0.06 [c]	
Trichlorometaphos	0.69 ± 0.15 [b]	0.62 ± 0.05
Hexachlorobiphenyl [d]	75 ± 17 [b]	69 ± 5
	77 ± 18 [c]	

[a] $\bar{x} \pm ts/\sqrt{n}$.
[b] Method: addition of indium salt to analytical concentrate.
[c] Method: direct feeding of indium chelate vapour into cavity.
[d] Soil pollution as a result of an accident in a transformer substation.

Table 5
Determination of total content of polychlorinated organic compound in water from various springs ($n = 5$; $P = 0.95$)

Site of sampling	Found ($mg\ l^{-1}$) [a]	
	Proposed method	Chromatography–mass spectrometry
Lake Shira	1.7 ± 0.3 [b]	1.45 ± 0.08
	1.52 ± 0.12 [c]	
Lake Svaticovo	0.38 ± 0.05 [b]	0.35 ± 0.02
Lake Uchum	1.8 ± 0.5 [b]	1.62 ± 0.07
River Chulym	2.8 ± 0.5 [b]	2.55 ± 0.09
	2.65 ± 0.15 [c]	
River Kizir	0.05 ± 0.02 [b]	0.01 ± 0.005
River Tom	52 ± 9 [b]	46 ± 3
River Yenisei	0.91 ± 0.15 [b]	0.89 ± 0.06
	0.90 ± 0.06 [c]	

[a] $\bar{x} \pm ts/\sqrt{n}$.
[b] Method: addition of indium salt to analytical concentrate.
[c] Method: direct feeding of indium chelate vapour into cavity.

Acknowledgement

The author is grateful to Dr. G.G. Alekseev for performing chromatographic–mass spectrometric measurements.

References

[1] H. Maier-Bode, Herbizides und ihre Rückstände, Ulmer, Stuttgart, 1971.
[2] I. Neupert, Acta Hydrochim. Hydrobiol., 11 (1983) 595.
[3] R.C.C. Wegman and P.A. Greve, Sci. Total Environ., 7 (1977) 235.
[4] N.S. Rajkov, M.S. Zacharov and A.V. Guntzov, Zh. Anal. Khim., 43 (1988) 666.
[5] D.T.E. Hunt and A.L. Wilson, The Chemical Analysis of Water. General Principles and Techniques, Royal Society of Chemistry, London, 1986.
[6] M.A. Brown (Ed.), Liquid Chromatography / Mass Spectrometry: Application in Agricultural, Pharmaceutical and Environmental Chemistry, American Chemical Society, Washington, DC, 1990.
[7] R. Belcher, S.L. Bogdanski, E. Henden and A. Townshend, Anal. Chim. Acta, 92 (1977) 33.

[8] M. Burguera, S.L. Bogdanski and A. Townshend, CRC Crit. Rev. Anal. Chem., 10 (1981) 185.
[9] K. Dittrich, CRC Crit. Rev. Anal. Chem., 16 (1986) 223.
[10] V.I. Rigin, Zh. Anal. Khim., 40 (1985) 1312; 42 (1987) 1778.
[11] D.A. Murray, J. Chromatogr., 177 (1979) 135.
[12] Manual of Analytical Methods for the Analysis of Pesticide Residues in Human and Environmental Samples, US Environmental Protection Agency, Washington, DC, 1979.

ELSEVIER

Analytica Chimica Acta 291 (1994) 127–136

ANALYTICA CHIMICA ACTA

Graphite furnace hydride preconcentration and subsequent detection by inductively coupled plasma mass spectrometry

Isam Marawi, Jiansheng Wang, Joseph A. Caruso *

Department of Chemistry, University of Cincinnati, Cincinnati, OH 45221-0172, USA

(Received 18th October 1993; revised manuscript received 5th January 1994)

Abstract

Preconcentration of multi-element volatile hydrides in a graphite furnace and the subsequent determination by inductively coupled plasma mass spectrometry (ICP-MS) is a relatively new method for elemental analysis. This method offers several advantages over direct hydride generation sample introduction. In this technique the excess hydrogen generated as a by-product of the reduction reaction of the analytes was not introduced into the plasma with the analytes, thus giving the plasma greater stability. The hydrides of arsenic, bismuth, and tellurium were trapped in the presence of metallic palladium inside the graphite tube of an electrothermal vaporization unit, and subsequently determined by the ICP-MS in a single run. The linearity obtained using this method was limited to a sub-ng/ml concentration range. The preliminary limit of detection calculated for arsenic is 0.002 ng ml^{-1}, this value was based on the slope value of the linear portion of the calibration curve. Effectiveness of the trapping method was determined by analysis of a standard reference material.

Key words: Inductively coupled plasma mass spectrometry; ETV graphite furnace; Hydride preconcentration; Preconcentration

1. Introduction

In recent years, the demand to find lower limits of detection for elements with environmental significance has been greater than ever before. Several elements which are considered an environmental hazard, and which can form volatile hydrides include As, Sn, Pb, Bi, Se and Te. The advantages of the hydride generation technique for sample introduction in atomic spectrometry have been described in several reviews [1–5].

One advantage of hydride generation is the ability to preconcentrate the analytes before they reach the atomizer. The method most often used for hydride preconcentration is the cold trapping technique, which was first introduced by Holak [6]. In this method the volatile products of the hydride generation reaction are purged through a liquid nitrogen trap. The hydride analyte condenses inside the trap while the hydrogen by-product vents. After the reaction is complete the trap is removed from the liquid nitrogen and heated rapidly to revolatilize the hydride. An argon purge carries the hydride from the trap into the atomizer. The rapid volatilization of the

* Corresponding author.

SSDI 0003-2670(94)00030-P

hydrides is a convenient way to introduce the analytes into the atomizer as a plug, consequently lower concentration limits of detection for those elements are achievable. However, the cold trapping method is limited due to poor recoveries of some elements after the trapping step [7].

Another method that can be employed for preconcentrating volatile hydrides is graphite furnace trapping. This technique, which has been discussed in earlier publications [7–12], relies on the fact that the gaseous hydrides of certain elements can be adsorbed on a hot graphite surface. The graphite furnace trapping method has gained popularity because of the high sample transport efficiency with in situ atomization and detection by atomic absorption spectroscopy (AAS). Lee [7] collected bismuth hydride in a modified carbon rod atomizer and reported collection efficiencies of 72%. Andreae [8] trapped tin hydride inside an unpyrolyzed graphite tube. However, most of the trapping efficiency was lost when a pyrolytically coated tube was used. Sturgeon et al. used the trapping technique to determine arsenic [9], tin [10] and lead [11]. In later work [12] they reported improved analytical figures of merit for the trapping technique by adding palladium metal as a modifier to the graphite furnace.

Inductively coupled plasma mass spectrometry (ICP-MS) has gained in popularity for trace elemental analysis over the last decade. Element specificity, low limits of detection, and multi-element determination capability are some of the advantages of this technique. Heitkemper and Caruso [13] combined continuous hydride generation with ICP-MS using a nebulizer and water cooled spray chamber as a gas–liquid separator. This method had the advantage of determining hydride-forming elements and non-hydride forming elements simultaneously. A concentration limit of detection of 17 pg ml^{-1} for arsenic was reported, one order of magnitude lower than the limit of detection reported for pneumatic nebulization without the hydride generation. However, the molecular hydrogen, which was the reduction reaction by-product, is also introduced into the plasma. The presence of the excess hydrogen in the plasma alters its ionization efficiency and stability. Also, the presence of chloride in the sample produced an isobaric interference with the determination of arsenic at mass-to-charge ratio (m/z) 75, due to the formation of the polyatomic ion $^{40}Ar^{35}Cl^{+}$ in the plasma. Several investigators [14–16] were successful in eliminating the $^{40}Ar^{35}Cl^{+}$ interference by preventing the chloride ion from reaching the plasma. They used a porous membrane as an in-line gas–liquid separator. These membranes allowed only the volatile products to reach the plasma.

Combining electrothermal vaporization (ETV) sample introduction with ICP-MS, should result in low absolute limits of detection. However, this method is volume limited to a maximum of 50 μl, and a preconcentration step is often required. Carey et al. [17] used a modified Perkin-Elmer graphite furnace for ETV sample introduction with the ICP-MS. An absolute detection limit of 1.5 pg for arsenic was reported using nickel nitrate as a matrix modifier.

The purpose of the present work was to examine the utility of preconcentrating the hydrides inside the graphite furnace with ICP-MS detection. This paper describes the instrumental setup, and presents details of the analytical procedure for the determination of arsenic and other volatile hydride forming elements. It also evaluates the analytical performance of the proposed technique and compares the results with those obtained using the direct hydride generation ICP-MS and the typical ETV-ICP-MS separately.

2. Experimental

2.1. Apparatus

The ICP-MS instrument was a VG PlasmaQuad PQ I (VG Elemental, Winsford, UK). Data were collected and analyzed by the instrument software, and manipulated by software written in-house. Some of the optimization work was carried out using a home-built inductively coupled plasma atomic emission instrument (ICP-AES). The ICP-AES radio frequency (RF) generator, the automatching network, and the control unit were from PlasmaTherm (PlasmaTherm, Kreeson, NJ). The monochromator, photomulti-

plier tube and the data collection software were obtained from Spex (Metuchen, NJ).

A modified graphite furnace unit (HGA 300, Perkin-Elmer, Norwalk, CT) was used for this work and has been described in an earlier publication by Carey et al. [17]. A further modification for this work was the addition of a two-way valve at the front end adapter of the unit. This valve controlled the introduction of the hydride carrier gas into the graphite furnace. The graphite tube was a typical pyrolytically coated tube without the sample introduction hole (Perkin-Elmer, Norwalk, CT).

The gas–liquid separator (GLS) is shown schematically in Fig. 1. The glass sleeve was similar to the design reported by Barnes and Wang [15] and Story et al. [16]. The sleeve was 7.0 mm i.d. and the distance between the two sidearms was 10 cm (DANA Enterprises Scientific Glass Blowing, West Chester, OH). The microporous membrane material used was Celgard hollow fiber (Celgard material, Hoechst Celanese, Charlotte, NC) with an internal diameter of 0.4 mm. This material had a reported bulk pore size of 0.075 μm and porosity of 40%. Six strands of the hollow fiber membrane were bundled and glued (Cyanoacrylate Adhesive 7432, Bostic, Middleton, MA) inside a PTFE reaction tube (10 cm × 2.0 mm i.d.). The exposed part of the membrane bundle was placed inside the glass sleeve of the GLS. The other end of the membrane was open to a waste container. The unit was made airtight by sealing both ends of the glass sleeve with epoxy. The reaction tube was connected to an Omnifit mixing tee, where the reagent and the analyte solutions were mixed. The flow of both the reagent and analyte solutions were provided by a two channel peristaltic pump (Gilson, Middleton, WI).

2.2. Reagents and standards

Both the hydrochloric acid (12 M, Instra-analyzed Reagent, Baker, Phillipsburg, NJ), and the nitric acid (70%, Reagent certified ACS, Fisher Scientific, Fairlawn, NJ) solutions were prepared by dilution with distilled deionized water (resistance 18 mΩ, Barnstead PCS, Boston, MA), to the desired concentrations. Sodium tetrahydroborate $NaBH_4$ solution was prepared fresh daily by dissolving 99% $NaBH_4$ powder (Analytical grade, Johnson Matthey, Ward Hill, MA) in a solution of 0.1 M NaOH (ACS, Reagent, Fisher Scientific, Fairlawn, NJ). Arsenic, tel-

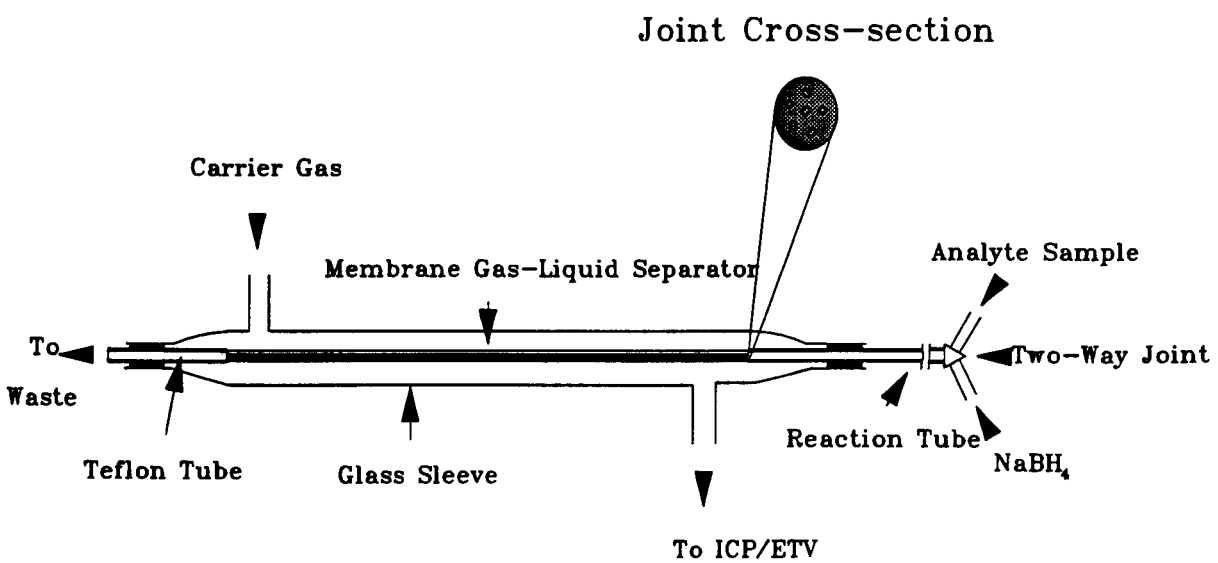

Fig. 1. Schematic of the in-line gas–liquid separator.

lurium and bismuth standard solutions were prepared by serial dilution from 1000 μg ml^{-1} stock (atomic absorption standard solution, Aldrich, Milwaukee, WI). The palladium nitrate solution was 2.0 mg/ml in 7% HNO_3 (Inorganic Ventures, Lakewood, NJ), and was used as a modifier.

2.3. Sample

Freeze-dried urine standard reference material (SRM 2670, NIST, Gaithersburg, MD) was reconstituted in 2% nitric acid following NIST instructions. A sample of the reconstituted solution was mixed with the palladium nitrate and used in the typical ETV work only. Another sample of the reconstituted solution was diluted 100 fold by mixing it with 4 M HCl solution, and was used in the direct hydride generation work. A third sample was diluted 1000 fold giving a final concentration of 0.4 ng ml^{-1} arsenic and was used in the hydride trapping.

2.4. Typical ETV-ICP-MS

A 10-μl aliquot of the analyte mixed with modifier solution was introduced on the L'vov platform inside the graphite furnace through the unit's front adapter opening using a micropipette (Eppendorf 4710, Brinkmann Instruments, Westbury, NY). The front adapter was then securely replaced, and the argon carrier gas purged the furnace. The temperature program for the ETV experiment is listed in Table 1a. This program consisted of six temperature steps. Initially, two drying steps evaporated all organic and aqueous solvents. An ashing step at 1200°C drove off all organic solids from the sample. The atomization step evaporated all analytes and carried them into the plasma. Finally, a two step cleaning procedure cleared out all residues to prepare the furnace for the next sample. The drying vent on the rear adapter was kept open to the atmosphere during the drying steps of the program. Ten seconds after the ashing temperature was

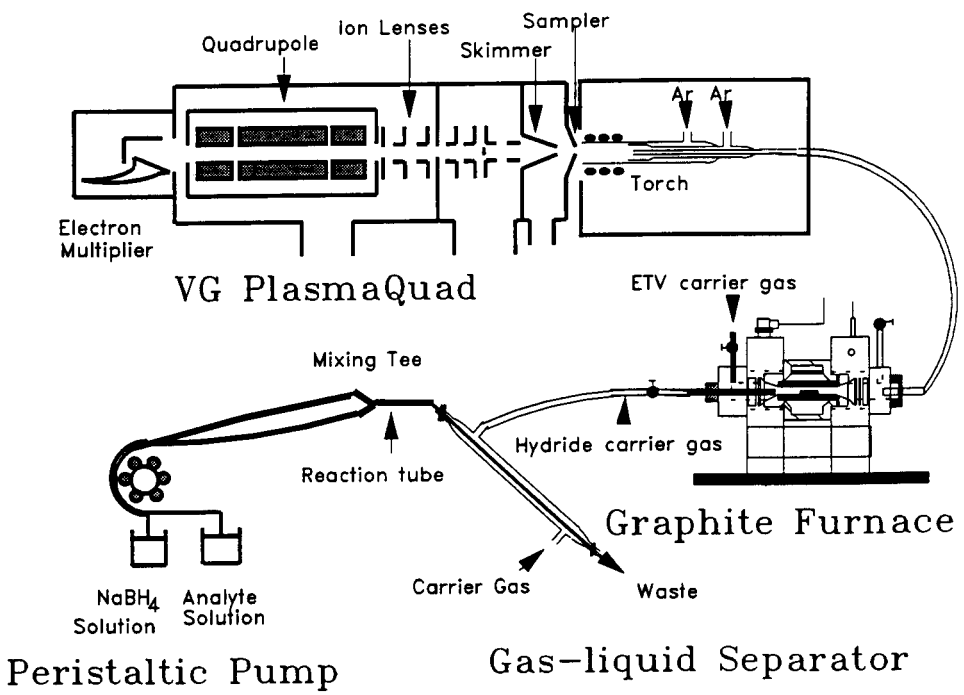

Fig. 2. Schematic of the instrument setup used for the hydride trapping ETV-ICP-MS.

Table 1
ETV controller programs

Program a: typical ETV				
Step No.	Step	Temp. (°C)	Ramp time (s)	Hold time (s)
1	Drying 1	90	10	30
2	Drying 2	170	10	30
3	Ashing	1200	10	30
4	Atomization	2300	1	10
5	Clean 1	1000	3	5
6	Clean 2	2650	3	1

Program b: hydride trapping ETV					
Step No.	Step	Temp. (°C)	Ramp time (s)	Hold time (s)	Cooling vent [a]
1	Dry	130	10	30	open
2	Trap	400	10	30	open
3	Ash	1200	10	30	open
4	Atomize	2300	1	10	closed
5	Clean 1	1000	3	5	closed
6	Clean 2	2650	3	1	closed

[a] Cooling vent open means that the gases are venting to the atmosphere and closed that the gases are venting to the plasma.

reached, the vent valve was opened to the plasma, and remained open until the program was complete.

2.5. Direct hydride generation ICP-MS

Reaction with borohydride in acid solution was used for the continuous formation of the hydrides. A two-channel peristaltic pump was used to feed both the analyte and reagent solutions at the same flow rate into a three-way mixing tee. The reduction reaction began when the two solutions came into contact and continued through the length of the reaction tube. The gaseous products (hydrides and excess hydrogen) were carried to the plasma through the GLS membrane with the purging argon gas. Liquids were drained from the GLS into a waste container at the other end of the membrane.

2.6. Hydride trapping ETV-ICP-MS

For hydride trapping the carrier gas outlet from the gas–liquid separator was connected to the two-way valve on the front adapter of the graphite furnace unit. Fig. 2 shows a schematic of the experimental set up. Ten μl palladium nitrate solution (20 μg) was deposited directly on the L'vov platform inside the furnace in the same manner the sample was introduced for the typical ETV study. The temperature controller program used in this part of the experiment was a modification of that used with the typical ETV study (Table 1b). The temperatures of the first and second step were changed to 130°C and 400°C respectively. The hydrides were introduced into the furnace by opening the hydride carrier gas valve, during the second step. Finally, at the end of this step the valve was closed, the ETV carrier gas was introduced, and the drying vent was opened to the plasma.

3. Results and discussion

3.1. Signal optimization

ICP-MS parameters were optimized for maximum arsenic signal at $m/z = 75$. The single ion monitoring (SIM) mode was used for the optimization of the detector response while arsine was continuously introduced into the plasma. The optimized conditions are listed in Table 2. The carrier gas flow rate was optimized separately for each method.

3.2. Hydride generation ICP-MS

The conditions for the hydride generation reaction were optimized for arsine generation. The effects of the acid and reagent concentrations on the hydride signal were tested over a wide range of concentrations. The optimum conditions were found to be similar to those reported in the literature [18]. The reagent ($NaBH_4$) concentration used was 1% (w/v) in 0.1 M NaOH. A 4 M HCl solution was used for the analyte matrix throughout the work. The optimum solution flow rate was found to be 1.30 ml min^{-1}. Fig. 3 (solid bars) shows the effect of the carrier gas flow rate on the arsenic signal, 500 ml min^{-1} which yielded the largest peak area. A short reaction tube (10

cm long) was used to minimize interference by transition metals with the analytes in the gaseous phase [19–21]. The analysis of the waste solution collected from the GLS found no significant amount of arsenic.

3.3. Typical ETV-ICP-MS

When ETV was used for sample introduction the signal was obtained using the single ion monitoring (SIM) mode of the mass spectrometer. This mode of detection allowed the observation of the analyte signal as a function of time. The effect of palladium as a matrix modifier on the analyte signal was examined in this study. The optimum concentration in the final analyte solution was determined to be 0.4 mg ml^{-1}. An undesired analyte peak produced during the second cleaning step of the controller program was eliminated at an atomization temperature of 2300°C. The effect of the argon carrier gas flow rate on the analyte signal was determined. Fig. 3 (cross-hatched bars) shows that 130 ml min^{-1} produced the best signal. The effect of the cooling gas flow rate on the analyte signal was found to be similar to the one reported by Carey et al. [17].

Table 2
Plasma and mass spectrometer operating conditions

Plasma	
Argon coolant gas flow	17 l/min.
Argon auxiliary gas flow	1.0 l/min.
Argon nebulizer gas flow	0.750 l/min.
Forward RF power	1500 W
Reflected RF power	< 1 W
Mass spectrometer	
Sampling depth	12 mm [a]
Sampler cone orifice	1 mm
Skimmer cone orifice	1 mm
Analyzer pressure	4×10^{-6} mbar
Expansion stage pressure	1.4 mbar
Intermediate stage pressure	10^{-4} mbar
Scanning conditions	
Dwell time	160 ms
Number of scans	100
Points per peak	3
SIM Conditions	
Dwell time	81920 ms
Number of channels	2048
Total time	168 s
TRA conditions	
Dwell time	10240 ms
Number of scans per peak	5
Points per peak	3
Detector	pulse

[a] Defined as the distance between the top coil of the load coil and the tip of the sampling cone.

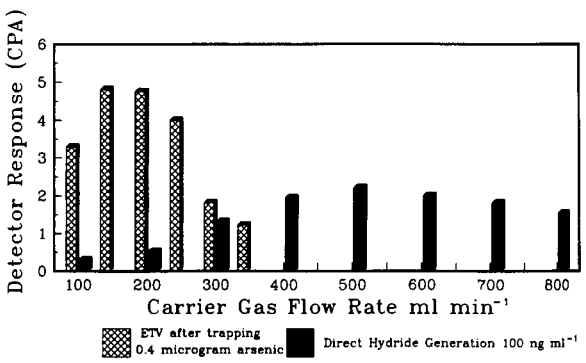

Fig. 3. The effect of the carrier gas flow rate on the analyte signal; solid bars, represent direct hydride generation method, and cross-hatched bars represent ETV method after trapping the analyte.

3.4. Hydride generation with trapping ETV-ICP-MS

The optimum conditions determined separately for arsine generation, and the electrothermal vaporization sample introduction technique were employed for the trapping method. Other parameters such as trapping temperature and amount of palladium were also optimized.

Fig. 4 shows the signal obtained when 400 ng of arsenic were trapped on the bare walls of a new pyrolytically coated graphite furnace. The plot clearly indicated that arsenic had no significant interaction with this type of surface. Fig. 5 shows the As signal after the deposition of 20 μg of palladium in solution on the L'vov platform inside the same furnace. The flat background, followed by the sharp peak at the atomization step is evidence that arsenic was trapped by the palladium. The two graphs in Figs. 4 and 5 were obtained while the drying vent on the back adapter of the graphite furnace unit was open to the plasma.

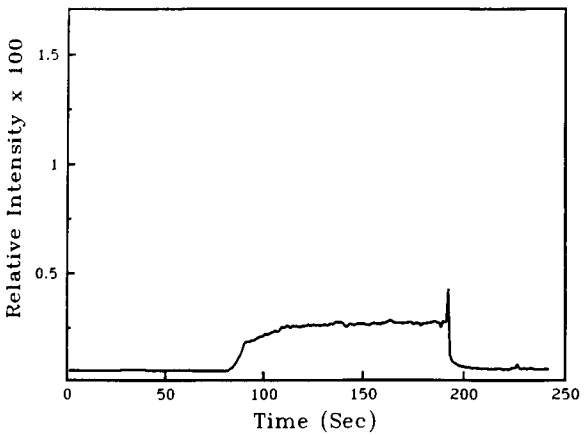

Fig. 4. Arsenic signal obtained from an attempt to trap 0.4 μg arsine on the bare walls of the pyrolytically coated graphite furnace at 400°C. The drying vent on the back adapter of the furnace unit was closed throughout the experiment. The trapping step was for 120 s, and the total volume was 2.0 ml.

The effect of the amount of palladium utilized on the analyte signal was examined (Fig. 6). The analyte signal intensity increased with the increase of palladium mass deposited and levelled off at 20 μg Pd. The effect of the trapping temperature on the analyte signal is shown in Fig. 7. The optimal temperature was found at 400°C. This finding agrees with the recently published data by An et al. [22], however, it disagrees with that reported earlier, i.e., that temperatures between 200°C and 800°C have no significant effect on the trapping efficiency [12,23].

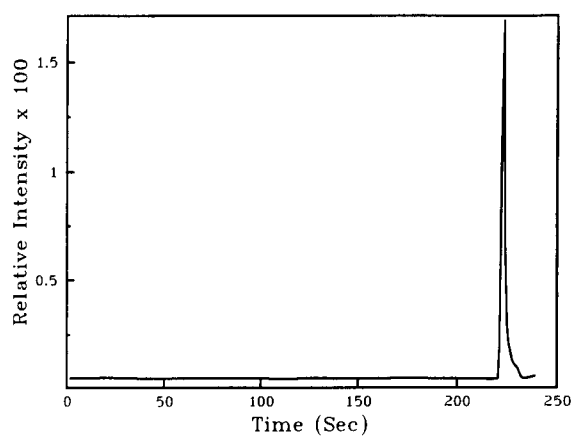

Fig. 5. Signal obtained under the same conditions as in Fig. 4 after the deposition of 20 μg of palladium inside the graphite furnace.

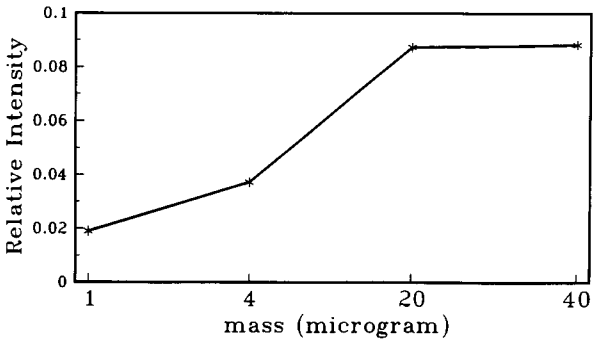

Fig. 6. Effect of palladium mass utilized for the trapping on the signal obtained from 400 ng arsenic used for the hydride trapping.

3.5. Analytical figures of merit

The limit of detection (LOD) was calculated based on LOD = $3\sigma/m$, where σ is the standard deviation of eight measurements on a blank and m is the slope from the calibration graph. The precision of each method was determined by measuring the relative standard deviations (R.S.D.) of a minimum of four replicates of a standard used in the calibration graph. Standard solutions containing various concentrations of arsenic were used to obtain the calibration curves. Table 3 presents the figures of merit obtained in each method for comparison purposes.

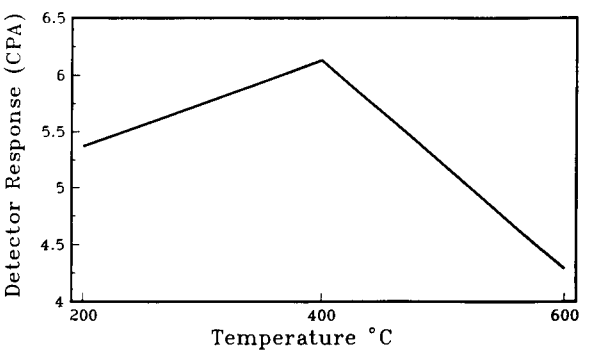

Fig. 7. The effect of the trapping temperature on the analyte signal.

3.6. Hydride generation

The arsenic concentration limit of detection obtained in this study was 0.015 ng ml^{-1}, in agreement with the value reported earlier in this laboratory [13]. The logarithm values of the detector response were plotted versus the logarithm values of the standard concentration log–log plot (Fig. 8a). The slope of the best fitted line of this graph was 0.99. The range of standard concentrations used to construct this graph was 1–100 ng ml^{-1}. The precision of this method was determined, and the R.S.D. value obtained was $< 3\%$ for six measurements of 10 ng/ml arsenic concentration.

3.7. Typical ETV-ICP-MS

The absolute limit of detection obtained for arsenic in this work was 1.9 pg. Because the sample volume was 10 μl, this value corresponds to a concentration limit of detection of 0.19 ng ml^{-1}. The slope from the log–log plot shown in Fig. 8b was 1.06, and was obtained over a range of standard concentrations from 1–1000 ng ml^{-1}. The R.S.D. value was $< 10\%$, and was obtained for six replicates at 10 ng ml^{-1} arsenic concentration.

3.8. Hydride trapping ETV-ICP-MS

Under the optimum trapping conditions mentioned above a calibration curve for arsenic was obtained using standard solutions containing 0.01–10 ng ml^{-1} concentrations. Fig. 8c shows the log–log plot, with the slope of the best fitted line of less than 0.7, indicating a nonlinear behaviour. Greater linearity is achievable at lower concentrations. Presumably this deviation from linearity was due to a loss of trapping efficiency at higher analyte concentrations. The collection rate of the analytes was limited by the palladium surface area and the number of active sites available. This presumption was supported by the fact that both the direct hydride generation and the typical ETV techniques gave linear responses over a similar range of concentrations. A limit of detection based on the slope value of the linear portion of the calibration curve (0.01–0.1 ng ml^{-1}) was calculated and has a value of 0.002 ng ml^{-1}. The R.S.D. value obtained was about 17% for six replicates at 0.01 ng ml^{-1} concentration. This LOD value which was obtained when utilizing the preconcentration step suggests an improvement of one order of magnitude may be available.

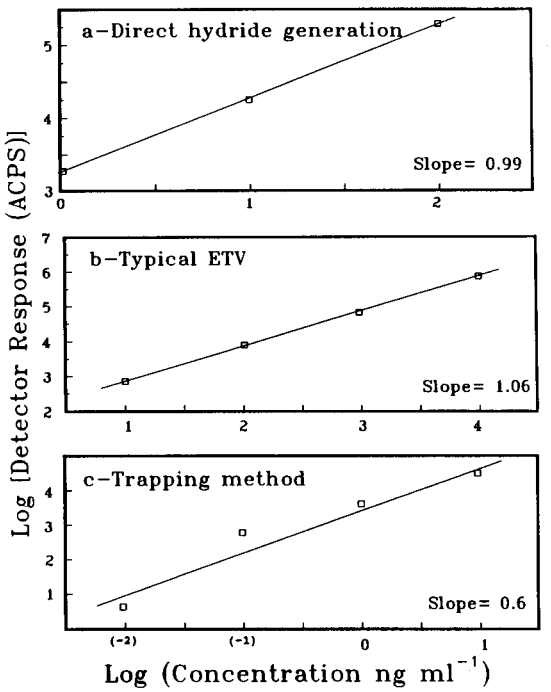

Fig. 8. The linearity of each method presented as a log–log plot of the standard response curve.

Table 3
Figures of merit obtained with the various methods

Method	Conc. LOD (ng/ml)	Absolute LOD (ng)	LDR (ng/ml)	R.S.D. [a] (%)
ETV-ICP-MS	0.190	0.0019	1–1000	< 10
HG-ICP-MS	0.015	–	1–1000	< 3
HG-Pd trap.-ETV-ICP-MS	0.002 [b]	–	0.01–0.1	< 17

[a] Based on minimum of six samples repetition.
[b] Based on the linear portion of the standard curve (see text).

Table 4
Arsenic concentration in standard reference material (SRM 2670) (freeze-dried urine)

Method	Concentration (mg ml^{-1}) [a]
Certified value	0.48 ± 0.10
ETV-ICP-MS	0.41 ± 0.16
HG-ICP-MS	0.44 ± 0.04
HG-Pd trap.-ETV-ICP-MS	0.40 ± 0.15

[a] All values are average ± 2σ.

3.9. Sample analysis

The analytical accuracy of preconcentrating the volatile hydride inside a graphite furnace, was examined by the determination of arsenic concentration in the SRM freeze-dried urine. The results obtained were comparable to the certified value. Table 4 lists the arsenic concentrations obtained with this method as well as those obtained from the direct hydride generation and the ETV. These values were presented as an average of eight runs plus/minus two standard deviations.

3.10. Multi-element analysis

A 1 ng/ml solution of As, Bi and Te mixture was tested by the hydride trapping ETV-ICP-MS to verify the method's ability for multi-element determination. Fig. 9 shows the peaks obtained from the mixture (0.6 ng each of As, Bi and Te). The mixture hydride was generated under the conditions optimized only for arsine generation. The trapping step used was also similar to that described earlier for arsine. The three analytes were atomized at the same time during the atomization step of the ETV program. The time resolved acquisition (TRA) mode of the mass spectrometer was used for the simultaneous quantification of the three elements. The detector displayed the results as a total-ion beam and each single mass was extracted from the total-ion beam.

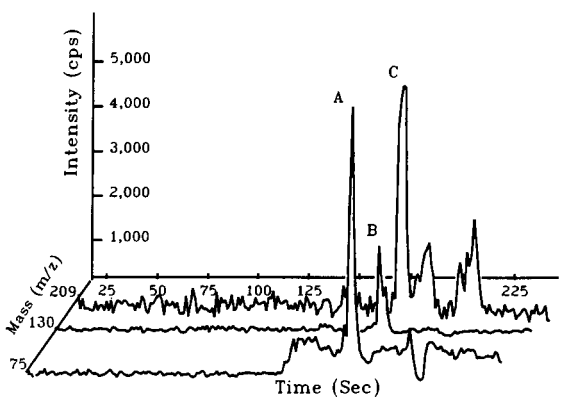

Fig. 9. One ng ml^{-1} solution of arsenic, bismuth and tellurium monitored by the hydride trapping ETV-ICP-MS in the time resolved acquisition (TRA) mode. The trapping step was for 30 s. Peaks: A, ^{75}As; B, ^{130}Te; C, ^{209}Bi.

4. Conclusions

The results obtained in this work show that the best trapping of the analytes on an ETV was possible only in the presence of palladium and at lower analyte concentrations (pg ml^{-1}). The preconcentration by trapping improved the detectability of the volatile hydride forming elements by an order of magnitude. A signal from 10 pg ml^{-1} arsenic solution was detectable with relatively good reproducibility. Detection of multiple elements by the hydride trapping method using ICP-MS capability was demonstrated. More work is needed to improve the trapping efficiency for samples containing multiple elements of interest at wider concentration range. Future work will also address the possibility of automating the technique and improving the sample throughput.

Acknowledgements

Support for this project is acknowledged through Grant No. ES 04908 from the National Institute of Environmental Health Sciences (NIEHS). The authors acknowledge the Hoechst Celanese Co. for the Celgard membrane gift. I.M. would like to give a special thanks to Marie G. Marawi for her valuable efforts in proofreading the manuscript.

References

[1] D.T. Heitkemper, K.A. Wolnik, F.L. Fricke and J.A. Caruso, in A. Montaser and D.W. Golightly (Eds.), Inductively Coupled Plasma in Analytical Atomic Spectrometry, VCH, New York, 2nd edn., 1992, Chap. 17, p. 781.
[2] J.A. Caruso, K.A. Wolnik and F.L. Fricke, in A. Montaser and D.W. Golightly (Eds.), Inductively Coupled Plasma in Analytical Atomic Spectrometry, VCH, New York, 1987, Chap. 13, p. 487.
[3] T. Nakahara, Prog. Anal. At. Spectrosc., 6 (1983) 163.
[4] M. Janghorbani and B.T.G. Ting, Anal. Chem., 61 (1989) 701.
[5] W.C. Story and J.A. Caruso, in Z.B. Alfassi and C.M. Wai (Eds.), Preconcentration Techniques for Trace Elements, CRC Press, Boca Raton, FL, 1992, Chap. 11, p. 333.
[6] W. Holak, Anal. Chem., 41 (1969) 1712.
[7] D.S. Lee, Anal. Chem., 54 (1982) 1682.
[8] M.O. Andreae, Anal. Chem., 56 (1984) 2064.
[9] R.E. Sturgeon, S.N. Willie and S.S. Berman, J. Anal. At. Spectrom., 1 (1986) 115.
[10] R.E. Sturgeon, S.N. Willie and S.S. Berman, Anal. Chem., 59 (1987) 2441.
[11] R.E. Sturgeon, S.N. Willie and S.S. Berman, Anal. Chem., 61 (1989) 1867.
[12] R.E. Sturgeon, S.N. Willie, G.I. Sproule, P.T. Robinson and S.S. Berman, Spectrochim. Acta, 44B (1989) 667.
[13] D.T. Heitkemper and J.A. Caruso, Appl. Spectrosc., 44 (1990) 228.
[14] S. Branch, W.T. Corns, L. Ebdon, S. Hill and P. O'Neill, J. Anal. At. Spectrom., 6 (1991) 155.
[15] R.M. Barnes and X.J. Wang, Anal. At. Spectrom., 3 (1988) 1083.
[16] W.C. Story, J.A. Caruso, D.T. Heitkemper and L. Perkins, J. Chromatogr. Sci., 30 (1992) 427.
[17] J.M. Carey, E.H. Evans and J.A. Caruso, Spectrochim. Acta, 46B (1991) 1711.
[18] M. Thompson, B. Pahlavanpour, S.J. Walton and G.F. Kirkbright, Analyst, 103 (1978) 568.
[19] B. Welz and M. Melcher, Analyst, 109 (1984) 569.
[20] M. Yamamoto, M. Yasuda and Y. Yamamoto, Anal. Chem., 57 (1985) 1382.
[21] A. Brockmann, C. Nonn and A. Golloch, J. Anal. At. Spectrom., 8 (1993) 397.
[22] Y. An, S.N. Willie and R.E. Sturgeon, Spectrochim. Acta, 47B (1992) 1403.
[23] Z. Li, S. McIntosh, G.R. Carnrick and W. Slavin, Spectrochim. Acta, 47B (1992) 701.

ELSEVIER

Analytica Chimica Acta 291 (1994) 137–140

ANALYTICA CHIMICA ACTA

Cold decomposition procedure for the spectrophotometric determination of manganese in rocks, ores and minerals

C.R.M. Rao

Chemical Laboratory, Geological Survey of India, Guindy, Madras 600 032, India

(Received 20th September 1993; revised manuscript received 30th November 1993)

Abstract

A cold decomposition procedure for the spectrophotometric determination of manganese in rocks, ores and minerals is described. Samples are allowed to react with hydrofluoric acid and aqua regia at room temperature for 24 h. Fluoride ions in the solution are complexed with boric acid and manganese is determined spectrophotometrically using potassium periodate as the reagent. No interferences were observed in the colour development and accurate values were obtained for a number of international reference standards. The entire decomposition procedure is carried out at room temperature utilizing only plastic ware. The method is ideal for large batch analyses.

Key words: Spectrophotometry; Geological materials; Minerals; Ores; Manganese

1. Introduction

The decomposition of silicate materials for the determination of manganese can be effected by evaporation to fumes with a mixture of nitric, sulphuric and hydrofluoric acid and the fusion of the resulting residue if necessary with potassium pyrosulphate [1,2]. In these methods, a heating step is necessary for decomposition and complete removal of fluoride ions has also to be ensured as they interfere in the colour development of manganese.

In the method proposed here, the samples are allowed to react with aqua regia and hydrofluoric acid at room temperature for 24 h and the fluoride ions are complexed by the addition of boric acid [3–5]. The need to remove fluoride ions by heating is thus avoided. Manganese is determined spectrophotometrically in the resulting solution as permanganate using potassium periodate as the oxidising agent. It was observed that fluoroborate ions have no deleterious effect on the colour development of manganese with periodate. An absorption maximum was obtained at 530 nm. Even a high-grade manganese ore such as SARM-16, containing 53.0% Mn, was found to yield a clear solution by this method, indicating its complete decomposition.

The accuracy of the method was established by analysing international standards. The reproducibility of the manganese values obtained by the suggested method was determined by taking

SSDI 0003-2670(94)00019-I

two samples containing 36.3 and 54.6% of manganese. Plastic ware was used for the decomposition stage. This method involves fewer stages in sample decomposition than other methods and is considered ideal for batch analyses of large number of rock samples. An additional advantage of this method is the suitability of the same sample solution for the estimation of silica [6], phosphorus [7], titanium [8] and iron [9].

2. Experimental

2.1. Apparatus and reagents

Polyethylene bottles of 100-ml capacity with screw-caps were used. Analytical-reagent grade chemicals were used throughout.

Phosphate buffer reagent was prepared by dissolving 10 g of sodium dihydrogenorthophosphate in 100 ml of 1:1 sulphuric acid. The 0.2 M nitric acid solution (used for making up the processed solutions to the standard volume of 25 ml) was prepared by boiling 1 l of the 0.2 M nitric acid with 0.1 g of potassium periodate, allowed to cool and stored in an all-glass wash bottle. Other reagents were potassium periodate, 40% hydrofluoric acid, boric acid and aqua regia.

2.2. Procedure

A 0.1-g amount of each of the powdered rock test samples (< 250 mesh) and two in-house standard rock samples (AMDEL 24413, granite, 0.08% MnO; AMDEL 24419, basalt, 0.16% MnO) and two ore samples (AMDEL 2112, 39.3% Mn; AMDEL 2111, 59.4% Mn) of known manganese content were weighed into polythene bottles. A blank was also run simultaneouly. A 2-ml volume of aqua regia and 6 ml of hydrofluoric acid were added and the capped bottles were allowed to stand at room temperature for 24 h. The contents of the bottles was diluted with 20 ml of demineralised water, then 5.6 g of boric acid were added and the contents of the bottles were transferred quantitatively into 100-ml volumetric flasks, diluted to volume with water and shaken thoroughly until a clear solution was obtained.

A 15-ml volume of the sample solution for rocks and 1-ml for manganese ores (MnO content not exceeding 0.15 mg) was pipetted into a 100 ml beaker, 5 ml of phosphate buffer solution [1] and 0.4–0.5 g potassium periodate were added and mixed. The contents of the beaker was boiled gently on a hot plate for a few minutes until the purple permanganate colour is fully developed [2]. The solution is allowed to cool, transferred to a 25-ml volumetric flask and diluted to volume with 0.2 M nitric acid solution. After 1 h the spectrophotometric analysis of test samples was done at 530 nm in comparison with the in-house standard samples. From the known manganese contents of the in-house standards, the values for the test samples were calculated.

A typical analysis of a sample containing 38% of manganese gave, for the suggested amount of sample and solution, an absorbance reading of 0.48. The test samples were also analysed for their manganese contents by adopting the conventional acid decomposition method [1].

3. Results and discussion

The results obtained by the proposed acid decomposition method agree very good with conventional methods (Table 1). Following the suggested method, nine independent determinations

[1] After the addition of phosphate buffer the yellow colour due to iron will disappear in most of the cases but in some cases which may contain higher amounts of iron, the yellow colour may still persist and in those cases a few crystals of solid sodium dihydrogenorthophosphate should be added and mixed well until the yellow colour disappears. Another advantage of this phosphate buffer is the elimination of the use of phosphoric acid employed by earlier workers to mask iron, as most of the phosphoric acid sample may contain appreciable amounts of manganese impurity thereby contributing to high blank levels. Further as this reagent sodium dihydrogen orthophosphate is available in a pure form and totally free from manganese contamination, the blanks were always very low and perfectly reproducible, hence this reagent is preferred.

[2] If the purple colour does not develop after boiling for 10 min, a further 0.4 g of potassium periodate should be added and boiling should be continued for a further 10 min.

Table 1
Comparison of the proposed method with the conventional acid-decomposition method [1]

Test sample (in-house standard)	MnO (%) [a]	
	Proposed method	Conventional method
1	0.12	0.13
2	0.18	0.17
3	1.06	1.08
4	50.74	50.37

[a] Each value is the average of three determinations.

were made on two samples containing 36.3 and 54.6% of manganese. The precision was satisfactory (Table 2). Further, a number of international standards were analysed by the proposed method and the results obtained compared favourably with the certified values (Table 3 and Table 4), demonstrating the efficacy of the method for the determination of manganese. The decomposition method described was also found to be suitable for the determination of manganese in iron formation rocks, magnesite, bauxite and related materials.

The use of plastic ware and the avoidance of heating at any stage of decomposition of the sample make the method rapid and adaptable for large batch analyses. An added advantage of this method is the negligible blank level obtained due to the replacement of phosphoric acid with a phosphate buffer. Further, the same sample solution (used for the estimation of manganese) can be successfully utilized for the determination of phosphorus, silica, titanium and iron, etc. Finally, a particular advantage of the proposed method is the limited personal attention required at the decomposition stage, which decreases the likelihood of errors.

Table 2
Reproducibicility of results for manganeese obtained by the proposed method

Determination	Mn (%)	
	Sample 1	Sample 2
1	36.45	54.87
2	35.98	53.94
3	36.94	54.60
4	35.82	54.39
5	36.48	55.04
6	37.05	54.63
7	36.25	54.32
8	36.81	54.78
9	36.54	54.52
S.D.	0.417	0.327
R.S.D. (%)	1.142	0.599

Table 3
Manganese contents of standard reference samples determined by the proposed method

Sample	Type	MnO (%)	
		Proposed method	Certified value
GH	Granite	0.04	0.05
FeR 2	Iron formation rock	0.11	0.12
BCS 319	Magnesite	0.15	0.14
W 1	Basalt	0.18	0.17
SY 2	Syenite	0.34	0.32
NBS 697	Bauxite	0.42	0.41
NIM L	Lujavrite	0.75	0.77
In-house standard (AMDEL 24413)	Granite	0.09	0.08
In-house standard (AMDEL 24419)	Basalt	0.15	0.16

Table 4
Manganese contents of standard reference ore samples determined by the proposed method

Sample	Type	Mn (%)	
		Proposed method	Certified value
SARM 17	Manganese ore	38.13	38.00
SARM 16	Manganese ore	53.46	53.00
In-house standard (AMDEL 2112)	Manganese ore	39.45	39.30
In-house standard (AMDEL 2111)	Manganese ore	59.22	59.40

Acknowledgements

The author thanks Shri C.R. Narayanan, Deputy Director General (Geo-chemistry), Geological Survey of India for helpful suggestions and the Australian Mineral Development Laboratories (AMDEL), Adelaide, for providing the standards.

References

[1] P.G. Jeffrey, Chemical Methods of Rock Analysis, Pergamon, Oxford, 1970, p. 446.
[2] W.W. Scott, Standard Methods of Chemical Analysis, Vol. 1, Van Nostrand, Princeton, NJ, 1956 p. 984.
[3] W.M. Johnson and J.A. Maxwell, Rock and Mineral Analysis, Wiley, New York, 1981, p. 264.
[4] F.J. Langmyhr and S. Sveen, Anal. Chim. Acta, 32 (1965) 1.
[5] J.T.H. Roos and W.J. Price, Analyst, 94 (1969) 89.
[6] C.R.M. Rao, G.S. Reddi and T.A.S. Rao, Anal. Chim. Acta, 268 (1992) 357.
[7] C.R.M. Rao and G.S. Reddi, Anal. Chim. Acta, 237 (1990) 251.
[8] G.S. Reddi, C.R.M. Rao, T.A.S. Rao and H.S. Muralidhar, Anal. Chim. Acta, 251 (1991) 205.
[9] G.S. Reddi, C.R.M. Rao, T.A.S. Rao and H.S. Muralidhar, Indian Minerals, (1993) in press.

ELSEVIER

Analytica Chimica Acta 291 (1994) 141–145

ANALYTICA CHIMICA ACTA

Spectrofluorimetric determination of reserpine in pharmaceutical preparations and biological fluids

F.A. Aly *, A. El-Brashy, F. Belal

Department of Analytical Chemistry, Faculty of Pharmacy, University of Mansoura, Mansoura 35516, Egypt

(Received 20th January 1993; revised manuscript received 17th August 1993)

Abstract

A rapid and highly sensitive fluorimetric procedure was developed for the routine determination of reserpine in bulk, in dosage forms and in biological fluids. The method is based on the fluorescence induced by oxidation of reserpine with 2-iodoxybenzoate in aqueous acetic acid. The oxidation product exhibits a greenish yellow fluorescence with its emission maximum at around 484 nm. The fluorescence intensity is a linear function of reserpine concentration over the range 0.02–0.32 μg ml^{-1} with a detection limit of 0.8 ng ml^{-1}. The advantages and disadvantages of the proposed method are discussed and its applicability to different formulations and biological fluids is demonstrated.

Key words: Fluorimetry; Biological samples; Pharmaceuticals; Reserpine

1. Introduction

The double therapeutic effect of reserpine as an antihypertensive drug and as a tranquillizer is well known [1]. Because of its therapeutic importance, several methods have been developed for the determination of reserpine. Most of these methods require several separation steps, using paper or column chromatography or paper electrophoresis. Schirmer [2] reviewed methods reported for the determination of reserpine up to 1975. Since then, spectrophotometric [3–7], densitometric [8,9], polarographic [10], radioimmunoassay [11], gas chromatographic [12] and liquid chromatographic [13,14] methods have appeared.

Reserpine has been determined spectrofluorimetrically in tablets after oxidation with nitrite [15,16], hydrogen peroxide [17], selenious acid [18], *p*-toluenesulphonic acid [19], sulphovanadic acid [20], vanadium pentoxide [21] and hexaamminecobalt(III) tricarbonatocobaltate(III) [22]. Recently, reserpine has been oxidized by periodate, catalysed by Mn(II) or Mn(IV) in acidic medium, producing yellow 3,4-didehydroreserpine, which could be detected spectrophotometrically at 385 nm [23].

The aim of this study was to study the oxidation of reserpine with 2-iodoxybenzoate in an attempt to develop a simpler and more sensitive method for the determination of reserpine. The method produced is highly sensitive and is suitable for the determination of reserpine in formulations where its concentration is very low and in biological fluids. The formation of the fluorescent product is immediate.

* Corresponding author.

SSDI 0003-2670(94)00003-5

2. Experimental

2.1. Apparatus

An Aminco-Bowman Model J4-8960 spectrofluorimeter with the excitation and emission slit controls set at 5 mm and the intensity scale control set at 100 was used. The excitation and emission wavelengths used were 368 and 484 nm, respectively. Measurements were performed with 1-cm silica cells.

2.2. Materials

Reserpine of pharmaceutical grade (Ciba-Geigy) was used as the working standard. Dosage forms were obtained from commercial sources. Plasma was obtained from Mansoura University Hospital and stored at 4°C until used.

2.3. Reagent

2-Iodoxybenzoic acid was prepared as described by Banerjee et al. [24] and a 5×10^{-3} M solution was prepared by dissolving 1.4 g of the free acid in a slight excess (about 5.2 ml) of 1 M potassium hydroxide solution, diluting to 1.0 l with distilled water and standardizing iodimetrically.

2.4. Sample preparation

A 1.0 mg ml^{-1} stock standard solution of reserpine in glacial acetic acid was prepared. This solution was further diluted with 10% acetic acid to give a 1.0 μg ml^{-1} reserpine working standard solution.

2.5. Calibration

Known volumes (usually 0.5–8 ml) of 1.0 μg ml^{-1} reserpine solution were transferred into 25-ml volumetric flasks. A 5-ml volume of 10% (v/v) acetic acid were added to each flask, followed by 2.0 ml of 5×10^{-3} M 2-iodoxybenzoate. The fluorescence was measured and the intensity plotted against the reserpine concentration.

2.6. Procedure for dosage forms

Tablets

Weigh and pulverise twenty tablets. Transfer an accurately weighed amount of the powder equivalent to 1.0 mg of reserpine into a small conical flask, add 30 ml of anhydrous acetic acid, stir for 15 min, filter into a 100-ml volumetric flask, wash the residue with 10% (v/v) acetic acid and dilute the combined solutions and washings to volume with the same solvent. Analyse a suitable volume as described above.

Ampoules

Mix the contents of twenty ampoules. Transfer an accurately measured volume equivalent to 2.5 mg of reserpine into a 100-ml volumetric flask and dilute to volume with 10% (v/v) acetic acid. Analyse a suitable volume as described above.

Tablets containing reserpine and dihydralazine sulphate

Weigh and pulverize twenty tablets. To an amount of the powder equivalent to 1.0 mg of reserpine add 10 ml of 2% citric acid solution and extract with three 25-ml portions of chloroform, shaking for 2 min each time. Wash the combined extracts with 10 ml of 1% sodium hydrogencarbonate solution. Evaporate the extract to dryness on a water-bath and dissolve the residue in 10 ml of anhydrous acetic acid. Transfer the solution into a 50-ml volumetric flask and dilute to volume with 10% (v/v) acetic acid. Filter through a dry filter-paper, transfer 25 ml of the filtrate into a 100-ml volumetric flask and dilute to volume with 10% (v/v) acetic acid. Transfer an aliquot containing a suitable amount of reserpine into a 25-ml volumetric flask and analyse as described above.

2.7. Procedure for spiked biological fluids

Add an aliquot of reserpine in ethanol to 5 ml of blood plasma and stir for 3 min. Add 10 ml of 2% citric acid solution and extract the reserpine with three 25-ml portions of chloroform, shaking for 5 min each time. Wash the combined extracts

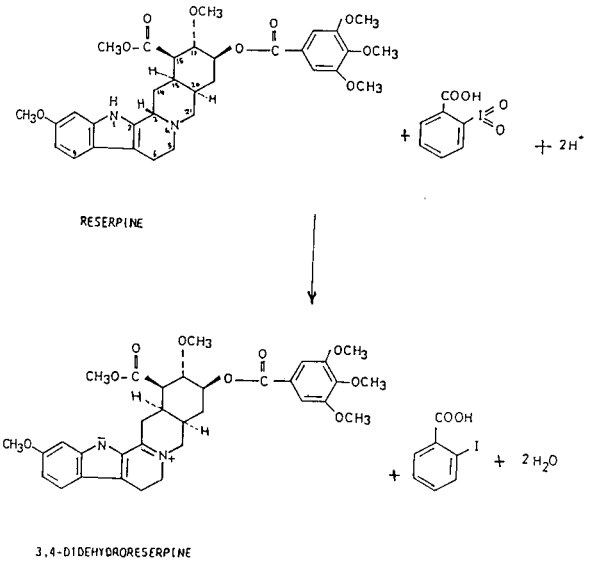

Scheme 1. Proposed reaction pathway between reserpine and 2-iodoxybenzoate.

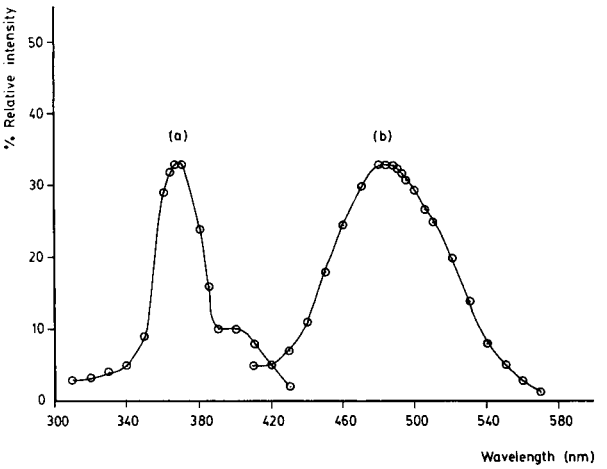

Fig. 1. Fluorescence spectra of the oxidation product of reserpine (0.1 μg ml^{-1}). (a) Excitation spectrum; (b) emission spectrum.

with 10 ml of 1% sodium hydrogencarbonate solution. Evaporate the extract to dryness on a water-bath and dissolve the residue in 10 ml of anhydrous acetic acid. Filter through a dry filter-paper into a 25-ml volumetric flask, add 2.0 ml of 5×10^{-3} M 2-iodoxybenzoate solution and complete the analysis as described above.

3. Results and discussion

The oxidation of reserpine by 2-iodoxybenzoate in acidic medium was found to give a fluorescent product. The reaction product is suggested to be 3,4-didehydroreserpine (Scheme 1). Fig. 1 shows the excitation and emission spectra obtained.

The effect of the experimental conditions on the fluorescence intensity was studied. A 2.0-ml volume of 5×10^{-3} M 2-iodoxybenzoate solution was found to be sufficient to produce the maximum fluorescence intensity; larger volumes of the reagent had no effect.

The fluorophore is formed immediately and remains stable for more than 1 h. The intensity is linearly related to the reserpine concentration over the range 0.02–0.32 μg ml^{-1}, with a limit of detection ($S/N = 2$) of 0.8 ng ml^{-1}. Linear regression analysis of the results gave a correlation coefficient of 0.9999 ($n = 6$).

The precision of the method was evaluated by analysing standard solutions of reserpine. The results in Table 1 were in accord with those obtained by the official method [3]. The method was also applied to some dosage forms containing reserpine, either alone or in combination with other drugs. The results in Table 2 agreed with those obtained by the official methods [3,4]. Statistical analysis [25] of these results using Student's t-test and the variance-ratio F-test showed no

Table 1
Analysis of standard reserpine samples by the proposed and official methods

Amount taken (μg)	Found (%) [a]	
	Proposed method [a]	Official method [3]
0.02	99.2	100.5
0.04	99.1	101.9
0.08	101.1	99.5
0.16	102.1	
0.24	102.5	
0.32	100.6	
Mean ± S.D.	100.8 ± 1.4	100.6 ± 1.2

[a] Each result is the average of three separate determinations.

Table 2
Analysis of some Ciba-Geigy dosage forms containing reserpine by the proposed and official methods

Preparation	Recovery (%)	
	Proposed method	Official method [a]
Serpasil ampoules (1.0 mg reserpine ml^{-1})	99.3	
	99.0	
	99.2	
Mean ± S.D.	99.2 ± 0.1	99.4 ± 0.2 [3]
Serpasil ampoules (2.5 mg reserpine ml^{-1})	100.8	
	101.7	
	101.2	
Mean ± S.D.	101.2 ± 0.3	100.8 ± 0.7 [3]
Serpasil tablets (0.1 mg reserpine per tablet)	101.0	
	101.4	
	100.8	
Mean ± S.D.	101.0 ± 0.2	101.3 ± 0.6 [3]
Serpasil tablets (0.25 mg reserpine per tablet)	99.2	
	99.4	
	99.5	
Mean ± S.D.	99.4 ± 0.1	99.8 ± 0.3 [3]
Adelphan tablets (0.1 mg reserpine + 10 mg dihydralazine sulphate per tablet)	99.6	
	100.2	
	99.8	
Mean ± S.D.	99.9 ± 0.2	100.0 ± 0.6 [4]

Each result is the average of three separate determinations and is expressed relative to the nominal reserpine content.
[a] Mean of four results.

significant difference between the performances of the two methods as regards accuracy and precision.

Tablet excipients such as talc, starch, gelatin, magnesium stearate and lactose did not interfere with the assay.

The method was also applied to the determination of reserpine added to blood plasma. The recovery was 92.08 ± 0.694% (mean ± standard deviation, $n = 4$).

Interference from drugs likely to be co-formulated with reserpine was studied. Hydralazine and dihydralazine sulphate decreased the fluorescence, probably being oxidized with the reagent, thus decreasing its amount. This problem was overcome by extraction of reserpine with chloroform after addition of citric acid solution. Chlorothiazide, hydrochlorothiazide and bendroflumethiazide did not interfere.

The reaction product is suggested to be 3,4-didehydroreserpine by analogy with the oxidation pathway reported for the use of nitrite [15], vanadium pentoxide [21] and *p*-toluenesulphonic acid [19]. The products have the same UV absorption and fluorescence spectra.

The proposed method has many advantages over other reported fluorimetric methods. The experimental conditions are very mild, neither corrosive acids nor heating being required. The nitrite method involves heating for 30 min [15]. Similarly, the *p*-toluenesulphonic acid method [19] involves heating in anhydrous acetic acid for 10 min.

The sole limitation of the proposed method is that the hydrolysis product, 3,4-didehydroreserpine, may interfere with the determination. However, the hydrolysis of reserpine is very unlikely to occur [2].

References

[1] W.O. Foye, Principles of Medicinal Chemistry, Lea and Febiger, Philadelphia, 1981.
[2] R.E. Schirmer, in F. Klaus (Ed.), Analytical Profiles of Drugs Substances, Vol. 4, Academic Press, New York, 1975, p. 380.
[3] British Pharmacopoeia 1988, H.M. Stationery Office, London, 1988, p. 488.
[4] United States Pharmacopeia XXII Revision, American Pharmaceutical Association, Washington, DC, 1990, p. 1215.
[5] D.S. Mangala, B.S. Reddy and C.S.P. Sastry, Indian Drugs, 21 (1984) 526.
[6] Y. Fujita, I. Mori and S. Kotano, Bunseki Kagaku, 33 (1984) 1985.
[7] N. Geeta and T.R. Baggi, Indian Drugs, 26 (1989) 421.
[8] J. Jarzebinski, M. Ciszewska and P. Suchocki, Acta Pol. Pharm., 37 (1980) 69.
[9] P. Corti, G. Corbini, E. Dreassi, C. Murratzu and L. Celesti, Pharm. Acta Helv., 65 (1990) 222.
[10] A. Taira and D.E. Smith, J. Assoc. Off. Anal. Chem., 61 (1978) 641.
[11] E. Thacker, Anal. Proc., 22 (1985) 136.
[12] L. DiSimone, G. Portelli, M.R. Del Giudice, F. Gatta and G. Settimj, Farmaco, Ed. Prat., 35 (1980) 223.

[13] U.R. Cieri, J. Assoc. Off. Anal. Chem., 68 (1985) 542.
[14] H.L. Rau, A.R. Aroor and, P.G. Rao, Indian Drugs, 28 (1990) 157.
[15] D. Banes, J. Am. Pharm. Assoc., 46 (1957) 601.
[16] B.N. Kabadi, J. Pharm. Sci., 60 (1971) 1862.
[17] E.B. Dechene, J. Am. Pharm. Assoc., 44 (1955) 657.
[18] R.B. Poet and J.M. Kelly, in Abstracts of 120th Meeting of the American Chemical Society, 1954, p. 83c.
[19] I.M. Jakovljevic, J.M. Fose and N.R. Kuzel, Anal. Chem., 34 (1962) 410.
[20] R. Stainier, J. Pharm. Belg., 28 (1973) 115.
[21] T. Urbanyi and H. Staber, J. Pharm. Sci., 59 (1970) 1842.
[22] M.I. Walash, F. Belal and F.A. Aly, Talanta, 35 (1988) 731.
[23] S.R. Varma, J.M. Calatayud and H.A. Mottola, Anal. Chim. Acta, 233 (1990) 235.
[24] A. Banerjee, G.C. Banerjee, S. Bhattacharya, S. Banerjee and H. Samaddar, J. Indian Chem. Soc., 58 (1981) 605.
[25] D.H. Sanders, A.F. Murph and R.J. Eng, Statistics, McGraw-Hill, New York, 1976.

ELSEVIER

Analytica Chimica Acta 291 (1994) 147–153

ANALYTICA CHIMICA ACTA

Surface-enhanced Raman spectrometry on a silver substrate prepared by the nitric acid etching method

A. Rupérez [a], J.J. Laserna *[,b]

[a] Department of Physical Chemistry and [b] Department of Analytical Chemistry, Faculty of Sciences, University of Málaga, E-29071 Málaga, Spain

(Received 17th November 1993)

Abstract

The potential use of a silver substrate for surface-enhanced Raman analysis was investigated. The substrate was prepared by nitric acid etching of silver foils and checked for nitrogen-containing aromatic compounds. The response stability of this substrate and its reversibility after several uses are studied. Analytical figures of merit, such as precision, linear dynamic range, and limits of detection for a variety of compounds are presented to demonstrate the analytical capability of this substrate.

Key words: Raman spectrometry; Surface-enhanced Raman spectrometry; Laser spectroscopy; Organic analysis

1. Introduction

Surface-enhanced Raman scattering (SERS) has been observed for an increasing number of metals including Ag, Au, Cu, Ni, Pd, Pt, Al, In, and others [1–8]. The particularly strong enhancement observed for the coinage metals Ag, Au and Cu, is understood [9] in terms of their optical and dielectric properties. SERS enhancements from Ni, Pd, Pt and others are orders of magnitude smaller because plasmon resonances are strongly damped for these metals. Silver has been the most widely employed metal, since surface plasmons are excited in the visible region where strong and stable laser lines are available. An important factor for the observed enhancement is the surface roughness. Metal substrates with appropriate roughness include colloidal silver [10–12], silver island films [13], silver films deposited on quartz or PTFE particles [14–16], chemically reduced silver films on glass slides [17] and filter papers [18–20]. Colloidal silver has been widely employed, because it is easily produced, provides fresh surfaces for adsorption of analyte molecules, and it can be made stable for weeks. Silver colloids have been adapted for use in flow-injection analysis (FIA) and liquid chromatography (LC) [21].

Suzan et al. [22] pointed out that pronounced SERS signals could be easily acquired by etching copper foils with concentrated nitric acid. Later, Xue et al. [23,24] reported SERS results for 2-mercaptobenzimidazole, 4-aminophenyl disulfide and thiophenols, using chemically etched silver.

* Corresponding author.

SSDI 0003-2670(94)00009-B

This sampling technique is particularly efficient under different environmental conditions, using aqueous as well as organic solutions. Also, spontaneous assembly of the analyte from its gaseous state results in high quality spectra [24]. This fact is attributed to the facile cleavage to silver of the sulfur atoms to form monolayer films. The capability of these supports as analytical substrates, such as their activity for other functional groups or their reversibility, was not investigated.

In this paper the characterization and several outstanding advantages of etched silver foils as analytical substrates are reported. The results show that intense and reproducible spectra for a number of compounds, containing heterocyclic nitrogen or amino groups, can be easily detected using solid silver media etched by nitric acid. The substrates are reversible, reusable and could be used as permanent records of analyzed samples.

2. Experimental

2.1. Instrumentation

The excitation source consisted of an argon-ion laser (Coherent, Model Innova 70) tuned at 488 nm, releasing about 30 mW at the sample, and focussed with a biconvex glass lens (30-cm focal length). Silver-foil rectangles of 0.8×1 cm^2 were used as the substrate for SERS. Samples were placed in a laboratory-constructed sample holder. Raman scattering was collected at right angles, dispersed with a double spectrometer (Spex, Model 1680B), and detected with a thermoelectrically cooled photomultiplier tube (Hamamatsu, Model R928) and a photon counting system (Stanford Research, Model SR400). Operation of the photon counter was controlled by an AT personal computer with Stanford Research SR465 software. The acquisition time by spectral element was 0.5 s and each spectrum consisted of 700 data points. The spectrometer resolution was generally set to 14 cm^{-1}. Frequencies were accurate to within 3 cm^{-1} for the bands studied. Spectral data were generated in binary code and converted to ASCII for processing in standard graphics software.

2.2. Chemicals and procedure

All chemicals were analytical reagent grade or equivalent, they are used without further purification. Chromatography-grade methanol was used throughout. A 0.003-mm thick silver foil was immersed into vigorously stirred (1 : 1) nitric acid at room temperature. Stirring continued for about 2–3 min until the foil became a milky surface. After etching, silver foils were thoroughly rinsed with distilled water and dried in air. The roughened foils were spotted with 15 μl of sample dissolved in methanol. After spotting, the excess liquid was blown off with air, and the foil placed in the sample holder for Raman examination.

3. Results and discussion

3.1. Substrate characterization and properties

Fig. 1 shows scanning electron micrographs of the silver foils, before (top) and after (bottom) etching with nitric acid. As shown, the etching process results in a rough surface with metal microstructures in the submicrometer scale. The scattering spectrum of etched silver foils is shown in Fig. 2 (top, a) and the spectrum of silver foils is shown in Fig. 2 (bottom, a); the strong peak at 1055 cm^{-1}, and the medium peak at 1577 cm^{-1}, correspond to non-lasing plasma lines of the argon-ion laser. Weak peaks appear when the spectrum is expanded, overcoat, in not etched silver foils, at 1131, 1168, 1323 and 1808 cm^{-1}. These peaks are marked with a star. The plasma line can be eliminated by placing a band-pass filter between the laser and the sample, for adequate identification of compounds containing active groups in this zone. The large background observed for this substrate is probably due to reflection and scattering by the milky surface of the etched foil, and scales linearly with the laser power employed.

Fig. 2 also shows the SERS spectra of acridine on a silver etched foil (top, b) and on a non-etched silver foil (bottom, b). The spectrum in non-etched foil shows a general increase in the no-lasing emission lines of the argon ion laser, but no

characteristic vibrational modes of acridine are observed. Fig. 2 (top, b) exhibits spectral features of acridine at 1220, 1262, 1324, 1409 and 1520 cm^{-1}.

3.2. Substrate stability

Freshly prepared substrates were evaluated with respect to the stability of SERS signals upon continuous irradiation with the laser beam. Fig. 3 shows the SERS spectrum of acridine on a freshly prepared substrate (top) and after 60 min of continuous irradiation (bottom). As with other compounds, the vibrational structure of acridine is maintained. The rapid heat conduction in the silver foil may account for the surface stability under the intense optical field. After 60 min, some of the substrate activity is lost, as manifested by a decrease in the ratio of the acridine intensity at 1410 cm^{-1} to the background intensity measured at 1364 cm^{-1}.

The long-term stability of the substrate was investigated by monitoring the SERS intensity of amiloride over a period of 20 days. After sample application, the doped substrate was placed in the holder and stored and evaluated in air in order to avoid differences in enhancement factors related to inhomogeneous distribution of molecules on the surface of foil. Fig. 4 shows the results. Curve a corresponds to the amiloride intensity at 1212 cm^{-1}, and curve b corresponds to the background signal measured at 1138 cm^{-1}. The inset shows the amiloride spectra obtained with the freshly prepared substrate (c) and after 12 days of sample doping (d). As shown, the amiloride signal and the signal-to-background (SB) ratio reaches a maximum after 1 day. The SB ratio decreases afterwards. Nevertheless, the inset shows that the spectral features of the analyte are maintained. These results reveal the potential of the substrate for use as a permanent record of stored samples.

3.3. Substrate reversibility

Silver foils show good capacity for desorption of the adsorbed analyte. This is an important property of the silver substrate. Fig. 5a shows the SERS spectrum of 9-aminoacridine obtained by casting 15 μl of a 10 $\mu g\ ml^{-1}$ solution onto a silver foil. Fig. 5b shows the spectrum of foil after dipping for 30 s in methanol. Fig. 5c shows the SER spectrum of triamterene after spotting with 15 μl of a 25 $\mu g\ ml^{-1}$ solution. As shown, 9-aminoacridine has been completely desorbed from the substrate after dipping, the substrate now being readily available for investigation of a new adsorbate. The time needed for complete desorption of an analyte will depend on its solubility in the solvent used for washing. For instance, triamterene, which is poorly soluble in methanol, needs at least 2 min for complete desorption.

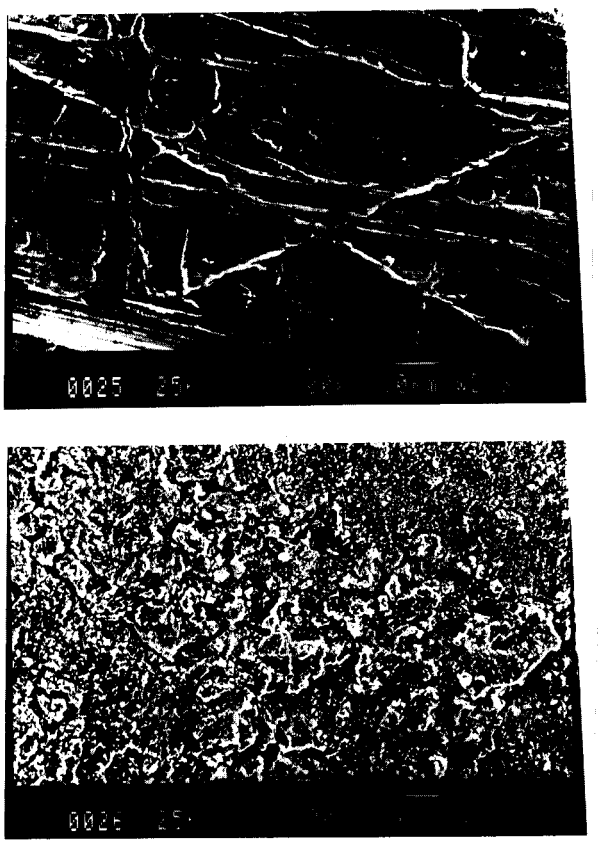

Fig. 1. Scanning electron micrographs of the silver foil substrate (top) and etched silver foil (bottom). The line in the photographs represent 10.0 μm.

3.4. SERS fingerprinting capability

The spectral fingerprinting capability of this substrate for the analysis of nitrogen containing aromatic compounds is illustrated in Fig. 6. The SERS spectra of anthracene (a), 2-aminoanthracene (b), 9-aminoacridine (c) and acridine (d) are displayed. Although the spectra have been shifted for clarity, the intensity scales are internally consistent. The Raman modes in this substrate agree quite well with those reported for these compounds on silver-coated filter paper [25] and silver colloid [26]. The results shown in Fig. 6 demonstrate that the nitrogen atom plays a key role in the SERS activity of a given analyte. The SERS spectra of compounds with the nitrogen atom in a ring system (acridine) or as an exocyclic amino group (2-aminoanthracene) are considerably richer than their counterpart with no nitrogen atom (anthracene).

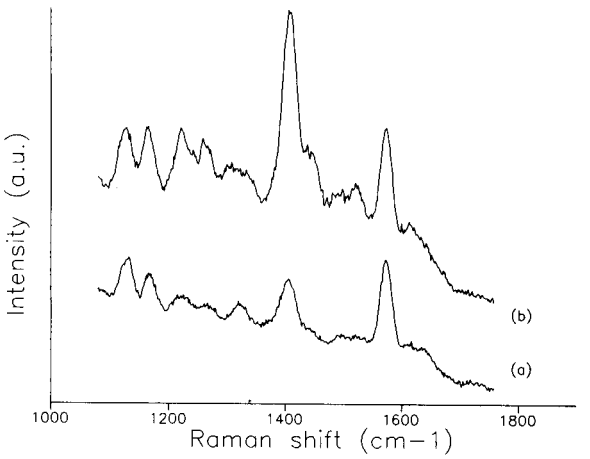

Fig. 3. Effect of laser irradiation on the SERS spectrum of acridine. Irradiation time (min): (a) 60; (b) 0.

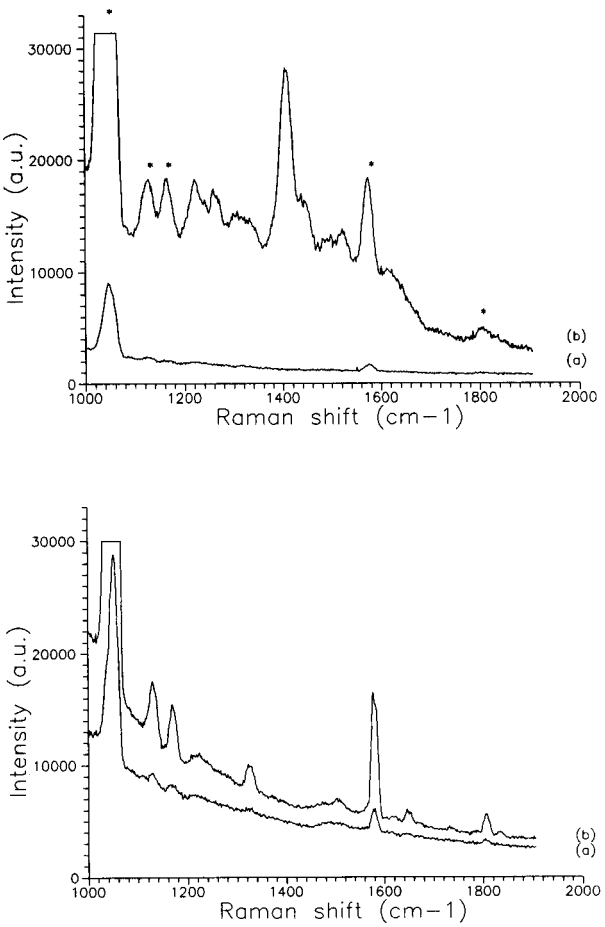

Fig. 2. Bottom: unroughened silver foil. Blank spectrum (a) and SERS spectrum of acridine (b). Top: roughened silver foil. Blank spectrum (a) and SERS spectrum of acridine (b).

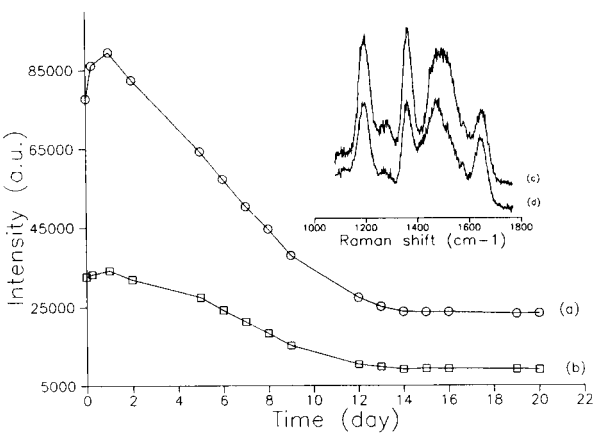

Fig. 4. Time dependence of the surface enhanced Raman intensity of amiloride (a) and of the background (b). The inset represents the amiloride SER spectra with the fresh substrate (c) and after 12 days (d).

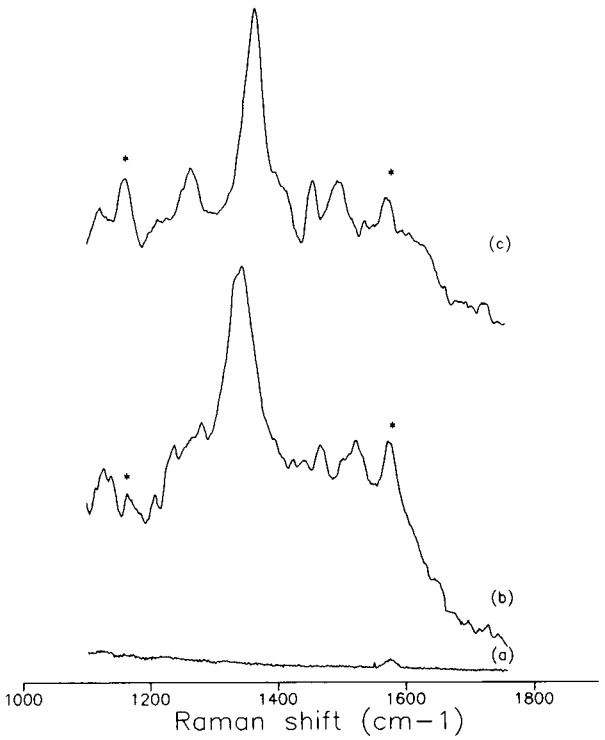

Fig. 5. SERS spectrum of 9-aminoacridine (150 ng) on etched silver substrate (a). Spectrum of etched silver foil after dipping for 30 s in methanol (b). SER spectrum after application of triamterene (250 ng) on the washed silver foil (c).

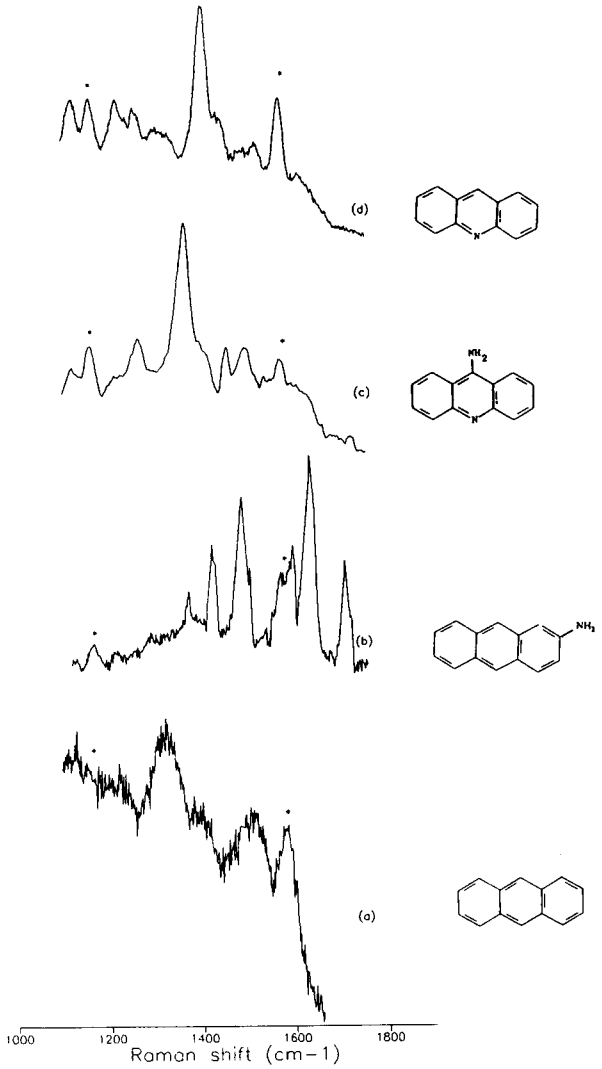

Fig. 6. SERS spectra on an etched silver foil: (a) anthracene; (b) 2-aminoanthracene; (c) 9-aminoacridine; (d) acridine. Drug concentration 25 μg ml^{-1}.

3.5. Quantitative study

In order to evaluate intersubstrate variations of SERS intensities, 10 foils were prepared. 15 μl of 9-aminoacridine (25 μg ml^{-1}) or triamterene

Table 1
Analytical figures of merit on nitric acid roughened silver-foil for 9-aminoacridine, acridine and 2-aminoanthracene

Analyte	Corr. coeff. [a]	Slope [b]	Upper limit (μg/ml)	LOD (μg/ml)	LOD (mol)
Acridine	0.998	774	26.9	0.086	8.94×10^{-15}
9-Aminoacridine	0.995	2110	11.3	0.033	2.5×10^{-15}
2-Aminoanthracene	0.992	435	26.7	0.102	1.73×10^{-14}

[a] $n = 6$.
[b] Arbitrary units.

(100 μg ml^{-1}) were added as a drop on the freshly prepared foil. The relative standard deviations of peak intensities were 9 and 11%, respectively. Table 1 summarizes other analytical figures of merit. The upper limit of the linear part of the calibration graph was estimated by polynomial interpolation. The linearity holds for more than two concentration decades. Limits of detection were estimated as follows [27]. If the 15 μl of sample used is distributed homogeneously in the 0.8×1 cm^2 substrate, with a 1-mm diameter laser beam focussed with a 30-cm focal-length lens, the sampling efficiency is about 1/800 of all analyte molecules applied. For 15-μl of 10 μg ml^{-1} 9-aminoacridine, about 4.6×10^{11} molecules are sampled. The absolute limit of detection can be found by calculating the concentration giving a signal-to-noise ratio of $3\sqrt{2}$. The peak intensity of the 1375 cm^{-1} 9-aminoacridine band at 10 μg ml^{-1} is 54273 counts and the noise signal is $32239^{1/2} = 180$; thus, at the limit of detection, the number of molecules within the laser beam is 0.033 μg ml^{-1}, corresponding to 1.5×10^9 molecules or 2.5×10^{-15} moles. The limits of detection for acridine and 2-aminoanthracene were calculated in a similar manner and appear in Table 1.

4. Conclusions

Strongly enhanced Raman spectra can be obtained from nitric acid roughened silver foils for nitrogen-containing aromatic compounds. Good stability under laser irradiation and upon aging is observed. The adsorbed analytes are easily desorbed from the substrate by rinsing with solvent, resulting in a fresh, reusable, SERS-active surface. This is a relevant advantage of the substrates as it offers prospect for their use as optical sensors for characterization of adsorbed molecules. The main drawback is related to the large background signals observed. Although the background often compromises the detectability and it is difficult to control on a routine basis, the results reported here are important steps in the direction of bringing SERS under experimental control for analytical applications.

Acknowledgements

The research was supported by Dirección General de Universidades e Investigación (Ministerio de Educación y Ciencia, Madrid, project PB90-0814) and by Dirección General de Universidades e Investigación (Consejería de Educación y Ciencia, Junta de Andalucía, Sevilla, Spain)

References

[1] W. Kasser, H. Ervens, A. Fadini and A. Renouprez, J. Raman Spectrosc., 9 (1980) 80.
[2] W. Krasser and A.J. Renouprez, J. Raman Spectrosc., 11 (1981) 425; Solid State Commun., 41 (1982) 231.
[3] H. Yamada and Y. Yamamoto, Chem. Phys. Lett., 77 (1981) 520.
[4] H. Yamada, Y. Yamamoto and N. Tini, Chem. Phys. Lett., 86 (1982) 397.
[5] R.E. Benner, K.U. von Raben, K.C. Lee, J.F. Owen, R.K. Chang and B.E. Laube, Chem. Phys. Lett., 96 (1982) 65.
[6] B. Pettinger, V. Wenning and H. Wetzel, Surf. Sci., 101 (1980) 409.
[7] J. Martin, M.J. Angebranndt and J.D. Winefordner, Talanta, 93 (1992) 569.
[8] J.J. Laserna, A. Berthod and J.D. Winefordner, Microchem. J., 38 (1988) 125.
[9] M. Fleischmann, P.J. Hendra and A.J. Mc Quillan, Chem. Phys. Lett., 26 (1974) 163.
[10] A. Rupérez, R. Montes and J.J. Laserna, Vib. Spectrosc., 2 (1991) 145.
[11] R. Montes, C. Contreras, A. Rupérez and J.J. Laserna, Anal. Chem., 64 (1992) 2715.
[12] J.J. Laserna, L.M. Cabalín and R. Montes, Anal. Chem., 64 (1992) 2006.
[13] H. Ishida, H. Fukuda, G. Katagiri and A. Ishitani, Appl. Spectrosc., 40 (1986) 322.
[14] T. Vo-Dinh, T. Hiromoto, G. Begun and R. Moody, Anal. Chem., 56 (1984) 1667.
[15] J.P. Goudennend, G. Begun and E. Arakawa, Chem. Phys. Lett., 92 (1982) 197.
[16] M. Meier, A. Wokaun and T. Vo-Dinh, J. Chem. Phys., 120 (1985) 301.
[17] D.W. Boo, S.W. Oh, M.S. Kim, K. Kim and H. Lee, Chem. Phys. Lett., 120 (1985) 301.
[18] C.D. Tran, Anal. Chem., 56 (1984) 824.
[19] A. Berthod, J.J. Laserna and J.D. Winefordner, J. Pharm. Biomed. Anal., 6 (1988) 599.
[20] J.J. Laserna, W.S. Sutherland and J.D. Winefordner, Anal. Chim. Acta, 237 (1990) 439.
[21] L.M. Cabalín, A. Rupérez and J.J. Laserna, Talanta, 40 (1993) 1741.

[22] K. Suzan, M. Baiker, A. Baiker, M. Meier and A. Wokaun, J. Chem. Soc., Faraday Trans. I, 80 (1984) 1305.
[23] G. Xue, J. Dong and M. Zhang, Anal. Chem., 63 (1991) 2393.
[24] G. Xue, M. Ma, J. Zhang, Y. Lu and K.T. Carron, J. Colloid Interface Sci., 150 (1991) 1.
[25] J.J. Laserna, A.D. Campiglia, and J.D. Winefordner, Anal. Chim. Acta, 208 (1988) 21.
[26] N. Calvo, R. Montes and J.J. Laserna, Anal. Chim. Acta, 280 (1993) 263.
[27] J.J. Laserna, A.D. Campiglia and J.D. Winefordner, Anal. Chem., 61 (1989) 1697.

ELSEVIER

Analytica Chimica Acta 291 (1994) 155–160

ANALYTICA CHIMICA ACTA

Gas chromatographic–mass spectrometric confirmation of a clostebol metabolite in urine

G. Debruyckere [a,*], R. de Sagher [a], C. Van Peteghem [a], G. Van Vyncht [b], G. Maghuin-Rogister [b], E. De Pauw [c]

[a] *Faculty of Pharmaceutical Sciences, University of Ghent, Harelbekestraat 72, 9000 Gent, Belgium,* [b] *Faculty of Veterinary Medicine and* [c] *Mass Spectrometry Unit, University of Liège, Bât. B42 Sart Tilman, 4000 Liège, Belgium*

(Received 16th December 1993; revised manuscript received 24th January 1994)

Abstract

Anabolic steroids are used as doping agents in sports. Notwithstanding the total EC ban, they are also used as growth promoters in animal production. The detection of anabolic steroids in the urine of untreated persons due to the consumption of contaminated meat has been described earlier. This paper describes further confirmation of a urine sample which was clostebol positive as a result of the above described interference phenomenon. This was done by gas chromatography–mass spectrometry. Both low resolution mass spectrometry (LRMS) and high resolution mass spectrometry (HRMS) were used after gas chromatographic separation. LRMS was used to determine the relative abundances of the ions and for calculating similarity indices. With HRMS, selectivity was increased by recording exact masses instead of nominal masses.

Key words: Gas chromatography–mass spectrometry; Anabolic steroids; Clostebol; Doping agents; Sports; Urine

1. Introduction

Anabolic steroids stimulate a strongly positive nitrogen balance and have a protein anabolic effect. They are used as performance enhancers in sports, but they are also illegally used in livestock farming in the European Community. The detection of anabolic steroids in urine due to the consumption of contaminated meat has been described earlier [1,2]. The detection was based on gas chromatographic–mass spectrometric (GC–MS) data. GC–MS is widely accepted for identification of doping agents in urine samples. For screening of anabolic steroids, e.g., three ions can be selected from the mass spectrum of the derivatized parent steroid or its metabolite. Some alternatives for the confirmation of a presumed clostebol positive urine sample will be proposed in this paper. These will be based on data obtained from gas chromatography–low resolution mass spectrometry (GC–LRMS) and gas chromatography–high resolution mass spectrometry (GC–HRMS).

* Corresponding author.

SSDI 0003-2670(94)00040-S

2. Experimental

2.1. Reference standard

The main metabolite of clostebol, i.e., 4-chloroandrost-4-en-3α-ol-17-one (CLOS-MET) was synthesized at the laboratory of Prof. M. Donike (Cologne) by W. Schänzer and kindly donated.

2.2. Urine samples

A presumed clostebol positive urine sample was obtained from a volunteer after he had consumed a meat sample, found to be contaminated with clostebol acetate. The urine sample was obtained 6.67 h after consumption and had a CLOS-MET concentration of 23 $\mu g\ l^{-1}$, as determined by GC–LRMS [2].

Reference clostebol positive urine samples were obtained from another volunteer, who received an intramuscular injection of Steranabol® (Farmitalia, Freiburg) which contained 40 mg clostebol acetate. Urine samples obtained 25, 30 and 35 days after intramuscular injection had CLOS-MET concentrations of 179 $\mu g\ l^{-1}$, 76 $\mu g\ l^{-1}$ and 11 $\mu g\ l^{-1}$, respectively.

2.3. Pretreatment of the urine samples

The pH of the urine (15 ml) was adjusted to pH 3 with 1 M HCl and the urine samples were divided in two parts for solid phase extraction by two separate C_{18} columns (Baker, Phillipsburg, NJ). The eluates were collected and further treated as described earlier [1] (enzymatic hydrolysis and solid phase extraction on C_{18} and NH_2 columns). The eluate obtained after solid phase extraction was evaporated to dryness under nitrogen and reconstituted in 150 μl methanol. 100 μl were injected in the liquid chromatography (LC) system.

2.4. LC fractionation

Equipment

The LC system consisted of a Waters Model 6000 A pump and a WISP 710 B automatic injector (Waters Assoc., Milford, MA). The variable wavelength absorbance detector was a Model SP 8400 (Spectra Physics, Santa Clara, CA) and the fraction collector was a Helirac 2212 system (Pharmacia LKB, Uppsala). The column was a LiChrospher® 100 RP-18 (5 μm), 12.5 cm × 4 mm i.d. (Merck, Darmstadt), guarded by a pellicular reversed-phase column (30–50 μm), 75 mm × 2.1 mm i.d. (Chrompack, Middelburg).

Experimental conditions

The urinary extract was fractionated by LC using a mobile phase of methanol–water (65:35, v/v) (Alltech, Deerfield) at a flow rate of 1 ml/min. A 4-ml fraction was collected (8.9–12.9 min) and evaporated to dryness under nitrogen.

2.5. Derivatization

The dry residue of the collected LC fraction was derivatized with 50 μl *N*-methyl-*N*-trimethylsilyltrifluoroacetamide (MSTFA)–ammonium iodide–dithioerythritol (1000:2:4, v/w/w) for 30 min [3].

2.6. GC

Equipment

Gas chromatography was carried out on a HP 5890 gas chromatograph, equipped with a fused-silica crosslinked 5% phenylmethylsilicone capillary column (DB5, J&W Scientific, Folsom, CA for GC–LRMS; Ultra 2, Hewlett Packard, Palo Alto, CA for GC–HRMS). The carrier gas was helium.

Experimental conditions

The injector temperature and transfer line temperature were at 280°C. The oven temperature was held at 100°C for 1 min, then programmed from 100 to 230°C at 40°C/min and from 230 to 280°C/min at 5°C/min, the final temperature being maintained for 15 min. 2 μl were injected in the splitless mode.

2.7. LRMS

A HP 5970 mass spectrometer was used. Electron impact ionization was done at an electron

beam voltage of 70 eV. The data system was a HP 59970C MS ChemStation (Pascal Series, Revision 3.2).

2.8. HRMS

The VG Analytical Autospec Q mass spectrometer was used. Electron impact ionization was done at 70 eV and the instrument was tuned to obtain a resolution of 8000. Perfluorokerosene was used as tuning agent (K&K Labs., Plainview, NY).

2.9. GC–LRMS experiments

Seven ions were selected from the electron impact (EI) mass spectrum of the trimethylsilyl (TMS)-enol–TMS ether derivatized CLOS-MET (Fig. 1) for a selected ion monitoring (SIM) program, using dwell times of 50 ms for each of the ions. SIM data were recorded for the reference standard in different amounts (20, 10, 5, 2.5 and 1.25 ng) and for the positive reference urine samples and the presumed positive reference urine sample. These data were used for calculation of the relative abundances of the ions and for calculation of similarity indices.

2.10. GC–HRMS experiments

For selected ion monitoring in GC–HRMS the exact masses of five ions typical for the TMS-enol–TMS ether derivatized CLOS-MET were recorded, using dwell times of 80 ms. The dwell time for the ion of the calibrant was 50 ms. The HRMS SIM data of the presumed positive urine sample were compared to the data of a positive reference urine sample.

3. Results and discussion

3.1. Calculation of ion ratios in GC–LRMS

When recording several ions in SIM, the relative abundances of the ions of the analyte can be calculated and compared to those of a reference compound. This is included in the EC legislation in a Commission Decision laying down the methods to be used for detecting residues of substances having a hormonal or thyrostatic action

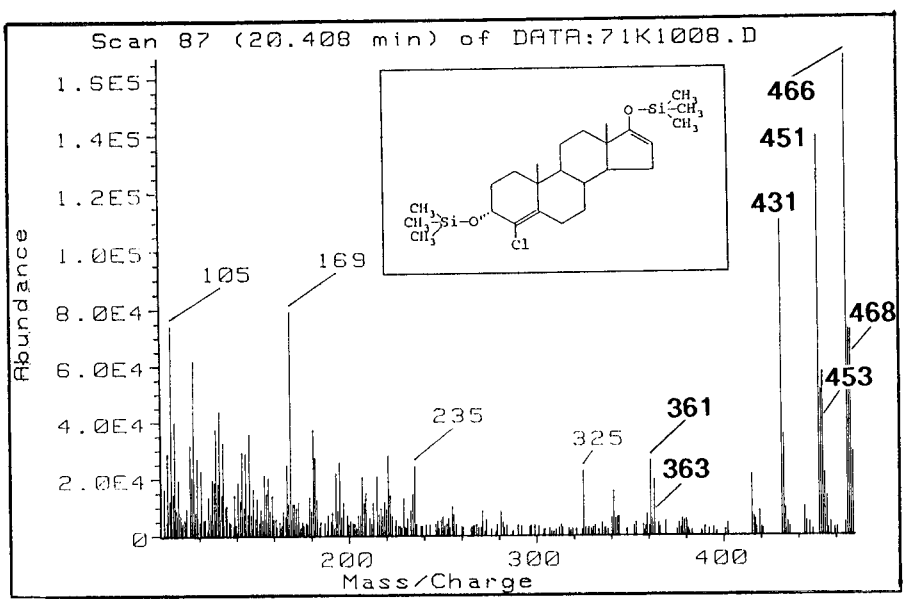

Fig. 1. Mass spectrum and structural formula of the TMS-enol–TMS ether derivatized clostebol metabolite (4-chloroandrost-4-en-3α-ol-17-one, CLOS-MET).

[4]. For use as a confirmatory method, the intensities of preferably at least four diagnostic ions should be measured and the relative abundances of all diagnostic ions monitored from the analyte should match those of a reference standard, preferably within a range of ±10% (EI mode). The results of the ion ratio determination of the reference standard, of the reference urine samples and of the presumed positive urine sample are shown in Table 1. EC criteria state that at least three ion ratios (since at least four diagnostic ions have to be detected) should match those of the reference standard. As can be seen from Table 2, this criterion is easily fulfilled for ions with m/z = 468, 466, 453 and 451. When comparing the presumed positive urine sample (23 $\mu g\ l^{-1}$, 9 ng injected on column) with the best matching reference (i.e., closest concentration or amount of the reference urine samples or the reference standard, respectively), the accordance was even more explicit. When comparing the presumed positive urine sample (9 ng injected on column) with the 10 ng reference standard, 5 of the 6 ions have a percentage deviation lower than 2%. When comparing the presumed positive urine sample with the 11 $\mu g\ l^{-1}$ reference urine sample, five out of six ions even have a percentage deviation lower than 1%.

Table 1
Mean ion ratio values ± standard deviation (n = 5) for the injections of the different solutions of the reference standard (A), the reference urine samples (B) and a presumed positive urine sample (C) (GC–LRMS analysis)

m/z values	468/466	451/466	453/466	431/466	361/466	363/466
(A) Reference standard						
20 ng	0.462 ± 0.003	0.814 ± 0.018	0.359 ± 0.009	0.570 ± 0.015	0.209 ± 0.015	0.091 ± 0.007
10 ng	0.450 ± 0.004	0.830 ± 0.009	0.366 ± 0.006	0.587 ± 0.009	0.215 ± 0.015	0.096 ± 0.004
5 ng	0.439 ± 0.003	0.839 ± 0.014	0.366 ± 0.004	0.593 ± 0.008	0.221 ± 0.009	0.091 ± 0.004
2.5 ng	0.428 ± 0.006	0.854 ± 0.017	0.359 ± 0.006	0.611 ± 0.017	0.245 ± 0.016	0.094 ± 0.003
1.25 ng	0.417 ± 0.019	0.849 ± 0.032	0.357 ± 0.009	0.658 ± 0.059	0.224 ± 0.019	0.083 ± 0.010
(B) Reference urines						
179 $\mu g\ l^{-1}$	0.481 ± 0.004	0.818 ± 0.005	0.362 ± 0.003	0.568 ± 0.005	0.206 ± 0.008	0.093 ± 0.004
76 $\mu g\ l^{-1}$	0.465 ± 0.003	0.808 ± 0.007	0.359 ± 0.003	0.564 ± 0.006	0.201 ± 0.005	0.090 ± 0.003
1 $\mu g\ l^{-1}$	0.442 ± 0.005	0.816 ± 0.007	0.358 ± 0.006	0.591 ± 0.016	0.207 ± 0.008	0.090 ± 0.004
(C) Presumed positive urine						
23 $\mu g\ l^{-1}$	0.445 ± 0.004	0.818 ± 0.010	0.358 ± 0.005	0.588 ± 0.010	0.206 ± 0.006	0.096 ± 0.003

Table 2
Percentage deviation of the ion ratios of the presumed positive sample in relation to the ion ratios of the (A) reference standard and (B) reference urine samples (italicized values exceed 10% deviation) (GC–LRMS analysis)

m/z value	468/466	451/466	453/466	431/466	361/466	363/466
(A) Reference standard						
20 ng	3.59	0.58	0.22	3.20	1.58	4.70
10 ng	0.96	1.35	1.94	0.15	4.05	0.10
5 ng	1.41	2.42	1.94	0.91	6.87	4.93
2.5 ng	4.04	4.15	0.19	3.86	*15.92*	2.35
1.25 ng	6.78	3.64	0.50	*10.64*	8.20	*15.72*
(B) Reference urines						
179 $\mu g\ l^{-1}$	7.36	0.00	0.91	3.54	0.19	3.35
76 $\mu g\ l^{-1}$	4.19	1.25	0.06	4.26	2.64	6.33
11 $\mu g\ l^{-1}$	0.68	0.33	0.22	0.47	0.72	6.81

3.2. Calculation of similarity indices in GC–LRMS

Unknown spectra can be compared to spectra of reference compounds in a library. Although this approach is most commonly used in the comparison of full mass spectra, we applied this to SIM spectra. Reference spectra obtained after injection of the different amounts of CLOS-MET and after injection of reference urine samples were stored in a users library. The library search is a forward search algorithm based on the ten most-significant peaks in each unknown mass spectrum. The significance of each peak is defined as mass times abundance. Ten peaks with the largest significance are selected for the search. The library entries (reference spectra) also consist of the ten most significant peaks. The comparison algorithm uses an equation that computes a similarity index (S.I.), defined as

$$\text{S.I.} = \frac{\sum_{i=1}^{10} A_m a_m}{\left[\sum_{i=1}^{10} (A_m)^2 \cdot \sum_{i=1}^{10} (a_m)^2\right]^{1/2}}$$

where A_m is the abundance of the ion in an unknown spectrum and a_m the abundance of the ion in a library spectrum. Since in our experiments where SIM data are recorded, seven ions are registered, the similarity indices are calculated by replacing Σ^{10} by Σ^{7}. The similarity index is computed for each spectrum in a library against a given unknown, and the results are rank ordered. The similarity indices are multiplied by 10000 and listed as match quality. The match qualities for the presumed positive urine samples are displayed in Table 3. Except for comparison with the 306 pg CLOS-MET standard, match qualities were higher than 99%, which can be considered as perfect matches.

3.3. GC–HRMS confirmation of the presumed clostebol positive urine sample

In high-resolution mass spectrometry ionic species having the same nominal mass but different exact masses can be separated. A numerical expression of resolution can be obtained from the ratio $m/\Delta m$, where m and $m+\Delta m$ are two adjacent peaks in the mass spectrum. The instrument was tuned on a resolution of 8000. For the choice of ions for the SIM program in HRMS, two factors had to be taken into account. The ions should be significant enough and they should lie in a rather limited m/z range around the m/z value of the ion of the calibrant. Because of the presence of the chlorine atom in clostebol, it was very convenient to find adequate ions to implement in the selected ion monitoring program. The chlorine isotope pairs of the molecular ion $M^{+\cdot}$ (ions of m/z 466 and 468) and of a

Table 3
Match qualities of the presumed positive urine sample

	Library index No.	Match quality
(1) 10 ng CLOS-MET standard	2	9997
(2) 5 ng CLOS-MET standard	3	9996
(3) Reference urine 179 ng/ml CLOS-MET	8	9995
(4) 20 ng CLOS-MET standard	1	9994
(5) Reference urine 76 ng/ml CLOS-MET	9	9993
(6) 2.5 ng CLOS-MET standard	4	9986
(7) Reference urine 11 ng/ml CLOS-MET	10	9984
(8) 0.6125 ng CLOS-MET standard	6	9963
(9) 1.25 ng CLOS-MET standard	5	9924
(10) 0.30625 ng CLOS-MET standard	7	9789

Table 4
Masses of the ions monitored in HRMS

Nominal mass	Exact mass	Dwell time (ms)
468	468.2389	80
466	466.2492	80
453	453.2240	80
451	451.2260	80
431	431.2800	80
455[a]	454.9728	50

[a] Fast lock-on mass of the tuning agent.

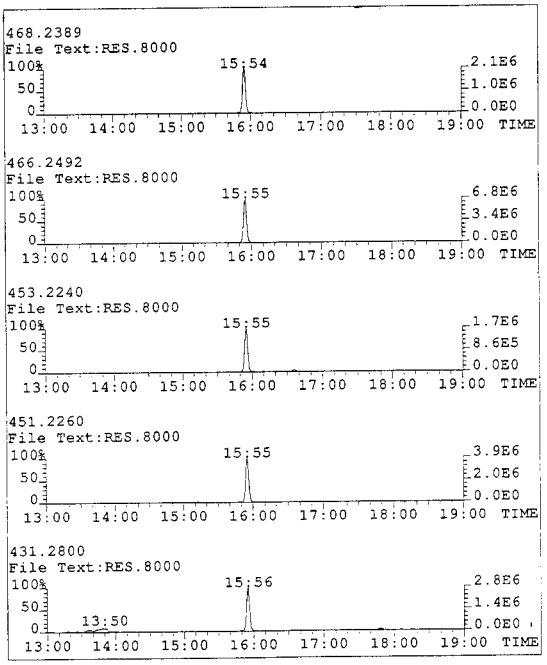

Fig. 2. Ion chromatograms (GC–HRMS) of the clostebol positive reference urine sample (76 $\mu g\ l^{-1}$).

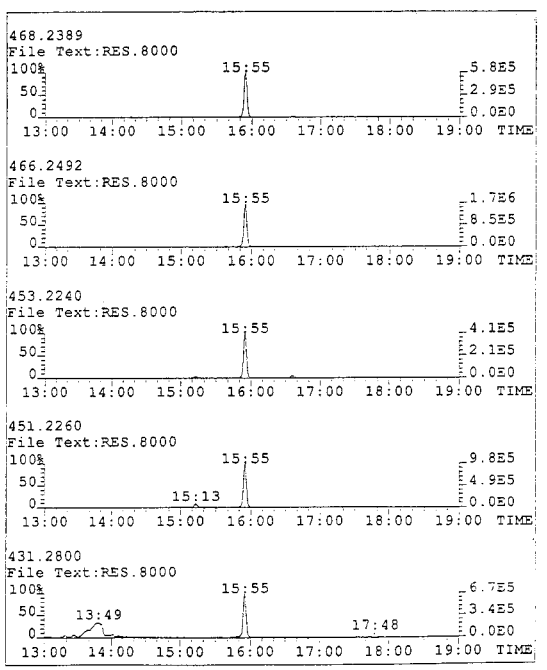

Fig. 3. Ion chromatograms (GC–HRMS) of presumed positive reference urine sample (23 $\mu g\ l^{-1}$).

fragment ion $(M-15)^+$ (ions of m/z 451 and 453) were chosen together with an ion of m/z 431, which results from the loss of the chlorine atom. The exact masses of the ions were calculated and presented in Table 4. The ion chromatograms for a reference urine sample are shown in Fig. 2. The five selected ions appear simultaneously at a retention time of 15.55 min. As can be seen from Fig. 3, both gas chromatographic (retention time) and mass spectrometric data (presence of the five ions) of the presumed positive urine sample correlate with that of the positive reference urine sample.

4. Conclusions

It can be concluded that the presence of clostebol metabolite in a presumed positive urine sample was confirmed by data obtained from the GC–LRMS and GC–HRMS experiments. The proposed strategy can add to the reliability of data interpretation, since on the one hand similarity of the analytical results with those of the reference compound can be expressed in figures (% deviation of the ion ratios, similarity indices and match qualities) and on the other hand higher selectivity is obtained by HRMS.

Acknowledgements

G.D. was Research Assistant of the National Fund for Scientific Research (Belgium). This work was supported by grant 3.0017.89 from the Fund for Medical Scientific Research.

References

[1] G. Debruyckere, R. de Sagher and C. Van Peteghem, Clin. Chem., 38 (1992) 1869.
[2] G. Debruyckere, R. de Sagher and C. Van Peteghem, Anal. Chim. Acta, 275 (1993) 49.
[3] W. Schänzer and M. Donike, Anal. Chim. Acta, 275 (1993) 23.
[4] Commision Decision of 14 April 1993 laying down the methods to be used for detecting residues of substances having a hormonal or a thyrostatic action (93/256/EEC), Official Journal of the European Communities, No. 118/64, May 14, 1993.

ELSEVIER

Analytica Chimica Acta 291 (1994) 161–167

ANALYTICA CHIMICA ACTA

Platinum species analysis in plant material by gel permeation chromatography

J. Messerschmidt, F. Alt *, G. Tölg

Institut für Spektrochemie und angewandte Spektroskopie, Bunsen-Kirchhoff-Strasse 11, D-44139 Dortmund, Germany

(Received 10th May 1993; revised manuscript received 3rd December 1993)

Abstract

Model experiments for the analysis of platinum species in extracts from native and platinum treated grass cultivation are described. The procedural steps are cultivation of the grass samples, preparative separation of the Pt species and analytical detection and characterisation of the separated species. The platinum uptake from the roots resulted by treating the grass cultivation with an aqueous solution of tetrammineplatinum(II) nitrate, $[Pt(NH_3)_4](NO_3)_2$. The grass was cut, the cell fluid extracted and the Pt species were separated by gel permeation chromatography. The extremely sensitive adsorptive voltammetry was used for the sequential determination of platinum in the elution fractions. The estimation and determination of the molecular weights were carried out by gel permeation and liquid chromatography. In the native grass extract only one Pt species (160–200 kD) was detected. In the platinum treated grass extracts several Pt species were observed. More than 90% of all the platinum is bound to a low molecular weight species (about 1 kD), whereas less than 10% of the platinum is bound to species with molecular weights from 19 up to > 1000 kD.

Key words: Permeation chromatography; Liquid chromatography; Plant materials; Species analysis; Platinum

1. Introduction

Heavy metals are of great importance in environmental discussions. In this context platinum emission from motorcars with catalytic cleaning of the exhaust gases represents a new additional factor of environmental pollution. The kind of platinum emission as small particles (sub-μm range) leads to a good bioavailability of this element [1,2]. The development of an efficient and extremely sensitive analytical procedure ensured the determination of baseline levels of platinum in many biological and environmental materials [3]. Furthermore the investigation of element species becomes of increasing interest. The knowledge of the binding state and binding partners of heavy metals in biological and physiological systems supply information about their bioavailability and consequently of their toxicological and nutrition physiological relevance. The influence on the metabolism in plants extends the investigation area.

Plants stand at the beginning of the food chain for man. The physiology and biochemistry of plant metabolism are of decisive importance to the

* Corresponding author.

SSDI 0003-2670(94)00015-E

degree of heavy metal uptake. Consequently, the binding forms of metals in plant materials have frequently been investigated in the last few years. In newer and fundamental publications Grill et al. [4–6] described the phytochelatins as the heavy metal binding principle of elements like zinc, cadmium, copper and lead. Other authors examined copper [7,8] and nickel phytochelatins [9]. The phytochelatins represent a class of heavy metal binding plant peptides functionally analogous to metallothioneins in humans, animals and special fungi. They are observed only in plants that are exposed to heavy metals in a higher degree than normal. The characterization of this class of metal binding peptides revealed homologous compounds of repetitive γ-glutamyl–cysteine units ($[\gamma\text{-Glu–Cys}]_n$–Gly), where n ranges from two to eleven. Heavy metal ions like Cd^{2+}, Zn^{2+}, Hg^{2+}, Cu^{2+}, Ag^{+}, Au^{3+}, Pb^{2+} and Bi^{3+}, but also anions like selenate and arsenate, can induce the formation of these special peptides [10]. In model experiments the necessary high heavy metal exposure is realized in many cases by addition of a slightly soluble metal salt into the cultivation substrate [11]. The binding partners of elements in naturally grown plants have so far been investigated only occasionally [12], although these plants have a great relevance to nutrition.

Platinum species in plant material have not been investigated until now. A separation method for metal species analysis has to fulfil at least two main conditions (beside others). On the one hand it should work on a preparative scale because of the expected low metal concentrations (especially in native plant material); on the other hand it should not attack the binding between platinum and the organic components to be separated [13]. Gel permeation chromatography offers good qualities in this context, because a relative large sample amount can be separated in one step. Furthermore the separation principle is based upon the molecular size and interactions between the separation medium (gel) and the samples are decreased to a minimum. For the sequential de-

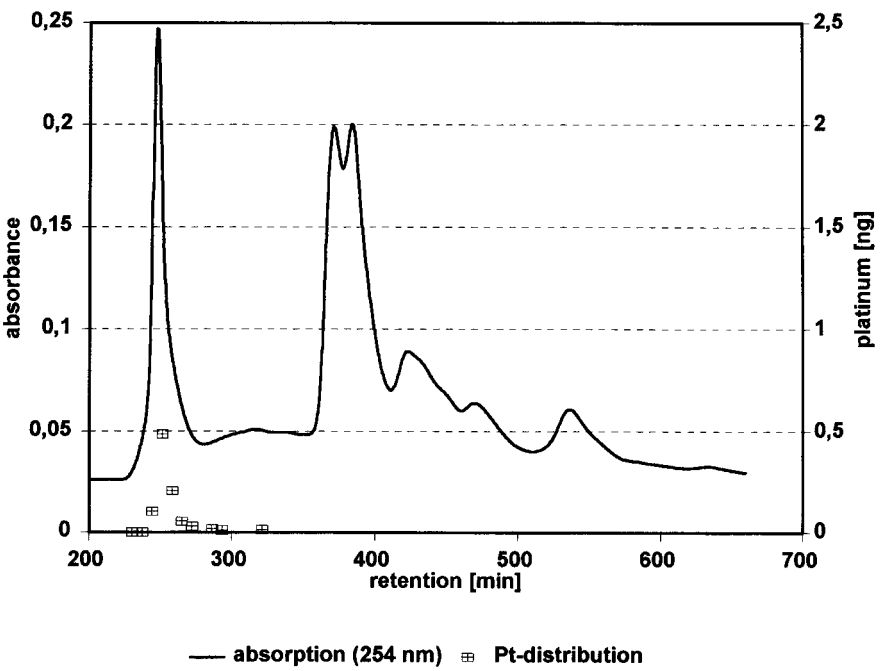

Fig. 1. Gel chromatographic separation of an extract from native grass material (UV absorbance detection) and the corresponding platinum distribution (separation medium Sephadex G25, superfine; column, 100 cm × 16 mm i.d.; elution buffer, 0.01 M HCl–0.05 M NaCl (pH 8)–Tris at 18 ml/h; complete elution).

termination of platinum in the eluted fractions a very sensitive method (adsorptive voltammetry) with detection limits in the sub-pg range is available [14].

2. Experimental

2.1. Plant cultivation and preparation of the grass cell fluid (extract)

For the model experiments we chose the cultivation of "Welsches Weidelgras" as a suitable and realistic sample material. This grass can be cultivated in the laboratory over the whole year. The grass seed was sown into market garden mould, the cultivations were realized in peat pots. The plants destined for Pt exposure were treated with a solution of tetrammineplatinum(II) nitrate, $[Pt(NH_3)_4](NO_3)_2$, in water, in the course of which contact of the solution with the grass was absolutely avoided. The platinum was exclusively taken up by the roots. When the grass was grown up to 5–7 cm, it was cut. The Pt addition amounted to 300 mg up to the first cut, and 100 mg between the second and the third cut (the total platinum addition amounted to about 0.8 mg/g soil). After the fifth cut, the cultivation was concluded.

A series of native (not treated with platinum) grass cultivations were grown parallel to the treated cultivations. These plants were only treated with deionized water; additional fertilizer was omitted.

Each grass cut was triturated with buffer solution (0.02 M ammonium acetate made up to pH 8.0 with Tris) in a centrifuge vessel, thus extracting the Pt species. The extracts were decanted, freeze-dried for concentration and the dried residues were stored at −20°C.

For the determination of platinum in the grass cuts and in the grass extracts, as well as in the garden mould, the sample material was decomposed with HNO_3–HCl (High Pressure Asher®, Kürner) followed by adsorptive voltammetric quantification of the platinum [13]. The Pt con-

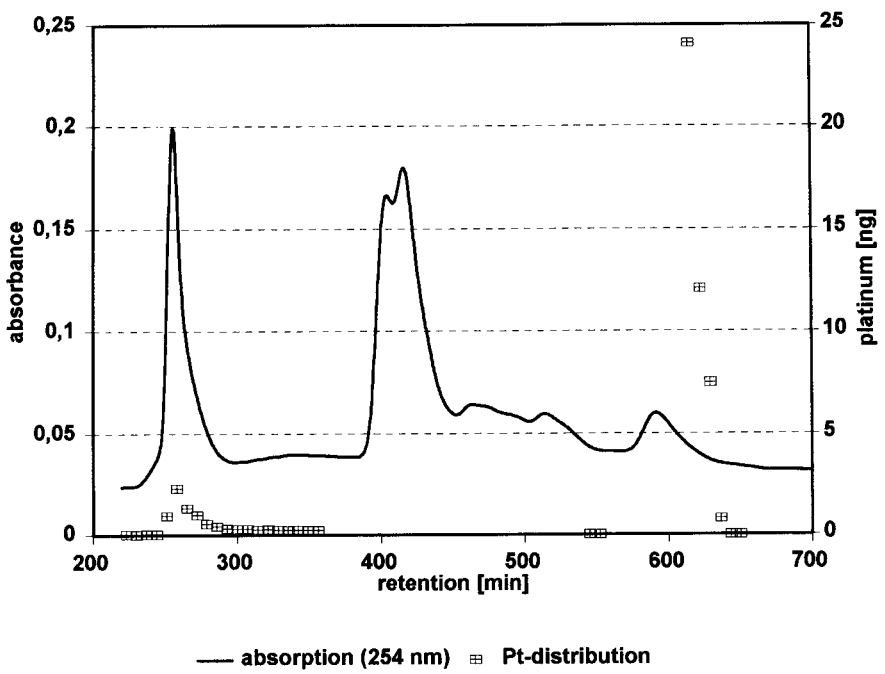

Fig. 2. Gel chromatographic separation of an extract from a platinum grass material and the corresponding platinum distribution (separation conditions, see Fig. 1).

tent of the untreated wet garden mould was found to be 0.3 ng/g (0.9 ng/g in relation to the dry weight). With the native grass a decrease of the Pt concentration from one cut to another (0.7 ng/g with the first cut down to 0.12 ng/g with the fourth cut) was observed. We considered this to result from a decrease of the platinum concentration in the mould. The treated grass showed an increasing Pt uptake from one cut to another up to 35 μg/g with the fifth cut. Relating to the total content in the grass cuttings, the Pt recoveries in the extracts amounted to > 80%.

2.2. Gel permeation chromatography

The freeze-dried residues according to 2.1 were dissolved in the pH 8.0 buffer solution and separated by gel chromatography. To optimize the separation for the relevant molecular weight (MW) range (1–1000 kD) several kinds of gels were used: for the low MW range Sephadex G25 superfine and Sephadex G50 superfine, for the high MW range Sephacryl S-400 HR (all from Pharmacia). Columns with a length of 100 cm and an inner diameter of 16 mm were used throughout. Different elution buffers (12 resp. 18 ml/h, Microperpex peristaltic pump, LKB) were tested: (a) 0.01 M HCl, 0.05 M NaCl; (b) 0.02 M ammonium acetate; (c) 0.025 M HCl (all made up to pH 8.0 by addition of Tris). The absorption profiles of the eluates were measured at 254 nm (UV spectrophotometric detector, Latek). Fractionation was carried out by a fraction collector (Multirac®, LKB), the fraction volumes amounting from 2 to 8 ml. An SP 4290 integrator (Spectra Physics) was used for data processing.

2.3. Platinum determination

Up to 1.5 ml of each fraction (see 2.2) was mixed with 0.3 ml HNO_3 (65%), 0.1 ml $HClO_4$ (70%) and 0.1 ml H_2SO_4 (96%) in 10-ml reaction vessels and heated in an aluminium heating block up to 130–140°C block temperature. After evaporating the sample to about 1 ml the block temperature was raised to 210–220°C within 40 min and

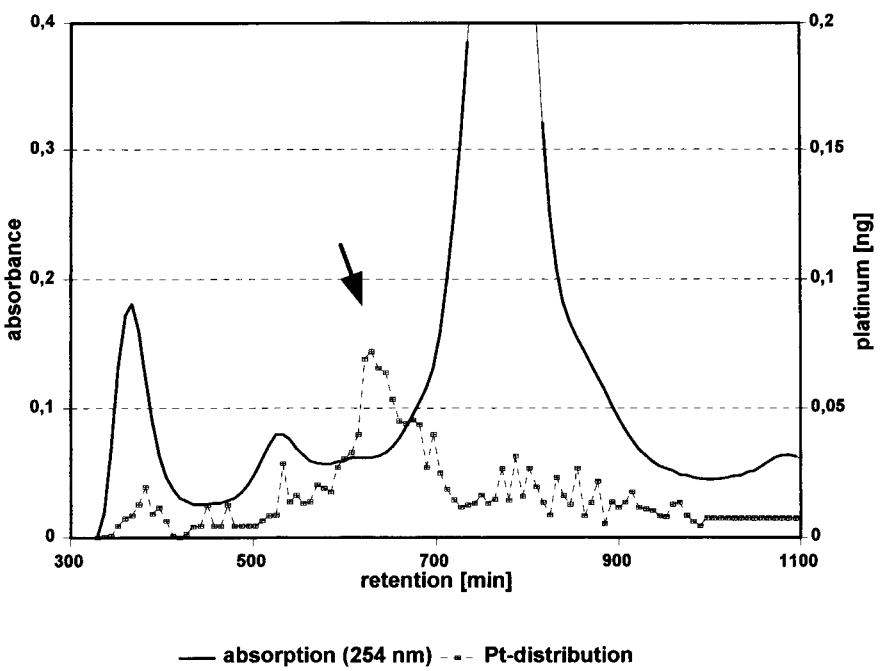

Fig. 3. Gel chromatographic separation of an extract from native grass material and the corresponding platinum distribution (separation medium, Sephacryl S-400 HR, same separation and detection conditions as in Fig. 1; eluted molecular weight range > 10 kD).

kept at this temperature for 10 min. Subsequently the vessels were taken out of the heating block for cooling. Afterwards 0.05 ml HNO_3 (65%) and 0.15 m HCl (30%) were added. The sample was evaporated to 0.3–0.4 ml at a block temperature of 170°C. After adding 0.2 ml HCl (30%) the volume was again decreased to give a residue of about 0.3 ml at the same temperature to remove the remaining HNO_3. Chloride ions must remain to stabilize the platinum. To be quite sure having removed the last residue of HNO_3, again 0.1 ml HCl (30%) was added (HNO_3 would interfere the subsequent voltammetric platinum determination). After cooling, the samples were made up with deionized water to 5.0 ml. This solution was 0.36 M in H_2SO_4. By adding 0.08 ml of 0.01 M hydrazinium sulfate and 0.01 ml of formaldehyde solution (37%) the platinum, present as Pt(IV), was reduced to Pt(II), and the Pt(II)–formazone complex was formed. The whole volume or an aliquot was taken for analysis. The solution was made up to a volume of 15 ml with a corresponding electrolyte solution (250 ml of 0.36 M H_2SO_4 + 0.375 ml of 0.1 M hydrazinium sulfate solution + 0.150 ml of 37% formaldehyde solution) and transferred into the voltammetric cell. Within a defined time (e.g. 1 min) the Pt(II)–formazone complex was adsorbed at the hanging mercury drop electrode. By increasing the voltage in the cathodic direction, a current peak was obtained in the differential pulse mode at −0.86 V (vs. Ag/AgCl (3 M KCl)). The peak height was directly proportional to the platinum concentration. The absolute limit of detection ($3s_{blank}$) was 2 pg of platinum. A VA-stand 663 in connection with a Polarecord 626 and a Timer E 608 (Metrohm) were used for the voltammetric measurements.

2.4. Estimation of the molecular weights of some platinum species

(a) For the estimation of the molecular weights the gel permeation chromatography column was calibrated by separation of a mixture of selected proteins under equal conditions as for the separation of the plant extracts. For calibration the

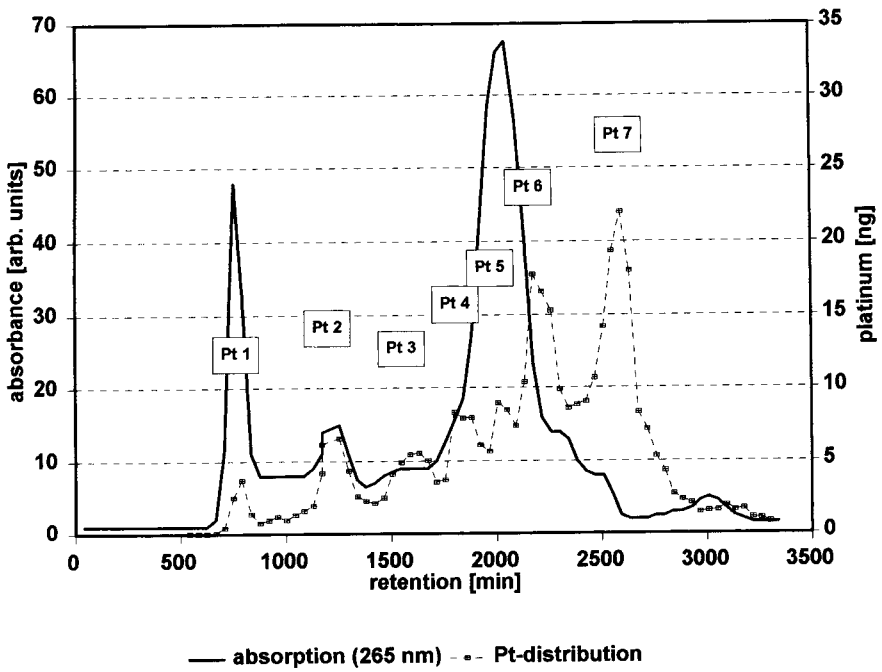

Fig. 4. Gel chromatographic separation of an extract from a platinum grass material and the corresponding platinum distribution (separation medium, Sephacryl S-400 HR; elution buffer, 0.025 M HCl (pH 8)–Tris at 12 ml/h; eluted molecular weight range > 10 kD).

following proteins were used: aldolase (158 kD), bovine serum albumin (68 kD), chymotrypsinogen A (25.6 kD) and cytochrome C (12.384 kD). The apparatus is described in 2.2.

(b) Analytical LC was carried out as an additional method for estimating molecular weights using Diol-bonded silica gel (Diol column, Knauer HY 077, 10 μm) [15]. 20 μl portions of selected fractions from the gel chromatographic separations were injected into the LC column. 0.025 M Tris with 0.5 M NaCl (pH 8.0) was used as elution buffer (elution 0.15 ml/min). The elution profile was measured at 254 nm. For calibration the same proteins as in gel chromatography were used. The apparatus used were an SP 8810 isocrated pump (Spectra Physics) and a SP 4290 integrator (Spectra Physics) for data processing together with an UV spectrophotometric detector (Latek).

2.5. Reagents

Reagents of analytical grade or Suprapur grade (Merck) were used. The platinum reagent blank was checked and controlled throughout the whole procedure.

3. Results and discussion

The gel permeation chromatogram and the corresponding platinum distribution in an extract from a native grass cultivation yielded only one platinum species in the molecular weight range of 160–200 kD. No species in the low molecular weight range (1-2 kD) could be detected. Figs. 1 and 3 (high molecular weight range) show the absorbance and platinum peaks after separation with Sephadex G25 superfine and Sephacryl S-400 HR. In the Figs. 2 and 4 (high molecular weight range) the corresponding separation pattern of an extract from one platinum grass cultivation is presented. Several platinum species are recognizable, a low molecular weight species (ca. 1 kD, Fig. 2), containing more than 90% of the whole platinum, and seven species (Pt 1 to Pt 7, Fig. 4) with higher molecular weights (up to > 1000 kD). The UV absorbing species in the figures derive

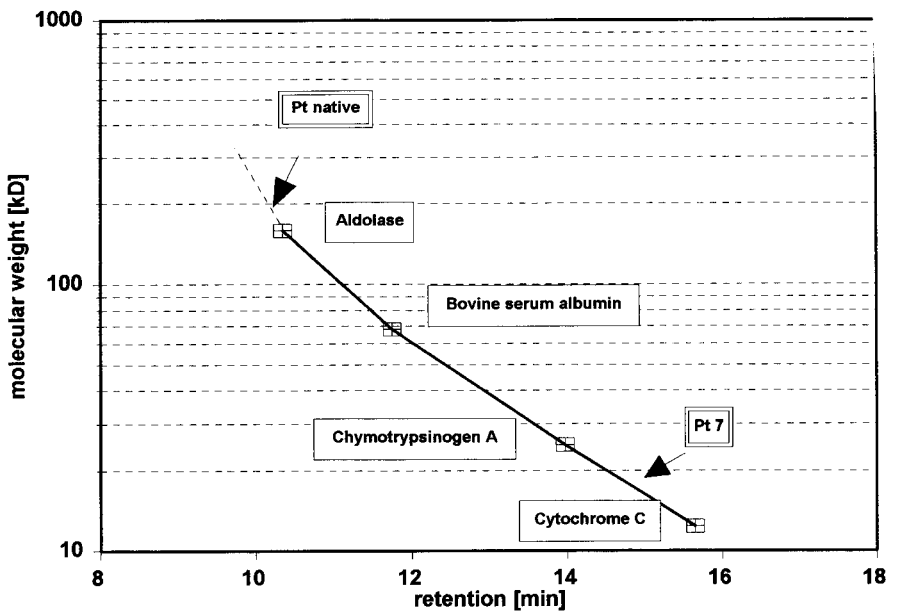

Fig. 5. Calibration graph for the determination of the molecular weights of platinum species (selected elution fractions) by LC.

Table 1
Estimated molecular weights of some platinum species in native and platinum treated grass extracts

Platinum species	Sample	Molecular weight (kD)	Calibration
Pt 1	treated grass	> 1000	gel chromatography
Pt 2	treated grass	600	gel chromatography
Pt 3	treated grass	225	gel chromatography
Pt 4	treated grass	160–200	gel chromatography
native bound Pt	native grass	160–200	LC
Pt 5	treated grass	80.7	gel chromatography
Pt 6	treated grass	27.8	gel chromatography
Pt 7	treated grass	19	LC

from grass proteins in the extracts and may not necessarily coincide with the UV absorptions of the platinum species. In spite of the low separation power of gel permeation chromatography a differentiated platinum pattern could be obtained from the extracts of treated grass cultivations.

A further estimation of the molecular weights of the native platinum species and the species Pt 7 was carried out by analytical LC. The calibration graph is shown in Fig. 5 and a survey of the platinum species is given in Table 1. The agreement of the molecular weights of the native platinum species and the platinum species Pt 4 does not necessarily demonstrate their molecular identity.

These investigations were made with the aim of developing analytical methods for the separation and identification of platinum species in plant materials. Physiological studies were not intended. This will remain for future work to be carried out by specialists. Therefore, the experiments described here are of a model character.

4. Conclusion

This contribution represents the first part of our investigations concerning platinum species in biological materials. Up to now the characterization of the separated platinum containing components is restricted to the estimation of their molecular weights. A further attempt will be made to get more information about the nature of these components. A particular problem to be investigated is whether there is a platinum species present in exposed plant materials that is comparable to the phytochelatins in plants exposed to cadmium or other heavy metals. For this purpose independent separation methods (for example electrophoresis) will be used.

Acknowledgement

This report is based upon a project "Edelmetallemissionen", which was financially supported by the Bundesminister für Forschung und Technologie (Germany) under the reference number 07 VPT 01A. The authors are grateful to Dr. K. Günther, University of Bonn, Germany, for carrying out one of the gel permeation chromatography separations.

References

[1] K.H. Schaller, J. Angerer, F. Alt, J. Messerschmidt, D. Weltle and G. Lehnert, Lecture at the International Symposium on Biological Monitoring, Kyoto, 1992.
[2] F. Alt, A. Bambauer, K. Hoppstock, B. Mergler and G. Tölg, Fresenius' J. Anal. Chem., 346 (1993) 693.
[3] F. Alt and J. Messerschmidt, in K. Dörner (Ed.), Akute und chronische Toxizität von Spurenelementen, Wissenschaftliche Verlagsgesellschaft, Stuttgart, 1993, p. 85.
[4] E. Grill, E.-L. Winnacker and M.H. Zenk, Science, 230 (1985) 674.
[5] E. Grill, E.-L. Winnacker and M.H. Zenk, Proc. Natl. Sci. USA, 84 (1987) 439.
[6] E. Grill, E.-L. Winnacker and M.H. Zenk, in H. Rennenberg (Ed.), Higher Plants, SPB Academic Publishing, The Hague, 1990, p. 89.
[7] D.E. Salt, D.A. Thurman, A.B. Tomsett and A.K. Sewell, Proc. R. Soc. London, Ser. B, 236 (1989) 79.
[8] J.A.C. Verkley, P. Koevoets and J. van't Riet, Mol. Biol. Chem., (1989) 347.
[9] R. Rieger, A. Michaelis and S. Takehisa, Mutat. Res., 244 (1990) 31.
[10] J.C. Steffens, Annu. Rev. Plant. Physiol. Mol. Biol., 41 (1990) 553.
[11] K. Lange-Hesse, L. Dunemann and G. Schwedt, Fresenius' J. Anal. Chem., 339 (1991) 240.
[12] K. Günther and F. Umland, Fresenius' J. Anal. Chem., 331 (1988) 302.
[13] G. Weber, Fresenius' J. Anal. Chem., 346 (1993) 639.
[14] J. Messerschmidt, F. Alt, G. Tölg, K.H. Schaller and J. Angerer, Fresenius' J. Anal. Chem., 343 (1992) 391.
[15] D.E. Schmidt, R.W. Giese, D. Conron and B.L. Karger, Anal. Chem., 52 (1980) 177.

ELSEVIER

Analytica Chimica Acta 291 (1994) 169–181

ANALYTICA CHIMICA ACTA

Chromatographic behaviour of novel zinc(II) carboxylates with nitrogen-donor ligands Part I. Formates and acetates

A. Oriňák [a,*], E. Matisová [b], K. Györyová [a], L. Šlesárová [c]

[a] *Department of Inorganic Chemistry, Faculty of Science, P.J. Safarik University, Moyzesova 11, 041 54 Košice, Slovak Republic*
[b] *Department of Analytical Chemistry, Faculty of Chemical Technology, Slovak Technical University, Radlinského 9, Bratislava, Slovak Republic*
[c] *Department of Chemistry, Biochemistry and Biophysics, University of Veterinary Medicine, Komenského 73, 041 81 Košice, Slovak Republic*

(Received 13th June 1993; revised manuscript received 10th December 1993)

Abstract

The basic characterization of novel $Zn(RCOO)_2L_n(H_2O)_q$ compounds including the determination of their melting points, solubility, UV–visible absorption spectra, polarity and chromatographic behaviour was performed. Thin-layer chromatography with flame ionization detection (FID) showed an intense FID signal for the zinc(II) carboxylate salts under examination. Liquid chromatographic analyses were carried out with organic and water–organic mobile phases. Reasonable results were obtained for analyses on Silasorb SPH Nitrile, Tessek HEMA-Bio 1000CM, LiChrosorb Si 60 and the best LiChrosorb RP-18 columns. It follows from the analyses that the retention behaviour of these structurally novel and pharmacologically interesting zinc(II) compounds is governed by the chromatographic properties of the corresponding ligand molecule binding. The alkyl chain of the acetate anion has a small effect on the retention behaviour of the whole molecule. The increase in retention time is greater with zinc(II) acetates with bound caffeine or phenazone molecules and the results confirm that the molecules of zinc(II) carboxylates move through the entire column.

Key words: Liquid chromatography; Thin-layer chromatography; Biological samples; Nitrogen donor ligands; Zinc carboxylates

1. Introduction

The synthesis of Zn(II) compounds with organic molecules is very popular at present. There are many possibilities of using synthesized preparations in pharmacy [1,2], plant photosynthesis [3] and agriculture [4,5]. The function of zinc and zinc compounds in living organisms is of special importance [6,7]. Zinc is a component of more than 90 metalloenzymes [8] and affects protein synthesis [9].

$Zn(RCOO)_2L_n(H_2O)_q$-type compounds have been synthesized at the Department of Inorganic

* Corresponding author.

SSDI 0003-2670(93)E0707-E

Chemistry, P.J. Safarik University, Košice, in an endeavour to develop a suitable, structurally simple skeleton as a drug and medicine carrier in which each part had a stimulating or synergistic effect on the action of the bound active component (ligand part). The identity of the individual zinc(II) carboxylate salts was confirmed by elemental analysis, infrared spectrometry and thermal analysis [10].

Information on the properties and possibilities of the chromatographic characterization and determination of zinc(II) carboxylate compounds is relatively scarce. It is also difficult to find data describing the chromatographic separation of similar compounds. There are papers on the separation, identification and determination of alkyl and alkylphenol ether carboxylates by means of liquid chromatography (LC) (on a LiChrospher 100 RP-18 column with refractometric detection [11]). The effect of pH and electrolyte concentrations on the retention of *n*-alkylcarboxylates has been examined by Brandts et al. [12]. The separation of sulphonate and carboxylate mixtures on a highly basic anion-exchange resin by ion-exchange chromatography (IEC) with gradient elution has been reported [13]. More frequent are papers concerned with the determination of metal chelates [14], metal dithizonates [15], acetylacetonates [16] and diethyldithiocarbamates [17] of zinc(II) using thin-layer chromatography (TLC) and LC methods.

LC methods for the determination of zinc(II) ions using exchange reactions or ligand-exchange chromatography [18] have also been elaborated. The separation of Zn, Cd, Pb, Ni, Cu and Hg complexes with biacetyl[bis(4-phenylthiosemicarbazone)] on a C_{18} column has been reported [19]. The individual eluates are detected by means of electrochemical detection [20] or oscillography [21]. Most frequently, detection is done by spectrophotometry (coloured compounds) after post-column derivatization [22–24].

There are descriptions of gas chromatographic (GC) and LC analyses of the organic molecules in some metal complexes and their metabolites (thiourea [25], phenazone [26], nicotinic acid [27,28], caffeine [29,30]).

This work is an introduction to the characteri-

Table 1
Selected physico-chemical properties of zinc(II) carboxylates with N-donor ligands

No.	Name	Abbreviation	M_r	M.p. (°C) ($\bar{x} \pm$ S.D., $n = 3$)	S.D.
1	Caffeine	caff	194.123	155	13.3
2	Urea	urea	60.055	139	3.6
3	Thiourea	turea	76.122	43 [43]	
4	Phenazone	phen	187.241	115.7	3.5
5	Nicotinic acid	nica	123.112	248.3	1.5
6	$Zn(HCOO)_2(urea)(H_2O)_x$		233.480	156.7	7.6
7	$Zn(HCOO)_2(urea)_2(H_2O)_{0.5}$		284.535	163.3	1.53
8	$Zn(HCOO)_2(turea)(H_2O)_{0.5}$		233.480	103.3	7.64
9	$Zn(HCOO)_2(turea)_2$		307.669	100.7	4.04
10	$Zn(HCOO)_2(nica)(H_2O)_x$		278.537	> 350	
11	$Zn(HCOO)_2(nica)_2(H_2O)_x$		401.649	> 350	
12	$Zn(HCOO)_2(caff)(H_2O)_{2.5}$		349.548	155.0	5.00
13	$Zn(HCOO)_2(caff)_2(H_2O)_{2.5}$		419.649	150.0	5.00
14	$Zn(CH_3COO)_2(urea)(H_2O)_x$		240.511	119.7	3.06
15	$Zn(CH_3COO)_2(urea)_2(H_2O)_{0.5}$		309.566	144.2	12.80
16	$Zn(CH_3COO)_2(turea)(H_2O)_{0.5}$		265.578	185.0	5.0
17	$Zn(CH_3COO)_2(turea)_2$		332.700	183.3	10.4
18	$Zn(CH_3COO)_2(nica)_2(H_2O)_x$		426.680	> 350	
19	$Zn(CH_3COO)_2(phen)_2(H_2O)_{1.5}$		581.938	105.3	1.53
20	$Zn(CH_3COO)_2(caff)(H_2O)_{2.5}$		419.579	150.0	8.70
21	$Zn(CH_3COO)_2(caff)_2(H_2O)_{3.5}$		631.702	155.0	5.00

The crystallic water contents was determined by thermogravimetric analysis.

zation of the fundamental qualitative physicochemical and chromatographic properties of novel $Zn(RCOO)_2L_n(H_2O)_q$ compounds (where R = H or CH_3, L = caffeine, nicotinic acid, urea, thiourea or phenazone, $n = 1$ or 2 and $q = 0.5$, 1.5, 2.5, 3.5 or variable, x is the water content determined by thermogravimetric analysis). It is the starting point for the development of TLC and LC methods and subsequently capillary GC methods for their determination in the non-metabolized form and for the possibility of the determination of metabolites in internal organ tissues and body fluids in experimental animals during testing of their biological activity.

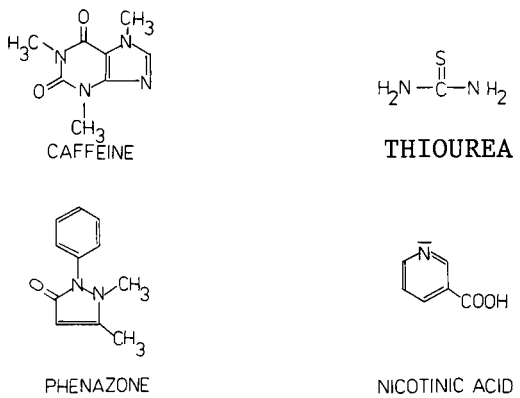

Fig. 1. Structures of N-donor ligands bound in zinc(II) carboxylates analysed.

2. Experimental

2.1. Chemicals

HCl, NaOH, $NaHCO_3$, citric acid, sodium dihydrogenphosphate dihydrate, diethyl ether, dimethylformamide (DMF) and dimethyl sulphoxide (DMSO) used in solubility tests of the synthesized zinc(II) carboxylate compounds were purchased from Lachema (Brno, Czech Republic) and were of analytical-reagent grade.

The solvents used in LC analyses, methanol (MeOH), chloroform and ethanol (EtOH), were purchased from Lachema, dioxane, *n*-propanol and propan-2-ol from Merck (Darmstadt) as hexane from Carlo Erba (Milan), all of analytical-reagent grade. Acetonitrile (ACN) was purchased from VEB Laborchemie (Apolda). Redistilled water (conductivity 0.4 μS) was prepared with an Ilmator Biplex device.

All standards of $Zn(RCOO)_2L_n(H_2O)_q$ compounds were recrystallized prior to analysis. A list of all compounds is given in Table 1 and the formulae of the ligands are shown in Fig. 1.

2.2. Determination of the melting points of $Zn(RCOO)_2L_n(H_2O)_q$ compounds

Compounds in their crystalline form were transferred on to the slide of the heating block of a melting point device (Boetius, Zeiss, Jena) and heated stepwise in increments of 4°C min^{-1} to melting of the crystal borders. The temperature at which this phenomenon was observed was noted as the melting point.

2.3. Solubility of $Zn(RCOO)_2L_n(H_2O)_q$ compounds

The solubility of the zinc(II) carboxylates was tested in 5% HCl, 5% NaOH, 5% $NaHCO_3$, diethyl ether and water according to the steps indicated in [31]. A compound was considered insoluble if it was not dissolved after 30 min of intensive stirring. The solubility of the zinc(II) compounds was also tested in DMF and DMSO.

2.4. UV–visible spectra of $Zn(RCOO)_2L_n(H_2O)_q$ compounds

The UV–visible spectra of the compounds examined were measured in aqueous solutions of the standards prepared by dissolution of a 5-mg sample in redistilled water (10-ml volumetric flask). A 0.2-ml volume of this stock solution (0.1 mg of the component) was pipetted into a quartz cuvette, 2 cm thick. The spectra were recorded from 200 to 440 nm on a Specord spectrophotometer (Zeiss).

2.5. TLC of $Zn(RCOO)_2L_n(H_2O)_q$ compounds with flame ionization detection

Analyses of chromatographic separation of $Zn(RCOO)_2L_n(H_2O)_q$ compounds by TLC–FID

were made on an Iatroscan MK5 (Newman-Howells). Samples of zinc(II) acetate with bound urea, thiourea, phenazone and caffeine and their carboxylate salts were developed in MeOH–EtOH (8 + 2, v/v) on Chromarod S III silica gel rods. The developed and dried chromatographic rods were subsequently analysed and peaks were evaluated with an integrator.

2.6. LC analysis of $Zn(RCOO)_2L_n(H_2O)_q$ compounds

Preparation of stock standard solutions

The solutions of substances **1–21** (Table 1) were prepared by dissolving 5 mg of each in 10 ml of redistilled water. Solutions of mixture 1 (ligands, compounds **1–5**), mixture 2 (formates **6–13**) and mixture 3 (acetates **14–21**) were obtained by dissolving 5 mg of compounds and diluting to volume with redistilled water. A 1-ml volume of 5% HCl was added to standards **5**, **6**, **7**, **10**, **12** and **13** to improve their solubility.

Preparation of McIlvaine buffers

McIlvaine universal buffers with increasing pH values (ranging from 2.0 to 8.0) were prepared from a 0.1 M solution of citric acid and a 0.2 M solution of $Na_2HPO_4 \cdot 2H_2O$ as described by Kuster and Thiel [32]. pH values were measured with an OK-104 pH meter (Radelkis, Budapest).

Analysis

LC analyses were made on LiChrosorb Si 60 [stainless steel (SS), 10 μm, 250 mm × 4.6 mm i.d., column A_1], LiChrosorb RP-8 (SS, 7 μm, 250 mm × 4.6 mm i.d., column B_1) and LiChrosorb RP-18 (SS, 10 μm, 250 mm × 4.6 mm i.d., column B_2) purchased from Knauer (Berlin), Silasorb SPH Nitrile (SS, 7.5 μm, 250 mm × 4 mm i.d., column A_2), Silasorb SPH Amine (SS, 5.9 μm, 250 mm × 4 mm i.d., column A_3) purchased from Lachema (Brno) and HEMA-Bio 1000CM (glass, 10 μm, 150 mm × 3 mm i.d., column A_4) obtained from Tessek (Prague) in an LC system with an LCP 4000 high-pressure pump from Ecom (Prague) connected with a Model 2082 UV–visible spectrophotometric detector (Ecom). To inject the samples, an injection valve (Rheodyne Model 7120) with a 20-μl sample loop was used. The optimum mobile phase composition in reversed phase (RP) LC analyses was selected using a PRISMA model and the program Solvent (Ecom). All liquids used were degassed ultrasonically.

The conditions used for the analyses were as follows: wavelength of the UV detector: 260–270 nm, and average 253 nm; flow-rate of mobile phase, 0.4 ml min^{-1} on column A_4 and 1 ml min^{-1} on the other columns, injection volume, 20 μl (10 μg); and temperature of the UV–visible detector cell, 25°C. Gradient elution was applied as follows, where solvent A is chloroform and solvent B is ethanol: 2 min, 100% A; 10 min 20% (v/v) B in A; 20 min, 40% B; and 30 min, 60% B.

3. Results and discussion

3.1. Results of characterization of basic physicochemical properties of $Zn(RCOO)_2L_n(H_2O)_q$ compounds

The results obtained in measuring the melting points of zinc(II) salts are given in Table 1. From these results it follows that compounds **10**, **11** and **18** appear to be the most stable to heat, their melting points surpassing the maximum temperature of the device of 350°C.

Absorption maxima in the UV–visible region of the spectrum of the compounds examined and their molar absorption coefficients are sufficiently high for use of the spectrophotometric detector of detection during LC analyses of the zinc(II) carboxylates.

From Table 2, it is evident that the analysis of urea and its carboxylates is not possible by means of spectrophotometric detection. The compounds under examination absorb light at 273, 234, 262 and 243 nm (caffeine, thiourea, nicotinic acid and phenazone, respectively).

The solubility test on the above-mentioned compounds indicated that they belong to the substances that have medium or high solubilities in water (the solubilities decrease from ligands to acetates); only compounds **5**, **6**, **7**, **10**, **12** and **13** are exceptions as they are completely dissolved

Table 2
Spectrophotometric analysis of compounds examined (2-cm cuvette)

Compound	λ_{max} (nm)	A_{max} (absorbance)	ϵ ($dm^3\ mol^{-1}\ cm^{-1}$)
1	273.2	0.11	14990
2	Non-absorbing		
3	236.2	3.24	9496
4	242.7	2.49	17950
5	261.8	1.37	6479
6	Non-absorbing		
7	Non-absorbing		
8	235.8	1.45	14846
9	228.5	4.00	51236
10	261.3	0.94	15374
11	262.4	1.22	2740
12	272.9	0.90	14564
13	273.2	1.29	31324
14	Non-absorbing		
15	Non-absorbing		
16	236.1	0.87	13506
17	236.1	1.76	18870
18	261.2	0.83	13409
19	242.5	0.58	9306
20	273.2	0.64	5729
21	273.2	0.70	8267

after adding 1 ml of 5% HCl to the sample. The results of the tests are summarized in Table 3. The pH values of the solutions prepared (in water only) ranged from 2.85 to 7.3. Compounds **7**, **9**, **13**, **15**, **17** and **21** are readily soluble in DMF, DMSO and acetic acid.

3.2. TLC–FID

TLC–FID analysis of zinc acetate, thiourea, phenazone and their acetate complexes revealed good FID responses to these substances. On the basis of the recordings obtained (Figs. 2 and 3), it is suggested that the inorganic part of the compound is probably shielded by the organic part of the molecule and the chromatographic properties are due to by the organic part of the molecule. In Fig. 2b, peak 2 probably relates to zinc(II) acetate as an impurity from the previous experiment. Separation of the Zn(II) carboxylates (Fig. 2c) leads to the suggestion that dissociation of the complex occurs by means of release of a thiourea

Table 3
Solubility of compounds tested

Compound	Water	5% NaOH	5% $NaHCO_3$	5% HCl	Diethyl ether	DMSO	DMF	Type
1	+	C	C	+	−	+	+	S_2
2	+				−	+	+	S_2
3	+				−	+	+	S_2
4	+				−	−	−	S_2
5	−	+	D	+	−	−	−	A_1–A_2
6	+	−	C	+	−	+	+	S_2
7	+	+	Cat	+	−	+	+	S_2
8	+	C	−	+	−	+	+	S_2
9	+	+	−	+	−	+	+	S_2
10	−	+	C	+	−	−	−	A_2
11	−	+	−	+	−	−	−	M–B
12	+	C	D	+	−	+	+	A_1–A_2
13	−	C	D	+	−	+	+	M–B
14	−	+	D	+	−	+	+	M–B
15	−	+	D	+	−	+	+	M–B
16	+				−	+	+	S_2
17	+				−	+	+	S_2
18	+				−	−	−	S_2
19	−	+	Cat	+	−	−	−	M–B
20	−	C	C	+	−	+	+	M–B
21	−	C	C	+	−	+	+	M–B

C = coagulation; Cat = cataract; D = decomposition; + = positive; − = negative; A_1 = acidic nature; A_2 = weakly acidic nature; B = weakly basic nature; M = neutral nature; S_2 = polar compound with more than one polar group in molecule.

molecule, which is then characterized by peak 1, whereas peak 2 refers to the complex. The weak peaks in Fig. 3, i.e., peaks 2 (Fig. 3a) and 3 (Fig. 3c) relate to zinc(II) acetate, whereas peaks 2 (Fig. 3b) and (Fig. 3c) probably present impurities.

3.3. Results of LC analysis

Liquid–solid chromatographic (LSC) separations on LiChrosorb Si 60

The separation of the zinc(II) formates and acetates with N-donor ligands is most suitably done on a LiChrosorb Si 60 column with an organic mobile phase (chloroform–ethanol, chloroform–methanol) with gradient elution. Separation is limited by the solubility of the single carboxylates and ligands in DMSO or DMF. Insoluble in DMSO are nicotinic acid and all its zinc(II) carboxylate salts and phenazone and its zinc(II) acetate salt. DMSO and DMF are highly polar solvents which in many of the carboxylates under examination may cause elimination of the organic molecule. The infrared spectra of zinc(II) carboxylates with thiourea and caffeine obtained from the evaporated residue of the solution of these substances in DMSO do not show any differences from the spectra of the original compounds.

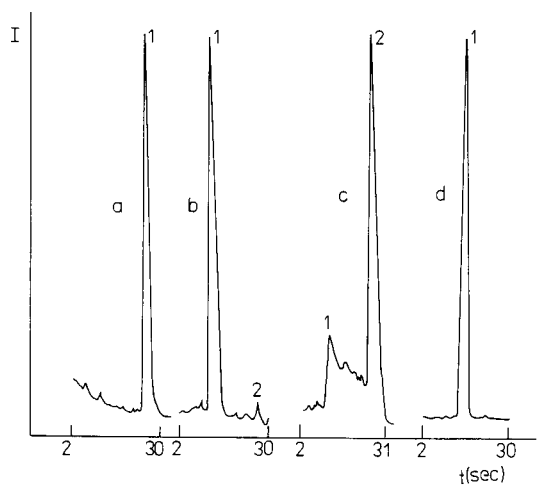

Fig. 2. TLC–FID of $Zn(acetate)_2L_n(H_2O)_q$. Peaks: (a) 1 = zinc(II) acetate; (b) 1 = thiourea, 2 = unknown; (c) 1 = unknown, 2 = $Zn(acetate)_2(tu)_2H_2O$; (d) 1 = phenazone.

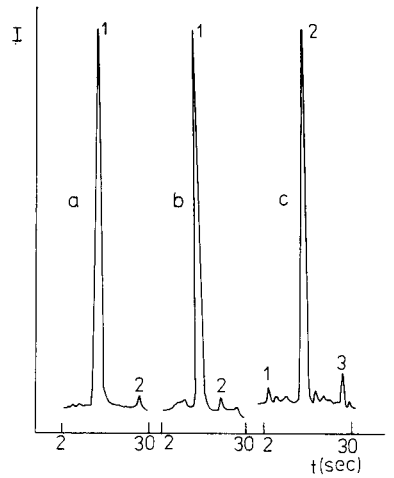

Fig. 3. TLC–FID of $Zn(acetate)_2L_n(H_2O)_q$. Mobile phase: methanol–ethanol (8 + 2). Peaks: (a) 1 = $Zn(acetate)_2$-$(phenazone)_2 1.5(H_2O)$, 2 = unknown; (b) 1 = caffeine, 2 = unknown; (c) 1 = unknown, 2 = $Zn(acetate)_2(caff)_2 3.5(H_2O)$, 3 = unknown.

According to Mikeš [33], the molecule with the highest number of carboxyl, hydroxyl or amino groups is the most strongly adsorbed on silica gel supports. The adsorption strength depends also on the type of the carbon chain. In an LC system with a non-polar, non-aqueous mobile phase and a polar silica gel support, the first to be eluted, e.g., with gradient elution with ethanol, is caffeine, the last being thiourea, because it contains two amino groups and a –C=S group. Solutes adsorbed on the support are removed from their sites by a more polar solvent (ethanol).

The solvent effect and the selection of the mobile phase underline the well known rule that the elution strength of the organic mobile phase is most frequently modified by the addition of dichloromethane, triethylamine and ethanol [34]. With the zinc(II) carboxylates observed, however, triethylamine could possibly cause replacement of the original ligand.

The optimum mobile phase found by zinc(II) carboxylate analysis by means of the TLC method with an LSC mechanism [35] showed that mixtures of ligands, formates and acetates started to move up the TLC layer in a mobile phase characterized by $E^*_{SiO_2} = 0.45$ (the elution strength E of the solvent is defined as the adsorption energy of

the solvent on unit surface area of an adsorbent with a standardized activity [36]). The use of benzene as a one component of the mobile phase is impossible because it absorbs UV light at 275 nm [37]. If, however, another composition of the mobile phase with a similar elution strength (e.g., 8% of methanol in diethyl ether) is used, then, on the basis of the same retention characteristics, LSC can be assumed to be the mechanism of separation.

The LSC separation mechanism on column A_1 with a chloroform–ethanol mobile phase seems to proceed by a competition mechanism. Chloroform, a weakly polar solvent, is weakly adsorbed on the polar silica gel support (forming a monolayer) and the retention of individual zinc(II) carboxylates depends on the competition for adsorption with ethanol (elution order: thiourea, caffeine), confirmed with results obtained in TLC analyses based on LSC [35] [$R_{F(\text{thiourea})} = 0.05$, $R_{F(\text{caffeine})} = 0.26$]. The use of polar solvents leads to the suggestion that the separation process proceeds via a solvent interaction model (elution order: nicotinic acid, thiourea, caffeine, phenazone), similarly to those in normal-phase liquid–liquid chromatographic (LLC) analyses.

Separations on LiChrosorb Si 60 and Silasorb SPH columns with mobile phases with high water contents

On the basis of TLC analysis in the single solvents, the following solvents were used for optimization of the mobile phase composition: ACN, MeOH, EtOH, propan-2-ol, dioxane and water.

The optimum separation of a ligand mixture (compounds **1–4**) on column A_1 was achieved with the mobile phase ACN–MeOH–EtOH–water (5.9 + 0.9 + 3.5 + 89.7, v/v). Nicotinic acid is the first to be eluted from the column at a flow-rate of 1 ml min^{-1} (retention time $t_R = 1.88$ min); it is followed by thiourea ($t_R = 3.29$ min), caffeine ($t_R = 4.0$ min) and phenazone ($t_R = 6.25$ min).

Mixture 2 (formates), analysed on the same column, with the same mobile phase, is separated into three peaks. The elution sequence of the single complexes is similar to that observed in elution of their ligands [first the complexes of nicotinic acid (nica), second thioureas and third caffeine salts]. The zinc(II) acetates (mixture 3), when eluted with the same mobile phase, give four peaks. The $Zn(CH_3COO)_2(nica)_2$ salt is separated first, then thiourea zinc(II) acetates are eluted together as the second peak, caffeine salts are third and the phenazone complex is last.

Separation on the column packed with nitrile-modified silica gel (column A_2) was better, the zones of the single analytes not being as spread as in the analyses on column A_1. The optimum separation of mixture 1 was obtained at a flow-rate of 1 ml min^{-1} with ACN–MeOH–EtOH–water (1 + 7 + 12 + 80, v/v) as the mobile phase. Mixture 2 was also separated into the groups of four separated zinc(II) acetate salts. The mechanism of separation is probably liquid–liquid partitioning in normal-phase chromatography. An LLC mechanism in analyses on silica gel with mobile phases containing more than 16% of water has also been reported by Mikeš [38]. Elution proceeds in order of solvents with increasing strength (very small differences) present in the mobile phase. Tailing of the peaks is more intense. A high water content in the mobile phase allows to substitute water for the buffer in the analysis of zinc(II) carboxylates and it is not necessary to use additive compounds to increase the solubility of zinc(II) carboxylates in water.

In contrast to analyses on the LiChrosorb Si 60 column, the results of analyses obtained on the Silasorb SPH Nitrile column with an aqueous mobile phase are characterized by greater symmetry of the peaks (Fig. 4). The good correlation between log k' obtained in zinc(II) carboxylates analyses on both columns (Fig. 5) leads to the result that the separation mechanism on column A_1 is closer to that on column A_2 (normal phase). The best correlation coefficients were obtained in pure ligand analysis (Table 4).

In all analyses with an aqueous mobile phase the greatest effect on the retention factors of the individual ligands occurred in the presence of methanol ($E_{SiO_2} = 0.73$). Whereas no great effect on the elution of nicotinic acid was found with increased methanol volumes in the mobile phase, the retention factor decreased with thiourea but

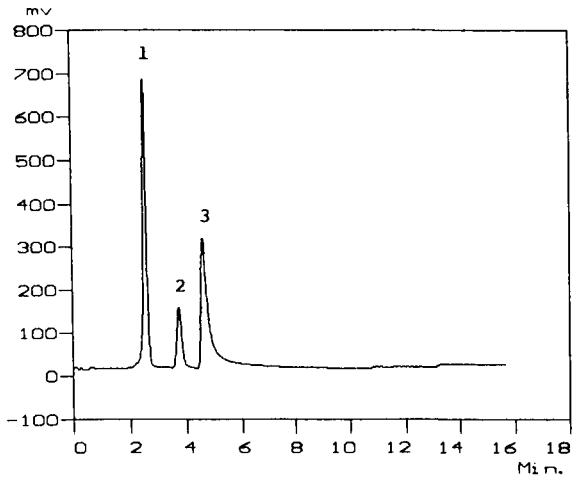

Fig. 4. LC of zinc(II) formate mixture on Silasorb SPH Nitrile. Mobile phase: ACN–MeOH–EtOH–H_2O (1+7+12+80, v/v); flow-rate, 1 ml/min; detection at 260 nm. Peaks: 1 = zinc(II) formate with nicotinic acid; 2 = zinc(II) formate with thiourea; 3 = zinc(II) formate with caffeine.

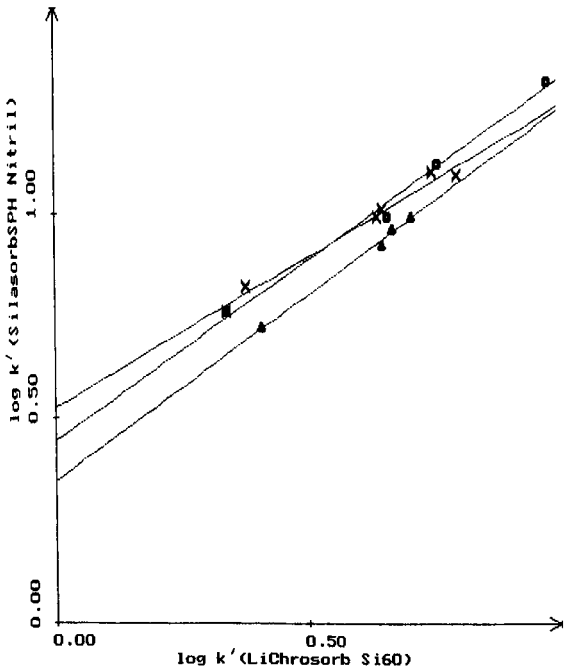

Fig. 5. Correlation between log k' obtained in analyses on LiChrosorb Si 60 and Silasorb SPH Nitrile columns. ■ = pure ligands; × = zinc(II) formates with ligands; ▲ = zinc(II) acetates with ligands.

increased with phenazone and caffeine with increasing methanol content in the mobile phase (Fig. 6).

Poor separations of the substances under examination were obtained on an amine-modified column (column A_3). The retention of substances chromatographed on columns A_1 and A_2 is evident from Tables 5 and 6.

Analyses on HEMA-Bio 1000CM cation-exchange resin

Analysis on the HEMA-Bio 1000CM cation-exchange column (weak by hydrophilic) with the mobile phase 10% ACN–0.1% H_3PO_4–water (pH 2.9) shows a reversed order of ligand elution and elution of their zinc(II) carboxylates. First nicotinic acid (t_R = 0.96 min) is eluted from the column, followed by caffeine (t_R = 1.09 min), phenazone (t_R = 1.16 min) and thiourea (t_R = 1.32 min). This elution order is the same as in LSC analyses on LiChrosorb Si 60 with a chloroform organic phase (samples dissolved in DMSO). A mixture of pure ligands, as follows from the

Table 4
Correlation of log k' obtained in analyses on the columns (LiChrosorb Si 60, Silasorb SPH Nitrile and LiChrosorb RP-18)

LiChrosorb Si 60 vs. Silasorb SPH Nitrile			
Pure ligands:	a = 0.4459	b = 0.8782	r = 0.9947
Zinc(II) formates:	a = 0.5271	b = 0.7325	r = 0.9917
Zinc(II) acetates:	a = 0.3488	b = 0.9020	r = 0.9966
LiChrosorb Si 60 vs. LiChrosorb RP-18			
Pure ligands:	a = 0.0136	b = 0.5130	r = 0.9562
Zinc(II) formates:	a = 0.2363	b = 0.3143	r = 0.8239
Zinc(II) acetates:	a = 0.9163	b = −0.6856	r = 0.7102

a,b = Coefficients of linear equation $y = ax + b$; r = correlation coefficient.

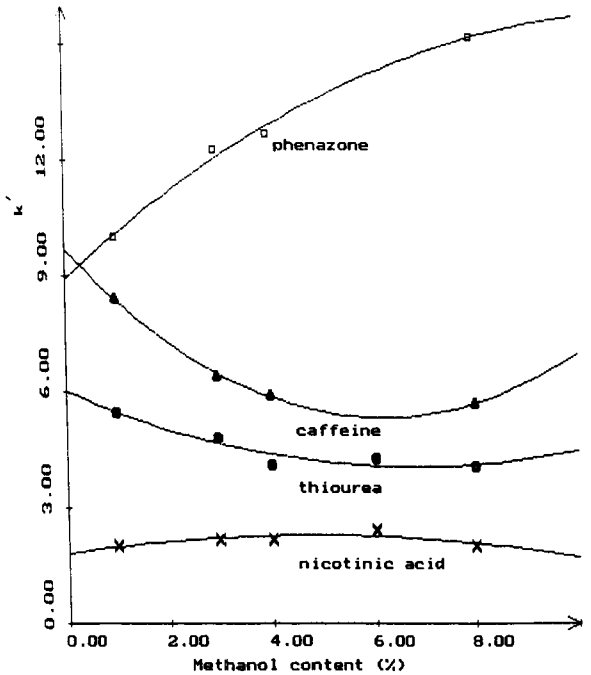

Fig. 6. Influence of methanol content in the mobile phase on retention factor (k') of pure ligand chromatographed. × = Nicotinic acid; ■ = thiourea; ▲ = caffeine; □ = phenazone.

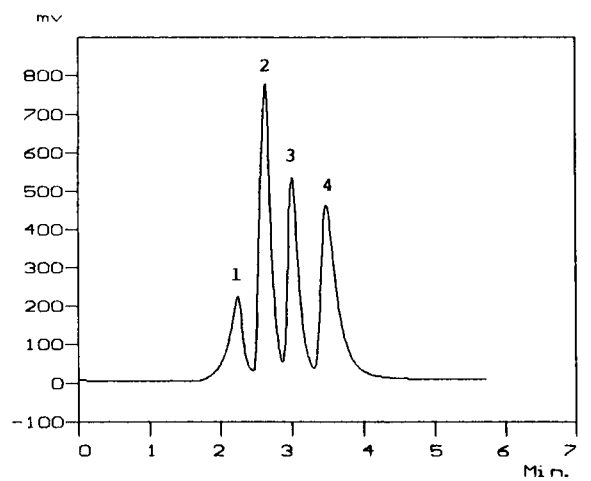

Fig. 7. LC of mixture 1 separated on a LiChrosorb RP-18 Column. Mobile phase: ACN–MeOH–propan-2-ol–water, P_S = 334, S_T = 1.9; flow-rate, 1 ml/min; detection at 253 nm. Peaks: 1 = nicotinic acid; 2 = thiourea; 3 = caffeine; 4 = phenazone.

Table 5
Retention data for zinc(II) carboxylates on LiChrosorb Si 60 column

Compound	t_R (min)	Log k' [a]	R_{ij} [b]
1	4.00	0.76	
2	4.81 [c]	0.85	
3	3.29	0.66	
4	6.25	0.98	
5	1.88	0.34	
Mixture 1	1.80	0.31	3.96
	3.20	0.65	3.17
	4.03	0.76	1.46
	6.13	0.98	2.58
6	Not detected		
7	Not detected		
8	3.15	0.64	
9	3.21	0.65	
10	1.99	0.38	
11	1.87	0.34	
12	4.28	0.80	
13	3.93	0.75	
Mixture 2	2.09	0.41	0.62
	2.99	0.61	2.82
	4.16	0.78	2.30
14	Not detected		
15	Not detected		
16	3.20	0.65	
17	3.24	0.65	
18	2.10	0.41	
19	3.59	0.71	
20	3.36	0.67	
21	3.38	0.67	
Mixture 3	2.04	0.39	0.36
	3.04	0.62	0.83
	3.45	0.69	2.01
	3.85	0.74	4.62

Column: LiChrosorb Si 60 (250×4.6 mm i.d., 10 μm). Mobile phase: ACN–MeOH–EtOH–water (5.9 + 0.9 + 3.5 + 89.7, v/v). $t_M = 0.59 \pm 0.1$ min. Detection at 260 nm.

[a] Rentention factor $k' = (t_R - t_M)/t_M$.

[b] Chromatographic resolution $R_{ij} = 2(t_{Ri} - t_{Rj})/Y_i + Y_j$. t_R = retention time (min); t_M = mobile phase holdup time; Y_i = peak width of i measured at the baseline; Y_j = peak width of j measured at the baseline.

[c] Measured at 196 nm.

retention times, is not separated effectively as caffeine and phenazone co-elute. Acceptable chromatographic separation was achieved in the analysis of the zinc(II) formate mixture. Zinc(II) acetates with caffeine and phenazone also co-elute.

Table 6
Retention characteristics of zinc(II) carboxylate on Silasorb SPH Nitrile column

Compound	t_R (min)	Log k' [a]	R_{ij} [b]
1	4.97	1.12	
2	Not detected		
3	3.76	0.99	
4	7.72	1.32	
5	2.36	0.76	
Mixture 1	2.07	0.69	
	3.21	0.91	2.35
	4.15	1.04	1.49
	6.27	1.23	1.95
6	Not detected		
7	Not detected		
8	3.83	0.99	
9	3.93	1.01	
10	2.65	0.82	
11	2.36	0.76	
12	4.65	1.09	
13	4.75	1.10	
Mixture 2	2.60	0.81	0.83
	3.44	0.95	2.32
	4.39	1.06	1.90
14	Not detected		
15	Not detected		
16	Not measured		
17	3.24	0.92	
18	2.16	0.72	
19	3.75	0.99	
20	3.53	0.96	
21	3.52	0.96	
Mixture 3	2.48	0.78	1.35
	3.29	0.92	0.98
	3.49	0.95	0.71
	3.79	0.99	0.86

Column: Silasorb SPH Nitrile (250×4.6 mm i.d., 7.5 μm). Mobile phase: ACN–MeOH–EtOH–water (5.9+2.6+3.5+90, v/v). t_M = 0.35 min. Detection at 260 nm.
[a,b] See Table 5.

The tested compounds were chromatographed using mobile phases with different pH values (2–8 from McIlvaine buffers). No explicit effect of pH on the retention times of the carboxylates was found.

Analyses on LiChrosorb RP-8 and RP-18 columns

Selection of the mobile phase for the chromatography of zinc(II) carboxylates with N-donor ligands on LiChrosorb RP-8 and RP-18 columns was carried out with the PRISMA model [39]. At an elution strength of $S_T = 0.5$ (S_T = total solvent strength of the mixture, $\Sigma_i S_i Q_i$, where S_i is the solvent strength weighting factor and Q_i the volume fraction in the mixture [40]) substances were separated that had been retained for a long time in the column (retention times > 30 min); in addition, in analyses of zinc(II) formates on the RP-8 column a suitable mobile phase composition could not be found. For analyses of zinc(II) carboxylates on the RP-18 column, the mobile phases ACN–MeOH–dioxane–water of elution strength $S_T = 2.15$ (phase A) and ACN–MeOH–propan-2-ol–water of $S_T = 1.95$ (phase B) were found to be the most suitable. With mobile phase B both ligands and zinc(II) acetates are well

Table 7
Retention characteristics of individual compounds on LiChrosorb RP-18 column.

Compound	t_R (min)	Log k' [a]	R_{ij} [b]
1	3.17	0.52	
2	2.61	0.38	
4	3.85	0.62	
5	2.21	0.30	
Mixture 1	2.51	0.38	
	2.83	0.45	1.18
	3.53	0.58	1.31
	4.31	0.68	1.41
8	2.55	0.39	
9	2.55	0.39	
10	2.43	0.36	
11	2.49	0.37	
12	3.16	0.51	
13	3.19	0.52	
Mixture 2	2.53	0.38	
	2.80	0.44	1.07
	3.48	0.57	1.22
16	2.59	0.40	
17	2.59	0.40	
18	4.00	0.69	
19	2.56	0.39	
20	3.28	0.54	
21	3.35	0.55	
Mixture 3	2.27	0.32	
	2.63	0.41	1.18
	3.23	0.53	1.22
	3.95	0.64	1.33

Column: LiChrosorb RP-18 (250×4.6 mm i.d., 10 μm). Mobile phase: P_S = 333, ACN–MeOH–propan-2-ol–water, S_T = 1.95. $t_M = 0.74 \pm 0.17$ min. Detection at 253 nm.
[a,b] See Table 5.

Table 8
Elution order of zinc(II) carboxylates with different columns and mobile phases

Column	Mobile phase	Mode	Elution order [a]			
			1	2	3	4
A_1	$CHCl_3$–MeOH	Gradient	caff			tu
A_1	8% MeOH–DEE [b]	Isocratic	nica	tu/phen [c]	caff	phen
A_1, A_2	ACN–MeOH–EtOH–H_2O	Isocratic	nica	tu	caff	phen
A_3	ACN–MeOH–EtOH water, $P_S = 811$, $S_T = 0.5$	Isocratic	phen	caff	nica	tu
B_1	ACN–MeOH–dioxane–H_{20}, $P_S = 333$, $S_T = 2.15$	Isocratic	nica	tu	caff	phen
B_1	ACN–MeOH–propan-2-ol–H_2O, $P_S = 343$, $S_T = 1.95$	Isocratic	nica	tu	caff	phen
B_2	ACN–MeOH–EtOH–water, $P_S = 118$, $S_T = 2.15$	Isocratic	Nica	tu	caff	phen

[a] For abbreviations, see Table 1.
[b] Diethyl ether.
[c] Co-elution.

separated from the mixture at the selectivity points $P_S = 163$ and 334 (P_S, the selectivity point, determines the mobile phase composition) and $S_T = 1.95$ (Fig. 7). Zinc(II) formates are best separated with mobile phase B at $S_T = 1.95$ and $P_S = 343$. The individual ligands, formates and zinc(II) acetates eluted from the RP-18 column in the same order as on LiChrosorb Si 60 and Silasorb SPH Nitrile columns with a high content of water in the mobile phase (nicotinic acid, thiourea, caffeine and phenazone).

The differences in the log k correlation graph obtained from results of analyses on LiChrosrb Si 60 and LiChrosorb RP-18 are significant (Table 7). The mechanism of separation on the LiChrosorb Si 60 column is more similar to liquid–liquid normal-phase than liquid–liquid reversed-phase separation. Retention data from reversed-phase separation are given in Table 8.

It follows from the analyses that it is more problematic to find suitable chromatographic conditions for separating the free molecule of ligands and competing zinc(II) carboxylate (binding one or two molecules of the same ligand) from mixtures.

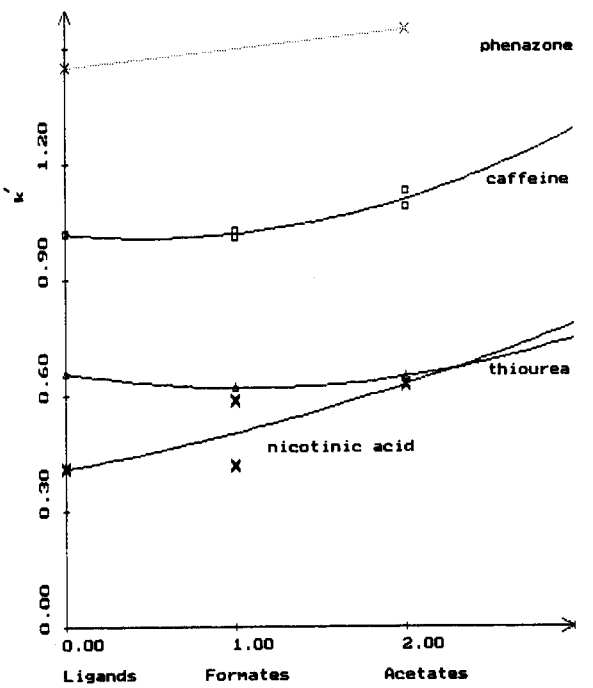

Fig. 8. Effect of aliphatic chain length on retention of zinc(II) carboxylate molecules. Hydrophobic effect started from zinc(II) acetates.

The hydrophobic character of the acetate alkyl chain has a small effect on the retention behaviour of the single zinc(II) carboxylates with phenazone and caffeine in analyses on a reversed-phase C_{18} column. A shift in the retention time of zinc(II) acetate with two molecules, however, is significant but not sufficient for acceptable chromatographic resolution from phenazone (Fig. 8, Table 8). This shift confirms that the molecule moves through the entire column.

In both kinds of analyses the low response of the spectrometric detector for urea and its zinc(II) carboxylates presents a problem. Fujinawa et al. [41] reported on the LC determination of urea by converting it into ammonia and subsequent *o*-phthaldehyde derivatization and fluorimetric detection at 455 nm (excitation at 349 nm). Müller [42] has reported the detection of urea at 196 nm.

4. Conclusion

The novel $Zn(RCOO)_2L_n(H_2O)_q$ compounds, which were synthesized with the aim of using them as skin drug carriers, were examined in preliminary experiments for their basic physicochemical and chromatographic properties. These preliminary analyses should serve as a first step for the development of extraction and determination methods for these compounds and their metabolites in the tissues and body fluids of experimental animals.

The LC analyses indicate the shielding of zinc(II) carboxylate by the organic molecules of the compound, with the result that the chromatographic properties of the entire complex are due mostly to the bound organic part of molecule. LSC separation results in elution in the order caffeine, phenazone, nicotinic acid and thiourea. Separation on silica gel with a mobile phase containing more than 20% of water probably occurs by means of an NP-LLC mechanism, with the elution order nicotinic acid, thiourea, caffeine and phenazone. The best results were obtained in analyses on a LiChrosorb RP-18 column with the mobile phase composition ACN–MeOH–propan-2-ol–water (10.1 + 11.5 + 20 + 58.4, v/v). A four-component mixture improves the separation of the compounds under examination.

Further work will be focused on confirmation of the identity of the separated molecules and reconsideration of the mechanism of separation.

Acknowledgements

The autors thank Dr. M. Ranny for TLC–FID measurements and Miss Marta Stroncekova for technical assistance. The financial support of the Slovak Ministry of Education by grant No. 1/990917/93 and is gratefully acknowledged.

References

[1] K. Nakajima, T. Yasuda and H. Nakazawa, J. Chromatogr., 502 (1990) 379.
[2] R.J. Fenn and M.T. Alexander, J. Liq. Chromatogr., 11 (1988) 3403.
[3] F. van Assche, H. Clijsters and F. van Assche, Plant Cell Environ. 13 (1990) 195.
[4] D.C. Martens and S.T. Reed, Solutions (USA), 35 (1991) 29.
[5] M.R. Gangwar, M.S. Gangwar and P.C. Srivastava, Oryza, 26 (1989) 156.
[6] S.C. Cunnane, Zinc: Clinical and Biochemical Significance, CRC Press, Boca Raton, FL, 1988.
[7] M.E. Wastney, I.G. Gokmen, R.L. Aamodt, W.F. Rumble, G.E. Gordon and R.I. Henkin, Am. J. Physiol. 260 (1991) R134.
[8] S.A. Rogers, Int. Clin. Nutr. Rev., 10 (1990) 253.
[9] I. Dorup and T. Clausen, Br. J. Nutr., 66 (1991) 493.
[10] K. Gyoryova and V. Balek, J. Thermal. Anal., 40 (1993) 519.
[11] H. König and W. Strobel, Fresenius' J. Anal. Chem., 338 (1990) 728.
[12] P.M. Brandts, W.J. Gelsema and C.L. de Ligny, J. Chromatogr., 438 (1988) 181.
[13] G.R. Bear, J. Chromatogr., 371 (1986) 387.
[14] J. Michal, Inorganic Chromatographic Analysis, Van Nostrand Reinhold, London, 1973.
[15] J.F.K. Huber, J.C. Kraak and H. Veening, Anal. Chem., 44 (1972) 1554.
[16] G. Schwedt, Chromatographic Methods in Inorganic Analysis, Hüthig, Heidelberg, 1981.
[17] M. Lohmuller, P. Heizmann and K. Ballschmitter, J. Chromatogr., 137 (1977) 165.
[18] H. Ge and G.G. Wallace, Anal. Chem., 60 (1988) 830.
[19] S. Hoshi, N. Takahashi, S. Inone and M. Macubara, Bunseki Kagaku, 35 (1986) 819.
[20] M. Marinov, Fresenius' Z. Anal. Chem., 319 (1984) 307.

[21] N. Chen and X. Zhang, Fenxi Huaxue, 11 (1983) 374.
[22] J.I. Toei, Chromatographia, 23 (1987) 355.
[23] F. Zhou and C. Xie, Huaxue Fenxi, 25 (1989) 68.
[24] G. Weber and G. Schwedt, Fresenius' Z. Anal. Chem., 316 (1983) 594.
[25] B. Grigorova and S.A. Wright, J. Chromatogr., 368 (1986) 444.
[26] J. Yuan, M. Ciu, N. Tang, F. Kong and Y. Qian, Zhongguo Yiyao Gongye Zasshi, 21 (1990) 22.
[27] C.Y. Chien, N.D. Jaku and P.A. Crooks, LC·GC 6 (1988) 53.
[28] H. Taguchi, Vitamins, 64 (1990) 19.
[29] I. Biagyioni, P. Subir and D. Robertson, Clin. Chem., 34 (1989) 2345.
[30] T.E.B. Leakey, J. Chromatogr., 507 (1990) 199.
[31] Z. Holzbecher and J. Churáček, Analytical Chemistry, SNTL, Alpha, Prague, 1987, pp. 535–536.
[32] F.W. Kuster and A. Thiel, Tables for Analytical Chemists, Academia Press, Prague, 1988, p. 179.
[33] O. Mikeš, Laboratory Chromatographic Methods, SNTL, Prague, 1980, p. 134.
[34] B. Buglio and V.S. Venturella, J. Chromatogr. Sci., 20 (1982) 165.
[35] A. Orinak, K. Gyoryova and S. Lancaricova, J. Planar Chromatogr., 6 (1993) 153.
[36] J. Garaj, D. Bustin and Z. Hladký, Analytical Chemistry, Alpha, Bratislava, 1987, p. 146.
[37] P. Pitter, Hydrochemical Tables, SNTL, Prague, 1987, p. 179.
[38] O. Mikeš, Laboratory Chromatographic Methods, SNTL, Prague, 1980, p. 137.
[39] A. Orinak, K. Gyoryova, E. Matisova, L. Slesarova, I. Rosival and M. Ganajova, J. Chromatogr., in press.
[40] S. Ahuja, Selectivity and Detectability Optimizations in HPLC, Wiley, New York, 1989, p. 80.
[41] S. Fujinawa, H. Todoroki, N. Ohashi, J. Toda and J. Terasaki, J. Food. Sci., 55 (1990) 1018, 1038.
[42] S. Müller, Fresenius' J. Anal. Chem., 332 (1988) 464.
[43] K. Andrlík, O. Uher, J. Wegiel and K. Dvořák, Chemical Tables, SNTL, Bratislava, 1967.

ELSEVIER

Analytica Chimica Acta 291 (1994) 183–188

ANALYTICA CHIMICA ACTA

Capillary micellar electrokinetic chromatography based on indirect semiconductor laser fluorescence detection

Tetsuhiro Fuchigami, Totaro Imasaka *

Faculty of Engineering, Kyushu University, Hakozaki, Fukuoka 812, Japan

(Revised 2nd September 1993; revised manuscript received 6th December 1993)

Abstract

Flavin adenine dinucleotide and deoxyadenosine monophosphate were measured by capillary micellar electrokinetic chromatography combined with semiconductor laser fluorimetry. Methylene blue was dissolved in a carrier solution as a dye for indirect fluorescence detection. In order to decrease the adsorption of the dye on the capillary surface, a quaternary ammonium salt was added to the solution and its concentration was adjusted above the critical micellar concentration. By this technique, the capillary surface negatively charged by dissociation of a silanol group, was changed into a positive charge with this cationic surfactant. The theoretical plate numbers observed were 2.5×10^5–3.0×10^5. The detection limit of flavin adenine dinucleotide was 100 fmol, which is several orders of magnitude better than reported values obtained by liquid chromatography based on indirect semiconductor laser fluorescence detection. The dynamic reserve and the transfer ratio were 250 and 4×10^{-4}, respectively. The advantages and the limitations of the method are discussed.

Key words: Electrophoresis; Fluorimetry; Deoxyadenosine monophosphate; Flavin adenine dinucleotide; Laser fluorimetry; Micellar electrokinetic chromatography; Semiconductor laser fluorimetry

1. Introduction

Analytical methods capable of providing ultra-high sensitivity and selectivity are strongly desirable in the life sciences. For example, the concentration level of nucleotides gives information concerning the metabolism of nucleic acids. Further, the concentrations of amino acids and proteins are currently measured for diagnostic purposes in hospitals. Recently, laser spectrometry has been developed and the detection of even a single molecule has been demonstrated in an extreme case [1]. However, normal analytical instruments must be simple and be operated easily for routine analysis even by non-experts. Unfortunately, a laser is generally complicated and has seldom been used in practical analyses.

A semiconductor laser was manufactured by mass production technology at the beginning of the 1980s, and semiconductor laser spectrometry has opened up a frontier in practical trace analysis, as reviewed elsewhere [2–9]. This is due to the compactness, low price, long lifetime and easy operation and maintenance of the semiconductor laser. Especially semiconductor laser fluorimetry provides ultrasensitivity, owing to the good beam focusing capability and good monochromaticity. They are advantageously used in the construction

SSDI 0003-2670(94)00007-0

of microdetectors for liquid chromatography [8]. Recently, a better separation resolution has been achieved by capillary zone electrophoresis, because of the smaller diameter of the separation column [10,11]. However, this method requires an extremely small detector volume (< 1 nl). In this case laser fluorimetry is essential for ultrasensitive detection and semiconductor laser fluorimetry has been used for this purpose [12]. Subattomole amounts of amino acids have already been determined after labelling them with a visible dye in the far-red region [13].

A biological molecule sometimes has no active site for labelling. In this event, the sample may be detected by indirect spectrometry; the dye is dissolved in the carrier solution and the dip in signal caused by dilution (exclusion) is recorded [14]. Many anions, nucleotides, proteins, mono- and divalent cations, amines, oligopeptides, etc. have been measured by laser fluorescence detection [15–17]. Such an approach has also been demonstrated using a semiconductor laser based on fluorimetry and absorption spectrometry [12,18].

Capillary zone electrophoresis can be applied only to charged chemical species. However, it is sometimes necessary to measure neutral molecules. Capillary micellar electrokinetic chromatography (MEKC) may be utilized for the separation of both neutral species and ionic species [19]. This technique is based on the partitioning of chemical species between an aqueous mobile phase and a pseudo-stationary phase of micelles. In this approach, the same analytical instrument can be used but a surfactant must be added to the carrier solution, providing a similar separation resolution to capillary zone electrophoresis. Semiconductor laser fluorimetry has already been combined with capillary MEKC [20]. Polycyclic aromatic hydrocarbons with no electric charge, such as benzo[*a*]pyrene and 1-aminoanthracene, are separated in the presence of sodium dodecyl sulphate (surfactant) and γ-cyclodextrin (additive to increase the solubility to the mobile phase), and the chemical species are detected by fluorimetry using the second harmonic emission (415 nm) of the near-infrared semiconductor laser (830 nm) as an exciting source. These molecules show strong native fluorescence in the visible region and can be detected sensitively. However, such a frequency-doubled semiconductor laser is expensive, of low stability and not very reliable. It is desirable to use a fundamental output of the semiconductor laser. Unfortunately, most biological molecules are not necessarily fluorescent in the near-infrared and far-red regions or even in the visible region. Moreover, a functional group for labelling is sometimes not available. Therefore, indirect fluorimetry must be applied for universal detection. Such indirect fluorimetry has been utilized in the detection of alcohols and phenols using a conventional 75-W xenon arc lamp (non-laser source) [21]. However, no investigation using a semiconductor laser as an exciting source has been reported (even using a conventional laser, to the best of our knowledge).

In this paper, we first report the indirect detection of chemical species with no active functional group by capillary MEKC combined with semiconductor laser fluorimetry. The instrument developed was applied to the trace analysis of nucleotides. The potential advantages and limitations of the method are also discussed.

2. Experimental

2.1. Apparatus

The instrument used is shown in Fig. 1. The sample solution was injected into a capillary (Polymicro Technology, 50 μm i.d., 375 μm o.d., effective length 50 cm, total length 65 cm) by a siphon method (10 cm, 5 s). The injection volume was 1 nl. A negative high potential (Matsusada Precision Devices Model HCZE30PN0.25, 0–30 kV, 0.25 mA) was applied to the solution on the sample inlet side. A semiconductor laser (ILEE Laser Innovation, LDA1001) emitting at 670 nm (3 mW) was used as an excitation source. The laser beam was passed through a short-pass interference filter (Asahi Bunko Model 680-50) to block non-lasing broadband emission. The laser beam was focused by an objective lens for a microscope (Nikon, magnification $\times 5$) into a section of the capillary tube, where the polyimide coating had been burnt off with a flame for

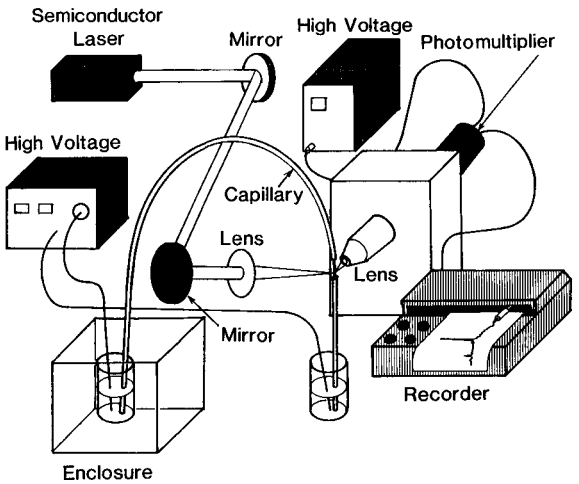

Fig. 1. Experimental apparatus for capillary electrophoresis. A semiconductor laser (670 nm, 3 mW) is used as an excitation source.

observation. Fluorescence was collected by an objective lens (Olympus, magnification ×50, numerical aperture 0.6) and passed through interference (Melles Griot Models 03FIV024 and 03FCG109) and spatial (laboratory-made, 0.5 mm i.d.) filters. The signal from a photomultiplier tube (EMI Model 9558QB) was directly measured with a strip-chart recorder (Hitachi Model 056).

The variation of the output power of the laser was measured by a silicon photodiode. The output voltage was converted into pulses by a voltage–frequency converter and the number of pulses in a specified time, typically 1 s, was measured by a counter (NF Circuit Design Block, PC-545A).

2.2. Reagents and procedure

The fluorescent dye methylene blue was purchased from Kanto Kagaku and was used as received. The concentration was adjusted to 1×10^{-5} M. The pH of the carrier solution was adjusted to 3.4 by mixing sodium acetate (4 mM) and HCl (4 mM). A quaternary ammonium salt, dodecyltrimethylammonium chloride, obtained from Tokyo Kasei was dissolved in the carrier solution at a concentration of 100 mM. Urea was also added to the solution, the concentration being adjusted to 2 M. Flavin adenine dinucleotide and deoxyadenosine monophosphate supplied by Wako were dissolved in distilled water and the solutions were diluted stepwise.

3. Results and discussion

3.1. Methylene blue and surfactant

In order to use an organic dye as a fluorophore in indirect fluorimetry, it must satisfy several requirements: the molar absorptivity and the fluorescence quantum yield should be sufficiently high at the specified wavelength; the dye should be stable enough in aqueous solution and micelles; the fluorescence characteristic must be changed in the presence of analytes; and adsorption of the dye on the capillary surface must be negligible, otherwise the separation resolution is seriously degraded and the background signal from the adsorbed dye increases. Methylene blue has a high molar absorptivity ($\epsilon = 6.66 \times 10^4$ l mol^{-1} cm^{-1} at $\lambda_{max} = 668$ nm) and is strongly fluorescent [22]. It is stable in aqueous solution and micelles and has already been used in many standard analytical protocols. We measured the fluorescence intensity of methylene blue at various surfactant concentrations. The fluorescence intensity increased to 120% on increasing the surfactant concentration to 1 mM and to 150% at 100 mM. This fluorescence enhancement is ascribed to suppression of radiationless transitions by attaching the fluorescent molecule to the surface of the micelle. Thus the fluorescence characteristic (e.g., intensity) changes by transfer of the fluorophore from the pseudo-stationary phase to the mobile phase. Methylene blue is positively charged, but the capillary surface is negatively charged by dissociation of the silanol group. Hence adsorption of the dye on the capillary surface is unavoidable. In fact, when methylene blue was injected into the capillary, a long tailing response was observed below pH 7, implying a strong interaction between the negative charge of the silanol group and the positive charge of the dye. In order to remove this unwanted effect, the

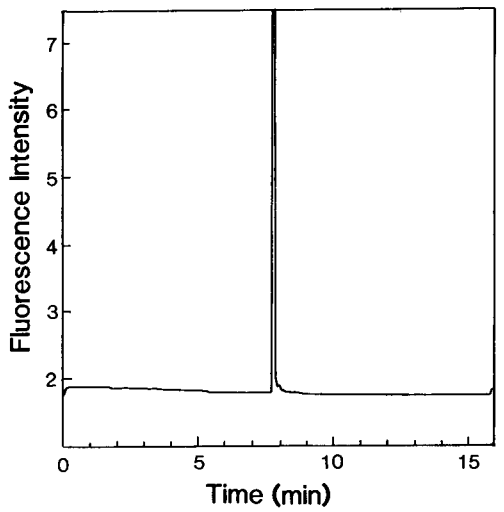

Fig. 2. Electropherogram for methylene blue (10 fmol, 1×10^{-5} M). High voltage, 20 kV, 0.036 mA; buffer, 4 mM sodium acetate–4 mM HCl (pH 3.4); surfactant, 100 mM dodecyltrimethylammonium chloride; additive, 2 M urea.

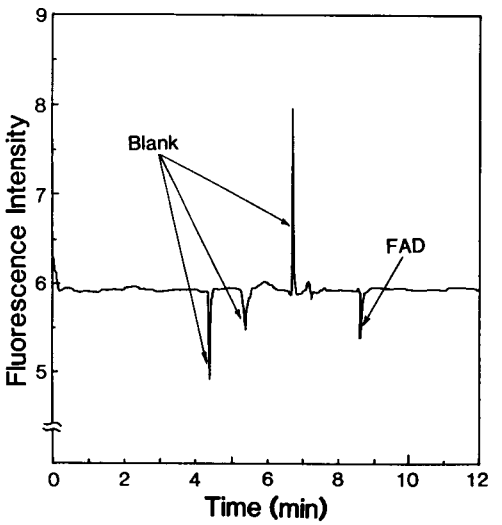

Fig. 3. Electropherogram for flavin adenine dinucleotide (FAD, 1 pmol, 1×10^{-3} M). Concentration of methylene blue, 1×10^{-5} M; other experimental conditions as in Fig. 2. "Blank" appears from the blank solution.

capillary surface was coated with alkylsilane in a previous study [12]. In this study, the silanol group was covered with the positively charged surfactant, and accordingly the charge was changed from negative to positive. By this technique, adsorption of methylene blue could be minimized. However, the direction of the electroosmotic flow is reversed, and then the negative potential must be applied to the sample inlet side [23,24].

In a preliminary experiment, methylene blue was injected into a capillary containing dodecyltrimethylammonium chloride. As shown in Fig. 2, a sharp chromatograph peak appeared and no appreciable leading edge and only a minor tail were observed. This result indicates that adsorption of methylene blue on the capillary surface is negligible under the present experimental conditions. The theoretical plate number achieved is 3×10^5, which is similar to the value reported elsewhere [12,20].

3.2. Chromatograms

A chromatogram for flavin adenine dinucleotide is shown in Fig. 3. A sharp signal peak appears at 8.6 min after sample injection, which is assigned to the analyte. Other signals appeared, even when water was injected into the capillary. They are assigned to a "Blank" value. By stepwise dilution of the sample, the linearity of the calibration graph was ascertained. The

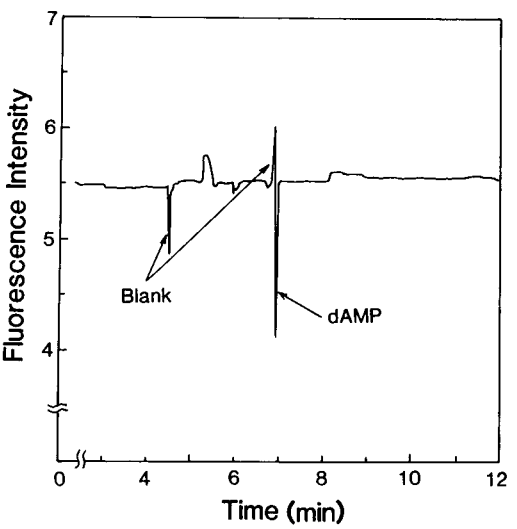

Fig. 4. Electropherogram for deoxyadenosine monophosphate (dAMP, 10 pmol, 1×10^{-2} M). Experimental conditions as in Fig. 2. "Blank" appears from the blank solution.

detection limit of flavin adenine dinucleotide (3σ) was 100 fmol (1×10^{-4} M). This is an order of magnitude better than the reported value obtained by using indirect semiconductor laser fluorescence detection combined with capillary zone electrophoresis [12]. A chromatogram for deoxyadenosine monophosphate is shown in Fig. 4. A sharp signal at 6.9 min is assigned to the analyte, and the others to "blanks". The theoretical plate numbers in the above experiments are 2.5×10^5–3.0×10^5.

3.3. Dynamic reserve and transfer ratio

In order to clarify the factors limiting the minimum detectability, we measured the dynamic reserve, defined as the ratio of the background signal to the background noise, and the transfer ratio, defined as the number of fluorophore molecules displaced by one analyte molecule [14,21]. The noise in the baseline fluorescence was 0.4%, so that the dynamic reserve achieved was 250. The variation of the output power of the semiconductor laser measured was less than 0.03%; the noise level reported in the manufacturer's specification was an order of magnitude smaller than this value, so that the present value might be determined by the precision of the detection electronics. This stability is much better than that obtained with a conventional laser such as an argon ion laser (ca. 1%). The stable output power of the semiconductor laser is obtained by feedback control of the diode current by monitoring the output power of the laser with an integrated photodiode. Thus the present dynamic reserve is not determined by the variation of the laser power but probably by the vibration of the components associated with a high potential, as the noise was substantially lowered by decreasing the output voltage of the power supply. Thus a 100-fold improvement in the dynamic reserve is theoretically possible by fixing the components tightly. It is noted that the baseline was changed more drastically after repetitive injections of the sample. This seems to originate from contamination of the carrier solution. Hence replacement of the carrier solution with fresh solution might be essential in trace analysis.

The transfer ratio observed in this study was 4×10^{-4}; 2500 sample molecules were necessary to displace a single dye molecule. The present value is much smaller than the value of 0.14 achieved in indirect fluorescence detection of alcohols and phenols by MEKC in which quinine sulphate was added as a fluorophore and as a buffer for adjustment of pH [21]. Hence there is a room for improvement of the transfer ratio by optimization of the experimental conditions, e.g., by decreasing the concentrations of the buffer, the fluorophore and the additive, adjustment of pH or addition of organic solvents.

3.4. Advantages and limitations

The proposed method is universal and is applicable to various neutral and ionio species. The instrument is fairly simple owing to the compactness of the semiconductor laser. Furthermore, it is less expensive and is smaller than a conventional light source such as a xenon arc lamp. The present approach using a cationic surfactant is easier than modification of the capillary surface with inert alkylsilane [12] and is more effective for decreasing adsorption of the fluorophore on the capillary surface. The detection limit achieved (100 fmol, 80 pg) is much better than the values obtained by liquid chromatography with indirect semiconductor laser fluorescence detection (sub-μg or 10 ng) [25–27].

In order to improve the sensitivity further, it is necessary to increase the transfer ratio by optimizing the experimental conditions. Further, strong fluorescence quenching is desirable for more sensitive detection. In the far-red region many fluorescent dyes are available, and some of them are used as hydrophobic probes, implying strong fluorescence in the pseudo-stationary phase of micelles and weak fluorescence in the aqueous mobile phase. Thus a larger dip in the signal might be observed in this case. These implications may lead to an improvement in sensitivity by a factor of 10^3.

In capillary zone electrophoresis, a fluorophore ion is displaced with a single sample ion, so that the transfer ratio is unity. Hence the detection limit can be substantially improved. A

low detection limit (20 amol) has already been reported using capillary zone electrophoresis with indirect fluorescence detection using a conventional laser. The estimated detection limit in the application using a semiconductor laser (100 fmol $\times 10^{-2} \times 10^{-3} = 1$ amol) compares favourably with this reported value. As the nucleotides measured in this study are partially dissociated in aqueous solution, capillary zone electrophoresis may be applied. If a dye with a negative charge is available, it is possible to decrease the adsorption of the dye on the negatively charged capillary surface. Hence organic synthesis of such a negatively charged dye could be very useful for improving the sensitivity and simplifying the analytical system.

Acknowledgements

The authors thank Takashi Kaneta for his advice to use a quaternary ammonium ion to decrease the adsorption of the dye on the capillary surface. This work was supported by Grants-in-Aid for Scientific Research from the Ministry of Education, Science and Culture of Japan, by the Steel Industry Foundation for the Advancement of Environmental Protection Technology (SEPT) and by Nakatani Electronic Measuring Technology Association of Japan.

References

[1] S.A. Soper, Q.L. Mattingly and P. Vegunta, Anal. Chem., 65 (1993) 740.
[2] T. Imasaka and N. Ishibashi, Am. Biotechnol. Lab., 6 (1988) 34.
[3] T. Imasaka and N. Ishibashi, Anal. Chem., 62 (1990) 363A.
[4] T. Imasaka and N. Ishibashi, Prog. Quantum Electron., 14 (1990) 131.
[5] T. Imasaka, Appl. Fluoresc. Technol., 2 (1990) 1.
[6] T. Imasaka, Anal. Sci., 6 (1993) 329.
[7] T. Imasaka, Spectrochim. Acta Rev., 15 (1993) 329.
[8] A.J.G. Mank, H. Lingeman and C. Gooijer, Trends Anal. Chem., 11 (1992) 210.
[9] S. Akiyama, in S.G. Schulman (Ed.), Molecular Luminescence Spectroscopy (Methods and Applications: Part 3), Wiley, New York, 1993, Chap. 6.
[10] W.G. Kuhr, Anal. Chem., 62 (1990) 403R.
[11] L.N. Amankwa, M. Albin and W.G. Kuhr, Trends Anal. Chem., 11 (1992) 114.
[12] T. Higashijima, T. Fuchigami, T. Imasaka and N. Ishibashi, Anal. Chem., 64 (1992) 711.
[13] T. Fuchigami, T. Imasaka and M. Shiga, Anal. Chim. Acta, 282 (1993) 209.
[14] E.S. Yeung and W.G. Kuhr, Anal. Chem., 63 (1991) 275A.
[15] W.G. Kuhr and E.S. Yeung, Anal. Chem., 60 (1988) 2642.
[16] L. Gross and E.S. Yeung, Anal. Chem., 62 (1990) 427.
[17] B.L. Hogan and E.S. Yeung, Anal. Chem., 64 (1992) 2841.
[18] S.J. Williams, E.T. Bergstrom, D.M. Goodall, H. Kawazumi and K.P. Evans, J. Chromatogr., 636 (1993) 39.
[19] S. Terabe, Trends Anal. Chem., 8 (1989) 129.
[20] T. Imasaka, K. Nishitani and N. Ishibashi, Analyst, 116 (1991) 1407.
[21] L.N. Amankwa and W.G. Kuhr, Anal. Chem., 63 (1991) 1733.
[22] T. Imasaka, A. Tsukamoto and N. Ishibashi, Anal. Chem., 61 (1989) 2285.
[23] S. Terabe, K. Otsuka, K. Ichikawa, A. Tsuchiya and T. Ando, Anal. Chem., 56 (1984) 111.
[24] K. Otsuka, S. Terabe and T. Ando, J. Chromatogr., 332 (1985) 219.
[25] S. Folestad and H. Ahlberg, presented at the International Symposium on Column Liquid Chromatography, Stockholm, 1989.
[26] S.J. Lehotay, A.M. Pless and J.D. Winefordner, Anal. Sci., 7 (1991) 863.
[27] H. Kawazumi, H. Nishimura and T. Ogawa, J. Liq. Chromatogr., 15 (1992) 2233.

ELSEVIER

Analytica Chimica Acta 291 (1994) 189–195

ANALYTICA CHIMICA ACTA

2,2′-Dithiobis(1-amino-4,5-dimethoxybenzene) as a highly sensitive, selective and stable fluorescence derivatization reagent for aromatic aldehydes in liquid chromatography

Shuuji Hara [a,*], Masaru Nakamura [a], Fumie Sakai [b], Hitoshi Nohta [b], Yosuke Ohkura [b], Masatoshi Yamaguchi [a]

[a] *Faculty of Pharmaceutical Sciences, Fukuoka University, Nanakuma, Jonan-ku, Fukuoka 814-01, Japan*
[b] *Faculty of Pharmaceutical Sciences, Kyushu University 62, Maidashi, Higashi-ku, Fukuoka 812, Japan*

(Received 21st October 1993)

Abstract

2,2′-Dithiobis(1-amino-4,5-dimethoxybenzene) was synthesized as a highly sensitive, selective and stable fluorescence derivatization reagent for aromatic aldehydes in liquid chromatography. The reagent reacts selectively with aromatic aldehydes in acidic media in the presence of tri-*n*-butylphosphine, sodium sulphite and disodium hydrogenphosphite. The reaction was complete within 60 min at 37°C. The fluorescent products from benzaldehyde and 4-hydroxybenzaldehyde are shown to be 2-phenyl-5,6-dimethoxybenzothiazole and 2-(4-hydroxyphenyl)-5,6-dimethoxybenzothiazole, respectively. The fluorescent derivatives of aromatic aldehydes can be separated by reversed-phase chromatography and their detection limits (signal-to-noise ratio = 3) are 8–20 fmol on-column.

Key words: Fluorimetry; Liquid chromatography; Aldehydes; Dithiobis(1-amino-4,5-dimethoxybenzene)

1. Introduction

In a previous study [1], various substituted 2-aminothiophenols (ATs) were evaluated as fluorescence derivatization reagents of aromatic aldehydes in manual spectrofluorimetry and liquid chromatography (LC); 2-amino-5-methoxythiophenol was the most favourable in practical use. In addition, it was reported that 2-amino-4,5-dimethoxythiophenol (DMOAT) might be suitable for use in LC. However, their ATs were not stable in air and rapidly became reddish in daylight. The unknown red compound(s) interfered with the sensitive determination of the aldehydes.

Recently, we found that 2,2′-dithiobis(1-amino-4,5-dimethoxybenzene) (DTAD), which is the disulphide of DMOAT, is superior to DMOAT in stability and sensitivity. In this work, DTAD was investigated to establish the optimum conditions for manual spectrofluorometric and LC methods. The method is based on the reaction of aromatic aldehydes with DTAD in acidic medium in the presence of tri-*n*-butylphosphine, sodium sulphite and disodium hydrogenphosphite. The structures

* Corresponding author.

SSDI 0003-2670(93)E0701-8

of the fluorescent products of benzaldehyde and 4-hydroxybenzaldehyde with DTAD were also investigated.

2. Experimental

2.1. Apparatus

Uncorrected fluorescence spectra and intensities were measured with a Hitachi (Tokyo) Model 650-60 spectrofluorimeter in 10×10 mm quartz cells; spectral bandwidths of 5 nm were used for both the excitation and emission monochromators. Electron impact mass spectra were recorded with a Jeol (Tokyo) DX-300 spectrometer. ^{1}H nuclear magnetic resonance (NMR) spectra were obtained with a Hitachi R-90H spectrometer at 90 MHz using a ca. 5% (w/v) solution of chloroform-d_1 or dimethyl-d_6 sulphoxide containing tetramethylsilane as an internal standard (abbreviations used: s, singlet; d, doublet; m, multiplet).

2.2. Chemicals and solutions

All chemicals were of analytical-reagent grade, unless stated otherwise. Deionized, distilled water was used. Stock standard solutions (10 mM) of aromatic aldehydes were prepared in water [or aqueous 50% (v/v) ethanol for weakly water-soluble aldehydes], and distilled with water before use. The stock standard solutions were stable for at least 1 month at when stored −20°C.

2.3. Synthesis of DTAD

DTAD was synthesized from 4-bromoveratrole in satisfactory yields by the following method (Fig. 1).

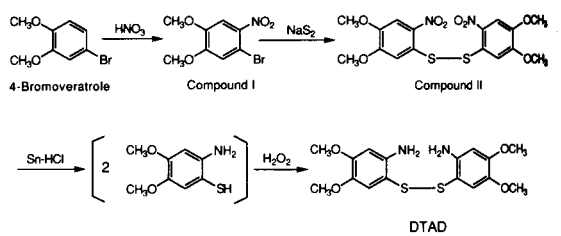

Fig. 1. Synthesis of DTAD.

4,5-Dimethoxy-2-nitrobromobenzene (compound I)

To a stirred solution of 4-bromoveratrole (20 g, 92.1 mmol) in acetic acid (60 ml) was added concentrated nitric acid (10 ml) dropwise while the temperature was kept at 10–30°C with occasional cooling. After the addition was complete, the reaction mixture was poured on to ice–water. The precipitate was collected, dissolved in hot ethanol (500 ml), treated with activated charcoal and filtered. Recrystallization was achieved by adding water (40 ml), yielding 12.30 g (51%) of **I** as a light-yellow crystalline solid, m.p. 121–122°C. Mass spectrometry (MS) showed $m/z = 262$ (M^+, base peak) and the ^{1}H NMR spectrum (chloroform-d_1) δ 3.94 (s, 3H, OCH_3), 3.97 (s, 3H, OCH_3), 7.12 (s, 1H, aromatic proton), 7.57 ppm (s, 1H, aromatic proton).

Di(4,5-dimethoxy-3-nitrophenylsulphide) (compound II)

To a solution of **I** (5.0 g, 19.1 mmol) in 95% ethanol (50 ml) was added sodium sulphide that had been freshly prepared by melting sodium sulphide nonahydrate (5.0 g) and sulphur (0.7 g). The resulting dark violet mixture was heated at reflux for 30 min and poured on to ice–water. A yellow crystalline solid was collected and recrystallized from dichloromethane to afford 3.35 g (82%) of **II** as yellow needles, m.p. 231–232°C. MS, $m/z = 428$ (M^+, base peak); ^{1}H NMR (chloroform-d_1), δ 3.81 (s, 3H, OCH_3), 3.95 (s, 3H, OCH_3), 7.34 (s, 1H, aromatic proton), 7.78 ppm (s, 1H, aromatic proton).

DTAD

To a solution of **II** (2.0 g, 6.5 mmol) in ethanol (300 ml) were added tin powder (8 g) and then concentrated hydrochloric acid (30 ml) dropwise. The resulting reaction mixture was made alikaline with 4 M sodium hydroxide solution and filtered to remove tin powder. The filtrate was diluted with water (200 ml) and extracted twice with benzene (100 ml). The extracts were combined and the solvent was removed under reduced pressure. The residue was mixed with ben-

zene (10 ml) and 10% hydrogen peroxide (2 ml) and the solution was stirred for 30 min. The resulting precipitate was recrystallized from ethanol to give DTAD (ca. 620 mg) as colourless needles, m.p. 155–156°C. Elemental analysis: calculated for $C_{16}H_{20}N_2O_4S_2$, C 52.27, H 5.50, N 7.65; found, C 52.16, H 5.47, N 7.60%; MS, $m/z = 368$ (M^+, base peak); ^1H NMR (chloroform-d_1), δ 3.66 (3H, s, OCH_3), 3.83 (3H, s, OCH_3), 4.13 (2H, broad s, NH_2), 6.29 (2H, s, aromatic proton), 6.66 ppm (2H, s, aromatic proton).

MTAD

MTAD was synthesized from 4-bromo-1,2-methylenedioxybenzene as in the preparation of DTAD.

DTAD and MTAD were stable for at least 1 year even at room temperature.

DTAD solution (1.1 mM) was prepared by dissolving 40 mg of DTAD in 100 ml of 0.8 M sulphuric acid containing 4.0 mM tri-*n*-butylphosphine and 10% methanol. The solution was usable for at least 1 month when stored at 4°C.

2.4. LC apparatus and conditions

A Hitachi Model 655A liquid chromatograph equipped with a Rheodyne Model 7125 syringe-loading sample injection valve (20-μl loop) and a Shimadzu RF-535 fluorescence monitor fitted with a 12-μl flow cell was used. The fluorescence spectrometer was operated at an excitation wavelength of 335 nm and an emission wavelength of 430 nm. A L-Column ODS column (250 mm × 4.6 mm i.d.; particle size 5 μm) (Chemical Inspection and Testing Institute, Tokyo) was used. The column temperature was ambient (25 ± 2°C). The mobile phase was methanol–water (70 + 30, v/v), which was delivered at a flow-rate of 0.8 ml min^{-1}.

2.5. Isolation of the fluorescent products of benzaldehyde (or 4-hydroxybenzaldehyde) with DTAD (or MTAD)

Products I–IV (Fig. 2)

To a methanolic solution of benzaldehyde (or 4-hydroxybenzaldehyde) (4 mmol in 10 ml) was added DTAD (or MTAD) solution [2.6 mmol DTAD (or MTAD) in 20 ml of methanol containing 0.6 g of tri-*n*-butylphosphine and 0.8 M disodium hydrogenphosphite]. The mixture was allowed to stand at 37°C for 1 h with stirring, followed by additional stirring for 6 h at room temperature (23–25°C). The precipitates were filtered, washed with methanol–water (1 + 1, v/v) and dried under reduced pressure. The crude

Table 1
Analytical data for compounds **I–IV**

Compound	M.p. (°C)	Yield (%)	MS: m/z [a]	^1H NMR [b] δ (ppm)
I	147–148	33	271	8.05–7.38 (5H, m, aromatic H), 7.51 and 7.28 (1H each, s each, aromatic H), 3.95 and 3.93 (3H each, s each, OCH_3)
II	235–236	37	287	7.85 and 6.92 (2H each, d each, aromatic H), 7.61 and 7.52 (1H each, s each, aromatic H), 3.86 and 3.85 (3H each, s each, OCH_3)
III	167–169	37	255	8.02–7.38 (5H, m, aromatic H), 7.44 and 7.22 (1H each, s each, aromatic H), 6.03 (2H, s, OCH_2O)
IV	167–169	38	271	7.84 and 6.92 (2H each, d each, aromatic H), 7.59 and 7.47 (2H each, d each, aromatic H), 6.12 (2H, s, O–CH_2–O)

All compounds were in the form of colourless needles.
[a] Base peak, M^+.
[b] The spectra were measured in dimethyl-d_6 sulphoxide.

product was chromatographed on a silica gel 60 column (25 × 2.7 cm i.d.) with *n*-hexane–ethyl acetate (1 + 1, v/v). The main fraction was evaporated to dryness under reduced pressure and the residue was recrystallized from aqueous 80–100% (v/v) ethanol. The properties of the four products are summarized in Table 1.

Products V–VIII (Fig. 2)

These products were prepared by the reaction of 2-amino-4- and -5-methoxythiophenols with benzaldehyde and 4-hydroxybenzaldehyde as described previously [1,2].

2.6. Procedure for spectrofluorimetric and LC determinations with DTAD

To 1.0 ml of aqueous test solution, 1.0 ml each of 8.0 mM sodium sulfite–2.8 M disodium hydrogenphosphite mixture and the DTAD solution were added. The mixture was warmed at 37°C for 60 min and the resulting fluorescence was measured at the excitation and emission maxima (see Table 2). To prepare the reagent blank, 1.0 ml of water in place of 1.0 ml of test solution was carried through the procedure.

For LC, the reaction mixture was neutralized to pH 6–7 with approximately 1 ml of 0.8 M sodium hydroxide solution and an aliquot of 20 μl of this solution was used.

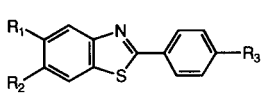

Product	R_1	R_2	R_3
I	CH_3O	CH_3O	H
II	CH_3O	CH_3O	OH
III	O- CH_2-O		H
IV	O- CH_2-O		OH
V	CH_3O	H	H
VI	CH_3O	H	OH
VII	H	CH_3O	H
VIII	H	CH_3O	OH

Fig. 2. Fluorescent products.

3. Results and discussion

3.1. Fluorescence properties of products I–VIII

The reaction products of DTAD (or MTAD) with benzaldehyde (or 4-hydroxybenzaldehyde) were found to be the corresponding benzothiazole derivatives (Fig. 2), based on the spectral data (Table 1). Further, the fluorescence properties (excitation and emission spectra and intensities) of their products were measured in various solvents (Table 2); the properties were investigated together with the products from 2-amino-4- and -5-methoxythiophenols (**V–VIII**) for comparison. As shown in Table 2, the products (**I–IV**) from DTAD and MTAD gave much more intense fluorescence than the other products (**V–VIII**), irrespective of the solvents used. Therefore, DTAD, which is easier to prepare than MTAD, was selected as a suitable reagent for aromatic aldehydes.

3.2. Conditions for the fluorescence reaction of 4-hydroxybenzaldehyde with DTAD

The optimum conditions for the reaction were established using 4-hydroxybenzaldehyde by the manual fluorimetric method. DTAD was reduced effectively with tri-*n*-butylphosphine (2.0–5.0 mM) to the thiol in the reagent solution; 4.0 mM tri-*n*-butylphosphine was employed in the reagent solution. Concentrations of DTAD ranging from 1.0 to 2.0 mM gave almost maximum fluorescence intensity; 1.1 mM is recommended. The reaction proceeded in sulphuric acid solution. The maximum reaction rate was attained at concentrations of 0.6–1.0 M sulphuric acid; 0.8 M was adopted for the procedure. Sodium sulphite and disodium hydrogenphosphite accelerated the fluorescence reaction of aromatic aldehydes with DTAD; 8.0 mM sodium sulphite and 2.8 M disodium hydrogenphosphite yielded the highest fluorescence intensity. Methanol was used to dissolve DTAD in the solution. Methanol–water (10 + 90, v/v) gave the highest intensity.

The DTAD reaction with the aldehydes (Fig. 3) occurred at temperatures above 0°C; higher temperatures allowed the fluorescence to develop

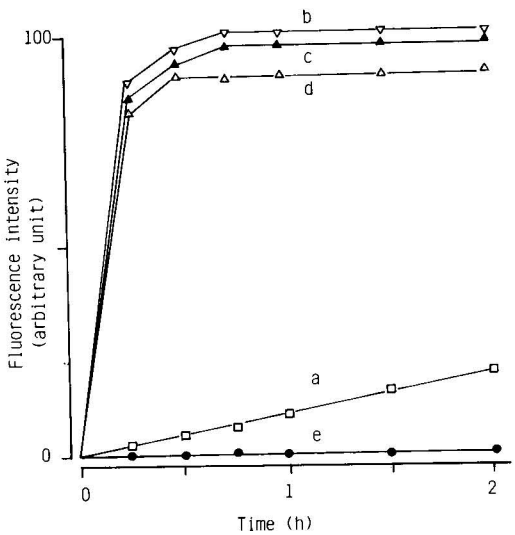

Fig. 3. Effect of reaction time and temperature on the fluorescence reaction of 4-hydroxybenzaldehyde with DTAD. Portions (1.0 ml) of 4-hydroxybenzaldehyde (10 nmol ml^{-1}) were treated as in the recommended procedure at different temperatures: (a) 0; (b) 37; (c) 50; (d) 70°C. (e) Reagent blanks at 0–70°C.

more rapidly. However, temperatures higher than 50°C caused a decrease in fluorescence, probably because of decomposition of the derivatives produced. The fluorescence intensities at 37°C reached maxima after standing for 45 min, and the resulting fluorescence was stable at 37°C for at least 2 h. Warming at 37°C for 60 min was selected for obtaining reproducible results.

The excitation and emission maxima of the fluorescence from 4-hydroxybenzaldehyde derivatives occurred at 371 and 482 nm, respectively. The fluorescence intensity of 4-hydroxybenzaldehyde with DTAD was ca. 20 times higher than that with 2-amino-4-methoxythiophenol. However, DTAD caused an intense blank fluorescence; the intensity was ca. 40 times of that with 2-amino-4-methoxythiophenol. These results indicate that DTAD is more suitable for LC than for a manual fluorimetric method.

3.3. Fluorescence from other aldehydes

Many aromatic aldehydes fluoresce under the conditions recommended. The excitation and emission maxima, and the lower limits of determination, are given in Table 3. However, arylalkyl aldehydes (e.g., phenylacetaldehyde, cinnamaldehyde and *p*-dimethylaminocinnamaldehyde) and aliphatic aldehydes (e.g., formaldehyde, acetalde-

Table 2
Excitation and emission maxima [λ(ex) (nm), λ(em) (nm)] and relative intensities (RFI) (in parentheses) of the fluorescence of compounds **I–VIII** in various solvents

Compound	Water		Methanol		Acetonitrile		Acetone		Chloroform		Hexane	
	λ(ex) (RFI) [a]	λ(em)	λ(ex) (RFI) [a]	λ(em)	λ(ex) (RFI) [a]	λ(em)	λ(ex) (RFI) [a]	λ(em)	λ(ex) (RFI) [a]	λ(em)	λ(ex) (RFI) [a]	λ(em)
I	333 (57.9)	433	335 (49.0)	417	335 (37.3)	413	341 (36.0)	411	338 (40.9)	408	335 (28.9)	399
II	335 (100.0)	422	337 (97.5)	409	336 (72.3)	401	341 (64.2)	399	337 (59.4)	403	337 (85.9)	399
III	337 (62.6)	433	337 (66.2)	416	337 (51.5)	413	342 (47.0)	410	338 (42.2)	402	335 (22.5)	390
IV	339 (46.5)	424	339 (97.8)	407	337 (73.8)	401	342 (68.2)	397	340 (70.3)	400	338 (81.5)	395
V	328 (1.4)	430	325 (1.6)	412	326 (1.5)	408	327 (5.6)	413	333 (1.5)	403	331 (2.6)	373
VI	333 (4.4)	416	333 (5.9)	401	339 (3.3)	386	328 (13.6)	410	335 (4.7)	392	339 (11.0)	386
VII	325 (3.9)	407	330 (3.8)	396	330 (3.8)	396	326 (14.7)	405	328 (3.5)	385	328 (3.4)	385
VIII	323 (68.0)	405	325 (66.3)	392	324 (42.4)	384	335 (43.7)	383	326 (40.4)	388	325 (58.8)	386

[a] The intensity of **II** in water was taken as 100.

hyde, propionaldehyde, isovaleraldehyde, *n*-butynaldehyde, crotonaldehyde and acrolein) do not fluoresce under the conditions recommended.

The reactivity of substances other than aldehydes was similar to that with 2-amino-5-methoxythiophenol [1].

3.4. Application of DTAD to LC

A mixture of six aromatic aldehydes (3,4-dihydroxybenzaldehyde, isovanillin vanillin, benzaldehyde, 4-methoxybenzaldehyde and 4-methylbenzaldehyde) was derivatized with DTAD and the derivatives were separated by reversed-phase LC on an L-Column ODS column with aqueous methanol–water (70 + 30, v/v) as the mobile phase. The excitation and emission maxima of the fluorescence derivatives in the mobile phase shifted to shorter wavelengths, and were almost the same as those of products **I–IV** in water and methanol (Table 1). Hence, the derivatives were determined tentatively at 430 nm with excitation at 335 nm. The optimum LC conditions were as described under Experimental.

Table 3
Excitation and emission maxima [λ(ex), λ(em)] of the fluorescence from various aldehydes with DTAD and the limits of determination (LOD) (signal-to-noise ratio = 2)

Aromatic aldehyde [a]	λ(ex) (nm)	λ(em) (nm)	LOD ($\times 10^{-8}$ M)
Benzaldehyde	354	483	36
2-Hydroxybenzaldehyde	382	481	21
3-Hydroxybenzaldehyde	353	476	13
4-Hydroxybenzaldehyde	371	482	44
2,4-Dihydroxybenzaldehyde	387	468	25
3,4-Dihydroxybenzaldehyde	381	477	75
2-Methoxybenzaldehyde	379	480	2
3-Methoxybenzaldehyde	353	485	9
4-Methoxyhenzaldehyde	373	484	27
Piperonal	378	482	24
Vanillin	378	480	41
Isovanillin	342	427	53
2-Chlorobenzaldehyde	338	480	25
4-Chlorobenzaldehyde	344	372	11
o-Phthalaldehyde	388	445	60
Terephthalaldehyde	348	384	8
Cinnamaldehyde	354	488	30
Veratralaldehyde	377	480	22

[a] Portions (1.0 ml) of 10 nmol ml^{-1} aromatic aldehyde solution were treated according to the procedure.

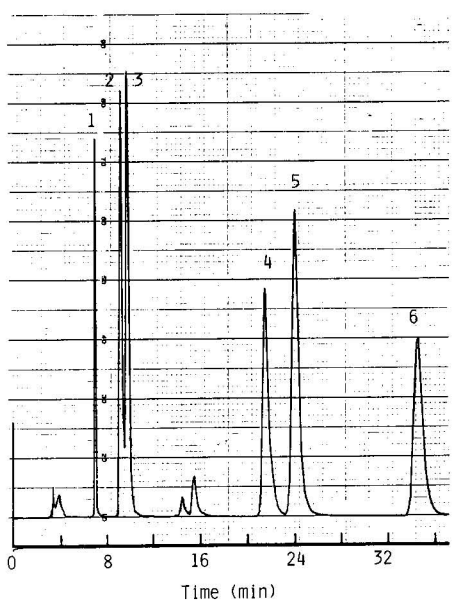

Fig. 4. Chromatogram of DTAD derivatives of aromatic aldehydes. A portion (1.0 ml) of a standard mixture of six aldehydes (0.1 nmol ml^{-1} each) was treated according to the procedure for the LC method. Peaks: 1 = 3,4-dihydroxybenzaldehyde; 2 = isovanillin; 3 = vanillin; 4 = benzaldehyde; 5 = 4-methoxybenzaldehyde; 6 = 4-methylbenzaldehyde; others = reagent blank.

Fig. 4 shows a typical chromatogram obtained with a standard mixture of the six aromatic aldehydes. The individual aldehydes each gave a single peak in the chromatogram. The fluorescent response of the DTAD derivatives of the aldehydes was stable for at least 24 h in daylight and 48 h at 4°C in the dark. Linear relationships were obtained between the peak heights and the amounts of the aldehydes up to at least 10 pmol per 20-μl injection. The precision was established by repeated injections ($n = 10$) of a mixture of the six aromatic aldehydes (1 nmol ml^{-1} each). The relative standard deviations did not exceed 2.5% for all the compounds. The detection limits were 10 fmol (3,4-dihydroxybenzaldehyde), 8 fmol (isovanillin), 8 fmol (vanillin), 17 fmol (benzaldehyde), 15 fmol (4-methoxybenzaldehyde) and 20 fmol (4-methylbenzaldehyde) on-column (signal-

to-noise ratio = 3). The sensitivities were 4–100 times better than those of the LC method with 2-amino-4-methoxythiophenol and the other ATs [1].

The proposed reagent is fairly stable in air and daylight and has excellent properties as regards sensitivity and selectivity for the derivatization of aromatic aldehydes. Hence, it should be applicable to the determination of aromatic aldehydes in small amounts of biological materials.

References

[1] H. Nohta, F. Sakai, M. Kai, Y. Ohkura, S. Hara and M. Yamaguchi, Anal. Chim. Acta, in press.
[2] R.L. Mital and S.K. Jain, J. Chem. Soc. C, (1969) 2148.

ELSEVIER

Analytica Chimica Acta 291 (1994) 197–204

ANALYTICA CHIMICA ACTA

A fluorogenic reagent for amino acids in liquid chromatography, 4-(2-cyanoisoindolyl)phenylisothiocyanate

Osamu Imakyure, Masaaki Kai, Yosuke Ohkura *

Faculty of Pharmaceutical Sciences, Kyushu University 62, Maidashi, Higashi-ku, Fukuoka 812, Japan

(Received 1st November 1993; revised manuscript received 3rd December 1993)

Abstract

A newly synthesized Edman-type fluorogenic reagent, 4-(2-cyanoisoindolyl)phenylisothiocyanate, reacted with 20 tested amino acids in a basic medium to produce the corresponding thiocarbamoyl derivatives. The derivatives were converted in an acidic medium to the thiohydantoin derivatives which were separated by reversed-phase chromatography and detected by fluorimetry. The on-column detection limits for amino acids ($S/N = 3$) were on the subpicomole level. Dipeptides, Leu–Ala and Ala–Gly also reacted with the reagent to produce the thiocarbamoyl derivatives which were cleft in an acidic medium at the peptide bonds to produce the thiohydantoin derivatives of the N-terminal amino acids.

Key words: Liquid chromatography; Edman-type fluorogenic reagent; Amino acids

1. Introduction

Phenylisothiocyanate (PITC) has been used for the amino acid compositional analysis [1] and the sequential analysis of peptides and proteins [2]. In recent years, reversed-phase liquid chromatography (LC) has been widely utilized for the determination of amino acids and peptides. The LC determination of the PITC–amino acid derivatives, has low sensitivity because the derivatives are monitored by UV detection only.

In this article studies on the analytical sensitivity of several PITC-type fluorogenic reagents such as fluorescein isothiocyanate [3,4], 4-(*N*,*N*-dimethylamino)-1-naphthylisothiocyanate [5], 4-(*N*-1-dimethyl-aminonaphthalene-5-sulfonylamino)-phenylisothiocyanate [6,7] are reported. More recently, 7-*N*,*N*-dimethylaminosulphonyl-4-(2,1,3-benzoxadiazolyl)isothiocyanate and 7-aminosulphonyl-4-(2,1,3-benzoxadiazolyl)isothiocyanate have been presented as fluorogenic Edman-type reagents [8]. However, those reagents have not performed well for the Edman degradation, because of their low reactivity to amino acids or peptides. 4-(*N*-*tert*-Butoxycarbonylaminomethyl) phenylisothiocyanate [9] was not utilized for the Edman degradation since a side reaction occurred during the cleavage step of thiocarbamoyl derivatives of peptides with anhydrous trifluoroacetic acid.

In this study, an Edman-type reagent, 4-(2-cya-

* Corresponding author.

0003-2670/94/$07.00
SSDI 0003-2670(93)E0705-C

noisoindolyl)phenylisothiocyanate (CIPIC) which has a highly fluorescent cyanoisoindolyl moiety (Fig. 1) was synthesized, in the hope that it would be a more reactive and more sensitive fluorogenic reagent than the above mentioned fluorogenic reagents. The reaction conditions of the precolumn fluorescence derivatization with CIPIC were investigated for the LC determination of amino acids. Applicability of the use of the reagent to the Edman degradation was also preliminarily examined using Ala–Gly and Leu–Ala as the simplest model peptides.

2. Experimental

2.1. Apparatus

Uncorrected fluorescence spectra were measured with a Hitachi F-2000 spectrofluorimeter in 10×10 mm quartz cells; spectral bandwidths of 10 nm were used in both the excitation and emission monochromators. ^{1}H Nuclear magnetic resonance (NMR) spectra were obtained with a JOEL JNM-PS-110 spectrometer at 270 MHz using approximately 5% (w/v) solution containing tetramethylsilane as as internal standard. The electron impact mass spectra (EIMS) were measured with a JOEL JMS-DX300 spectrometer interfaced to a JOEL JMS-3500 data system.

2.2. Chemicals and solutions

Amino acids were obtained from Takara Kohsan (Tokyo) and Ala–Gly and Leu–Ala were purchased from Sigma (St. Louis, MO). Other chemicals and solvents were of analytical reagent grade or LC grade. CIPIC (10 mM) was dissolved in acetonitrile. The reagent solution was usable for at least one month when stored in the dark at room temperature.

2.3. Synthesis of CIPIC (Fig. 1)

A mixture of *o*-phthalaldehyde (536 mg, 4 mmol), *p*-aminoacetanilide (600 mg, 4 mmol), potassium cyanide (260 mg, 4 mmol) in 1 ml of water and 15 ml of methanol was stirred for 90 min at room temperature (25–28°C). The resulting insoluble product (compound I) was filtered, and washed with 5 ml of cold methanol. Compound I was suspended in 60 ml of ethanol, and refluxed in the presence of 30 ml of 1 M hydrochloric acid for 10 h. The reaction mixture was concentrated in vacuo to give a colourless bright crystalline powder (compound II, approximately 100 mg). Compound II (84 mg, 0.36 mmol) was suspended in 40 ml of benzene–tetrahydrofuran (1 : 1, v/v), and refluxed in the presence of triethylamine (65 mg, 0.64 mmol) and thiophosgene (40 mg, 0.35 mmol) for 1 h. After concentration in

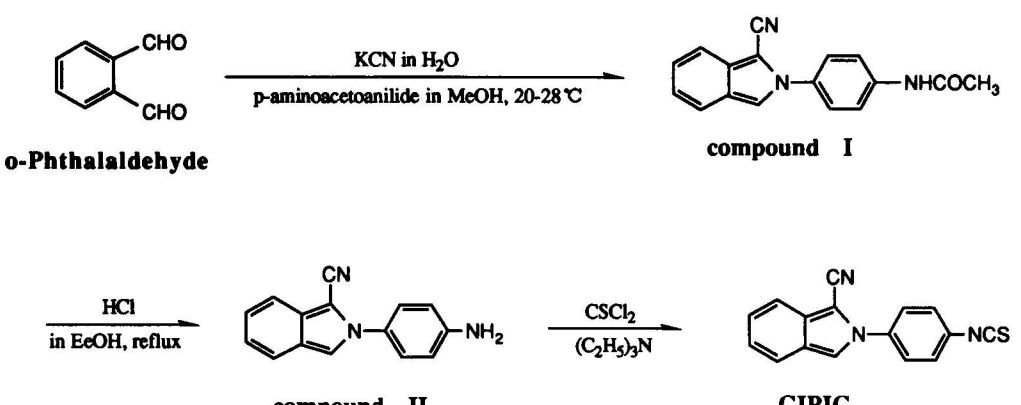

Fig. 1. Synthetic route of CIPIC.

vacuo, the resulting residue was recrystallized from acetonitrile to give CIPIC as colourless needles; yield, 37 mg (3.3% based on *o*-phthalaldehyde); m.p. (uncorrected), 172°C; EIMS (*m/z*), 275 (M^+); elemental analysis, calculated for $C_{16}H_9N_3S$, C 69.82, H 3.27, N 15.27%, found, C 69.67, H 3.29, N 15.22%. ^1H NMR spectrum (δ, ppm), 7.14–7.75 (9 H, multiplet, aromatic protons).

2.4. Derivatization procedure (Fig. 2)

A portion (50 μl) of 0.1 mM amino acids or Ala–Gly and Leu–Ala in acetonitrile–water (90:10, v/v) was mixed with 50 μl of acetonitrile–triethylamine–pyridine (90:1.25:8.75, v/v) for amino acids or acetonitrile–triethylamine (90:10, v/v) for the peptides and 50 μl of 10 mM CIPIC solution. The mixture was heated at 80°C for 5 min. To the reaction mixture after cooling in an ice–water bath were added 200 μl of 25 mM sodium phosphate buffer (pH 8.5) for amino acids or of water for the peptides and 200 μl of carbon tetrachloride. After rigorously mixing and then centrifuging, a portion (20 μl) of the aqueous layer containing the coupling derivatives (thiocarbamoyl derivatives) was subjected to LC. For the conversion of the derivatives to the corresponding thiohydantoin derivatives, the aqueous layer (100 μl) was successively mixed with 50 μl of 2.5 M hydrochloric acid and then heated at 80°C for 5 min. A 20-μl portion of the mixture was used for LC.

2.5. Procedure for the measurement of amino acids and peptides that remained unreacted

After the above mentioned coupling reaction of amino acids or the peptides with CIPIC and the carbon tetrachloride extraction, a portion (100 μl) of the aqueous layer was mixed with 10 μl of an *o*-phthalaldehyde reagent solution [prepared by dissolving 50 mg of *o*-phthalaldehyde in 1.25 ml of methanol followed by the addition of 50 μl of 2-mercaptoethanol and 11.2 ml of 0.4 M sodium borate buffer (pH 8.5)]. The final reaction mixture (20 μl) was subjected to reversed-phase LC with fluorescence detection at 350 nm excitation and 460 nm emission according to the literature [10].

2.6. LC system and its operating conditions

The LC system consisted of a Hitachi 655 liquid chromatograph equipped with a Rheodyne 7125 syringe-loading sample valve (20-μl loop) and a Tosoh FS-8000 fluorescence spectrometer fitted with a 15-μl flow cell. The fluorescence detector was operated at an excitation wavelength of 260 nm and an emission wavelength of 410 nm. The column was a TSKgel ODS-120T (150 × 4.6 mm i.d., particle size 5 μm; Tosoh,

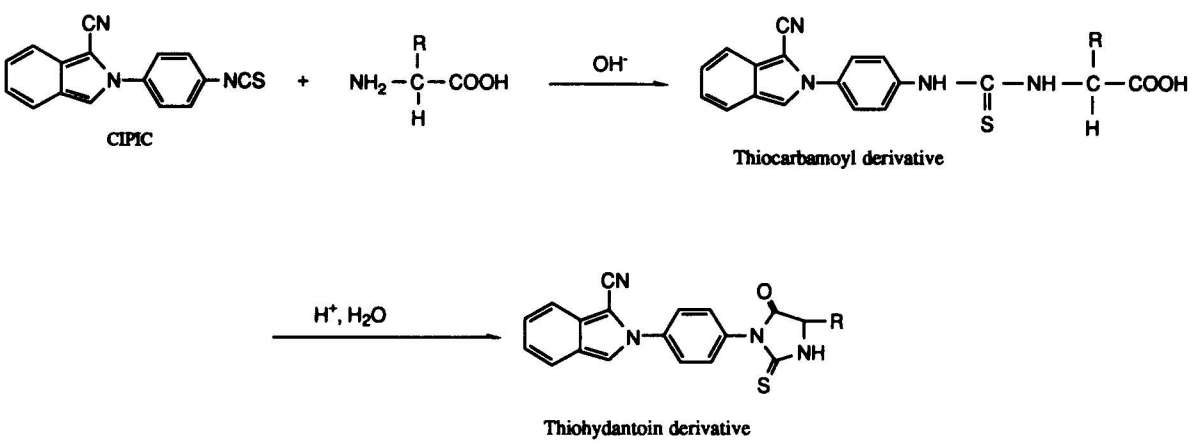

Fig. 2. Possible derivatization route of amino acid with CIPIC.

Tokyo). The column temperature was ambient (24 ± 4°C). For the separation of the fluorescent derivatives from amino acids and the peptides, a gradient elution of acetonitrile concentration was carried out using two eluents: acetonitrile–tetrahydrofuran–50 mM triethylamine acetate (pH 8.5)–water (20:5:10:65 and 80:5:10:5, v/v) (see Figs. 3–5). The flow-rate was 1.0 ml/min.

3. Results and discussion

CIPIC was synthesized by three-step reactions starting from *o*-phthalaldehyde and *p*-aminoacetanilide (Fig. 1). The chemical structure of CIPIC was confirmed by the spectral data and elemental analysis data described in the Experimental section. In this study, the derivatives of amino acids or peptides with CIPIC were not isolated. CIPIC possessed an isothiocyanate moiety in the molecule, and thus CIPIC seemed to behave in the same manner as PITC: CIPIC reacts with amino acids or the peptides in a basic medium to produce the corresponding thiocarbamoyl derivatives (coupling step), and then the derivatives were converted in an acidic medium to the corresponding thiohydantoin derivatives of the amino acids, or of the *N*-terminal amino acids of the peptides (conversion step) (Fig. 2).

Fig. 3 shows chromatographic separation of the reaction mixture of Gly, Ala and Leu, used as model amino acids in the investigations, with CIPIC after either coupling reaction or subsequent conversion reaction. LC was performed on a reversed-phase ODS column with a gradient elution of acetonitrile concentration (20–74%, v/v) in the mobile phase containing 10 mM triethylamine acetate (pH 8.5) and 5% (v/v) of tetrahydrofuran.

The fluorescent derivatives formed by the coupling reaction of the amino acids with CIPIC were eluted earlier than the peaks due to ammonia and reagent-blank (Fig. 3A). A derivative from ammonia (peak 4 in Fig. 3A) was observed

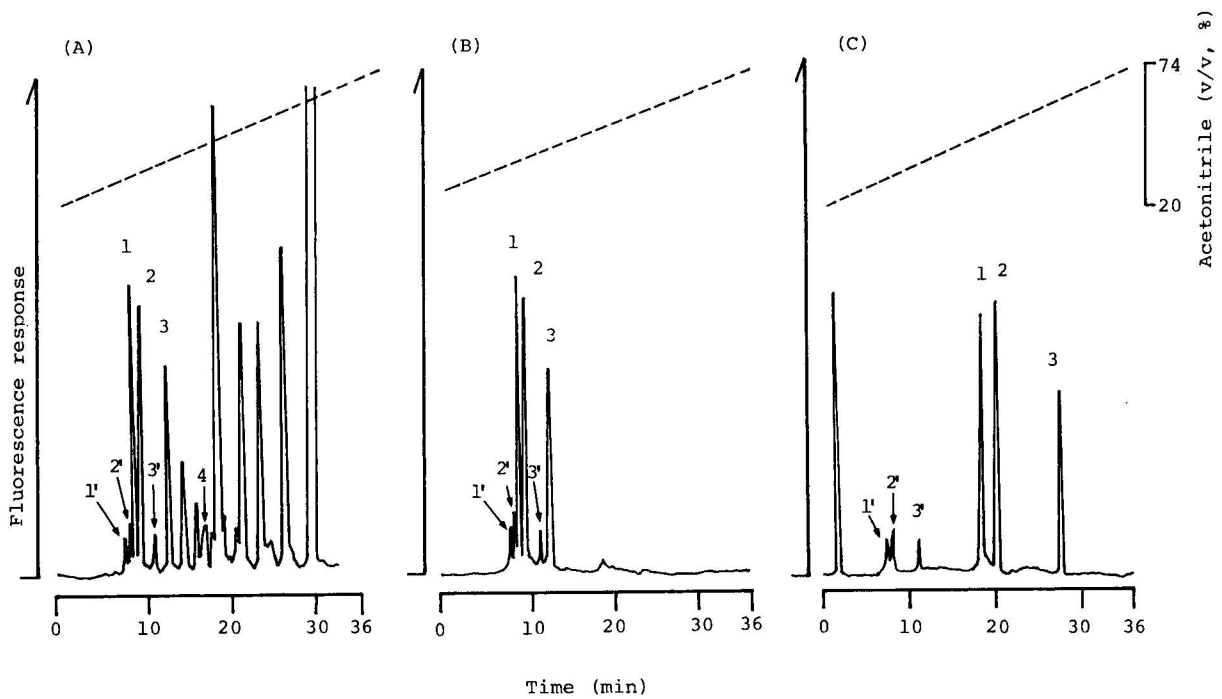

Fig. 3. Chromatograms of a coupling reaction mixture (A) before and (B) after washing with carbon tetrachloride, and of (C) its conversion reaction mixture of the amino acids (5 nmol each per reaction tube). Peaks: 1 = Gly; 1′ = by-product for Gly; 2 = Ala; 2′ = by-product for Ala; 3 = Leu; 3′ = by-product for Leu; 4 = ammonia; others = reagent blank.

in the chromatogram after the coupling reaction, but its by-product was not detected even when treatment with 10 mM ammonia was performed throughout the procedure. The reason remained unknown. The blank and ammonia peaks at retention times of 14–30 min disturbed the detection of the peaks for the thiohydantoin derivatives of the amino acids (Fig. 3A and C). Therefore, in the recommended procedure, the interfering substances in the reaction mixture were removed by extraction with carbon tetrachloride after the coupling reaction (Fig. 3B).

The coupling reaction with CIPIC afforded two peaks for each of the model amino acids (Fig. 3A and B). Their thiohydantoin derivatives were formed from the latter peaks (peaks 1, 2 and 3) for each of the amino acids, and the former peaks (peaks 1′, 2′ and 3′) were found to be due to by-products for the respective amino acids (Fig. 3B and C). The by-products still remained undegraded in the reaction mixture even after the acidic conversion reaction. The by-products were observed in the 20 tested amino acids other than Cys which could not afford fluorescent peak(s). However, the conversion reaction allowed the thiohydantoin derivatives of amino acids to be separable from the by-products. In addition, secondary amines such as Pro and Hyp also reacted with the reagent to produce their thiohydantoin derivatives.

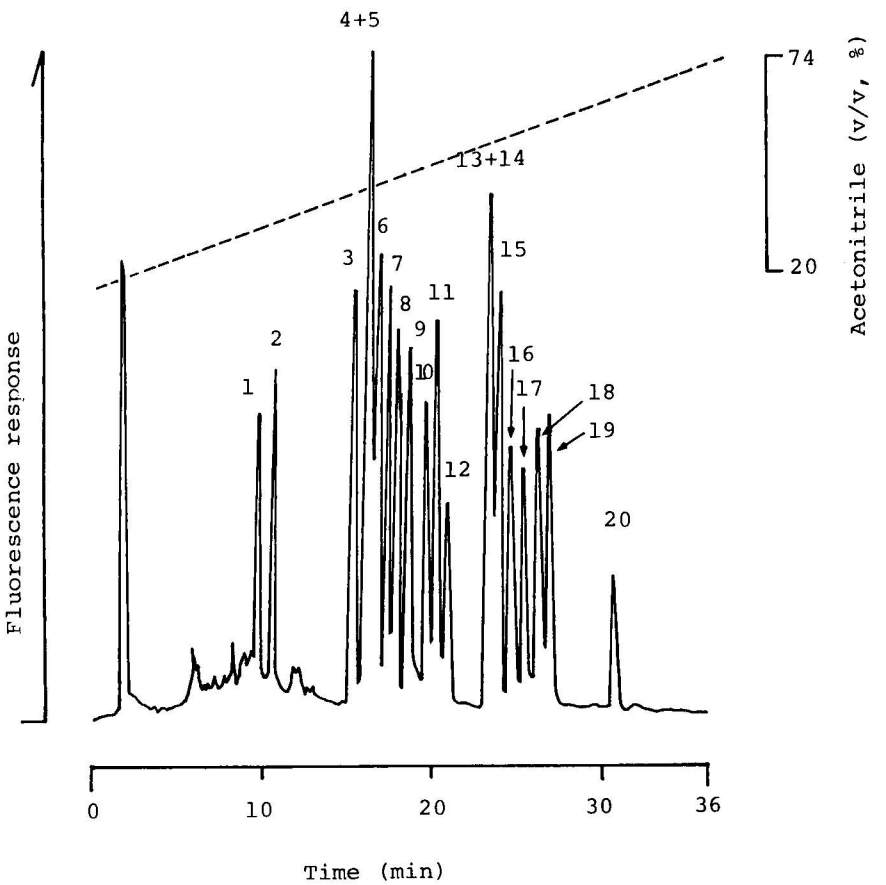

Fig. 4. Chromatogram of the thiohydantoin derivatives of 20 amino acids (5 nmol each per reaction tube) in the conversion reaction mixture following the coupling reaction. Peaks: 1 = Asp; 2 = Glu; 3 = Asn; 4 = His 5 = Gln; 6 = Ser; 7 = Thr; 8 = Arg; 9 = Gly; 10 = Hyp; 11 = Ala; 12 = Tyr; 13 = Pro; 14 = Met; 15 = Val; 16 = Trp; 17 = Phe; 18 = Ile; 19 = Leu; 20 = Lys; others = by-products and reagent blank.

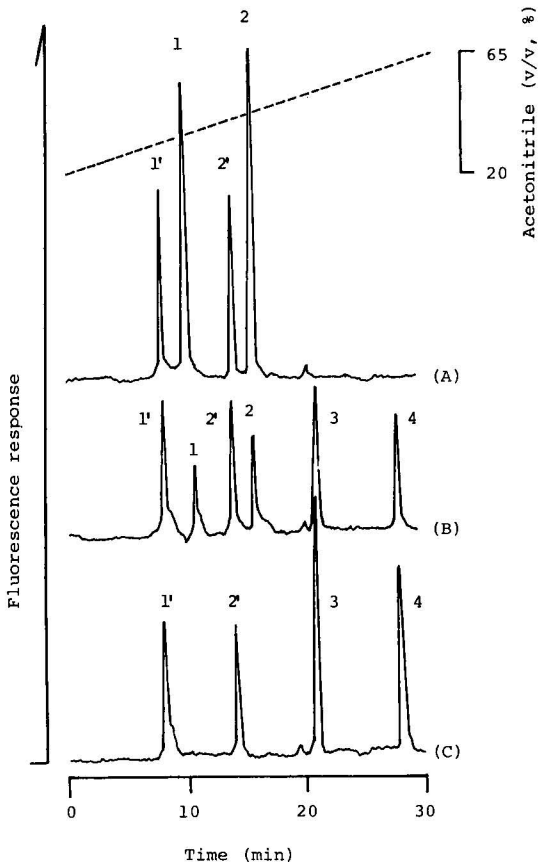

Fig. 5. Chromatograms of (A) a coupling reaction mixture and its conversion reaction mixture of Ala–Gly and Leu–Ala (5 nmol each per reaction tube) at reaction times of (B) 2 min and (C) 5 min. Peaks: 1 = Ala–Gly; 1′ = by-product for Ala–Gly; 2 = Leu–Ala; 2′ = by-product for Leu–Ala; 3 = N-terminal Ala; 4 = N-terminal Leu.

Fig. 4 depicts the chromatogram of the final reaction mixture of the 20 amino acids. All tested amino acids were derived to the corresponding single thiohydantoin derivatives by the conversion reaction. However, the derivatives were not completely separated by LC with linear gradient elution of acetonitrile (20–74%, v/v) in the mobile phase. The peaks of Gln and Met overlapped with those of His and Pro, respectively. In the chromatogram, the small plural peaks other than peaks 1 and 2 at retention times of 5–15 min were the by-products, which were produced from each amino acid by the coupling reaction.

The fluorescence spectra of the fractionated peaks of Gly, Ala, Leu, His, Asp and Hyp in the chromatography were measured. The excitation and emission maxima for those peaks as both the thiocarbamoyl and thiohydantoin derivatives were around 260 nm and 410 nm, respectively.

On the other hand, Ala–Gly and Leu–Ala also reacted in a basic medium with CIPIC to produce the thiocarbamoyl derivatives (peaks 1 and 2 in Fig. 5A). The coupling reaction gave by-products (peaks 1′ and 2′ in Fig. 5A) for the peptides. When the coupling reaction mixture was subjected to the conversion reaction, the peaks for the thiocarbamoyl derivatives disappeared with reaction time, and the thiohydantoin derivatives (peaks 3 and 4 in Fig. 5B and C) of their N-terminal amino acids were alternatively produced. The production of the thiohydantoin derivatives of the N-terminal amino acids was confirmed by treating the respective peptides according to this procedure.

The fluorescence excitation and emission maxima of the eluents from the peaks were around 260 and 410 nm, respectively.

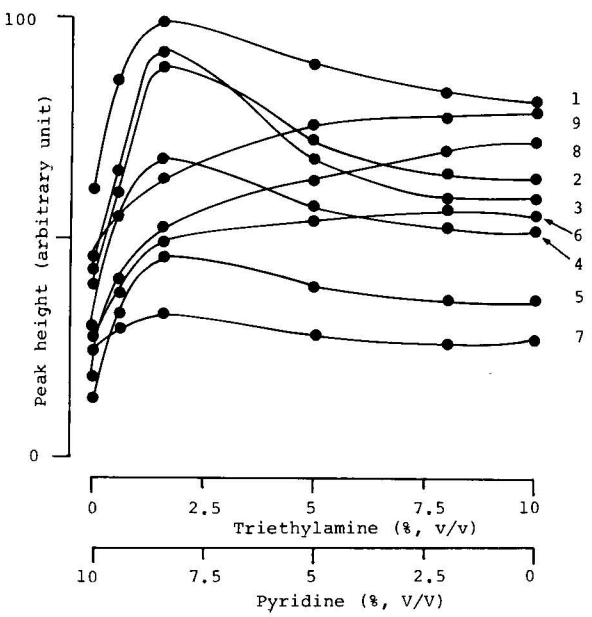

Fig. 6. Effect of triethylamine and pyridine concentrations on the coupling reaction of the amino acids and dipeptides (5 nmol each per reaction tube). Curves: 1 = Gly;2 = Ala; 3 = Arg; 4 = Val; 5 = Leu; 6 = Glu; 7 = Trp; 8 = Ala-Gly; 9 = Leu-Ala.

The optimum reaction conditions of amino acids (Gly, Ala, His, Glu, Val, Trp and Leu) and the dipeptides with CIPIC were investigated utilizing reversed-phase LC with fluorescence detection.

The coupling reaction proceeded well in the presence of amines, triethylamine and/or pyridine; in their absence, the peak heights for the coupling products were reduced to approximately 5% of the peak heights obtained in their presence. The maximum peak heights for the amino acids were attained by the use of an acetonitrile solution containing 1.25% triethylamine and 8.75% pyridine (Fig. 6), and the maximum heights for the peptides were obtained at a concentration of triethylamine of 10% in the absence of pyridine.

Higher temperatures in the range 50–100°C allowed both the coupling and conversion reactions to proceed more rapidly; the maximum peaks heights for the amino acids and peptides were attained at 80°C for 5 min or longer in both the coupling and conversion reactions (Fig. 7) and thus heating at 80°C for 5 min was recommended in the procedure.

The formation of by-products in the coupling reaction of the amino acids and peptides (Figs. 3 and 4) was not significantly affected by the concentrations of triethylamine and/or pyridine, and the reaction times. However, water content in the coupling reaction mixture affected the yield of the by-products: for instance, when the amount of water was increased to 50% in the coupling reaction mixture (200 μl), the peak heights of the by-products increased approximately five times and those of the thiocarbamoyl derivatives decreased to approximately half of those given in the recommended procedure. The structure of the by-products remained unknown.

The yields of the thiocarbamoyl derivatives from the 20 amino acids and the dipeptides (5 nmol each in the reaction mixture) by the coupling reaction with CIPIC under the recommended conditions were estimated by measuring amounts of amino acids or peptides that remained unreacted. The measurement was per-

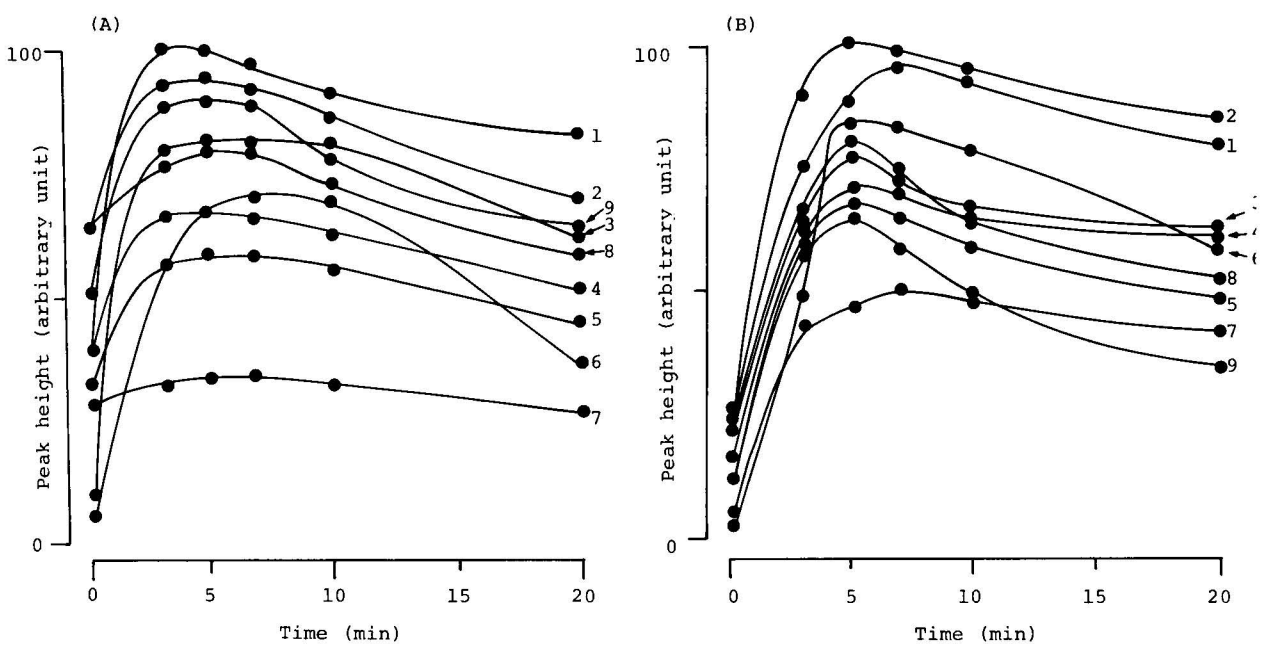

Fig. 7. Effect of reaction time on the formation of (A) coupling derivatives for for amino acids and dipeptides, and (B) thiohydantoin derivatives for the amino acids and N-terminal amino acids of the dipeptides (5 nmol each per reaction tube) at 80°C. Curves: 1 = Gly; 2 = Ala; 3 = Arg; 4 = Val; 5 = Leu; 6 = Glu; 7 = Trp; 8 = Ala-Gly; 9 = Leu-Ala.

formed by reversed-phase LC with precolumn derivatization using *o*-phthalaldehyde and 2-mercaptoethanol, fluorogenic reagents for primary amines [10]. The amino acids and peptides that remained in the reaction mixture could not be detected; the concentrations were less than 0.01 nmol per reaction tube. Therefore, it was assumed that approximately 100% of the amino acids or peptides reacted with CIPIC produced the thiocarbamoyl derivatives and the by-products.

The thiocarbamoyl and thiohydantoin derivatives of the amino acids and dipeptides in the respective reaction mixtures were stable since the corresponding peak heights were not changed significantly after the reaction mixtures were allowed to stand at room temperature (20–28°C) for 1 h.

In the conversion reaction, introduction of 0.8 M hydrochloric acid in the reaction mixture provided the amino acids with the maximum peak heights. This acidic concentration caused the coupling products of the peptides to cleave the peptide bonds to yield the corresponding thiohydantoin derivatives of N-terminal amino acids.

The calibration graph for each of the tested amino acids and the two peptides showed a linear relationship between the peak heights of their thiohydantoin derivatives and the amounts (0, 0.5, 1.0, 2.5, 5.0 nmol per reaction tube, $n = 2$ for each plot). The regression equations for the graphs were $y = 21.4x - 0.648$ ($r = 0.999$) for Gly, $y = 22.1x - 0.414$ ($r = 0.994$) for Ala, $y = 14.8x - 0.586$ ($r = 0.999$) for Val, $y = 17.0x - 0.379$ ($r = 0.997$) for Arg, $y = 18.3x - 0.169$ ($r = 0.998$) for Glu, $y = 7.60x - 0.019$ ($r = 0.994$) for Trp, $y = 11.9x - 0.130$ ($r = 0.995$) for Leu, $y = 18.0x - 0.240$ ($r = 0.998$) for Ala–Gly and $y = 11.4x + 0.523$ ($r = 0.996$) for Leu–Ala, in which y, x and r represent the peak height (mm), the amount (nmol) and the correlation coefficient, respectively. In addition, their calibration graphs were linear up to at least 50 nmol per reaction tube. The precision of the present method was established with five replicated determinations using the amino acids and dipeptides (5 nmol each per reaction tube). The relative standard deviations were 3.7–6.8%. The detection limits for the amino acids at a signal-to-noise ratio of 3 were 0.3–0.7 pmol per 20-μl injection volume.

In conclusion, the newly synthesized reagent, CIPIC, was usable for the fluorescence derivatization of amino acids under the reaction conditions similar to those for the Edman reagent, PITC. The detection sensitivity in LC with fluorescence detection was at least two order-of-magnitude higher than that using the PITC reagent in LC with UV detection [1], and nearly the same as those using other fluorogenic reagents [5–8]. The reactivities of CIPIC to the amino acids and dipeptides were sufficiently high. It was also possible to determine the N-terminal amino acids of the dipeptides by this reaction with CIPIC. These facts suggest that CIPIC is a promising fluorogenic Edman-type reagent; application to the Edman degradation of large peptides using CIPIC is in progress including some modifications of the LC conditions for the satisfactory separation of the 20 amino acid–thiohydantoin derivatives.

References

[1] S.A. Cohen, B.A. Bildlingmeyer and T.L. Tavin, Nature (London), 320 (1986) 769.
[2] G.E. Tarr, in M. Elizinga (Ed.), Methods in Protein Sequencing Analysis, Humana Press, Clifton, NJ, 1982, p. 233.
[3] H. Kawauchi, K. Tujimura, H. Maeda and N. Ishida, J. Biochem., 66 (1969) 783.
[4] K. Muramoto, H. Kamiya and H. Kawauchi, Anal. Biochem., 141 (1984) 446.
[5] H. Ichikawa, T. Tanimura, T. Nakajima and Z. Tamura, Chem. Pharm. Bull., 18 (1970) 1493.
[6] S.-W. Jin, G.-X. Chen, Z. Palacz and B. Wittmann-Liebold, FEBS Lett., 198 (1986) 158.
[7] H. Hirano and B. Wittmann-Liebold, Biol. Chem. Hoppe-Seyler., 367 (1986) 1259.
[8] K. Imai, S. Uzu, K. Nakashima and S. Akiyama, Biomed. Chromatogr., 7 (1993) 56.
[9] J.J. L'Italien and S.B.H. Kent, J. Chromatogr., 283 (1984) 149.
[10] B.N. Jones and J.P. Gilligan, J. Chromatogr., 266 (1983) 471.

ELSEVIER

Analytica Chimica Acta 291 (1994) 205–210

ANALYTICA CHIMICA ACTA

Determination of 2,4,6-trinitrotoluene and its biodegradation products by normal-phase liquid chromatography

Hanfa Zou [a,*], Shifen Zhou [b], Xin Hu [b], Mingfang Hong [a], Yukui Zhang [a], Peichang Lu [a]

[a] *National Chromatographic R&A Centre, Dalian Institute of Chemical Physics, Academia Sinica, Dalian 116011, China*
[b] *Department of Enviromental Engineering, East China University of Technology, Nanjing 210014, China*

(Received 9th December 1993)

Abstract

A normal-phase liquid chromatographic (LC) method with silica as the stationary phase for the separation of 2,4,6-trinitrotoluene (TNT) and its biodegradation products was developed. Baseline separation of TNT, 2,4-dinitrotoluene, 2-amino-4,6-dinitrotoluene, 4-amino-2,6-dinitrotoluene, 2,4-diamino-6-nitrotoluene and 2,6-diamino-4-nitrotoluene was achieved. Extraction methods for the preparation of samples from TNT reduction ponds in a TNT-making factory are described, and extracted samples were analysed by the developed LC method.

Key words: Liquid chromatography; Extraction; Trinitrotoluene

1. Introduction

2,4,6-Trinitrotoluene (TNT) is a common main constituent in explosives. TNT and its reduction products have been found in water and soil. This contamination is a result of TNT waste-disposal practices during the manufacture, loading and packing of explosives [1,2]. The biotransformation products of TNT include 2- and 4-aminodinitrotoluenes and 2,4- and 2,6-diaminonitrotoluenes [3]. Plants can take up TNT and metabolize it to 2- and 4-aminodinitrotoluenes [4], and so it could enter the food chain. TNT reduction products have been identified in the blood and urine of personnel in explosive manufacturing plants [5]. Because of the mutagenicity of these compounds, analytical methods for TNT and its reduction products have important enviromental and biomedical applications. The isomers have proved difficult to separate by gas, liquid or thin-layer chromatography. Kaplan and Kaplan [6] developed a gradient liquid chromatographic method to separate TNT and eight reduction products. Feltes and Levsen [7] also developed a method of reversed-phase liquid chromatography (RPLC) with photodiode-array detection to determine nitroaromatics in surface water. An RPLC method with electrochemical detection to determine nitroaromatics in enviromental waters was developed by Zhang and Lin [8]. However, baseline separation of monoaminodinitrotoluene isomers was not achieved. Walsh and Jenkins [9] described an LC method in which two C_{18}- and

* Corresponding author.

SSDI 0003-2670(93)E706-D

CN-bonded columns were connected in series for the baseline separation of TNT and its reduction products. It is well known that normal-phase (NP) LC with silica as the stationary phase is very effective for the separation of isomers [10–12]. In this work, the separation of TNT and its reduction products by NPLC with silica as the stationary phase was developed and samples taken from TNT reduction ponds in a TNT-making factory were analysed.

2. Experimental

2.1. Materials

Analytical standards for TNT, 2,4-dinitrotoluene, 2-amino-4,6-dinitrotoluene, 4-amino-2,6-dinitrotoluene, 2,4-diamino-6-nitrotoluene and 2,6-diamino-4-nitrotoluene were obtained from Laboratory 306, East China University of Technology. Other chemicals were of analytical reagent grade.

2.2. Apparatus

The NPLC experiments were done by using a stainless-steel column (300 × 40 mm i.d.) packed with Spherisorb silica gel of 5-μm particle diameter (Phase Separations, Deeside, UK). The column used were packed at the National Chromatographic R&A Centre, Dalian. The mobile phases were delivered by a Waters Model 510 pump. Eluates were detected at 254 nm with a Waters Model 490 programable multi-wavelength detector. The flow-rate of the mobile phase was 10 ml/min. The samples were loaded with a laboratory-made injection valve.

Table 1
Recovery of TNT and its reduction products by the acidic, salt and ammonia extraction methods

Extraction method	Run	Recovery (%) [a]				
		TNT	2-A	4-A	2,4-DA	2,6-DA
Acidic	1	96.5	96.7	85.6	–	–
	2	97.5	99.2	78.0	–	–
	3	96.8	95.3	80.8	–	–
	Average	96.9	97.1	81.5	–	–
Salt	1	48.3	15.7	50.0	8.1	10.9
	2	50.8	8.8	37.8	5.6	9.0
	3	56.7	11.0	42.5	7.2	7.1
	Average	51.9	11.8	43.4	7.0	9.0
Ammonia	1	78.9	100.0	89.1	66.1	74.1
	2	81.6	88.1	92.0	62.5	66.7
	3	73.7	92.7	91.8	63.5	63.0
	Average	78.1	93.6	91.0	64.0	67.0

[a] TNT = trinitrotoulene; 2-A = 2-amino-4,6-dinitrotoluene; 4-A = 4-amino-2,6-dinitrotoluene; 2,4-A = 2,4-diamino-6-nitrotoluene; 2,6-DA = 2,6-diamino-4-nitrotoluene.

2.3. Preparation of samples

The extraction of TNT and its biodegradation products from water was studied. In the acidic extraction method, 500 ml of water containing standard samples were passed through a filter and the particles and supernatant in the water were removed. The pH of the filtered water was adjusted to 1–2 with dilute HCl. The acidic solution was transferred to a separating funnel and 50

Table 2
Capacity factors of TNT and its biodegradation products in silica-based NPLC with different compositions of hexane–propan-2-ol as the eluent

Solute	Concentration of isopropanol (%, v/v)				
	5	9	13	18	21
TNT	0.18	0.13	0.10	0.08	–
2,4-Dinitrotoluene	0.46	0.37	0.26	0.17	0.19
4-Amino-2,6-dinitrotoluene	3.67	1.61	0.93	0.51	0.45
2-Amino-4,6-dinitrotoluene	4.58	2.07	1.22	0.69	0.61
2,6-Diamino-4-nitrotoluene	21.70	11.12	6.49	3.39	–
2,4-Diamino-6-nitrotoluene	32.36	16.17	9.12	4.85	–

ml of diethyl ether were added and shaken for 5 min. The upper liquid phase was removed into a flask and evaporated on a rotary evaporator nearly to dryness at 50°C. A 2-ml volume of propan-2-ol was used to dissolve the analytes for injection into the LC system.

In the salt extraction method, 75 g of NaCl were added to filtered water; the other operations were the same as in the acidic extraction method. In the ammonia extraction method, the pH of the filtered water was adjusted to 7–8 with dilute ammonia solution; the other operations were the same as in the salt extraction method.

2.4. Calibration

Calibration graphs for the external standards (TNT, 2,4-dinitrotoluene, 4-amino-2,6-dinitrotoluene and 2-amino-4,6-dinitrotoluene) were determined. TNT (69.8 mg), 2,6-dinitrotoluene (114.1 mg), 2-amino-4,6-dinitrotoluene (123.9 mg) and 4-amino-2,6-dinitrotoluene (132.2 mg) were weighed into 50-ml volumetric flasks and diluted to volume with propan-2-ol. Volumes of 1.0, 1.5, 2.0, 2.5 and 3.0 ml of the solutions of each standard solute were placed in 10-ml volumetric flasks and diluted to volume with propan-2-ol. These dilute standard solutions were used to determine the calibration graphs for each solute.

3. Results and discussion

The recoveries of TNT and its biodegradation products by the acidic, salt and ammonia extraction methods and the reproducibilities are given in Table 1. The acidic extraction method gave a high recovery and reproducibility for TNT, 2- and 4-monoaminodinitrotoluenes, but very low recoveries for 2,4- and 2,6-diaminonitrotoluenes, possibly because one of the active amino groups in 2,4- and 2,6-diaminonitrotoluene is protonated in acidic extraction. The recoveries of 2,4- and 2,6-diaminonitrotoluenes in the salt extraction method were higher than those in the acidic extraction method, but the recoveries for TNT and 2- and 4-monoaminodinitrotoluenes by the salt extraction method were low. In the ammonia extraction method, the protonation of monoaminodinitrotoluenes and diaminonitrotoluenes was almost completely suppressed, which increased their solubility in the diethyl ether solution. It can be seen that the ammonia extraction method gives fairly high recoveries and good reproducibilities for TNT, monoaminodinitrotoluenes and diaminonitrotoluenes. This method was used to extract the TNT and its biodegradation products from the samples from the TNT

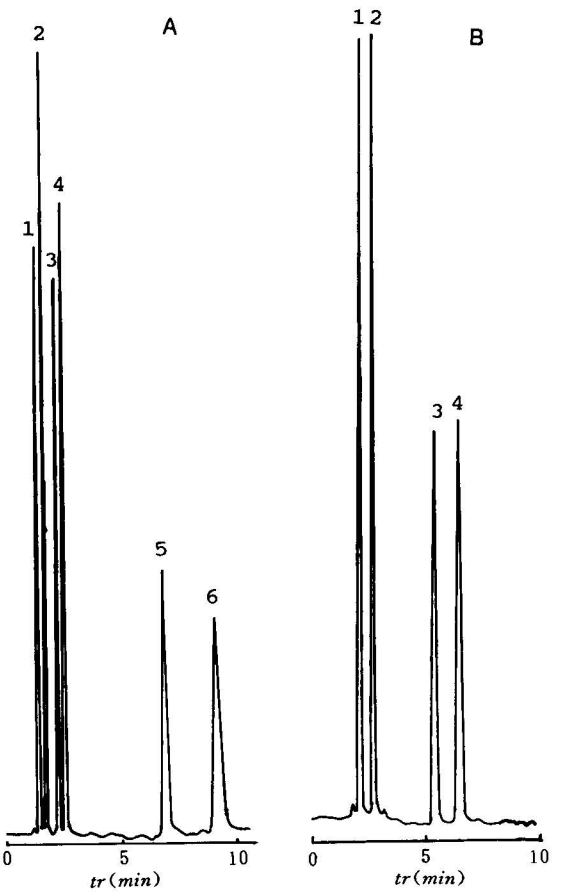

Fig. 1. Chromatograms for separation of a standard sample of TNT and its reduction products by silica-based NPLC. Column, 300×4.0 mm I.D. packed with Spherisorb (5 μm). Flow-rate, 1.0 ml min^{-1}; detection wavelength, 254 nm. Mobile phase: (A) hexane–propan-2-ol (79 : 21, v/v); (B) hexane–propan-2-ol (90:10, v/v). Peaks: 1 = TNT; 2 = 2,4-dinitrotoluene; 3 = 4-amino-2,6-dinitrotoluene; 4 = 2-amino-4,6-dinitrotoluene; 5 = 2,6-diamino-4-nitrotoluene; 6 = 2,4-diamino-6-nitrotoluene.

biodegradation ponds in a TNT-making factory.

It is well known that silica-based NPLC is one of the most effective means for the separation of isomers. The retention times of six solutes including isomers of 2- and 4-aminodinitrotoluenes and 2,4- and 2,6-diaminonitrotoluenes in silica-based NPLC with different compositions of propan-2-ol–hexane as eluents were measured, and the capacity factors with propan-2-ol–hexane as the eluents were calculated and are given in Table 2. Fig. 1 shows two chromatograms for the separation of a standard sample with propan-2-ol–hexane as the eluent. It can be seen that for TNT and its biodegradation products baseline separation can be achieved. The retention of 2-amino-4,6-dinitrotoluene or 2,6-diamino-4-nitrotoluene is always lower than that of 4-amino-2,6-dinitrotoluene or 2,4-diamino-6-nitrotoluene, possibly owing to be the steric effect of the methyl group, which decreases the interaction between the amino group in the analytes and the silanol group on the silica surface. The relative retentions (α) for pairs of isomers of 2- and 4-aminodinitrotoluenes and 2,4- and 2,6-diaminonitrotoluenes as a function of propan-2-ol concentration in the eluent are shown in Fig. 2. It can be seen that there is no serious effect of propan-2-ol concentration on the relative retention values for the pairs of isomers.

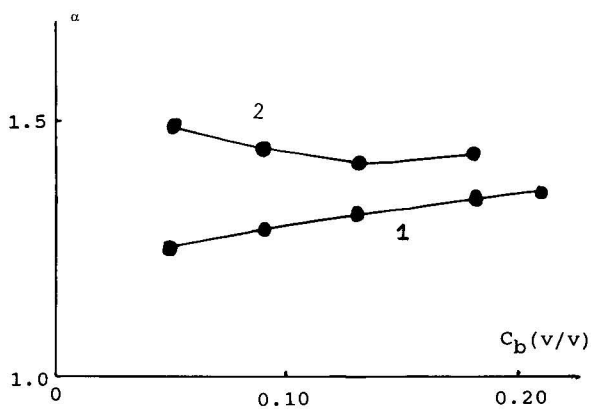

Fig. 2. Relative retention values (α) of pairs of isomers as a function of the propan-2-ol concentration (c_b) in the eluent. Curves: 1 = 2-amino-4,6-dinitrotoluene–4-amino-2,6-dinitrotoluene; 2 = 2,4-diamino-6-nitrotoluene–2,6-diamino-4-nitrotoluene.

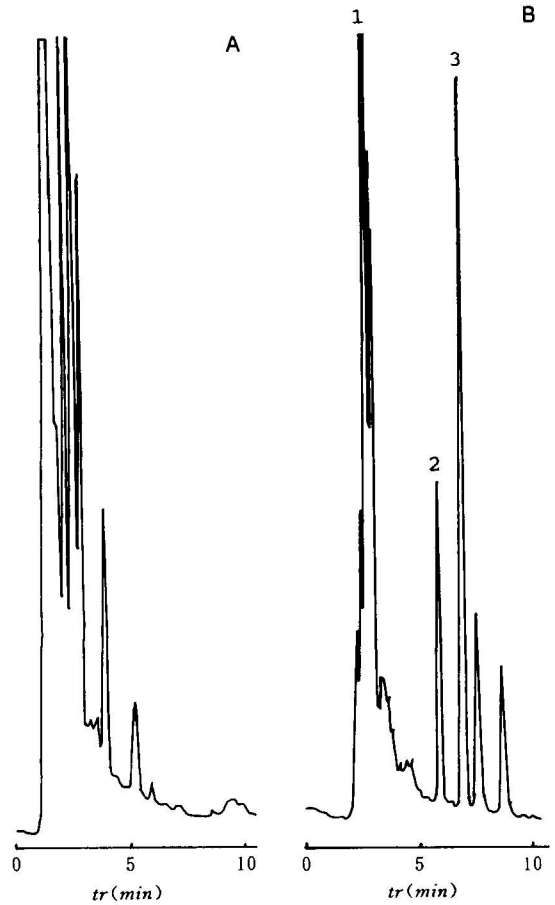

Fig. 3. Chromatograms for the separation of TNT and its reduction products in a sample taken from reduction pond 1 in a TNT-making factory. Mobile phase: (A) hexane–propan-2-ol (79:21, v/v); (B) hexane–propan-2-ol (90:10, v/v). Peaks: 1 = TNT; 2 = 4-amino-2,6-dinitrotoluene; 3 = 2-amino-4,6-dinitrotoluene.

For practical separations, 500 ml of the sample solutions were taken from TNT biodegradation ponds Nos. 1, 2, 3 and 4 in a TNT-making factory, and the sample solutions were prepared by the ammonia extraction method. Fig. 3A and B shows the chromatograms of the extracted solution from pond 1 and Fig. 4A, B and C shows the chromatograms of extracted solutions from ponds 2, 3 and 4, respectively. It can be observed that with exception of a peak with a retention of 1.2 min, no TNT on its biodegradation products were detected in ponds 2, 3 and 4, which means that TNT was completely biodegraded or no wastewa-

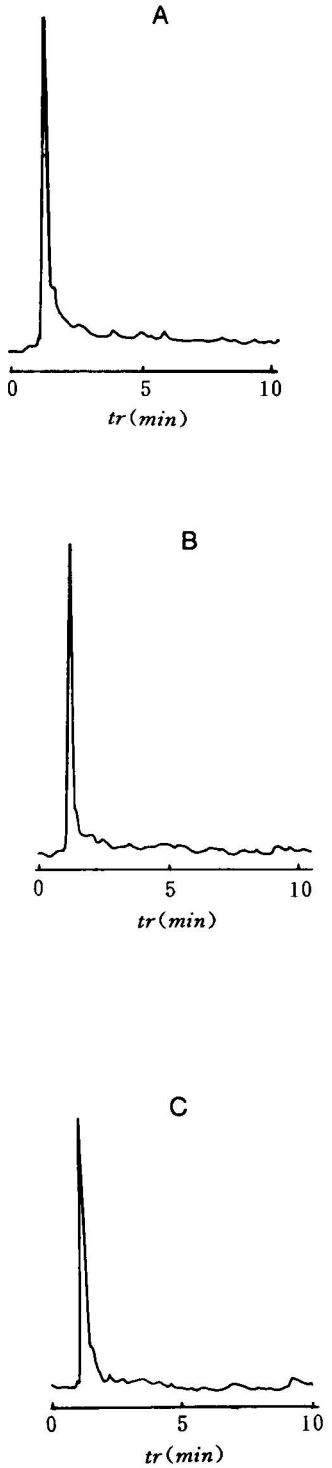

Fig. 4. Chromatograms for the separation of TNT and its reduction products in samples taken from reduction ponds (A) 2, (B) 3 and (C) 4 in a TNT-making factory. Mobile phase: hexane–propan-2-ol (79:21, v/v).

Table 3
Calibration graphs of peak height H (cm) versus solute concentration C (mg l^{-1}) for TNT and its biodegradation products

Solute	Calibration graph	r	Range of linearity (ng)
TNT	$H = 19.2C - 2.42$	0.9937	1–8370
2,4-Dinitrotoluene	$H = 13.3C + 0.06$	0.9917	1–6850
4-Amino-2,6-dinitrotoluene	$H = 14.1C + 0.07$	0.9963	1–7940
2-Amino-4,6-dinitrotoluene	$H = 20.3C + 0.10$	0.9989	1–7430

ter had been poured into these ponds. Fairly high amounts of TNT and its biodegradation products, 2- and 4-aminodinitrotoluenes, were detected in pond 1, which means that TNT was being biodegraded in that pond. In order to determine the amounts of TNT and 2- and 4-aminodinitrotoluenes in pond 1, their calibration graphs were obtained under the experimental conditions in Fig. 1B; Table 3 gives the relationships between peak height and injected concentration. The minimum detectable level (MDL), equal to twice the baseline noise, together with the injected concentration, injected volume and the response value of the analytes and the noise of baseline are presented in Table 4. It can be seen that the MDL of TNT and its reduction products in this study is about 0.1 ng, which is higher than the value of 1.0 ng obtained by RPLC with photodiode-array detection as reported by Feltes and Levsen [7]. The amounts of the compounds found

Table 4
Concentrations of the standard samples and their response values, noise values of the baseline and minimum detectable levels (MDL)

Solute	Injected concentration (μg ml^{-1})	Response value (mV)	Noise value (mV)	MDL (ng)
TNT	27.9	557	0.1	0.10
2,6-Dinitrotoluene	22.8	351	0.1	0.13
4-Amino-2,6-dinitrotoluene	26.5	430	0.1	0.12
2-Amino-4,6-dinitrotoluene	24.8	588	0.1	0.08
2,6-Diamino-4-nitrotoluene	22.2	226	0.1	0.20
2,4-Diamino-6-nitrotoluene	25.1	122	0.1	0.41

Injection volume = 10 μl.

in pond 1 by NPLC were TNT 2.04, 4-amino-2,6-dinitrotoluene 0.04 and 2-amino-4,6-dinitrotoluene 0.09 mg l^{-1}.

The results demonstrate that the baseline separation of TNT and its biodegradation products including isomers by NPLC can be achieved, which is very useful for the peak identification and determination of these compounds. The MDL of TNT and its reduction products is ca. 1 ng by NPLC with UV detection at 254 nm.

References

[1] W.E. Pereira, D.L. Short, D.B. Manigold and P.K. Roscio, Bull. Environ. Contam. Toxicol., 21 (1979) 554.
[2] T.F. Jenkins, M.E. Walsh, P.W. Schumacher, P.H. Miyares, C.F. Bauer and C.L. Grant, J. Assoc. Off. Anal. Chem., 72 (1989) 890.
[3] N.G. McCormick, F.E. Feeherry and H.S. Levinson, Appl. Environ. Microbiol., 31 (1976) 949.
[4] A.J. Pallazzo and D.C. Leggett, J. Environ. Qual., 15 (1986) 49.
[5] J. Yinon and D.G. Hwang, Biomed. Chromatogr., 1 (1986) 123.
[6] D.L. Kaplan and A.M. Kaplan, Anal. Chim. Acta, 136 (1987) 425.
[7] J. Feltes and K. Levsen, J. High Resolut. Chromatogr., 12 (1989) 613.
[8] Y.-H. Lin and R.-K. Zhang, Xiamen Daxue Xuebao Ziran Kexueban, 28 (1989) 292.
[9] M.E. Walsh and T.F. Jenkins, Anal. Chim. Acta, 231 (1990) 313.
[10] L.R. Snyder, J.W. Dolan and J.R. Gant, J. Chromatogr., 165 (1979) 3.
[11] P. Jandera and J. Churacek, Adv. Chromatogr., 19 (1981) 125.
[12] Y. Zhang, H. Zou and P. Lu, J. Chromatogr., 515 (1990) 13.

PUBLICATION SCHEDULE FOR 1994

	S'93	O'93	N'93	D'93	J	F	M	A	M	J	J	A
Analytica Chimica Acta	281/1 281/2 281/3	282/1 282/2 282/3	283/1 283/2	283/3 284/1 284/2	284/3 285/1–2 285/3	286/1 286/2 286/3	287/1–2 287/3 288/1–2	288/3 289/1 289/2	289/3 290/1–2 290/3	291/1–2 291/3 292/1	292/2 292/3 293/1–2	293/3 294/1–2 294/3
Vibrational Spectroscopy		6/1			6/2		6/3		7/1		7/2	

INFORMATION FOR AUTHORS

Detailed "Instructions to Authors" for *Analytica Chimica Acta* was published in Volume 289, No. 3, pp. 381–384. Free reprints of the "Instructions to Authors" of *Analytica Chimica Acta* and *Vibrational Spectroscopy* are available from the Editors or from: Elsevier Science B.V., P.O. Box 330, 1000 AH Amsterdam, The Netherlands. Telefax: (+31-20) 5862459.

Manuscripts. The language of the journal is English. English linguistic improvement is provided as part of the normal editorial processing. Authors should submit three copies of the manuscript in clear double-spaced typing on one side of the paper only. *Vibrational Spectroscopy* also accepts papers in English only.

Rapid publication letters. *Letters* are short papers that describe innovative research. Criteria for letters are novelty, quality, significance, urgency and brevity. Submission data: max. of 2 printed pages (incl. Figs., Tables, Abstr., Refs.); short abstract (e.g., 3 lines); *no* proofs will be sent to the authors; submission on floppy disc; *no* revision will be possible.

Abstract. All papers and reviews begin with an Abstract (50–250 words) which should comprise a factual account of the contents of the paper, with emphasis on new information.

Figures. Figures should be prepared in black waterproof drawing ink on drawing or tracing paper of the same size as that on which the manuscript is typed. One original (or sharp glossy print) and two photostat (or other) copies are required. Attention should be given to line thickness, lettering (which should be kept to a minimum) and spacing on axes of graphs, to ensure suitability for reduction in size on printing. Axes of a graph should be clearly labelled, along the axes, outside the graph itself. All figures should be numbered with Arabic numerals, and require descriptive legends which should be typed on a separate sheet of paper. Simple straight-line graphs are not acceptable, because they can readily be described in the text by means of an equation or a sentence. Claims of linearity should be supported by regression data that include slope, intercept, standard deviations of the slope and intercept, standard error and the number of data points; correlation coefficients are optional.

Photographs should be glossy prints and be as rich in contrast as possible; colour photographs cannot be accepted. Line diagrams are generally preferred to photographs of equipment. Computer outputs for reproduction as figures must be good quality on blank paper, and should preferably be submitted as glossy prints.

Nomenclature, abbreviations and symbols. In general, the recommendations of IUPAC should be followed, and attention should be given to the recommendations of the Analytical Chemistry Division in the journal *Pure and Applied Chemistry* (see also *IUPAC Compendium of Analytical Nomenclature, Definitive Rules*, 1987).

References. The references should be collected at the end of the paper, numbered in the order of their appearance in the text (*not* alphabetically) and typed on a separate sheet.

Reprints. Fifty reprints will be supplied free of charge. Additional reprints (minimum 100) can be ordered. An order form containing price quotations will be sent to the authors together with the proofs of their article.

Papers dealing with vibrational spectroscopy should be sent to: Dr J.G. Grasselli, 150 Greentree Road, Chagrin Falls, OH 44022, U.S.A. Telefax: (+1-216) 2473360 (Americas, Canada, Australia and New Zealand) or Dr J.H. van der Maas, Department of Analytical Molecular Spectrometry, Faculty of Chemistry, University of Utrecht, P.O. Box 80083, 3508 TB Utrecht, The Netherlands. Telefax: (+31-30) 518219 (all other countries).

0003-2670/94/$07.00

This issue is printed on acid-free paper.

PRINTED IN THE NETHERLANDS

Flow-Through (Bio)Chemical Sensors

By **M. Valcárcel** and **M.D. Luque de Castro**, Department of Analytical Chemistry, University of Córdoba, 14004 Córdoba, Spain

Techniques and Instrumentation in Analytical Chemistry Volume 16

Flow-through sensors are more suitable than classical probe-type sensors for addressing real (non-academic) problems. The external shape and operation of flow-through (bio)chemical sensors are of great practical significance as they facilitate sample transport and conditioning, as well as calibration and sensor preparation, maintenance and regeneration, all of which result in enhanced analytical features and a wider scope of application. This is a systematic presentation of flow-through chemical and biochemical sensors based on the permanent or transient immobilization of any of the ingredients of a (bio)chemical reaction (i.e. the analyte, reagent, catalyst or product) where detection is integrated with the analytical reaction, a separation process (dialysis, gas diffusion, sorption, etc.) or both.

The book deals critically with most types of flow-through sensors, discussing their possibilities and shortcomings to provide a realistic view of the state-of-the-art in the field. The large numbers of figures, the wealth of literature references and the extensive subject index complement the text.

Contents: 1. Sensors in Analytical Chemistry. Analytical chemistry at the turn of the XXI century. Analytical information. What is a sensor? Sensors and the analytical process. Types of sensors. General features of (bio)chemical sensors. (Bio)chemical sensors and analytical properties. Commercial availability. Trends in sensor development.
2. Fundamentals of Continuous-Flow (Bio)Chemical Sensors. Definition. Classification. The active microzone. Flow-through cells. Continuous configurations. Regeneration modes. Transient signals. Measurement modes. The role of kinetics. Requirements for proper sensor performance.
3. Flow-Through Sensors Based on Integrated Reaction and Detection. Introduction. Flow-through sensors based on an immobilized catalyst. Flow-through immunosensors. Flow-through sensors based on an immobilized reagent. Flow-through sensors based on an *in situ* produced reagent.
4. Flow-Through Sensors Based on Integrated Separation and Detection. Introduction. Integrated gas diffusion and detection. Integrated liquid-liquid separation and detection. Integrated retention and detection. Flow-through sensors for multi-determinations based on integrated retention and detection. Ion-selective electrodes (ISEs) and ion-sensitive field-effect transistors (ISFETs).
5. Flow-Through Sensors Based on Integrated Reaction, Separation and Detection. Introduction. Integration of gas-diffusion, reaction and detection. Integration of dialysis, reaction and detection. Integration of sorption, reaction and detection.
Index.

© 1994 332 pages Hardbound
Price: Dfl. 355.00 (US$ 202.75)
ISBN 0-444-89866-2

ELSEVIER SCIENCE

ORDER INFORMATION
ELSEVIER SCIENCE B.V.
P.O. Box 330
1000 AH Amsterdam
The Netherlands
Fax: (+31-20) 5862 845

For USA and Canada
P.O. Box 945
Madison Square Station
New York, NY 10159-0945
Fax: (212) 633 3680

US$ prices are valid only for the USA & Canada and are subject to exchange rate fluctuations; in all other countries the Dutch guilder price (Dfl.) is definitive. Customers in the European Union should add the appropriate VAT rate applicable in their country to the price(s). Books are sent postfree if prepaid.